THE UNIVERSITY OF HULL

Surface Enhanced Raman Spectroscopy for Single Molecule Detection and Biosensing

being a Thesis submitted for the Degree of Doctor of Philosophy

in the University of Hull

by

Addison Robert Lee Marshall B.Sc. (Hons.)

September 2017

Contents

Acknowledgements

I would like to express my gratitude towards my supervisors: Ali Adawi, Nicole Pamme, Jenny Waby and John Proctor for their support and guidance. John was the reason for me wanting to pursue a PhD in the first place, working alongside someone so dedicated to their field on my BSc project was a fantastic and insightful experience.

In particular though, a special thanks goes to Ali, who throughout the entire project pushed me to achieve thorough and meticulous research techniques scrutinizing the details I alone may have overlooked, all while allowing me the flexibility to pursue our ideas. Not only this, he also gave me confidence, reassuring me that I was capable of the course material when I doubted myself, overall he provided me with the tool-set I needed to make me the researcher I am today. He was the best supervisor I could have asked for and was a pleasure to work with. As well, I thank Jean-Sébastien who challenged my work and helped me understand the importance of having a depth of understanding of the theory. I feel privileged to have the experience to work with these people and couldn't speak more highly of them.

Being a part of the Physics department since the start of my Foundation degree and moving through the BSc, I was taught by a number of the academic staff, all of whom helped me develop my skill-set in the field of physics so I thank you all. In particular, I would like to thank Martin Buzza who was another role model of mine when it came to physics, his deep understanding of a field as a whole is something I will always strive towards.

I would also like to extend my gratitude to my fellow postgraduates: Nick Appleyard, Bethany Newton, Rajpal Thethi, Mohammed Ibrahem, Anthony Edwards, Francesco Viscomi, Lee Smith, Charlotte Eling and everyone else in the offices who contributed their knowledge and experience towards my work. Mohammed and I both began our postgraduate journey together and will always be a close friend of mine. Especially, I would like to thank Anthony Edwards and Jamie Stokes who gave keen insight into the subject

material and were happy to provide their time to me when I had questions. Additionally I extend my gratitude to Dan Naylor who was always there to offer advice. I would also like to thank Brian Lambert and Will Harrison for their experience and knowledge of the laboratory.

I would like to thank my friends Kyle Granaghan and Tim Miles, who for some reason still want to spend time with me even though we have shared a living space on multiple occasions. They have provided me with the sanity I needed to see through the course of the degree.

My fiancée Thais, I couldn't ask for anyone better to spend my life with. Your support and encouragement through this work has been invaluable. I must apologise for the late night lab sessions, me waking up at 2 am to run another simulation before my timeslot ends as well as you spending recent months only seeing my back while I work at my desk, hopefully it is worth the effort.

Of course, I couldn't forget to thank my parents: Teresa and Adam Marshall and my sisters: Charlene and Rosalee who always believed in me. Their support throughout my life and the good upbringing they provided me made me what I am today.

In addition, I would like to thank the University of Hull for funding the project, Professor Steffen Petersen from the Medical Photonics Group at Aalborg University in Denmark for supplying the lysozyme samples for the biosensing chapter, as well as Shin-Sung Kim from Lumerical's engineering team.

Try not to become a man of success, but rather try to become a man of value.

— Albert Einstein

For my parents.

Declaration of Authorship

I declare that the work presented in this thesis is my own and has not been submitted in any form for examination in any previous work. The experimental and theoretical work carried out in the results chapters are my own work and have been presented in conference presentations listed in this thesis. The literature review and theory which contains figures and equations from journals and books are cited from the appropriate references throughout.

Publications

1. Dual-modal SERS/fluorescence AuNP probe for mitochondrial imaging [1]
2. Determining Molecular Orientation via Single Molecule SERS in a Plasmonic Nanogap [2]
3. Crossover between liquidlike and gaslike behavior in CH_4 at 400 K [3]

Conferences

- The 6th PhD experience Conference 2015 - Poster Presentation.
- SPIE Photonics Europe 2016 - Oral presentation.
- SPP8 - Poster Presentation.
- Optical Nanospectroscopy IV - Poster presentation
- Surface Enhanced Raman Scattering - SERS: Faraday Discussions - Poster presentation.

Abstract

The aim of this thesis is to design plasmonic nano-gaps capable of detecting materials down to sufficiently low concentrations such that single molecule characteristics are observed. We begin first, by discussing the theory of plasmonics. Then, we assess the recent literature on the subject to develop an understanding in the field of plasmonics and to describe the fundamental concepts behind how plasmonic nano-sensors operate. Also, this allows us to show where our research fits in.

Firstly, we utilise Finite Difference Time Domain (FDTD) methods and analysis of 3D models of electrodynamic interactions with simulated devices. These simulations provide an abundance of information regarding how the device behaves and where the optimum conditions are met regarding; film thickness and nanoparticle shape and size, allowing tunablility of the system to a specific light source to be possible. The Figure of Merit (FoM) we used takes into consideration both the near-field excitation enhancement, as well as the far-field emission enhancement projected directly from the position of our target material and how they would be collected via an $NA = 0.55$ objective lens. We find that the photon scattering efficiency is far greater for the dipolar rather than the quadrupole mode and is the main contributor to the enhancement of the Raman signal, which we confirm through experimental measurements.

The second area of research involves practical Surface Enhanced Raman Spectroscopy (SERS) experiments from our optimized nano-gaps. The nano-gaps were doped with the molecular dyes Rhodamine 6G and Crystal Violet at concentrations of $2 \times 10^{-7}\ M$. SERS measurements revealed differences in the relative intensities of their respective SERS peaks at low concentrations when compared to the SERS spectra measured from gaps doped the same dye at higher concentrations of $2 \times 10^{-5}\ M$. Time dependent SERS measurements showed that the SERS signal is stable over a long period of time, indicating the observed relative intensity changes are due to changes in molecular orientation from one gap to another, demonstrating that our optimized nano-gaps have single molecule sensitivity. When exciting at 532 *nm*, the 118 *nm* silver spheres used to form the nano-gap with the silver film below were shown to enhance the Raman signal by $4.2\times$ relative

to the 200 *nm* silver nano-spheres, and up to 7.73$\times$ relative to the 60 *nm* silver nano-spheres. When compared to our simulation results for the same structures excited with a Gaussian source with $NA = 0.55$, we showed the information collected from the Raman study correlated well with the theoretical data.

Following our work investigating single molecule characterisation of fluorescent materials, we began looking at trace levels of a conjugated polymer (F8-PFB). The previous investigation had been from a purely electromagnetic enhancement perspective using a secondary polymer matrix buffer which was optically transparent in the region of interest for the Raman spectra of our target molecule. This polymer provided a barrier between the target material and the metallic nanostructure, thereby minimizing the potential of photo-induced chemical processes in the Raman signal. In this study, the material itself forms the basis of the cavity between the particle and the film below. This system classifies the single molecule regime via the observation of intensity blinking events, which are characteristic of Single Molecule SERS (SM-SERS).

We also demonstrated the biosensing applications of our research, where nanoparticle clusters on a metallic film were used to produce spectra from bio-molecules undergoing conformation changes as a result of UV light exposure. The SERS spectra revealed decreased intensity from the Tryptophan (Trp) modes and appearance of disulphide bonds as time under UV light exposure progresses for lysozyme.

Our final chapter shows that by using nanoparticles coupled to different substrates such as Distributed Bragg Reflectors (DBRs) and dielectric slabs, the hybrid modes improved the Quality-factor (Q-factor) of the scattering spectra. Therefore, these systems theoretically have great potential for refractive index sensing with high sensitivity to binding activity of molecular targets. The highest Q-factor of the systems we investigated was the 200 *nm* gold particle coupled to the 2 μm dielectric slab at 22.48, followed by the same particle deposited on a 700 *nm* stop-band DBR at 7.41.

Chapter 1

Introduction

1.1 Nanoscale Sensing

Plasmonics has proved to be a flourishing field of interest in recent years. When coupled with advancements in Raman techniques, which provide detailed, nonintrusive information regarding the molecular fingerprint of a target analyte down to the single molecule level, it becomes a tremendously powerful spectroscopic tool for material analysis. In this chapter, we aim to introduce the concepts used throughout the thesis and describe the significance of the research and its impact on the field.

The underlying principles of plasmonics function around the utilization of metallic nanostructures, where plasmon resonances are generated by the coupling of optical excitations with the delocalized sea of electrons within the material. When light impinges metallic structures, the delocalized electrons in the material oscillate, these oscillations can be exploited by matching their frequency to that of the incident light. These phenomena are collectively known as plasmons [4–8].

The optical properties of metals on the nano-scale have been exploited for centuries, with the most famous example stemming from the Lycurgus Cup from the 4^{th} Century AD, which demonstrated dichroic optical effects. Usually it resembles an opaque dull green colour, however during light transmission through the glassware, the cup shines a brilliant red. It wasn't until many centuries later though that this subject was better understood [9]. The phenomenon was attributed to the presence of gold nanoparticles within the material, and throughout the 19^{th} and 20^{th} centuries Michael Faraday was able to make this connection publishing his work on the subject in 1857 [10]. Following this, in 1861 and 1862, James Clerk Maxwell gave us a set of equations that would define our classical

perspective on light matter interactions. “Maxwell’s Equations” describe the electric and magnetic field interactions and how they are affected through the influence of charge and currents [11]. Then, at the turn of the 20^{th} century in 1908, Gustav Mie formulated his electromagnetic solution to Maxwell’s equations for describing plane wave light scattering via a homogeneous sphere, hence Mie theory was born [12]. Rufus Ritchie predicted the existence of surface plasmons in 1957, this prompted the research environment of plasmonics [13].

Surface Plasmon Polaritons (SPPs) are electromagnetic interactions which propagate along the material’s surface at the interface between a conductor and dielectric. They have electric field which oscillates perpendicular to the surface, and arise as a result of oscillations of the metal’s surface electron plasma. The electrons in the conducting material are displaced by the incoming electric field and then oscillate as a result of the restoring force of the metallic ionic cores. Their most alluring property stems from their ability to confine light at the metal-dielectric interface at sub-wavelength scales. The drawback of SPPs stems from their dispersion relation properties, when we consider this relation in terms of energy and momentum; surface plasmons always have a larger momentum than a photon of the same frequency. Because energy and momentum are always conserved, additional momentum is required to access the SPP and account for this mismatch. So, as surface plasmons cannot be directly coupled to incident light, light on a smooth metal surface will never generate a surface plasmon [4, 14].

Alternatively, Localised Surface Plasmons (LSPs) can be generated via the use of metallic nanostructures such as spheres, cubes or rods [15–19]. The resonance in this case can then be tuned via the change in shape, size or material of the nanostructure under investigation. LSPs, as their name suggests, behave as non-propagating excitations of the conduction electrons of metallic nanostructures coupled to the electromagnetic field. LSPs are confined to the nanostructure (typically gold, silver or copper). Gold is often preferred as it is highly chemically stable, also its plasmonic behaviour is well documented as well as it being resistant to surface oxidation [20, 21]. Silver also has its advantages, exhibiting very narrow plasmon resonances in the visible light frequencies. However, it is

susceptible to oxidisation under normal laboratory conditions [19, 20, 22, 23]. The high signal output from metallic nanostructures is a well documented effect in plasmonics and can be attributed to the confinement of areas of high signal intensity generated which are known as "hot spots" [24–29].

Plasmonics has many applications, not only in the field of sensing [22, 30, 31], but also for solar cells [32], as well as nano-imaging beyond the diffraction limit [33]. Because of these alluring properties, plasmonics is becoming a rapidly growing area of research and when coupled with Raman spectroscopy, metallic nanostructures hold a wealth of information [34]. Raman spectroscopy was first discovered by Sir C. V. Raman owing to his work published in 1928 [35], which later earned him the Nobel prize in physics in 1930. When incident light impinges a material, it interacts with the bonds of its molecules. The scattered light then provides a molecular fingerprint of the molecule under investigation based on the vibrational modes associated with each molecular bond. Typically, Raman spectroscopy produces a very weak output due to low levels of photon generation, with cross sections of single molecules being $\sim 10^{-29}\ cm^2$ [36]. However, it is possible to enhance this by using plasmonic nanostructures, this leads us to Surface Enhanced Raman Spectroscopy (SERS). SERS was first observed from pyridine molecules adsorbed on electrochemically roughened silver electrodes by a research group from Southampton UK in 1973 [37]. Nano-gaps, for instance formed between metallic nanostructures can achieve $\sim 10^8\times$ enhancement of signal [38]. When coupled with the resonance Raman effect (SERRS), Raman cross sections can be amplified to $\sim 10^{-15}\ cm^2$, opening up the possibilities for single molecule SERS (SM-SERS) [36]. These fundamental principles are the foundation of our work, coupling refined, optimised plasmonic nanostructures with SERS.

The applications of SERS extend to many research areas due to its ability to identify chemical species and acquire structural information of the target molecule [39]. For example, SERS has been shown to be a useful technique in the field of biosensing, detecting various biological targets such as proteins, various diseases, lipids as well as applications to glucose detection for diagnosis of diabetes [40–47]. Not only this, but SM-SERS

allows for the detection of trace quantities of materials, this has numerous applications allowing for the authentication of artwork [48], chemical detection in environmental sciences [49, 50], as well as forensic science [51]. Therefore, SERS is a powerful tool for material analysis with cross disciplinary importance, which is why we utilise it throughout this thesis.

1.2 Thesis Structure

Our research focuses on using nanoparticles on a film to produce nano-gaps between the nanoparticle and a metallic layer below, these nano-gap formations are used throughout the thesis. We begin in Chapter 2 by describing the underlying theory, which describes the optical phenomena we are investigating. Then, Chapter 3 details the most relevant work published in the field with critical analysis of the techniques involved. After this, we show our research methodology in Chapter 4, explaining the experimental procedures, and device fabrication techniques used throughout the research.

Chapter 5 provides a complete theoretical description of the particle on a film geometry. These structures were analysed via FDTD methodology using Lumerical solutions, which is a commercial Maxwell equation solver and is used as a standard within this field for light matter interaction calculations. By presenting this systematic study of the nanoparticle geometry and nano-gap parameter sweeps, we are able to fully refine the structure for generation of large electromagnetic fields both in the near-field excitation, and far-field emission. This will be integral toward achieving the photon output necessary for single molecule detection, which we aim towards in later parts of the experimental sections. It is shown that examining optimisation characteristics of the plasmonic nano-gap regarding nanoparticle size and gap width is extremely important to generating the fields required for single molecule detection [38, 52–65].

Following this, Chapter 6 gives a fully descriptive account for SM-SERS of fluorescent dyes. SERS spectra are acquired from materials suspended in a polymer matrix cavity of 5 *nm* thickness between metallic nanoparticles and a 100 *nm* thick metal film. Maximum enhancement has been shown to take place in localized hot spots within these

gaps [24, 25, 27]. We show the optimisation process to prepare the most ideal nano-gap structure from gold and silver nanoparticles of different sizes and shapes, allowing us to select the most suitable structure to coincide with our excitation wavelength for single molecule investigations.

Practical investigations of Rhodamine 6G (R6G), and Crystal Violet (CV) were performed both separately, as well as in mixtures at low concentrations. Single molecule detection in this case is defined when orientational effects take place. At higher concentrations, the SERS signal will be attributed to many molecules of random orientation and the average effect will present all Raman modes within the collected spectra. However, when concentrations of the target material drop sufficiently, certain modes from the spectra will diminish or be lost all together. This is because the dipole moment of the molecular bonds from this orientation are either aligned, or misaligned with the electric field of the nanostructure, which dictates whether the signal is enhanced or not. SERS has the benefit that, unlike fluorescence, quenching does not occur when materials are in close proximity to the metallic structures, allowing these small minimalist structures to be fabricated with no spacing layers from the material to the metal. These fluorescent dyes have a well categorised Raman spectrum [66–70], and are shown to be distinguishable via these methods when in a mixture. The research deals with detecting the materials together, down to significantly low concentrations such that the spectra provided via scattered light from the nanostructure will be attributed to single molecules, and both materials can be successfully distinguished from one another. The work is integral to understanding SERS sensing and has wide applications, most notably, as we show in later parts of the thesis, in the field of biosensing.

Continuing the work on single molecule detection, Chapter 7 investigates Raman spectra from fluorescent conjugated polymers, which form the cavity between the particle and the metal film below. This system differs from the previous case as no secondary polymer was used to suspend the material. Therefore, nano-gaps were not kept at a uniform thickness and become narrower as concentration is reduced. The benefit of this is that it is possible to take advantage of the higher enhancement effects of the narrower

nano-gap, however, we can no longer define the single molecule regime as we did before. In this case, we define single molecule characteristics by the ***blinking effect***. The lack of polymer matrix to form a barrier between the target analyte and the metallic nanostructure means it is in direct contact, and therefore chemical enhancement effects can attribute an additional $10^1 - 10^2\times$ enhancement [71]. We show this intensity blinking effect via fluctuations in the 1605 cm^{-1} C-C stretching mode, which is the most prominent peak visible for F8-PFB via continuous measurements of individual particle cavity systems. Although the mechanisms behind the blinking effect in SERS is still a topic of debate and not fully understood, intensity blinking is considered to be a good indication of single molecule characteristics. One explanation suggested for the fluctuation of intensity is thermal diffusion of the single molecule in and out of the hot spots produced by the nanostructures which generate the large enhancement of signals [36, 72, 73].

Chapter 8 shows the potential for the nano-gap in this configuration to be used with biosensing. We demonstrate the system being used on lysozyme and Bovine Serum Albumin (BSA), which are proteins commonly found in living organisms. The lysozyme work deals with understanding the changes in the material's structure when exposed to UV light for given periods of time. UV light possesses a considerable amount of energy, sufficient to break C-C bonds, and capable of ionising an aromatic residue via photo-oxidation. Photons in the UVB range from $280 - 315$ *nm* have energies between 3.94–4.43 eV, which is likely to be sufficient for ionization of Tryptophan (Trp), a key component of lysozyme. We show through successive Raman spectra of lysozyme under UV light exposure, changes in the conformation of the material as time progresses. Following this, we examined BSA to give clear, defined peak positions of a biological analyte using the particle on a film geometry. We compare the spectra recorded from the nanoparticle clusters mixed with the BSA, with respect to the BSA in absence of the particles to quantify the enhancement they provide. The data suggests an enhancement of $\sim 15.5\times$ from the nano-clusters relative to the film. We can see that these devices are fully capable of detection of biological materials even at low concentrations from these preliminary results. However, more optimisation and a deeper understanding about the

functionality of these systems is necessary to design a LSP based biosensor tuned to our laser setup.

Following this, Chapter 9 details work performed via the theoretical study of dielectric slabs and Distributed Bragg Reflectors (DBRs) coupled to nanoparticles. In the previous results chapters, we have shown that there is typically a broad plasmon resonance associated with the system, however, coupling to dielectric slabs produces narrower hybridised modes. In order to improve the line-width, and hence the Quality factor (Q-factor) of the coupled hybrid system, a methodical, theoretical study was carried out. The Q-factor is a measure of the peak scattering relative to its respective line-width, the higher the Q-factor, the higher the FoM the device has for plasmon based sensing. First, we showed the difference between the particle on its own compared to the system with a dielectric slab or DBR. Then, scattering cross sections were recorded for a particle size sweep with a fixed DBR stop-band. The nanoparticle was shown to be scattering dominated within its extinction spectrum when its diameter exceeded 150 *nm*. Afterwards, a sweep of DBR stop-bands was performed for the 200 *nm* gold particle. This allowed the system to be properly tuned together and proper coupling to be achieved. When using a 700 *nm* stop-band DBR, we notice optimisation in the peak intensity with high Q-factor of the hybridised modes. The 200 *nm* gold particle coupled to the 2 μm thick dielectric slab produced the largest Q factor of our structures investigated, however there was a trade-off with its scattering cross section being lower.

Finally, a summary of the main points from each chapter is detailed in the conclusion of the report, we summarise the main findings and discuss any future projects the results detailed here may open the possibilities to.

Chapter 2

Theory

This chapter aims to outline the main theoretical concepts and introduce the background knowledge applicable to the research undertaken. This will encompass the general theory of plasmonics describing how surface plasmons and localised surface plasmons are generated where plasmonic events are described by oscillations in the delocalised sea of electrons of noble metals. Throughout this chapter, we show the main principles of electron behaviour in noble metals under the influence of incident light which forms the foundation of plasmonics governed by Maxwell's equations. We describe the behaviour of electrons mathematically with the Drude-Lorentz theoretical model. Following this, the concepts of surface and localised surface plasmons are introduced. Within these sections we discuss the principles used to understand the optical properties of metals in which we outline the main principles of the quasistatic approach as well as Mie theory.

Next, a breakdown of radiative and non-radiative processes are described through the use of energy level diagrams, where we discuss absorption and emission as described by Fermi's golden rule. Subsequently we apply our knowledge of plasmonics to Raman scattering. Then through the application of plasmonic nanostructures we show the enhancement characteristics of surface enhanced Raman scattering which forms the fundamental basis to our experimental chapters.

Lastly, we delve into the theoretical characteristics of Finite Difference Time Domain (FDTD) calculations. We show how they are utilised to calculate the electrodynamic field behaviour both in the near-field, as well as projected to the far-field. As well as this, we discuss the limitations of these simulation environments.

The intention therefore, is to describe the fundamental principles of these research environments and the way in which they function.

2.1 Maxwell's Equations

Plasmonics is a rapidly developing field of research which investigates the interaction mechanisms of electromagnetic fields impinging on metallic structures. The optical properties of metallic nanostructures have been utilised for many years dating as far back as the $4th$ century AD where the Romans used nanostructures in glasses to scatter and generate brilliant colours [9]. The same techniques are also used in church windows as seen in Figure 2.1.1.

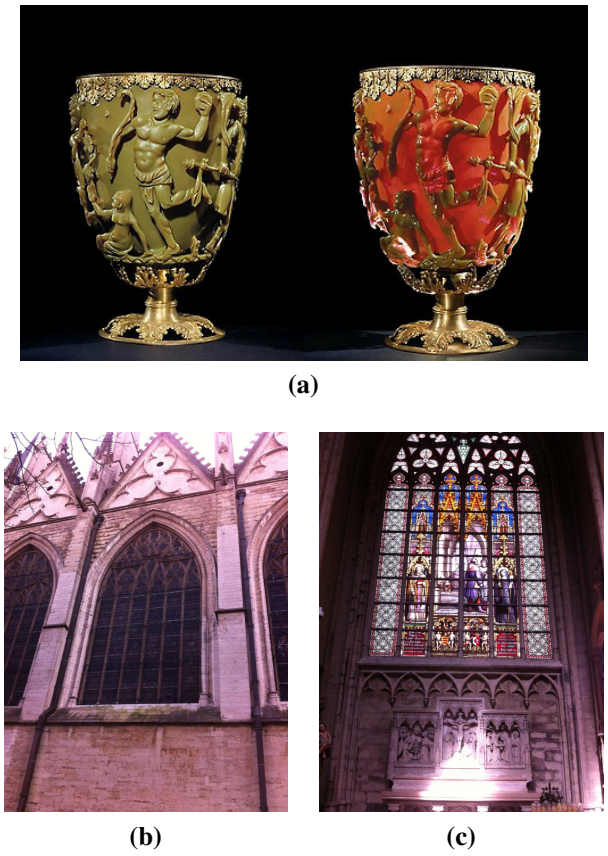

(a) **(b)** **(c)**

Figure 2.1.1 – (a) Lycurgus cup, green in colouration on the left, and red on the right when light scatters through. Stained glass windows from (b) outside and (c) inside from The Cathedral of St. Michael and St. Gudula is a Roman Catholic church in Brussels, Belgium during the SPIE Photonics Europe 2016 conference.

Today, the field of plasmonics is flourishing with developments in nano-fabrication techniques and utilisation of nanostructures for investigations into material analysis. This section describes the principle theory behind the science used throughout the thesis. We focus on plasmonics as described by the properties of metals via electromagnetism. Plas-

monics can be described via electromagnetic interaction mechanics of light with materials. We use the classical macroscopic picture of a metal where plasmons behave as charge density waves that oscillate relative to the ionic lattice of positive charged nuclei. From this outlook the plasmons are damped in the electron-hole pairing via a restoring force which will be discussed in later sections.

We begin with Maxwell's equations, which completely describe how electromagnetic fields interact with metals in the classical sense. In this classical representation, the plasmonic response via a driving electromagnetic field is described as the local polarisation of the metal particle's Fermi sea of electrons. By implementing the macroscopic dielectric response of the material, the plasmon modes and optical response can be determined. Therefore, Maxwell's equations are incredibly powerful foundations for descriptions of plasmonic behaviour under classical optical fields and are given by [4, 74]:

$$\nabla \cdot \mathbf{D} = \rho_{ext} \tag{2.1.1a}$$

$$\nabla \cdot \mathbf{B} = 0 \tag{2.1.1b}$$

$$\nabla \times \mathbf{E} = -\frac{\partial \mathbf{B}}{\partial t} \tag{2.1.1c}$$

$$\nabla \times \mathbf{H} = \mathbf{J}_{ext} + \frac{\partial \mathbf{D}}{\partial t} \tag{2.1.1d}$$

The equations shown in 2.1.1 intimately link the four macroscopic fields: **D**, the dielectric displacement, **E** and **H**, the electric and magnetic fields respectively, **B** the magnetic induction/flux density, along with $\mathbf{J_{ext}}$, the external current density and ρ_{ext} which represents the external charge density. Where in this case the total current and charge densities would be represented by $\mathbf{J_{tot}} = \mathbf{J_{ext}} + \mathbf{J}$ and $\rho_{\mathbf{tot}} = \rho_{\mathbf{ext}} + \rho$ respectively. Where we use **J** to represent the internal current density and ρ for the internal charge density. Additionally, given linear, isotropic material properties we can link the polarisation **P** and magnetisation **M** by the following:

$$\mathbf{D} = \varepsilon_0 \mathbf{E} + \mathbf{P} \tag{2.1.2}$$

$$\mathbf{H} = \frac{1}{\mu_0}\mathbf{B} - \mathbf{M} \tag{2.1.3}$$

Where we have the dielectric constant ε_0 ($8.854 \times 10^{-12}\ F \cdot m^{-1}$), and μ_0 is the magnetic permeability ($1.257 \times 10^{-6}\ H \cdot m^{-1}$) in a vacuum. We can neglect $\mathbf{M}$ as we limit our discussion to non-magnetic media, $\mathbf{P}$ represents the electric dipole moment per unit volume within the material as a result of the contribution from the alignment of media's dipoles. We can relate this term to the internal charge density $\nabla \cdot \mathbf{P} = -\rho$, and for charge conservation $\nabla \times \mathbf{J} = -\partial\rho/\partial t$, requires that internal charge and internal current densities satisfy:

$$\mathbf{J} = \frac{\partial \mathbf{P}}{\partial t} \tag{2.1.4}$$

Because the macroscopic electric field contains all polarisation effects, both the induced as well as the external fields are contained within the following relation. By substituting equation 2.1.2 into equation 2.1.1a we arrive to Gauss's law:

$$\nabla \cdot \mathbf{E} = \frac{\rho_{tot}}{\varepsilon_0} \tag{2.1.5}$$

For linear materials we define the following:

$$\mathbf{D} = \varepsilon\varepsilon_0 \mathbf{E} \tag{2.1.6}$$

$$\mathbf{B} = \mu\mu_0 \mathbf{H} \tag{2.1.7}$$

Here, ε and μ represent the relative permittivity and relative permeability respectively (for non magnetic media $\mu = 1$), they are both related to the complex refractive index of the material via $n = \sqrt{\varepsilon\mu}$. That is, the complex identities of the permittivity and refractive

index can be expressed as $\varepsilon(\omega) = \varepsilon_1(\omega) + i\varepsilon_2(\omega)$ and $n(\omega) = n(\omega) + i\kappa(\omega)$ respectively. Each component of the relative permittivity is given by $\varepsilon_1 = n^2 + \kappa^2$ and $\varepsilon_2 = 2n\kappa$, where κ is the extinction coefficient and determines the absorption attributed to electromagnetic waves propagating through a medium. As the light progresses along the surface of the medium, its exponential decay in intensity can be described by ***Beer's law*** which, for light propagating in the x direction is given by $I = I_0 \exp(-\beta x)$. Where the absorption coefficient is given as:

$$\beta(\omega) = \frac{2\kappa(\omega)\omega}{c} \tag{2.1.8}$$

Dispersion in the medium is attributed to the real part of the complex refractive index $n(\omega)$, whereas the imaginary part is responsible for the absorption. We can also define the dielectric susceptibility χ and its relationship with $\mathbf{P}$ and $\mathbf{E}$:

$$\mathbf{P} = \varepsilon_0 \chi \mathbf{E} \tag{2.1.9}$$

So, substituting equations 2.1.2 and 2.1.9 into 2.1.6 yields $\varepsilon = 1 + \chi$. We can say therefore, that through Maxwell's equations, which govern the properties of electromagnetic interactions with media, we can describe the response of electrons within noble metals such as gold and silver under the influence of a driving field via the dielectric function $\varepsilon(\omega)$.

2.2 Drude-Lorentz Model

2.2.1 Drude Model

The Drude model describes the optical properties of metals, where we consider the conduction electrons in a metal as being free and unbound, therefore being uniformly distributed throughout the material. This is also referred to as the ***plasma model*** where a plasmon is a collective oscillation in this free electron sea. This section will deal with summarizing the optical response of a material when dealing with plasmonic events. The

Drude model takes into consideration electrons in metals near the Fermi level, where they are able to be excited to another energy state by incoming photons and are hence considered delocalised. A visual representation of the Drude model can be seen in Figure 2.2.1.

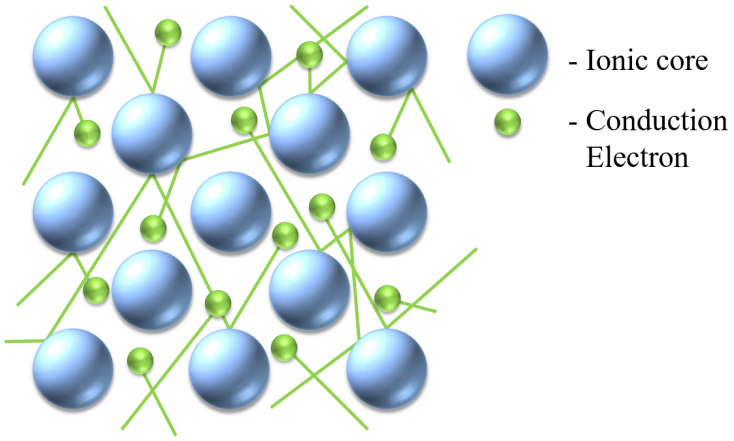

Figure 2.2.1 – Drude model demonstrating the kinetic behaviour of electrons interacting with heavier positive ions.

In the plasma model, the electrons in a metal are treated as a "sea" or gas cloud with effective mass m and among a lattice of positively charged ions. This model is governed by the equation of motion [4, 74]:

$$m\frac{d^2x}{dt^2} + m\gamma\frac{dx}{dt} = -e\mathbf{E} \tag{2.2.1}$$

When an electric field $\mathbf{E}(t) = \mathbf{E}_0 \exp(-i\omega t)$ is applied, the electrons will begin to oscillate, γ is the damping term and corresponds to the collision rate of the electrons with the positive ions (ignoring electron-electron interactions). We can express our damping term as $\gamma = \frac{1}{\tau}$ where τ is the relaxation time of the free electrons (with $\tau \approx 10^{-14}$ s at room temperature). These oscillations can be given for the electron as $\mathbf{x}(t) = \mathbf{x}_0 \exp(-i\omega t)$ and this complex amplitude can be expressed in response to the driving field as:

$$\mathbf{x}(t) = \frac{e}{m(\omega^2 + i\gamma\omega)}\mathbf{E}(t) \tag{2.2.2}$$

For a free electron gas in a given cubic volume with mass m, where e is the charge of an electron ($1.60217662 \times 10^{-19}$ C). Although the electrons experience no interaction with

one another, they collide and interact with the lattice of atomic cores. The displacement of electrons generates a polarisation given by $\mathbf{P} = -n_e e\mathbf{x}$, where n_e (m^{-3}) is the number density of the free electron gas. Inserting this into equation 2.1.2 yields:

$$\mathbf{D} = \varepsilon_0 \left(1 - \frac{\omega_p^2}{\omega^2 + i\gamma\omega}\right)\mathbf{E} \tag{2.2.3}$$

Where ω_p is the plasma frequency, which describes the natural frequency of the delocalised electron sea. Below this frequency, electric fields are reflected from metals. However, once exceeded, surface plasmons are generated. We can write the plasma frequency as:

$$\omega_p = \sqrt{\frac{n_e e^2}{\varepsilon_0 m}} \tag{2.2.4}$$

Therefore this brings us to the expression for the Drude model:

$$\varepsilon(\omega) = 1 - \frac{\omega_p^2}{\omega^2 + i\gamma\omega} \tag{2.2.5}$$

Separating the real and imaginary parts gives:

$$\mathfrak{Re}(\varepsilon(\omega)) = 1 - \frac{\omega_p^2\tau^2}{1 + \omega^2\tau^2} \tag{2.2.6}$$

$$\mathfrak{Im}(\varepsilon(\omega)) = \frac{\omega_p^2\tau}{\omega(1 + \omega^2\tau^2)} \tag{2.2.7}$$

When dealing with larger frequencies, with ω approaching ω_p, $\omega\tau \gg 1$ making the damping coefficient negligible, hence $\varepsilon(\omega)$ will reduce to predominantly its real component with:

$$\varepsilon(\omega) = 1 - \frac{\omega_p^2}{\omega^2} \tag{2.2.8}$$

On the contrary, when dealing with very low frequencies such that $\omega \ll \gamma$, the absorption, given by $\mathfrak{Im}(\varepsilon(\omega))$, is large relative to the real component and the energy attributed to the electromagnetic wave dissipates into the material. In this case, the real and imagin-

ary components of the refractive index are given by:

$$n \approx \kappa = \sqrt{\frac{\Im\mathfrak{m}(\varepsilon)}{2}} = \sqrt{\frac{\tau\omega_p^2}{2\omega}} \tag{2.2.9}$$

The absorption coefficient can be given as:

$$\beta = \left(\frac{2\omega_p^2\tau\omega}{c^2}\right)^{\frac{1}{2}} \tag{2.2.10}$$

And by introducing the conductivity term $\sigma_0 = \frac{n_e e^2 \tau}{m} = \omega_p^2 \tau \varepsilon_0$ we get:

$$\beta = \sqrt{2\sigma_0\omega\mu_0} \tag{2.2.11}$$

This leads us to δ which is known as the ***skin depth*** which for low frequencies Beer's law of absorption tells us that fields decay inside a metal as $\exp(-z/\delta)$. The skin depth describes the penetration depth of electromagnetic waves into the metal and can be expressed as:

$$\delta = \frac{2}{\beta} = \frac{c}{\kappa\omega} = \sqrt{\frac{2}{\sigma_0\omega\mu_0}} \tag{2.2.12}$$

When dealing with real metals, there are some corrections that must be made in order for the Drude model to resemble that of experimental data. An extension of the model is required to describe the highly polarised environments when $\omega > \omega_p$ due to the the positive background of the ion cores. We can account for this by modifying equation 2.1.2 with $\mathbf{P}_\infty = \varepsilon_0(\varepsilon_\infty - 1)\mathbf{E}$. The effect is then described by the dielectric constant ε_∞ (typically $1 \leq \varepsilon_\infty \leq 10$) allowing us to write:

$$\varepsilon(\omega) = \varepsilon_\infty - \frac{\omega_p^2}{\omega^2 + i\gamma\omega} \tag{2.2.13}$$

The Drude model has limiting factors however, not taking into account interband transitions i.e. bound electrons being optically excited to higher energy levels. This then leads to an increase in $\Im\mathfrak{m}(\varepsilon(\omega))$ at higher frequencies. We can see this in Figure 2.2.2 where the real and imaginary parts of the dielectric constant are plotted for silver using

experimental data from Johnson and Christy [75] and using the Drude model [4].

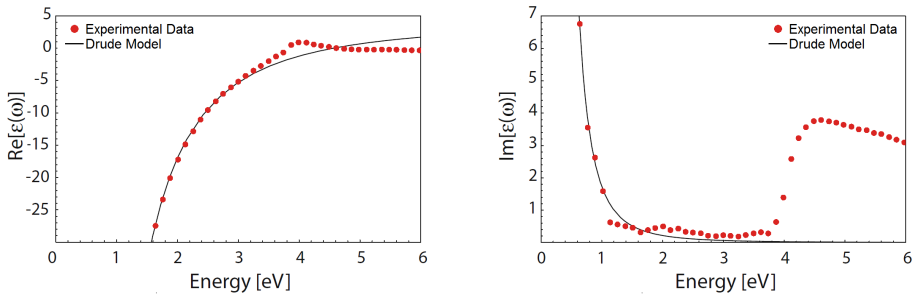

(a) **(b)**

Figure 2.2.2 – $\Re\mathfrak{e}(\varepsilon(\omega))$ and $\Im\mathfrak{m}(\varepsilon(\omega))$ for silver using experimental data from Johnson and Christy (red dots), [75] as well as the Drude model fit of the data (black lines) [4].

We can see the interband transitions in the high energy region, where electrons from the valance band which are excited to higher bands are not accounted for with the Drude model. This is where the Lorentz model comes into practice and an additional term must be added to more accurately describe the data. Lorentzian line-shapes are used to model the contributions of interband transitions [4, 74].

2.2.2 Lorentz Corrections

The Lorentz oscillator model proposed by Dutch physicist Hendrik Antoon Lorentz in the 19^{th} century describes the optical response of atoms and molecules, taking into consideration band effects and interband transitions. The model considers the atom as a mass (nucleus) connected to a smaller mass (the electron) via a spring as seen in Figure 2.2.3.

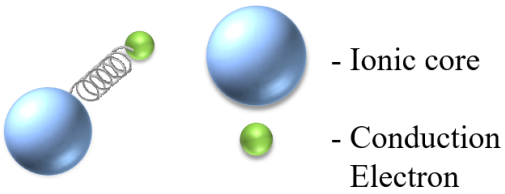

Figure 2.2.3 – Lorentz oscillator model.

The spring oscillates in response to the electric field interacting with the negative charge of the electron and operates classically under Hooke's law. The field attracts or repels the electron which in turn compresses or stretches the spring, this concept forms the basis of the Lorentz oscillator model [76]. To overcome the deficiencies in the Drude

model, we modify the equation of motion to describe a damped harmonic oscillator model which has a natural frequency $\omega_0(rads \cdot s^{-1})$. Therefore the classical forced harmonic oscillator can be described with damping as:

$$m\frac{d^2\mathbf{x}}{dt^2} + m\gamma\frac{d\mathbf{x}}{dt} + m\omega_0\mathbf{x} = -e\mathbf{E} \tag{2.2.14}$$

In this case, this solves to the **Drude-Lorentz model** where:

$$\varepsilon(\omega) = \varepsilon_\infty - \frac{\omega_p^2}{\omega^2 + i\gamma\omega} + \frac{A_i}{\omega_i^2 - \omega - i\gamma_i\omega} \tag{2.2.15}$$

Here, A_i is the oscillator strength of the transition at ω_i with damping constant γ_i. This can be extended for multiple transitions and provide better fitting shown by:

$$\varepsilon(\omega) = \varepsilon_\infty - \frac{\omega_p^2}{\omega^2 + i\gamma\omega} - \sum_{i-1}^{N} \frac{A_i}{\omega_i^2 - \omega - i\gamma_i\omega} \tag{2.2.16}$$

Where the oscillator strength satisfies the condition that $\sum_i A_i = N$, where N is the number of electrons in the molecule [76, 77]. The Drude-Lorentz model helps give very accurate relations with electromagnetic processes in metals.

The Drude model is generally valid for describing the optical response of metals where the photon energies are less than that required to achieve interband transitions. However, when describing noble metals such as gold or silver, which are most commonly used in plasmonics, the approach becomes unreliable as interband transitions occur in the UV-visible part of the spectrum for these metals. This is where the Drude-Lorentz model is required.

The classical approach to nano-gaps between metallic structures assumes a defined interface between the surfaces, where there is no exchange between the abrupt gap of the materials. However, at sub-nanometre distances between plasmonic structures classical descriptions of electrodynamics begins to break down and a quantum description of the system is required due to non-local screening and the spill out of electrons [78–81]. Models have been formulated to account for these effects which typically occur below 1 *nm* [82]. As these events tend to occur at smaller distances than what we have investigated in

the work of this thesis, they are not discussed here.

2.3 Surface Plasmons and Localised Surface Plasmons

Surface Plasmon Polaritons (SPPs) as their name suggests, are electromagnetic interactions which propagate at the interface between a conductor and dielectric with an electric field oscillating perpendicular to the surface. They arise as a result of oscillations of the metal's surface electron plasma. The electrons in the conducting material are displaced by the incoming electric field. Their most alluring property stems from their ability to confine light at the metal-dielectric interface at sub-wavelength scales [4].

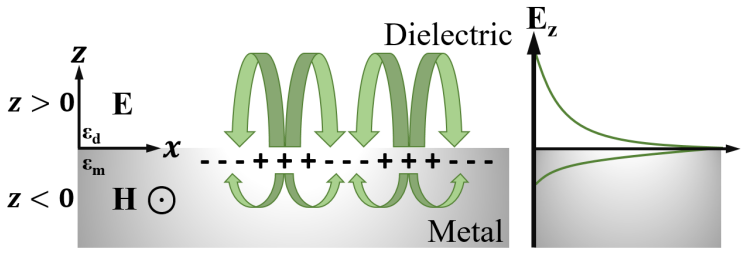

Figure 2.3.1 – Surface plasmon propagation at a metal dielectric interface depicting the electromagnetic wave penetration and exponential decay in both mediums. $H\odot$ represents the magnetic field direction into the page.

Given the appropriate circumstances, incident electric fields can excite a longitudinal wave of electrons, this electron wave then produces its own electromagnetic wave. Due to electromagnetic waves penetration depths being shallow in metals (referred to as the skin depth of the material), the wave is confined to its surface, it then exponentially decays away from it as shown in Figure 2.3.1 [83].

The dispersion relation for SPPs at a metal air interface can be expressed in the following form:

$$\frac{ck_x}{\omega_p} = \sqrt{\frac{1}{2}\left(\frac{\frac{\omega^2}{\omega_p^2}-1}{\frac{\omega^2}{\omega_p^2}-\frac{1}{2}}\right)\left(\frac{\omega}{\omega_p}\right)^2} \tag{2.3.1}$$

Where c is the speed of light and k_x is the propagation constant of the wave which corresponds to the wave vector in the x direction. This equation is shown graphically in

Figure 2.3.2.

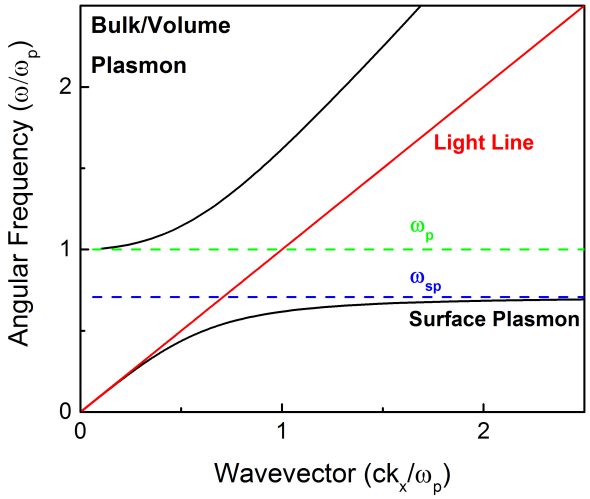

Figure 2.3.2 – SPP Dispersion relationship. The black line represents the bulk plasmon frequency, the red is the light line (where $k_{lightline} = n\omega/c$ so when normalised $ck_{lightline}/n\omega_p = \omega$), the green is the plasma frequency and the blue is the surface plasmon frequency.

By plotting the dispersion relationship for light and the surface plasmon, it can be shown that because the wavenumber is inversely proportional to the wavelength, the wavenumber of a surface plasmon is always larger than that of a photon. Thus it can be said that a surface plasmon has a shorter wavelength than light of the same frequency [4, 74].

The drawback from SPPs having a different dispersion relation is that when we consider this relation in terms of energy and momentum, surface plasmons always have a larger momentum than a photon of the same frequency. Because energy and momentum are always conserved, additional momentum is required to access the SPP. This can be seen in Figure 2.3.2 where the momentum mismatch with the incident light line forbids direct coupling. As surface plasmons cannot be directly coupled to incident light, therefore, light on a smooth metal surface will never generate a surface plasmon. The most common methods of overcoming this feature of SPPs involve indirect coupling either through a prism, or alternatively via surface features such as periodic gratings or roughness. These methods are not investigated through this thesis so are not delved into with great detail in this theoretical section [4].

Localised Surface Plasmons, or LSPs, behave as non-propagating excitations of the conduction electrons of metallic nanostructures coupled to the electromagnetic field. LSPs are confined to the nanostructure (typically gold, silver, aluminium or copper). Gold is often preferred as it is highly chemically stable, as well as being resistant to surface oxidation, also, its plasmonic behaviour is well documented. Silver also has its advantages exhibiting very narrow peak spectra and has been shown to be strong when used for plasmonic experimentation in the visible light frequencies, it is however susceptible to oxidisation under normal laboratory conditions [19]. For biosensing purposes noble metal nanostructures in the form of nanoparticles are used to generate LSPs coupled to their surface via interactions of incoming electromagnetic waves with the nanoparticles.

When light interacts with a metallic nanoparticle the electric field causes a collective oscillation in the nanoparticles electron cloud. At certain frequencies of incident light, Localised Surface Plasmon Resonances (LSPRs) can occur, where the incident electromagnetic radiation matches the natural oscillations of the electrons. The curvature of the nanoparticle creates an effective restoring force on the electrons which leads to the resonance of their oscillations. This is shown diagrammatically in Figure 2.3.3.

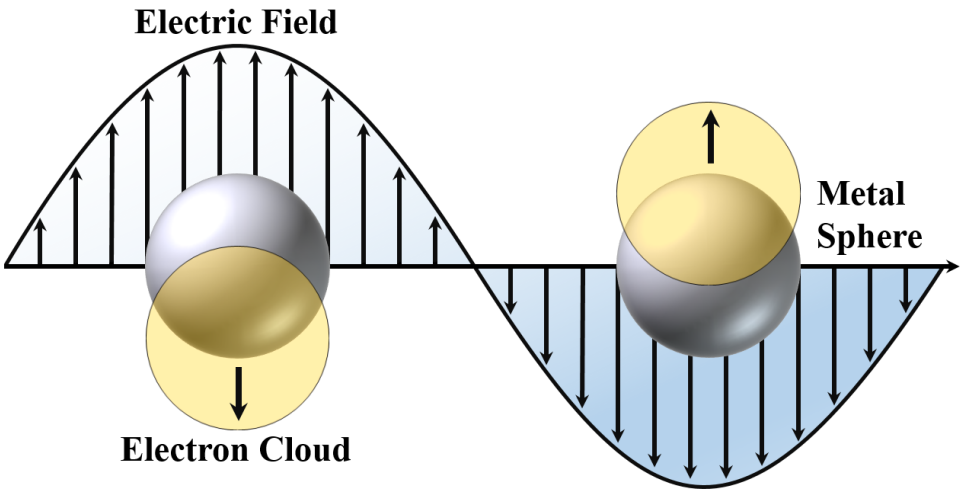

Figure 2.3.3 – Plasmon oscillation displaying the electron cloud (yellow) oscillating about the nuclei due to the incident electric field (blue) [14, 15, 74].

When considering nanoparticles, the oscillations of charge within the confines of the material and field distribution on the surface of the material is quantised in 3 dimensions. Therefore, the particle will support discreet plasmon modes, the most basic of which is

depicted by the dipolar mode confined to a spherical nanoparticle depicted in Figure 2.3.4.

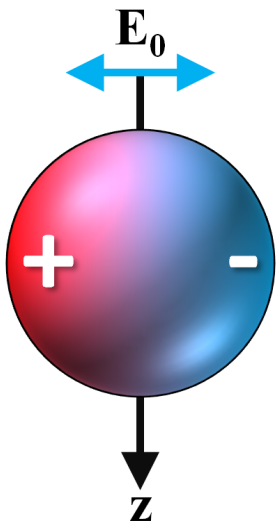

Figure 2.3.4 – Dipolar mode for a spherical particle illustrated with the driving external field.

In contrast to the propagating modes described previously with wavevector k, the modes confined to nanoparticle structures are standing waves with resonance dictated by the form of the nanostructure itself which can be coupled to directly. This is a beneficial contrast to SPPs which require extra techniques in order to couple the incident light and overcome the momentum mismatch. It is important to note that although the modes confined to a nanoparticle are considered to be at a specific wavelength, the resonance itself is quite broad, especially past high frequencies due to damping in the metal. The resonances correspond to collective displacement of the Fermi electrons relative to the particle as a result of the driving electromagnetic field. This then generates a restoring force between the negatively charged electrons and the positively charged ion cores within the metal. The charge accumulates at the surface and positive and negative charges appear on either side of the nanoparticle as indicated in Figure 2.3.4. The magnitude of the restoring force is dependant on the distribution of these charges. The restoring force, successively, defines the oscillation frequency, and so the LSPR thus depends on the dimensions of the nanoparticle.

We can then intuit that the positions and densities of the electron charges will be determined by the particle geometries. Noble metals have plasmon resonances in the

visible and near-infrared regions of the light spectrum due to their high free electron densities. LSPs are responsible for the intense fields confined to the surface of metallic nanoparticles and arise due to excitation at resonant frequencies [74].

For small particles, LSPs can be described via the quasistatic approximation.

2.3.1 Quasistatic Approximation

The electrostatic, or quasistatic approximation, allows for retardation effects to be ignored under the assumption that the nanoparticle is of the order of size much below that of the excitation wavelength. Therefore, the electric field is considered to be uniform across the particle so $d \ll \lambda$ where d is the particle diameter. This solution is capable of adequately approximating scattering characteristics for small nanoparticles relative to the incident wavelength (typically < 100 *nm* in diameter) [4, 74].

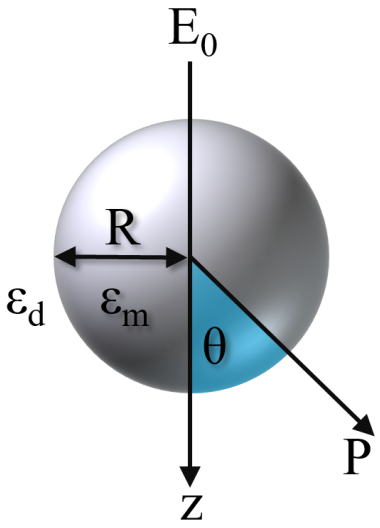

Figure 2.3.5 – A metallic sphere with radius R under the influence of an electrostatic field in the z direction.

Assuming the electric field is uniform across the nanoparticle, the nanoparticle behaves as a dipole, with dipole moment μ in the z direction and the polarisibility can be expressed as:

$$\alpha = 4\pi\varepsilon_0 \left[\frac{\varepsilon_m - \varepsilon_d}{\varepsilon_m + 2\varepsilon_d} \right] R^3 \tag{2.3.2}$$

Where $\alpha \equiv \mu / E_0$ is the polarisability of a spherical particle [74]. Therefore, maximal

enhancement occurs at the resonant excitation $\varepsilon_m = -2\varepsilon_d$ [84]. This relationship is known as the Fröhlich condition. This collective coherent oscillation is described as the dipole plasmon resonance of the particle [15]. The polarisability can then be used to calculate the absorption and scattering cross section for the particle in a vacuum or air.

$$\sigma_{abs} = \frac{k}{\varepsilon_0}\Im\mathfrak{m}(\alpha) = 4\pi k R^3 \Im\mathfrak{m}\left(\frac{\varepsilon_m - \varepsilon_d}{\varepsilon_m + 2\varepsilon_d}\right) \tag{2.3.3}$$

$$\sigma_{scatt} = \frac{\omega^4}{6\pi\varepsilon_0 c^4}|\alpha|^2 = \frac{8}{3}\pi k^4 R^6 \left(\frac{\varepsilon_m - \varepsilon_d}{\varepsilon_m + 2\varepsilon_d}\right)^2 \tag{2.3.4}$$

Where the wave vector is given by k. We can see therefore that $\sigma_{abs} \propto R^3$ scaling as a function of volume V, whereas $\sigma_{scatt} \propto R^6$ scaling as a function of V^2 due to scattering being a two step process involving absorption and then re-emission of light. These equations function for small spherical nanoparticles, however adjustments must be made for ellipsoidal particles where more detail is given in the referenced material [4, 74].

When the laser light is resonant with the surface plasmon a dipolar electric field E_{sp} is radiated dependent on the nanoparticle radius R, its distance from the nearby or adsorbed molecule $r_{molecule}$, the dielectric constant ε and the incident field E_0. This relationship is shown in equation 2.3.5 [85].

$$E_{sp} = \frac{\varepsilon_m - \varepsilon_d}{\varepsilon_m + 2\varepsilon_d}\left(\frac{R}{R + r_{molecule}}\right)^3 E_0 \tag{2.3.5}$$

When a nanoparticle is irradiated with light the electron cloud is displaced from the nuclei, the oscillation then occurs due to the restoring coulombic force attracting the negatively charged electrons back to the nuclei. From this, at certain frequencies, dipole plasmon resonance occurs. The frequency of the oscillation is determined by four factors: electron density, effective mass of electrons as well as the size and shape of the charge distribution [16, 17]. Common variants of nanoparticle shapes include but are not limited to spheres, nano-rods, cubes, triangular prisms, discs and triangles.

2.3.2 Mie Theory

Until now we have only described the optical properties of nanoparticles within the electrostatic limit where the particle diameter $d \ll \lambda$. For larger particles the validity of the electrostatic approximation breaks down and the optical response becomes more complex, where higher order modes can be excited in the particle. The methods of describing these optical properties were developed in 1908 and are known as Mie Theory [12]. Because of the complexity of these calculations we do not describe them in detail here, however, they can be found in literature [76, 86]. Instead, as an example we show the extinction, scattering and absorption cross sections for gold and silver nano-spheres 100 *nm* in diameter in a medium with refractive index $n = 1$ to illustrate this in Figure 2.3.6.

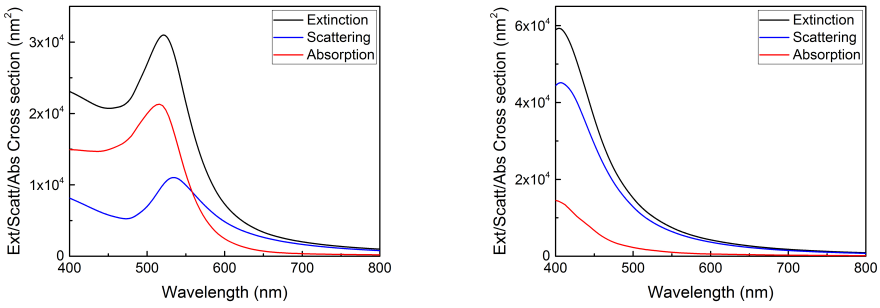

Figure 2.3.6 – Extinction, scattering and absorption cross sections of (a) gold, and (b) silver nano-spheres 100 *nm* in diameter using Mie theory [87].

The quasistatic approximation does not work for particles of this size as the electric field is not uniform across them. Therefore, Mie theory gives a more accurate representation of their optical properties. Mie theory expresses the electromagnetic field solutions as a series (infinite sums) of vectors known as vector spherical harmonics. From this point it is possible to calculate the optical phenomena such as scattering and absorption cross sections. Software can be used to calculate these fields for N terms to produce reasonable results (where generally $N \approx 100$ ensuring convergence for larger N).

2.3.3 Plasmon Hybridisation

When SPPs from different nanostructures are brought together, coupling occurs between them, the effect is known as ***Plasmon hybridisation***. The hybridisation model has been formulated to describe the plasmon response when coupling nanostructures to one another [88]. The results have been shown to give exact agreement with Mie scattering theory for nano-shells, where the interaction strength is dictated by the thickness of the metal shell layer. This allows for the plasmon response to be tuned via changing the thicknesses of these layers [88]. In the plasmon hybridization model, the plasmons interacting with one another are expressed as the primitive plasmon components associated with each elementary surface of the system. The plasmons of each nanostructure can be viewed as incompressible deformations of the electron gas of the particle against a uniform, rigid background of positive charge [89].

Plasmon coupling between nanoparticles can be viewed as the hybridisation of their component plasmon modes. In this model, for nanoparticle dimers, the plasmon modes of the interacting nanoparticles hybridise either in, or out of phase which leads to either a lower energy ***bonding mode***, or a higher energy ***antibonding mode*** respectively. This is represented in Figure 2.3.7.

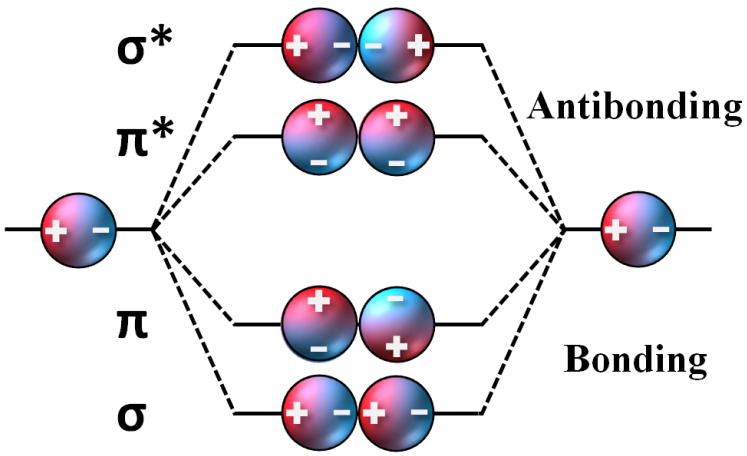

Figure 2.3.7 – Plasmon hybridisation model for a nanoparticle dimer. The combination of the plasmon modes for the dimer is expressed as an interaction of the constituent plasmon modes of each particle [90].

The in, and out of phase combinations correspond to the bonding (σ), and antibonding

(σ^*) modes for incident light polarised along the longitudinal axis of the nanoparticle dimer. When bonding occurs in this configuration, the electric field is localised to the gap between the particles and the LSPR is red-shifted. However, for antibonding, the electric fields are at the ends of the nanoparticle dimer and the LSPR is blue-shifted.

Alternatively, when the incoming light is transverse polarised along the short axis of the nanoparticle dimer, the in phase mode corresponds to the antibonding mode (π^*), whereas the out of phase mode reflects the bonding mode (π). In the case of transverse polarisation, the LSPR shifts are much weaker. Also, it is important to note that the out of phase modes do not exist in homodimers as a result of the cancellation of the dipoles on the two particles which are equal but opposite in direction.

In our work, we investigate a system with a particle on an extended film with a small spacing layer between them. In this case, the system has two types of interacting plasmons: The LSP confined to the nanoparticle, and the SPP which is described as electron density oscillations bound to the surface, yet free to propagate along the metal below [91]. The interaction of the LSP and the surface plasmon continuum of the film typically produces two resonances in the case of the spherical particle system; The low energy mode which is attributed to the SPP in the film, and the higher energy LSP mode associated with the nanoparticle [91].

This system has also been modelled with the plasmon hybridisation method [92]. Showing that when nanoparticles are in close proximity to a metallic surface, there is a shift in the plasmon energy as a function of separation distance. This is a result of hybridisation between the solid nano-sphere and the extended metallic film below [92].

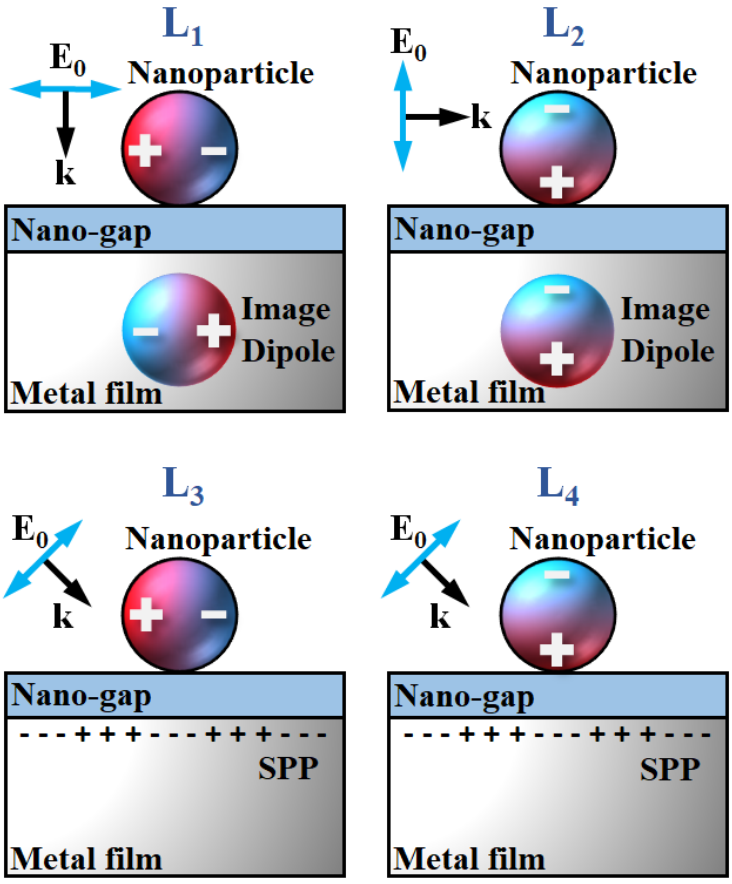

Figure 2.3.8 – Mode coupling diagrams for a nanoparticle on a metallic film separated by a thin dielectric spacer. Where, L_1 represents the horizontal image dipole coupling. L_2 represents coupling to the vertical image dipole. Whereas, L_3 and L_4 show the horizontal and vertical LSPR coupling to the SPP in the film respectively [93].

Four coupling modes exist for this system: L_1 and L_2 modes represent the coupling for the horizontal and vertical image dipoles of the system, while the L_3 and L_4 modes show the horizontal and vertical LSPR-SPP coupled modes respectively. It should be also be noted that the presence of the dielectric spacer between the nanoparticle and the metallic film facilitates the excitation of SPP modes via off-normal excitation overcoming the momentum mismatch from the incident light [93]. A similar effect can also be seen from metallic nano-tips separated by nanometre distances from metallic films [94].

It has also been shown that for nanoparticles near a metallic surface, the interaction is dependent on the thickness of the metallic film [89]. In the case of thin films, it is shown that the high energy hybridised plasmon is a result of the LSPR of the nano-sphere, whereas the broad, low energy mode results from SPPs in the film and can be viewed as an incomplete image-like response from the nanoparticle coupling to it [89].

It can therefore be said, that the complex plasmon response in coupled metallic nanostructures occurs as a result of interaction between the individual components of the system. The plasmons generated in these hybridised systems are a result of interactions between each structure.

2.4 Radiative and Non-Radiative Processes

The following sections detail the electromagnetic processes involved in the transitions between energy levels of molecules. The most beneficial property of this in spectroscopy is the ability to acquire material information via excitation of a target with laser light. The incident light has the potential to reveal material properties via radiative processes of a target molecule. Light matter interactions can be visualised using the Jablonski energy level diagram in Figure 2.4.1.

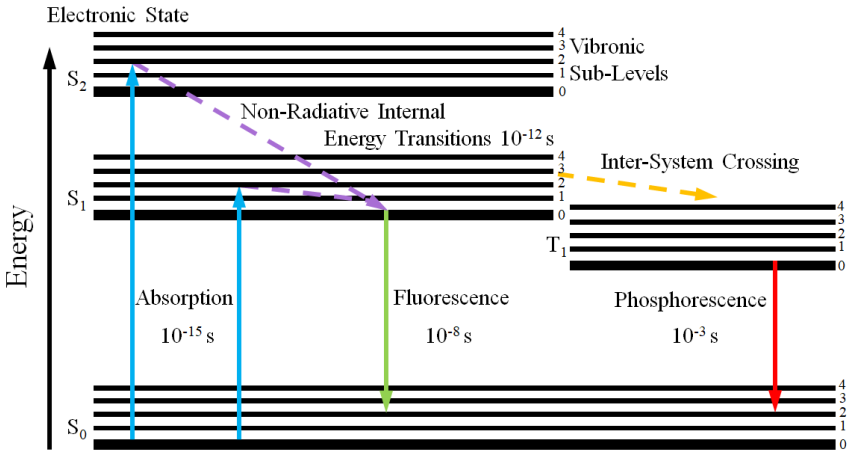

Figure 2.4.1 – Jablonski energy level diagram detailing the energy level transitions of molecules in radiative and non-radiative transitions of states. Blue arrows represent absorption processes occurring over times of the order of 10^{-15} s. Purple arrows are the internal energy transitions with the environment or within the molecule itself as a result of losses via heat (usually over the time-frame of the order 10^{-12} s). The green arrow is the relaxation of the molecule from the excited state back to the ground state, this process occurs over times of the order of 10^{-8} s. The red arrow shows the transition from a triplet state back to the ground state through phosphorescence, this process occurs over times of the order of 10^{-3} s or more [95].

The Jablonski diagram is named after Professor Alexander Jablonski who is regarded as the father of fluorescence spectroscopy due to his contributions to the field [96]. The electronic energy levels here are represented by the thicker black bars depicted as S_0,

S_1 and S_2 with the thinner bars being used to represent the vibrational energy levels the fluorescent chemical compound can reside in. The singlet ground state S_0 is the lowest energy level of the molecule and each subsequent number 1, 2 and so on is used to refer to the next excited state. Transitions occur in very short time-frames as shown in the diagram, these times are too short for significant displacement of nuclei which is known as the Franck-Condon principle [95]. We can illustrate the Frank-Condon principle for the transition probability for vibrational energy levels in Figure 2.4.2.

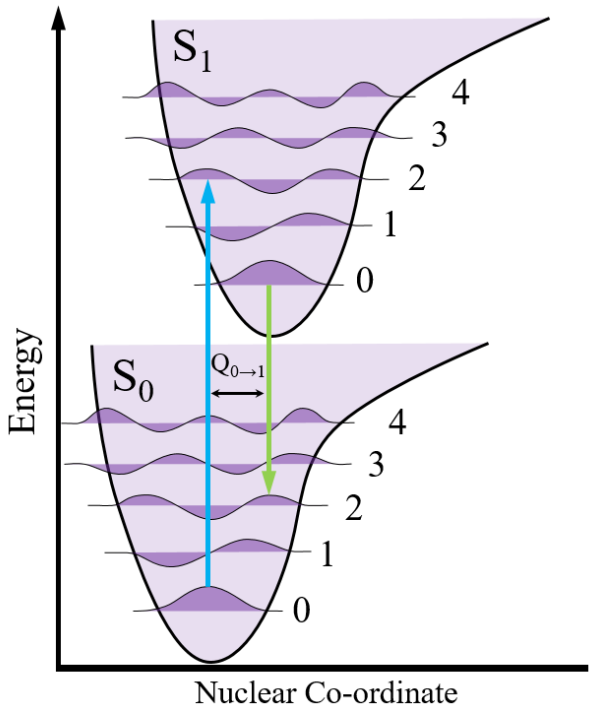

Figure 2.4.2 – Transition probabilities between energy states for a molecule in the ground state promoted to an excited state and relaxing back for the favoured energy transitions due to overlap in the initial and final vibrational wave functions [97].

Once in the excited state, the electron rapidly decays through the vibrational energy levels (shown by the thinner black bars in Figure 2.4.1). This process is known as internal conversion and happens over a period of 10^{-12} seconds. During internal conversion, energy is lost to the environment or within the molecule itself as a result of heat losses via vibration. After this, the electron will be in the lowest level of the S_1 state. From there, the electron will decay to one of the sub levels of the S_0 state, a photon will be emitted with sufficient energy to conserve the difference from the transition, this process will happen over a period of around 10^{-8} seconds. As energy is proportional to the frequency for the

photon, and the emitted photon has less energy than the absorbed photon, it is shifted to a longer wavelength.

2.4.1 Absorption

The process of optical absorption involves the energy transfer of an incoming photon to the molecule, the photon is then said to be absorbed. Absorption requires conservation of energy such that $E = E_f - E_i$. Therefore, a molecule at energy level E_i will be promoted to an energy level E_f by an incoming photon of energy E [76]. There are two main types of optical absorption; infrared absorption and electronic absorption and they involve the promotion of an electron to a vibrational and electronic state respectively. Infrared absorption is not used in our work in this thesis, so we go into no further detail here.

Electronic absorption involves electrons in their ground state S_0 being promoted to an excited state via the absorption of a photon. For fluorophores, this transition occurs in the visible region of the light spectrum and provides a complementary absorption spectrum associated with the molecule for its allowed transitions [86].

2.4.2 Emission

Emission is the reverse process of absorption, a molecule in the excited state E_f relaxes back to its ground state E_i and emits a photon equal to their difference in energy. Emission can be divided in two categories; spontaneous (Figure 2.4.3a) and stimulated (Figure 2.4.3b) emission.

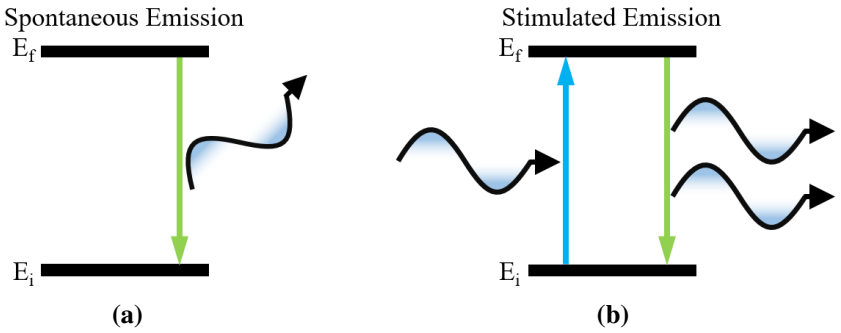

Figure 2.4.3 – The emission process for (a) spontaneous and (b) stimulated emission.

Stimulated emission involves an incident photon of equivalent energy as an available

transition for a molecule to produce the emission of a photon of the same energy, phase and direction as the photon stimulating its release.

Spontaneous emission however occurs spontaneously as the name suggests, resulting from photons in the vacuum field. A molecule in the excited state relaxes back to its ground state and thus emits a photon in the absence of the influence from stimulation from an external source. This decay process occurs randomly, however, the distribution of electrons decaying over the lifetime τ will be described by an exponential function. In the absence of nonradiative processes, this radiative decay rate, $\Gamma = \frac{1}{\tau}$ [95, 98], can be described by ***Fermi's Golden Rule*** in section 2.4.2.1.

2.4.2.1 Fermi's Golden Rule

Fermi's Golden Rule describes the transition from an excited state to a lower energy state via a radiative process [99]. The rate of spontaneous decay can be expressed in the following form:

$$\Gamma_{1\to 0} = \frac{2\pi}{\hbar} |\left\langle E_f \left| H_{int} \right| E_i \right\rangle|^2 \rho(\omega) \tag{2.4.1}$$

Where H_{int} is the Hamiltonian operator , E_f and E_i are the excited and ground states shown in Figure 2.4.3. The Hamiltonian operator describes the transition as a result of the interaction of the electric field amplitude ($\mathbf{E}$) and the electric dipole (μ) of the atom $H_{int} = -\mu \mathbf{.E}$. Finally, $\rho(\omega)$ is the ***density of photon states*** available for an emitted photon with frequency ω. The density of states is defined such that $\rho(\omega) dE$ is the number of final states per unit volume that fall within the energy range for transition for the emitted photons. The density of photon states in a vacuum is given by:

$$\rho(\omega) = \frac{\omega^2}{\pi^2 c^3} \tag{2.4.2}$$

Fermi's Golden Rule can therefore be said to characterise the spontaneous decay rate for excited atoms via the emission of photons and is proportional to the density of final states. [100, 101].

2.4.3 Luminescence

Luminescence describes the emission of light from a material via the transition of electrons from an excited state to a lower energy level. It can be divided into two categories; ***fluorescence*** and ***phosphorescence***, and is dependent on the nature of the excited state in question. Fluorescence occurs from electrons in excited singlet states, where the electron in the excited state is paired to a complementary electron in the ground state with opposite spin. Emission via phosphorescence results from photons in the triplet excited states. In this case, the electron in the excited state has the same spin as that of its paired counterpart in the ground state. Because of the Pauli exclusion principle, transitions to the ground state are forbidden resulting in slow emission rates (typically around 10^3 to 10^0 s^{-1}) [86].

2.4.4 Fluorescence

Fluorescence is the culmination of the processes described in the previous sections, where electromagnetic radiation is absorbed and then re-emitted at a longer wavelength. The emission process is irrespective of the excitation wavelength (known as Kasha's rule). The incident photon is absorbed by the target molecule and the electron at the ground state is promoted to a higher energy state. When the electron relaxes back to the ground state, it emits a photon with less energy which corresponds to a different wavelength.

2.4.4.1 Quenching

Quenching is a process that can occur during fluorescence leading to a decrease in the intensity. It can result from a number of different mechanisms, for example, collisional quenching occurs when the fluorophore in the excited state collides with another molecule in the solution (known as the quencher). Collisional quenching prevents the emissive process of the fluorophore and instead returns it to its ground state via a non-radiative process. [95].

2.4.5 Conjugated Polymers

Conjugated polymers consist of chains of repeated sequences of alternating single and double carbon bonds. In this thesis, we investigate Raman spectra from F8-PFB which is a conjugated polymer, where the chemical structure is shown in Figure 2.4.4.

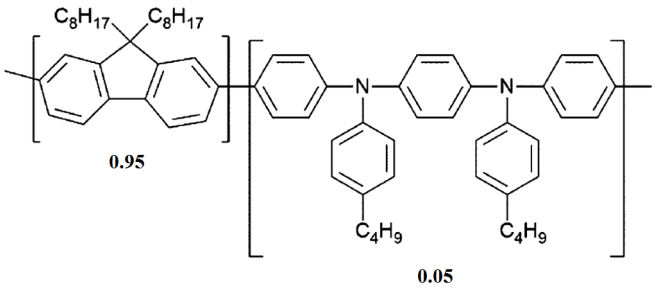

F8-PFB

Figure 2.4.4 – Chemical structure for F8-PFB [102].

Conjugated polymers are known for their light emitting properties with their properties applying to many different research environments such as light emitting diodes [103], photovoltaics [104] and even bio-sensing [105]. Due to the absence of work regarding their detection at the single molecule regime via Raman spectroscopy, they are of particular interest for investigations throughout this thesis.

2.4.6 Scattering

When electromagnetic waves interact with matter, the incident wave excites the discrete electric charges within the material. These charges then re-radiate electromagnetic energy, the secondary radiation is therefore a result of the absorption and emission processes and the resultant photon is said to be scattered light [76, 86]. Scattering is an immensely important area of physics as it describes the interaction of light with media. All media will scatter light in some way and scattering processes are used to describe how these phenomena occur [86]. Scattering can be classified in two ways, as either elastic, or inelastic scattering which we will discuss in terms of the Raman effect.

2.5 The Raman Effect

Raman scattering was first discovered in 1928 by C.V. Raman (who won the Nobel Prize for his work) and K.S. Krishnan in India. It was also discovered independently by Leonid Mandelstam and Grigory Landsberg at a similar time [35, 100]. Raman spectroscopy is a very powerful, non-invasive technique for material studies. It functions via the creation and annihilation of quantum vibronic modes in the target molecule which shift the frequency of the scattered photon as seen in Figure 2.5.1 [100].

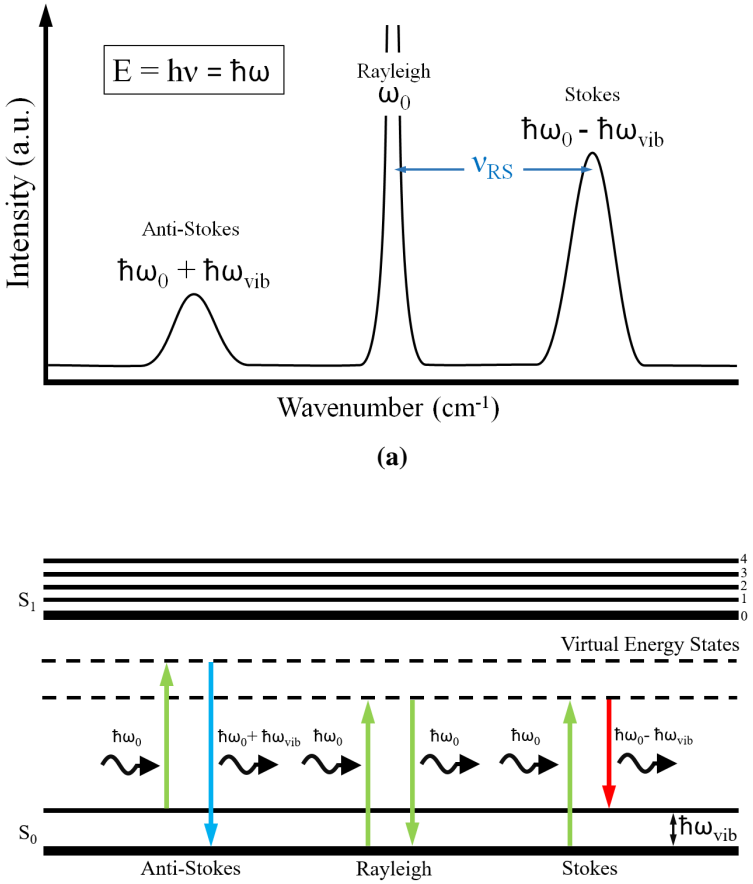

Figure 2.5.1 – Energy level diagram of Raman scattering showing elastically scattered light in the form of Rayleigh scattering, as well as inelastically scattered light in the forms of Stokes and anti-Stokes scattering [76].

When electromagnetic waves are incident on a material, they interact with matter in a number of ways, the Raman effect exploits certain characteristics of light scatter-

ing. When light interacts with a material the majority of photons are scattered ***elastically*** in the form of Rayleigh scattering, however, the small percentile of ***inelastically*** scattered photons leads to the Raman effect. The energy difference between the incident and scattered photons is equal to the energy of a high-frequency vibration in the target related via $E = \hbar\omega$. Where, $\hbar$ (known as the reduced Planck constant) is equal to $h/2\pi$ and h is Planck's constant ($6.636070040 \times 10^{-34}\ J \cdot s$). This vibration corresponds to either a phonon in the crystal lattice of the target or a vibrational mode in a molecule.

Light emitted via Raman scattering functions differently to what we have seen previously in the emission process. In this case, Raman occurs without changes in the electronic state of the molecule. The scattered photon is created in the Stokes or anti-Stokes process with the molecular vibration upon interaction of incident light with the molecule. Therefore, instead of considering the molecule to be excited to discreet energy levels, we describe the transition so that the energy exchange between light and the molecule can be thought of as involving a ***virtual*** state as seen in Figure 2.5.1b [74]. In the cases of Stokes and anti-Stokes scattering, the photon shifts in frequency to account for the change in energy. The Stokes and anti-Stokes processes are dependent on the populations of the initial states of the material, which in turn depend on the temperature. At room temperature, the the upper state will be less populated than the lower state. Therefore, transition rates from the more populated lower state to the upper state (Stokes transitions) will be higher than in the opposite process (anti-Stokes transitions). Accordingly, Stokes scattering peaks are stronger than anti-Stokes scattering peaks. The ratio between Stokes and anti-Stokes scattering depends on the temperature, and can therefore be exploited to measure it. Because the transition associated to Raman scattering is very fast ($\tau_{RS} \approx 0.66\ ps$ [106]), which we can calculate from the following relationship [107–109]:

$$\tau_{RS} \approx \frac{h}{4\pi\Delta E_{RS}} \tag{2.5.1}$$

Where the lifetime τ_{RS}, is related to $\Delta E_{RS}(eV)$ (used to denote the line-width of the Raman mode [110]) via Heisenberg's uncertainty principle. Therefore, the quenching effect described in section 2.4.4.1 does not have time to occur [95]. The anti-Stokes

process is typically much weaker than that from regular Stokes scattering and requires the molecule to already be in an excited energy state, therefore Stokes is more commonly used [76].

The Raman spectrum of a target material has a unique "chemical fingerprint" used to identify its molecular structure. The Raman peak positions are dependent on the frequencies of the Raman-allowed vibrational modes of the molecule, while the peak intensities depend on the symmetries of the vibrations. The Raman shift υ_{RS} (cm^{-1}), which is used in spectroscopy to define the shift in frequency relative to the excitation wavelength can be expressed as:

$$\upsilon_{RS} = \left((1/\lambda_{laser}) - \left(1/\lambda_{signal}\right)\right) \times 10^7 \tag{2.5.2}$$

Where λ_{laser} (nm) and λ_{signal} (nm) are the wavelengths of the laser source and the peaks in the Raman spectrum associated to the target respectively. Through observations of Raman spectra, different features such as shifts in frequency or increased intensity to the observed peaks give indications that changes to the position of the target analyte or enhancement have taken place. The peaks produced in Raman spectra are very narrow, typically around $5-20\ cm^{-1}$ varying in intensity based on surface selection rules [76].

Raman scattering rate, which describes the probability Γ_{RS} of scattering into a mode of frequency ω_1 can be written in the form [100, 111]:

$$\Gamma_{RS}(\omega_0, \omega_1) = \frac{2\pi^2}{\hbar^2}\omega_0\omega_1 N(\omega_0)\,|S|^2 \left(N(\omega_1) + \frac{1}{4\pi}\rho(\omega_1)\right) \tag{2.5.3}$$

Where S is the matrix element for the transition in question, while $N(\omega_0)$ and $N(\omega_1)$ are the photon numbers for the incident and scattered frequencies of light. The first and second terms in the brackets of the equation describe the stimulated and spontaneous scattering processes respectively. The coefficient $1/4\pi$ means the density of states is calculated per unit solid angle. Since our work only considers spontaneous Raman processes, by substituting in the expression for the photon density of states in a vacuum from equation 2.4.2, we can rewrite this expression for spontaneous Raman scattering as:

$$\Gamma_{RS}(\omega_0, \omega_1) = \frac{1}{\hbar^2}\omega_0 N(\omega_0)\,|S|^2\,\frac{1}{4\pi}\frac{\omega_1^3}{c^3}n^3 \tag{2.5.4}$$

Where the refractive index term, n, comes from the medium in question. As $\omega_0 \approx \omega_1$, we can state that the spontaneous scattering is proportional to ω_0^4 [111].

2.5.1 Raman vs Fluorescence

The main drawback from Raman when compared to fluorescence is the low efficiency. Fluorescence cross sections for fluorescent dyes ($d\sigma_{fluo}/d\Omega \sim 10^{-16}\ cm^2/sr$), are much larger than the equivalent Raman cross sections ($d\sigma_{fluo}/d\Omega \sim 10^{-24}\ cm^2/sr$), even for the most ideal case scenarios. As fluorescence can be 10^{7-8} times more efficient than Raman at scattering light, this means Raman signal is typically overpowered by the fluorescence background [68]. Fluorescence is capable of single molecule detection on a routine basis, whereas Raman requires enhancement from surface characteristics and metallic features to produce the signal output required.

Raman does have advantages however, offering 10^{2-3} times sharper signals than fluorescence [68]. Raman offers full fingerprint spectra of the molecule being studied. The spectra will be unique with highly specific features dependent on the molecular vibrations from the bonds within the molecule. It is also "label free", which is an attractive feature as fluorescence usually requires fluorescent tagging of a non-fluorescent molecule. As Raman is label free, the surface binding characteristics of the molecule under investigation are unchanged.

Raman is more flexible, functioning at almost any wavelength of excitation. Not only this, but Raman can be achieved from analytes adsorbed directly to the metallic substrate, whereas quenching would occur given this situation for fluorescence measurements [112]. Although each technique provides its own benefits, Raman offers far more specificity and molecular identification. Dealing with its shortcomings in signal output is achievable through careful experimentation and systematic optimisation via surface enhanced Raman spectroscopy, which is why this thesis utilises this technique.

2.6 Surface Enhanced Raman Scattering

By combining the fundamental principles of plasmonics with Raman spectroscopy, we arrive at Surface Enhanced Raman Spectroscopy (SERS). SERS allows for the generally weak Raman signals to be amplified over several orders of magnitude, via the inclusion of metallic nanostructures as a result of the highly localised regions of field enhancement generated at their hot spots [71]. SERS offers non-invasive, label free detection characteristics from these structures, which are extremely beneficial when working with biological systems [38, 40–42, 54, 84, 113–119]. The narrow spectral width of the vibrational Raman bands, and the relatively large spectral bandwidths of plasmonic resonances combine to make SERS a highly versatile sensing tool for providing specific information about the target molecule of interest.

Generally, Raman cross sections tend to be very low, usually of the order of $\sim 10^{-26}\ cm^2$ [57], and $\sim 10^{-29}\ cm^2$ for single molecules [36]. However, it has been shown that using metallic nanostructures boosts the low yield given from Raman signal, enhancing by orders of 10^{7-8} and even as high as 10^{10-11} within nano-gaps and via the use of metallic tips [38, 76]. Still, the exact enhancement is difficult to quantify due to the estimation of the exact number of molecules contributing to it. Also, it is worth noting that these numbers are generated from the *maximum* area of enhancement from the substrate or device where the hot spots are generated, and the enhancement levels are generally lower for *average* enhancement across the samples. This enhancement can be attributed to two main mechanisms; ***electromagnetic*** and ***chemical*** enhancement.

The main contributing factor is the electromagnetic enhancement via the light interaction with the metals and is a direct relationship to the plasmon resonances discussed earlier in the thesis. Electromagnetic enhancement is described by enhanced fields at the surface of the metal which boost field strengths of materials in close proximity. Enhancement factors of the orders of 10^{7-8} [38] have been reported and detection of materials down to single molecule levels has been proven on numerous occasions [38, 52, 53, 56, 61–63, 113, 120, 121].

Secondly, chemical enhancement involves molecules with lone pair electrons or electron rich compounds which only has been shown to contribute around $10^1 - 10^2$ times to the enhancement [71]. In this process, the analyte adsorbed to the surface of the SERS active site begins a charge transfer complex. The excitation radiation in this case generates an electron-hole pair and charge is transferred between the metal and analyte through the bond generated between them. The Raman process occurs in the molecule and the energy is transferred back to the metal for scattering to occur [112]. The actual cause of this effect is controversial and still subject to debate.

2.6.1 Electromagnetic Enhancement Factor

To simplify concepts, we use the electrostatic approximation demonstrated in section 2.3.1, where the electromagnetic field is constant over the area of the sphere due to its diameter d being much less than the incident wavelength of light given as λ_{inc}. In other words, during excitation, the sphere is within the confines of a homogeneous external field E_0, resulting in an induced dipole moment. The polarisation P is related to the magnitude of the electric induced field within the sphere in the following way:

$$E_{ind} = \frac{P}{3\varepsilon_0} \tag{2.6.1}$$

As the polarisation is defined as the sum of dipole moments per unit volume, in this instance P can be represented by:

$$P = \frac{\mu_{ind}}{4/3\pi R^3} \tag{2.6.2}$$

The induced dipole moment $\mu_{ind} \propto E_0$, where this proportionality is given via the polarisability α, therefore leading to $\mu_{ind} = \alpha E_0$. Given the electrostatic approximation, the polarisability for a sphere can be given by:

$$\alpha = 4\pi\varepsilon_0 \left[\frac{\varepsilon_m(\omega) - \varepsilon_d}{\varepsilon_m(\omega) + 2\varepsilon_d} \right] R^3 \tag{2.6.3}$$

Where ε_m and ε_d are the dielectric constants for the metal and the surrounding medium

respectively. By substituting the polarisation and polarisability from equations 2.6.2 and 2.6.3 into equation 2.6.1, the following expression, which relates the induced electric field with the dielectric constants of the material and surrounding medium as well as the magnitude of the external electric field is given by:

$$E_{ind} = \left[\frac{\varepsilon_m(\omega) - \varepsilon_d}{\varepsilon_m(\omega) + 2\varepsilon_d} \right] E_0 \tag{2.6.4}$$

Relating these concepts back to plasmonics, it can be stated that the magnitude of the induced electric field is expressed in terms of the optical properties of the sphere, the surrounding medium and the magnitude of the external field. This in turn leads to the induced dipole moments within the metal which is attributed to the collective oscillation of the delocalised sea of electrons within the metal oscillating with respect to the ionic core lattice. In this instance, the LSP generated here not only enhances the incident field $\left(| E(\omega_0) |^2 \right)$ but also the scattered field $\left(| E(\omega_1) |^2 \right)$. Where ω_0 is the frequency of the incident photon and ω_1 is the frequency of the scattered Raman photon. Therefore, the enhancement factor G is given as [62]:

$$G = \left[\frac{\varepsilon_m(\omega_0) - \varepsilon_d}{\varepsilon_m(\omega_0) + 2\varepsilon_d} \right]^2 \left[\frac{\varepsilon_m(\omega_1) - \varepsilon_d}{\varepsilon_m(\omega_1) + 2\varepsilon_d} \right]^2 \tag{2.6.5}$$

We can plot equation 2.6.5 for gold and silver under the assumption of the electrostatic approximation using experimental data provided from Johnson and Christy [75]. This is shown in Figure 2.6.1.

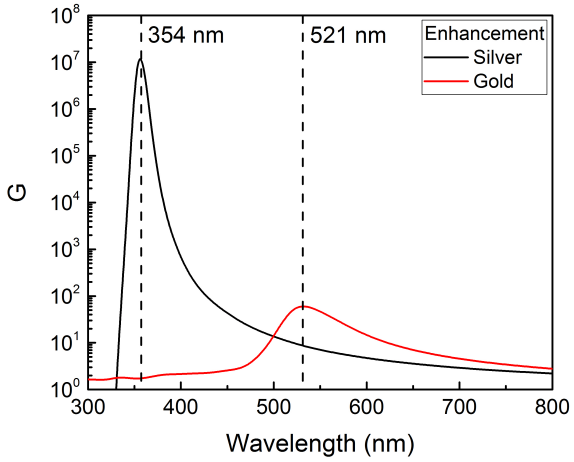

Figure 2.6.1 – Electromagnetic enhancement factor G plotted from equation 2.6.5 for gold and silver under the assumption of the electrostatic approximation. The experimental data is provided from Johnson and Christy [75].

As stated previously, and shown in section 2.3.1, the induced field is enhanced optimally when $\omega = \omega_p$ and $Re\left[\varepsilon\left(\omega_0\right)\right] \approx -2\varepsilon_d$, leading to the excitation of the LSP.

2.7 The Figure of Merit Linking Near to Far-Field SERS Emission

In Raman scattering, the maximum available near-field enhancement due to electromagnetic mechanisms is proportional to the fourth power of the ratio of the overall electric field to the incident electric field at the location of the molecule, corresponding to enhancement at both the excitation and emission stages. Additionally, consideration must be given to the orientation of the Raman active dipole moments, and therefore of the molecule relative to the direction of the local enhanced electric field. By considering the enhancement of the incident field (excitation stage) and the increase in the optical density of states (emission stage) due to the presence of the metallic nano-structure, the SERS enhancement can be expressed as a contribution of these factors, which we use as our Figure of Merit (FoM) [74, 112]:

$$FoM = \left(\frac{|\mathbf{E}(\omega_0)|^2}{|\mathbf{E}_0(\omega_0)|^2}\right)\left(\frac{\rho(\omega_1)}{\rho_0(\omega_1)}\right)\left(\frac{\left|\hat{\mathbf{E}}\cdot\hat{\mu}\right|^2}{\left|\hat{\mathbf{E}}_0\cdot\hat{\mu}\right|^2}\right) = G_{ex}\times G_{em}\times S_\mu \approx \frac{|\mathbf{E}(\omega_0)|^4}{|\mathbf{E}_0(\omega_0)|^4} \quad (2.7.1)$$

Where $\mathbf{E}_0$ is the incident electric field, $\mathbf{E}$ is the electric field at the location of the molecule, ω_0 is the frequency of the incident photon and ω_1 is the frequency of the photon after Raman scattering. $\hat{\mathbf{E}}_0$ and $\hat{\mathbf{E}}$ are the polarization directions of the incident electric field and the electric field at the molecule respectively, while $\hat{\mu}$ refers to the orientation of molecular dipole associated with the Raman transition. ρ is the optical density of states in the presence of the plasmonic nano-gap and ρ_0 is the vacuum optical density of states. Arguably, this is regarded as one of the most fundamental principles of SERS [76]. The enhancement in SERS processes is particularly strong when the incident and scattered fields align with the plasmon resonance.

It is common to approximate the Raman enhancement scaling to the 4^{th} power of the field enhancement [76, 85]. However, this makes the assumption that the plasmon resonance is sufficiently broad such that the shift in frequency from the incident and scattered photons is smaller than the line-width of the plasmon resonance. Moreover, a calculation involving an incident plane wave will provide a local field, $\mathbf{E}(\omega_1)$, for a particular incident wave vector. However, the vacuum field that is responsible for spontaneous Raman scattering contains all possible wavevectors. That is, the molecule interacts with its own radiated Stokes field scattered back from the metal nanoparticle. Therefore, more accurate calculations for SERS enhancement should consider *both* the enhancement in the excitation and emission stages.

The first term, G_{ex}, describes the Raman ***excitation enhancement*** whereas the second term, G_{em}, describes the ***emission enhancement*** due to the increase in the optical density of states in the presence of the plasmonic nano-gap. S_μ represents the alignment of the transition dipole moment with respect to the local enhanced field.

In terms of the electric field, the near-field excitation enhancement is given by:

$$G_{ex} = \frac{|\mathbf{E}(\omega_0)|^2}{|\mathbf{E}_0(\omega_0)|^2} \tag{2.7.2}$$

With Raman cross sections being considerably low, the enhancement given via metallic nanoparticles is an extremely beneficial attribute when excitation takes place at their LSPR. For the emission enhancement, we can equate the ratio of the density of photon states with and without the metallic structure to the electric field projected to the far-field. This is characterised by:

$$G_{em}(\omega) = \frac{\rho(\omega_1)}{\rho_0(\omega_1)} = \frac{W_{rad}}{W_0} \tag{2.7.3}$$

Where W_{rad}/W_0 is the ratio of the radiated power in the presence, and in absence of the metallic nanostructure, θ represents the emission angle from the gap and ω_1 is the frequency of the scattered photon. The ratio of the radiated power in the presence and the absence of the metallic nanostructure is equal to the ratio of the electromagnetic density of states.

2.7.1 Single-Molecule SERS: Molecular Orientation

The molecular orientation relative to the field associated with the plasmonic nanostructure is very important, especially when considering very low concentrations of the target analyte. The Raman scattering process results directly from the analyte within the hot spot of the plasmonic nanostructure. Therefore, the dipole moment associated with the Raman mode aligned with the local enhanced electric field of the plasmonic nanostructure will generate higher intensities than those not aligned [74, 112]. Also, this effect will be more pronounced when reaching very low concentrations of the target material as the contribution to the scattered Raman signal will be attributed to few or single molecules.

When considering orientational effects, the effective single molecule enhancement factor differs relative to the molecular position and orientation to the metallic nanostructure it is in contact with. Due to the random orientation of molecules, at high concentrations the contribution of the analyte orientation averages to around 1, leading to the

full fingerprint spectrum of the material being observed. However, when concentrations drop to sufficiently low values, this averaging disappears and only the modes for which the Raman dipole aligns with the enhanced electric field are expected to be observed in the SERS signal, depending on the molecular orientation relative to the nano-gap field [63]. An in depth study of the literature regarding single molecule sensing is provided in section 3.1.2 of Chapter 3.

2.7.2 Surface Enhanced Resonant Raman Spectroscopy

Another feature of Raman spectroscopy occurs when the excitation frequency used to generate the Raman scattering is close in electronic energy to a chromophore in the target analyte. This effect is known as **Resonance Raman Spectroscopy** (RRS). However, even in the case of this resonant Raman scattering, no real electronic transitions are involved. The intensities from fluorescent dyes have been shown to be $\approx 10^6$ larger from RRS than its normal Raman counterpart [76].

When coupled with plasmonics, Surface Enhanced Resonant Raman Spectroscopy (SERRS) amplifies the signal from the normal SERS signal. For example, SERS measurements from pyridine have been calculated at 10^6. Whereas, SERRS measurements have been shown to produce enhancements of 10^{13-15} for R6G [112]. SERRS can be attributed to the contribution of the electrodynamic enhancement being boosted by the molecular resonance of the analyte under investigation. SERRS has been shown to be able to detect analytes to the single molecule level [55]. Molecules such as dyes have higher Raman cross sections of the order of $10^{-27} - 10^{-28}$ for SM-SERRS, typically requiring enhancement factors of 10^{7-8} to be detectable. Whereas, for non-resonant molecules, which have cross sections $10^{-29} - 10^{-30}$ SM-SERS requires enhancements of the order 10^{9-11} [122].

2.8 Finite-Difference Time-Domain

The Finite-Difference Time-Domain (FDTD) method is a powerful technique for solving Maxwell's equations and analysing electromagnetic interactions with materials in 1, 2 or 3 dimensions. It is a useful tool for plasmonics research as it allows devices to be tested in a simulation environment prior to fabrication and enables their design to be optimised for a desired resonance wavelength [77, 123]. The algorithm for FDTD methodology was first proposed in 1966 by Kane Yee [124], and has become the standard for optical simulations. It is incredibly useful for modelling homogeneous media with the added benefit of providing reliable field interactions from metals and lossy media, making it an effective method for modelling in research [28, 60]. The system involves solving Maxwell's equations (detailed in section 2), if an object's dimensions are much less than the wavelength of incident light then quasistatic approximations are suitable for providing solutions, otherwise, alternate methods are required.

2.8.1 The Yee Algorithm

The FDTD method is applied by solving Maxwell's equations via finite differences or approximations to the spacial and temporal derivatives of Ampere's and Faraday's laws. The Yee algorithm can be broken down into these basic steps [125].

1. Begin by replacing the derivatives in both Ampere's and Faraday's laws with finite differences. Allow the electric field and magnetic field to be staggered in both space and time.

2. Solve the difference equations such that the following equations express the fields to be projected into the future in terms of the fields preceding them.

3. Extrapolate the magnetic fields one time step into the future making them known effectively making them the past fields

4. Repeat step 3 for the electric fields

5. Repeat steps 3 and 4 throughout the course of the simulation. (Usually until a preset time has passed or the field has dissipated to a desired level).

In an FDTD workspace, the 3 dimensional environment is formed by a grid of electric and magnetic fields with every E component surrounded by four circulating H components and vice versa. We can see this illustrated in Figure 2.8.1.

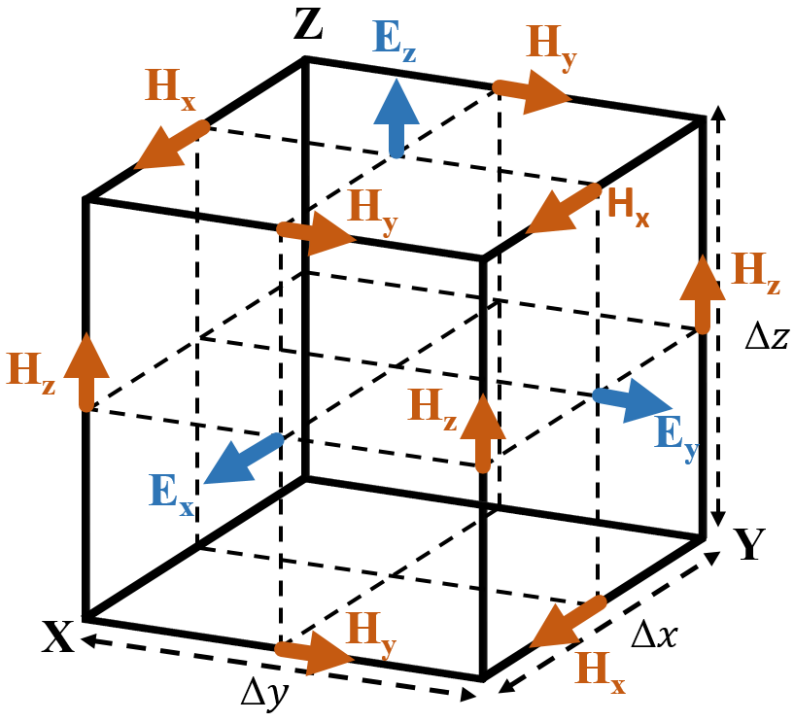

Figure 2.8.1 – Yee cell showing the E and H components along the x, y and z axis [124].

By using Maxwell's curl equations in time and space, it is possible to solve both the electric and magnetic fields. To implement this, we can present the Yee algorithm in one dimension. Starting with Faraday's law for an electric field with a z component propagating in the x direction [125]:

$$-\mu\frac{\partial \mathbf{H}}{\partial t} = \nabla \times \mathbf{E} = -\hat{a}_y\frac{\partial E_z}{\partial x} \tag{2.8.1}$$

In this case H_y is the non zero term of the magnetic field with varying time. Now, for Ampere's Law:

$$\varepsilon\frac{\partial \mathbf{E}}{\partial t} = \nabla \times \mathbf{H} = \hat{a}_z\frac{\partial H_y}{\partial x} \tag{2.8.2}$$

Therefore we can say for the scalar terms

$$\mu \frac{\partial H_y}{\partial t} = \frac{\partial E_z}{\partial x} \tag{2.8.3}$$

and

$$\varepsilon \frac{\partial E_z}{\partial t} = \frac{\partial H_y}{\partial x} \tag{2.8.4}$$

The equations here give the temporal derivative of the magnetic field in terms of the spacial derivative of the electric field for equation 2.8.3, and vice versa in 2.8.4 respectively. Therefore, equation 2.8.3 is used to project the magnetic field in time, whereas equation 2.8.4 is used to project the electric field in a consecutive process. This is known as the ***leapfrog method*** and is intrinsic to the Yee algorithm. Where electric fields are calculated at a point for a particular time from a previously calculated magnetic field, and the subsequent magnetic field is then calculated from this. We can see this illustrated for a 2 dimensional space in Figure 2.8.2.

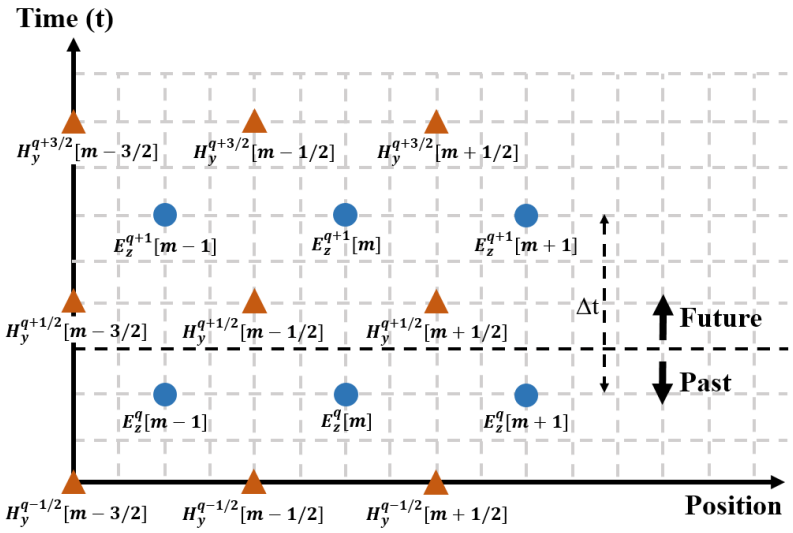

(a)

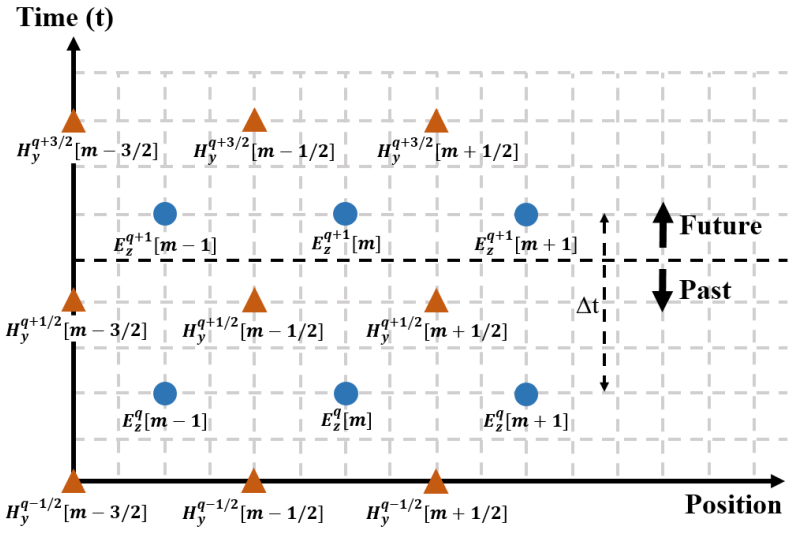

(b)

Figure 2.8.2 – E and H field nodes represented by dots (E field), and triangles (H field), as a function of space and time on the x and y axis respectively. The dashed line indicates the crossover between the past and the future field projections. Where (a) is the point in time before, and (b) is the point in time after updating H_y field.

Then accordingly, in 1 dimension the half step progression is represented in Figure 2.8.3.

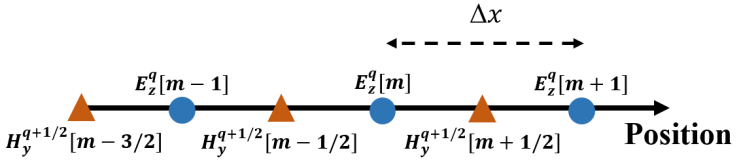

Figure 2.8.3 – 1D FDTD calculation for spacial offset of the E and H fields.

Where, in these figures we use Δx and Δt to refer to the spacial and temporal offset respectively, m represents the incremental step in space and q here represents the step in time. Figure 2.8.2 shows the E and H fields (with their nodes represented by the dots and triangles respectively) are offset by Δx and Δt in space and time. The Yee algorithm dictates the passage of these fields from below the dashed line considered to be in the past to the future state, i.e. projecting the fields from their previous step.

As fields propagating in the simulation domain are dictated by the fields at the previous node, in order to prevent temporal steps becoming too large a stability check can be performed using the *Courant number* denoted by S_c where [125]:

$$S_c = \frac{c\Delta t}{\Delta x} = 1 \tag{2.8.5}$$

Stability checks restrict simulation steps from becoming too large, and hence meaningless results from the Yee algorithm. For the optimum ratio of energy propagation for a single temporal time-step we get a value of 1 for ideal conditions.

2.8.2 Perfect Matching Layer

The Perfect Matching Layer or PML, is a standard boundary condition used in FDTD solvers to terminate fields at the bounding interfaces of the simulation grid. It is designed to absorb fields with little reflection, regardless of angle or frequency. The basis of a PML is to act essentially as an anisotropic lossy material to absorb all incoming fields. It was originally proposed in 1994 by J.P. Berenger [126] who, in his original work divided the field components into two parts, such that the PML could be defined with the necessary phase velocity and conductivity to eradicate the interfacial reflections at the PML's interface. Berenger's proposed method is referred to as the "Split field" PML. It is significantly advantageous to terminate boundaries of a simulation environment with a PML due to its inherent material independence i.e. it will eliminate fields regardless of whether the material is dispersive, lossy, inhomogeneous or non linear.

Throughout the work in this thesis, we use Lumerical solution's FDTD Maxwell solver which employs a PML based on the stretched coordinate formulation proposed

by Gedney and Zhao [127]. The main purpose of the PML is to terminate the fields via absorption with minimal reflection.

2.8.3 Near to Far-Field Transformations

When studying electric field interactions in a simulation environment, it is often useful to determine their projected behaviour when considering the far-field. The benefits of far-field projections from near-field monitors is that it allows for the far-field behaviour to be determined without the need to extend the FDTD domain, thus saving calculations times and memory requirements. We use the built in far-field calculation methods which are included with Lumerical's FDTD Maxwell solver [128].

In this thesis, the far-field scattering efficiency is calculated from a projection of the near-field at the centre of the nano-gap formed between the nanoparticle and an extended metal film. This is where the target material will be located in practical SERS measurements. Hence, it represents the Raman scattering to be obtained from our nano-gaps. We can see this configuration in Figure 2.8.4.

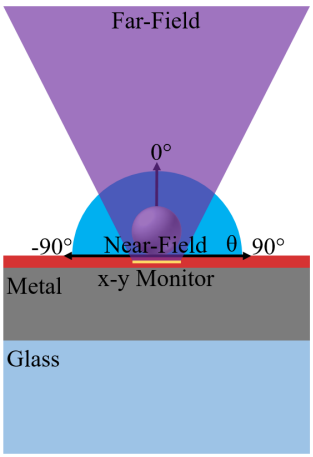

Figure 2.8.4 – Near to far-field transformation diagram where the near-field is projected to the far-field from the monitor located at the centre of the nano-gap.

A full description of transformations of Near To Far-Fields (NTFF) in the time domain was first presented in A Finite-Difference Time-Domain Near Zone to Far Zone Transformation [129]. The method used in this paper describes an approach for transformations of the NTFF in FDTD computations by calculating the tangential electric and magnetic fields from a closed surface encompassing the scatterer at each time-step. Post processing

takes place after the simulation to convert these vector fields to the far-field region. In order to obtain the results in the frequency domain, it is necessary to perform Fourier transformations. NTFF transformations in the frequency domain are generally only valid at single frequencies and require subsequent calculations to be performed if further frequencies are required. A more in-depth discussion of the mathematical principles for projecting the far-field from the near-field can be found in Computational Electrodynamics the Finite Difference Time Domain Method [130].

2.8.4 Limitations of FDTD

FDTD methodology although powerful, does have its drawbacks. The modelling environment must be gridded sufficiently around the structures involved to produce reliable results. This means that fine geometrical features such as arrays or nanoparticles in the simulation domain can draw large memory requirements. This factor scales as a function of the volume and wavelength such that the memory requirements for $2D$ are approximately equal to $\sim a \times (\lambda/dx)^2$. Whereas for $3D$, this factor becomes $\sim V \times (\lambda/dx)^3$. Where a and V are the area and volume in each case, and dx is the mesh size. Similarly, the simulation time will scale as $\sim a \times (\lambda/dx)^3$ and $\sim V \times (\lambda/dx)^4$ for $2D$ and $3D$ calculations accordingly, meaning that times for simulations to be carried out can increase rapidly.

Far-field projections from near-field monitors usually require post processing which can take time. Because the modelling environment must be finite, FDTD solvers utilise Absorbing Boundary Conditions (ABCs) to terminate fields at their boundaries. An ABC, such as the PML provides the best means to prevent internal reflections within the domain.

Staircasing is another problem that arises when considering a Yee lattice to provide solutions to the electric field interactions. A square lattice may be sufficient for most structures, however when complex geometry is involved, such as a spherical nanoparticle, problems can occur. We can see the problem with using a grid mesh to represent a spherical particle in Figure 2.8.5 where at the boundaries of the structure more than one material will occupy each cell shown more clearly in Figure 2.8.5b.

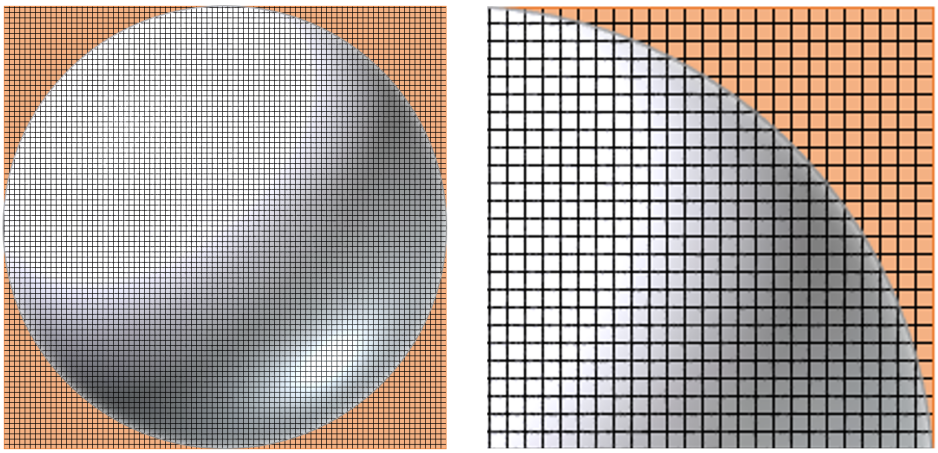

(a) (b)

Figure 2.8.5 – Using Yee cells to simulate the curvature of a spherical nanoparticle we can see that even when fine meshing is used more than one material can occupy the same Yee cell.

Different methods can be applied to deal with this issue such as volume averaging or conformal FDTD methodology. One such conformal method is proposed by Wenhua Yu and Rah Mittra in 2001, and is a basis for the theory applied behind Lumerical solutions at curved interfaces [131]. Their method makes use of an individual electric field component along the edges of the Yee cell, as opposed to other methods which calculate the volume which is partially filled with dielectric medium. By doing so, it utilises the information at the edges of the cell to formulate an update algorithm for the field. Because the technique outlined here can produce accurate results, whilst satisfying a case in which all sides of the cell represent a different dielectric constant, it is possible to apply this to cells housing more than two different material properties. The technique agrees with other theoretical analysis of curved surfaces and eliminates the need for volume calculations of materials within cells or ultra fine gridding to nullify the staircasing effect.

Chapter 3

Literature Review

This review describes the relevant papers researched throughout the project categorised by the field, taking the beneficial information towards forwarding the experiments to be carried out. The review analyses the conditions used for optimal research with plasmonic devices and their experimental procedures. Also, this chapter takes the form of a critical discussion, showing insight and an awareness of differing arguments, theories and approaches. We give a comparison of different approaches to the work detailing their methods and opinions on the subject, noting areas of disagreement. Methodology will be taken into scrutiny to establish correct and proper techniques for the work to be completed. Any gaps in the research will be shown to allow for work in these highlighted areas to be improved upon with the work in this thesis. Carrying out a study of this nature is important to reduce the possibility of reproduction of work and to allow efficient research practices as well as establishing the current meta of the field.

3.1 Plasmonics

Optical properties of noble metal nanoparticles have been a focus of study for many researchers, the LSPRs achieved are subject to the nanoparticle spacing, size, shape, composition and dielectric environment [15, 17, 18, 23, 25, 34, 65, 132–136]. Mie theory, which was first described in 1908 can be utilized to understand LSPRs in a simple sphere, however, in more complex geometry more advanced numerical methods are required for the description of nanoparticle properties [12].

Plasmonic nanostructures can be utilised for refractive index sensing which relies on measuring the spectral shift of resonant modes of the structure relative to changes in the refractive index of the surrounding media. Changes to the dielectric environment in

proximity to plasmonic nanostructures produce shifts in the LSPR peak location and can be exploited to detect binding events from molecules. In a study by Sherry *et al.* [22], the LSPR from silver nano-cubes with a glass substrate is investigated using dark field microscopy. Two resonance peaks are discovered when the silver nano-cube interacts with the glass substrate. One is red-shifted relative to the bulk spectrum and the other is blue shifted and considerably narrower which makes it very suitable for applications in plasmonic sensing due to its high figure of merit. The second peak was later confirmed with theoretical simulations using FDTD electrodynamic calculations. This can all be seen in Figures 3.1.1a and 3.1.1b.

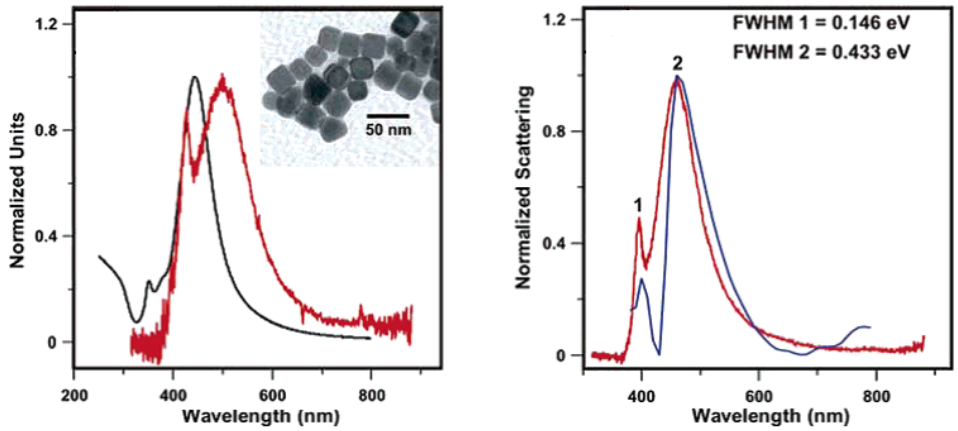

Figure 3.1.1 – (a) Nano-cube ensemble extinction (black) single nano-cube via dark field scattering (red). (b) Single nano-cube via dark field scattering (red) and FDTD theory (blue) for a 36 *nm* silver nano-cube on a glass substrate [22].

From the work in this paper, it can be seen that nanoparticle geometry holds the key to higher sensitivity in detection methods. Cube shaped particles are ideal for the production of two resonances with the blue shifted peak having high potential for sensing capabilities due to its extreme sharpness [22].

3.1.1 Nano-Gaps for Raman Enhancement

As plasmonic systems are brought into close proximity to one another, the nano-gap created at their boundaries allows the surface plasmons in each system to interact together. The coupling of plasmons is known as plasmon hybridisation, and leads to intense regions

of confined field known as hot spots.

In 2010, Min Hu *et al.* published a paper titled "Single Particle Spectroscopy Study of Metal-Film-Induced Tuning of Silver Nanoparticle Plasmon Resonances" [133]. It presents an experimental study of the tunability of the silver nanoparticle LSPR in close proximity to a gold film substrate, via exploitation of the strong electromagnetic coupling between the nanoparticle and the film. Single particle spectroscopy took place on 250 separate silver nanoparticles and distinct resonance features were presented for the excitation at the horizontal and vertical modes which were based on dipole-dipole interactions. The paper presents promising results in the fields of plasmon enhanced sensing applications in the visible regime as well as SERS methodology.

The nanoparticles exhibit peak resonance wavelengths within the range $450-490$ *nm*. A significant red-shift was observed for silver nanoparticles deposited onto the glass substrate and then subsequently onto the gold film. It should be noted that the particles deposited on the gold film exhibit a stronger scattering intensity compared to those on glass by a factor of $2-3$. By varying the dielectric spacer layer of the substrate, different resonance peaks were observed for the coupling of the nanoparticle and the gold film as shown in Figure 3.1.2a.

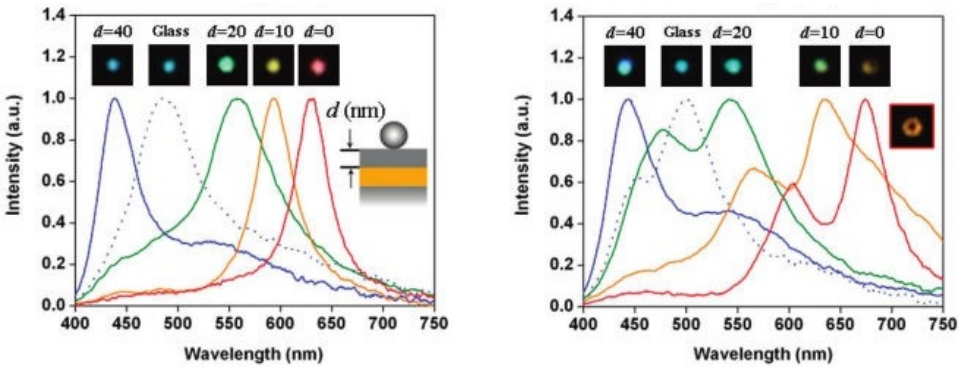

Figure 3.1.2 – Optical scattering spectra for silver nanoparticles on varying substrate thicknesses [133].

The peak wavelength passes through the entire visible spectrum 440 to 670 *nm*. Notably, the silver nanoparticles exhibit a resonance very close to the wavelength of a Helium Neon (HeNe) laser at 632 *nm* meaning that using this setup in conjunction with SERS is

a possibility. It is clear that by reducing the spacer layer between the gold film and silver nanoparticle, the spectra exhibit a red-shift in the plasmon resonance. The red-shift can be described by a simple dipole interaction model, whereby both the horizontal, and vertical LSP modes can be excited on the particle. These vertical and horizontal modes also play a role in the single and double peaks exhibited in Figure 3.1.2b.

This study shows the large LSPR for single silver nanoparticles and the tunability of silver nano-spheres near a thin gold film through changing the distance of the particle to the metal film via a dielectric spacer layer. The single particle spectroscopy in this experiment revealed high tunability for the silver nano-spheres from the near UV to near IR spectrum by varying the coupling strength to the particle and film. However, higher enhancement factors could be found through more thorough optimisation of nano-gap spacing and plasmonic nanostructure hybridisation [133].

A theoretical paper by Hill *et al.* studies the features of gold nanoparticles and the behavioural characteristics they exhibit through 3 dimensional FDTD methods during dark field excitation [29]. The paper studies the plasmonic interaction when nano-gaps are introduced between the nanoparticle and the substrate surface. The results shown in Figure 3.1.3d demonstrate that although the nanoparticles exhibit strong enhancement in the near-field, the effect decays quickly as the size of the spacing layer is increased. We also see in Figure 3.1.3c that the scattering has a related effect with higher scattering efficiency associated to the narrower gaps, also red-shifting as a function of gap width.

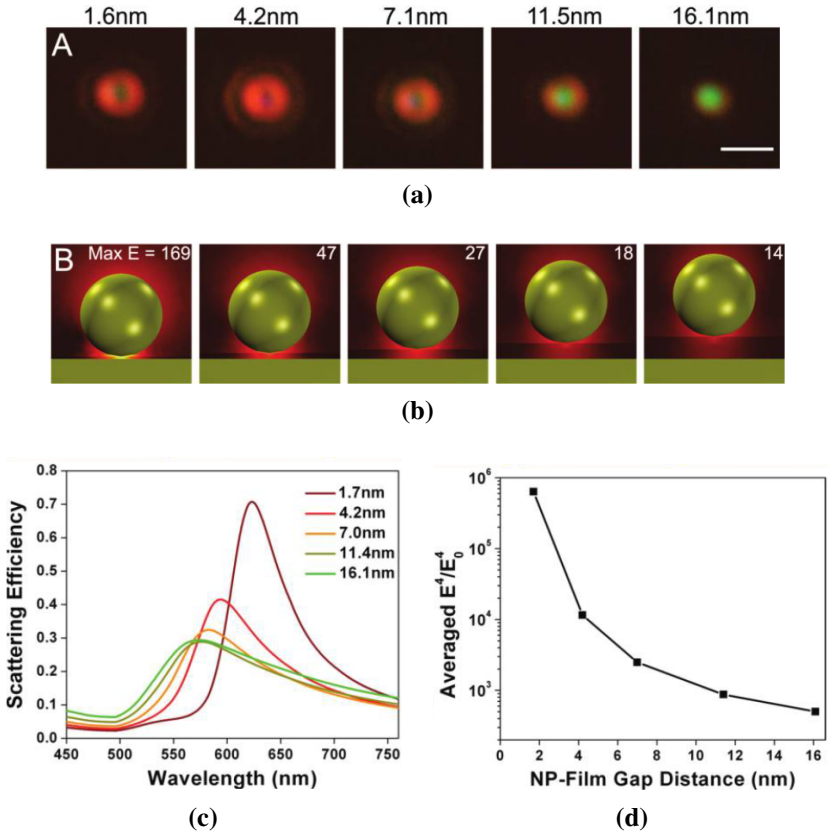

Figure 3.1.3 – (a) White light scattering due to nanoparticles separated from gold substrate via spacing layer (scale bar used at 1 μm). (b) Electric field distribution via dark field illumination from 633 *nm* exciter. Max E gives the highest field obtained in each configuration. (c) Scattering efficiency taken from the scattering cross section integrated over the numerical aperture $NA = 0.9$ at different spacing levels. (d) Averaged values for E^4/E_0^4 for dark field measurements at 633 *nm* plotted against the NP spacing layer thickness [29].

This data is very useful for comparison with the modelling done in Chapter 5, and will allow the validity of the results to be referenced [29]. It gives a clear indication of the sensitivity of device fabrication and the scattering characteristics of nanoparticles.

A study by Kleinman *et al.* also investigated hot spot dominated systems. In this case, single nano-antennae consisting of 90 *nm* gold nanoparticles functionalised with a reporter molecule, lightly aggregated and then coated with a SiO_2 protective shell [137]. The paper investigated the dependence of far-field scattering properties in relation to the LSPR and subsequently the enhancement characteristics of the plasmonic system for hot spot based structures.

The paper used LSPR-Transmission Electron Microscopy (TEM) to investigate the SERS spectra of the material. The single nano-antennae in this study revealed peak en-

hancement factors for excitation wavelengths of lower energy red-shifted from the scattering peak of the system. Overall, the enhancement factor ranged from $(2.5 \pm 0.6) \times 10^4$ to $(4.5 \pm 0.6) \times 10^8$ where the maximum enhancement occurred at 785 *nm*.

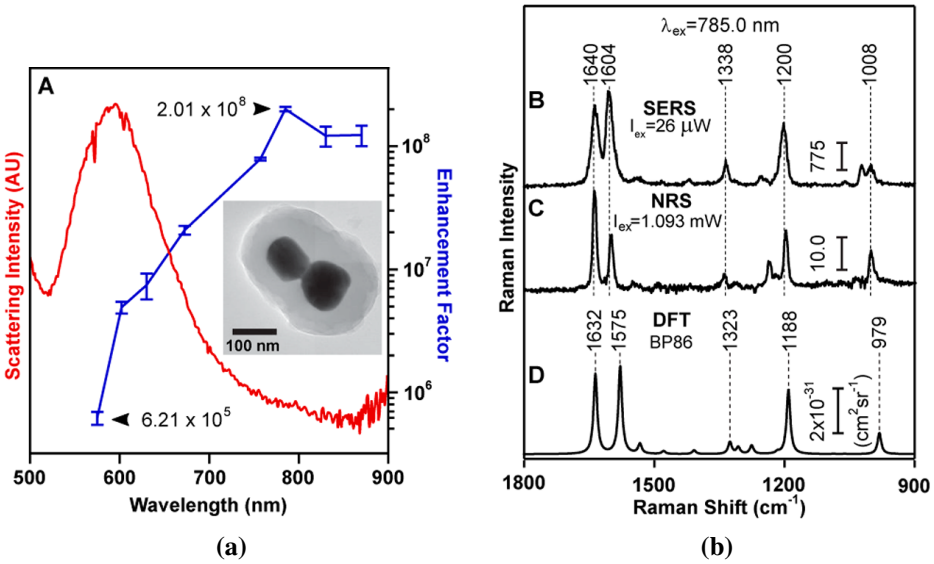

Figure 3.1.4 – (a) Scattering spectrum for the nano-antenna dimer (red), plotted with the excitation profile of the 1200 cm^{-1} Raman band of the target material at different excitation wavelengths. (b) Line (B) represents SERS spectra from the 785 *nm* excitation of BPE coated nano-antennae. Line (C) shows Raman spectra from the same material in solution while (D) represents the theoretical analysis of trans-1,2-bis(4-pyridyl)-ethylene (BPE) modes [137].

This study presented SERS measurements from fourteen individual nano-antennae including two dimers and three trimers with varying gap sizes, these basic structures were the main focus of the investigation. The paper states that SERS behaviour is dominated by hot spots, which is influenced by the excitation of dark plasmon resonances. It attempts to do so by utilising eight excitation wavelengths (575.0, 602.1, 630.0, 672.4, 757.0, 785.0, 830.0 and 870.0 *nm*) to generate the excitation profile as shown in Figure 3.1.4a.

The study found that independent of cluster composition of the nano-antenna, the highest electric fields from the SERS was observed for excitation wavelengths of 785 and 830 *nm*. It claimed that the enhancement trend of a hot spot dominated system is independent of the spectral position of the LSPR. Their reasoning being, that the interfering excitations of conduction electrons, which generate large enhancement of electromagnetic fields in the near-field do not have phase coherence with the individual particle plasmons

in the far-field.

Lombardi *et al.* shows a similar system to the one used throughout this thesis to probe the near-field optical response, and compare it to the far-field to see the relationship between them [138]. The experiment uses spectral-scanning from a tunable laser to record SERS spectra via dark field from individual nanostructures. The nanostructure configuration used in this study involves 60 *nm* gold nanoparticles deposited onto a gold film with a p-terphenylthiol (TPT) molecular spacer between them, known as the Nanoparticle on Mirror (NPoM) geometry as seen in Figure 3.1.5.

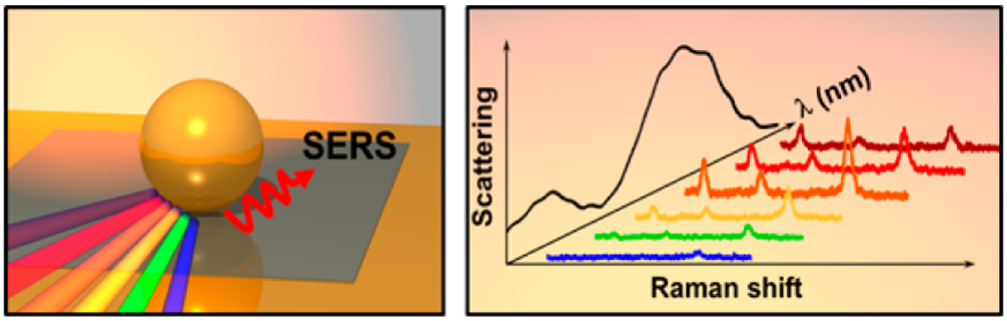

Figure 3.1.5 – (a) NPoM diagram. (b) Raman spectra as a function of scattering wavelength. [138].

The near-field NPoM resonance in this configuration was found to be blue-shifted from the scattering peak in contrast to the red-shifts found in isolated nanoparticles. This is explained via transformation optics to show that individual modes will give different radiative processes interfering constructively in the near-field, while destructively in the far-field.

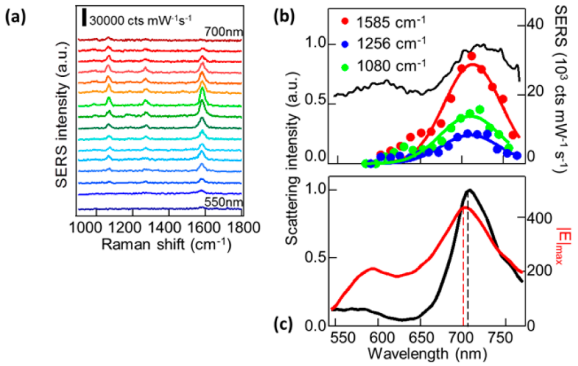

Figure 3.1.6 – (a) SERS spectra from individual 60 *nm* NPs with laser excitation ranging from $\lambda_p = 500 - 700$ *nm* in 10 *nm* intervals. (b) SERS intensity of TPT molecules peak wavelength, inlaid with the scattering spectrum (black). (c) FDTD simulations of scattering (black) and maximum near-field (red) [138].

There is no shift with the change in wavelength of the SERS peak wavelengths, however, at 640, 650 and 670 *nm* the 1585, 1256 and 1080 cm^{-1} modes respectively show increased intensity. The results show when analysing a range of NPoMs, the near-field resonance is always blue-shifted from the far-field resonance by 4 to 55 *meV* depending on the nanoparticle.

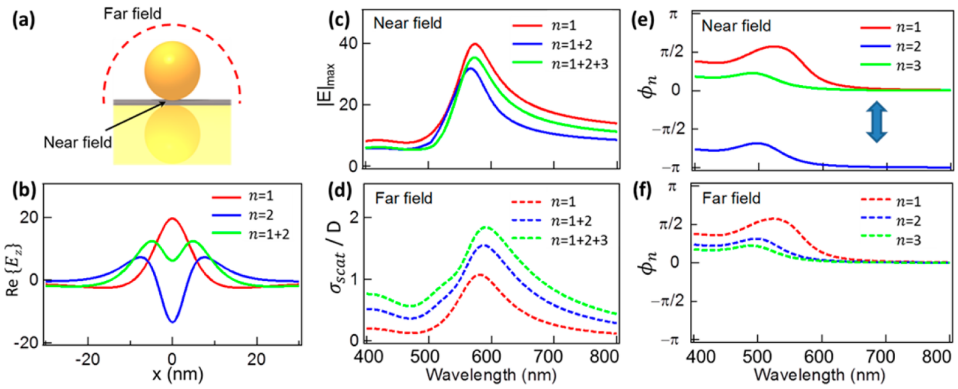

Figure 3.1.7 – (a) Simulation diagram. (b) Field distribution perpendicular to NP surface for dipolar and quadrupolar modes, labelled $n = 1$ and 2 respectively. (c) Maximum field in the gap (near-field) vs wavelength. (d) Scattering (far-field) vs wavelength. (e) Phase of modes $n = 1$, 2 and 3 in the near-field. (f) Phase of modes $n = 1$, 2 and 3 in the far-field [138].

It is interesting to see from Figure 3.1.7 that the plasmonic resonance from modes $n = 1$ and $n = 2$ strongly interfere with one another. Most importantly, noting that from (e) that they are opposite in phase in the near-field causing destructive interference. Whereas, in the far-field they radiate coherently, owing to the blue-shifts in resonance in the near-field and red-shifts in resonance in the far-field, as seen in (c) and (d).

The simulations in this report suggest these shifts based on a classical treatment of the system, neglecting non-locality and the electron crossover between metals. However, they note that the quantum effects here would be negligible as both the experimental and theoretical resonance shifts agree.

Fu *et al.* used SERS on silver nano-cubes on a silver grating to experimentally demonstrate that the performance of this strategy can be improved vastly over the use of a silver film substrate [139]. This is because the silver nano-cubes have more areas of interaction with the substrate which result in hot spots leading to further enhancement of the Raman signal.

The experiment compared two substrates; one with a silver film technique and the other using the silver grating, from this, a comparison of performance was shown. The nano-cubes measured around 70 *nm* in all directions. The target molecule R6G identified in the spectra shown in Figure 3.1.8 was used and detected in low concentrations.

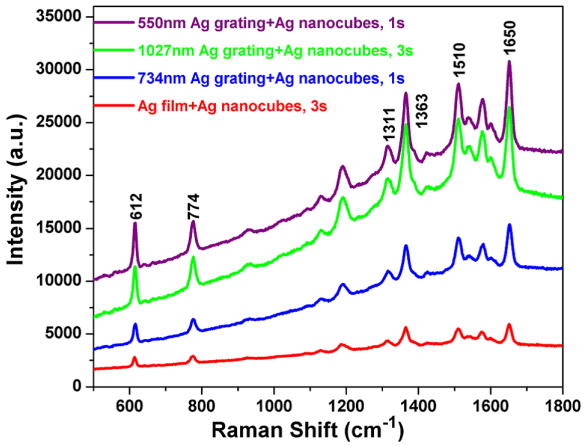

Figure 3.1.8 – Rhodamine 6G Raman spectra for three dual layer SERS substrates [139].

The results in Figure 3.1.8 show that for gratings with a 550 *nm* separation the Raman signal was enhanced by 15.6 times for the silver grating over the simple silver film and a further 78.8 times for the silver grating with silver nano-cubes. It was also discussed during the paper that the concentration of nano-cubes affected the enhancement of the Raman signal. It is anticipated here that this strategy will be useful for high sensitivity biosensing methods [139]. The silver grating with nano-cubes were then used in conjunction with decreased quantities of R6G to enable the system to detect down to essentially single molecule levels. Figure 3.1.9 shows the spectra taken from sample concentrations of 10^{-6}, 10^{-8}, 10^{-10} and 10^{-12} M with integrations times of 0.3, 1, 3 and 10 seconds respectively.

As shown, the decreased concentrations correlate with a lowering of intensity in the Raman scattered signal. However, with an increase in detection time, the experimental setup still has the detection capabilities to this level. The methodology used in this paper was very useful and the spectra are comparable for reference to those taken in Chapter 6. It signifies the importance of the strong coupling between nanoparticles and the film geometry below. It should be noted however, that the contribution of Raman signal also

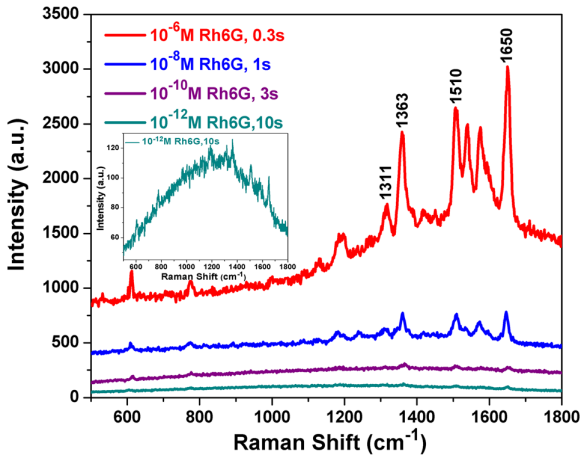

Figure 3.1.9 – Raman spectra for Rhodamine 6G at decreasing concentrations [139].

arises due to clustering effects shown by SEM images from the paper which is difficult to reliably reproduce.

A similar effect has been seen in other research [140], where enhancement around the scattering modes is said to stem from phase-coherent excitation of LSPRs. Whereas, alternate high field strength regions result from the collective, and coherent excitations of conduction electrons in the metal that have interfered and dephased because of the scattering of plasmons and light from surface and gap features.

This work aims to shed light on understanding scattering and enhancement from metal nanoparticle aggregates, and is less applicable to consistent nano-gap geometry.

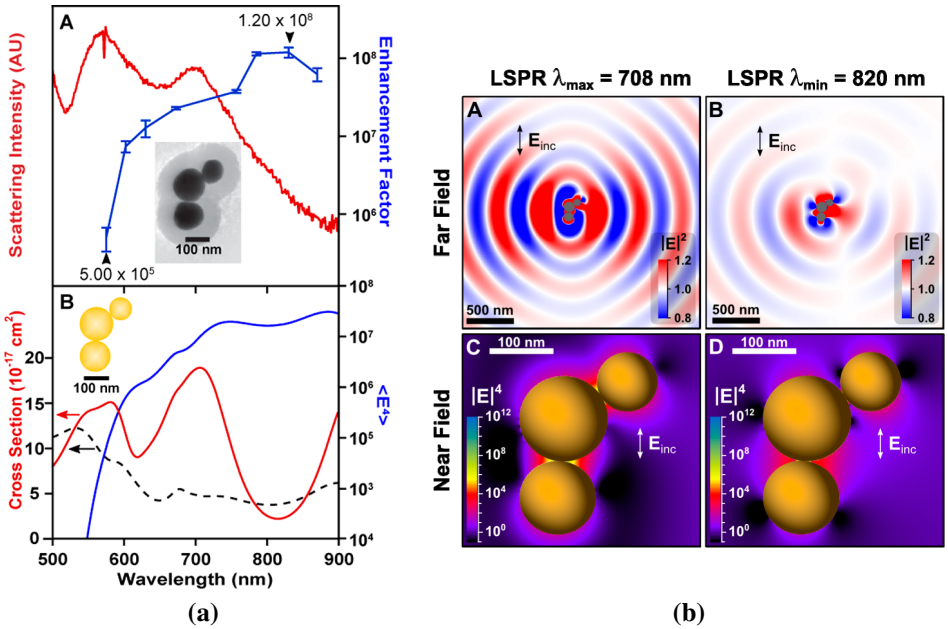

Figure 3.1.10 – (a) Experimental and calculated LSPR and SERS data for the nano-antenna trimer: Experimental dark field scattering (red) and excitation profile of the 1200 cm^{-1} Raman band (blue). (b) Far-field (top row) and near-field (bottom row) for the nano-antenna trimer, A and C represent the 708 *nm* excitation, whereas B and D represent the 820 *nm* excitation [137].

We can see in Figure 3.1.10b, the top images depict that the far-field scattering intensity ($|E|^2$) is lower at 820 *nm* than at 708 *nm*. This can be attributed to the destructive interference of the multipole contributions to the polarization of the individual spheres when the excitation wavelength is 820 *nm*. The plasmon resonance modes which are difficult to excite are termed ***dark modes***. The authors conclude that the measurements demonstrate there is no relationship between far-field scattering of a system, with a hot spot and the SERS wavelength response. However, the conclusions drawn do not take into consideration the absorption component of the extinction spectrum we have covered in our work. By presenting both the absorption and scattering components, a clearer picture of the behaviour of the structure is presented. This information is needed to describe whether the structure is dominated by scattering or absorption at the wavelengths investigated. Also the scattering here is a result of the entire system and not from discrete nano-gaps. In our work, we project the far-field directly from the nano-gap we are investigating at the location of the analyte under investigation. On top of this, the non-locality of the system has not been accounted for. At gaps < 1 *nm* the quantum regime takes precedent and

the classical approach no longer applies [79]. This is evident in their structures, so their approach can not apply to the broad sense of all hot spot dominated systems.

Wang *et al.* presents work performed using a nano-gap situated between gold nanoparticle dimers (55 *nm* diameter) deposited onto a gold film (200 *nm* thickness) [27]. The research involved both experimental and theoretical work to investigate the enhancement for the system, as well as SERS from probe molecules at certain excitation wavelengths. Because 98% of SERS signal is only contributed to 2% of molecules adsorbed to the hot spot regions of a plasmonic nanostructure, it is therefore of the utmost importance to optimize the conditions for generating these regions. Therefore, it can be said that a SERS probe molecule can be used to detect the location of the strong near-field enhancement of these structures. By using two Raman probe molecules with distinct Raman fingerprints but similar cross sections located at different regions of the nanoparticle, the system can then be investigated with different excitation frequencies to selectively excite both probe molecules.

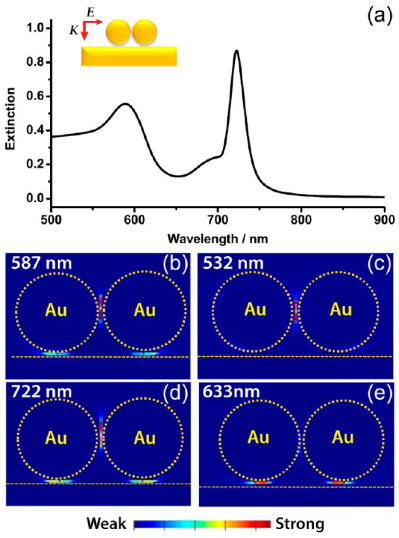

Figure 3.1.11 – (a) Extinction spectrum from nanoparticle dimer on gold film system via FDTD. Electric field distribution from; (b) 587 *nm*, (c) 532 *nm*, (d) 722 *nm*, (e) and 633 *nm* [27].

The 587 *nm* peak from Figure 3.1.11 (a) is contributed from the LSPR mode of the gold nanoparticle relating to a relatively low electric field, whereas the 722 *nm* mode results due to the coupling mode of the SPR and the two gold nanoparticles, here the electric field is much more enhanced. Although the 722 *nm* excitation electric field is

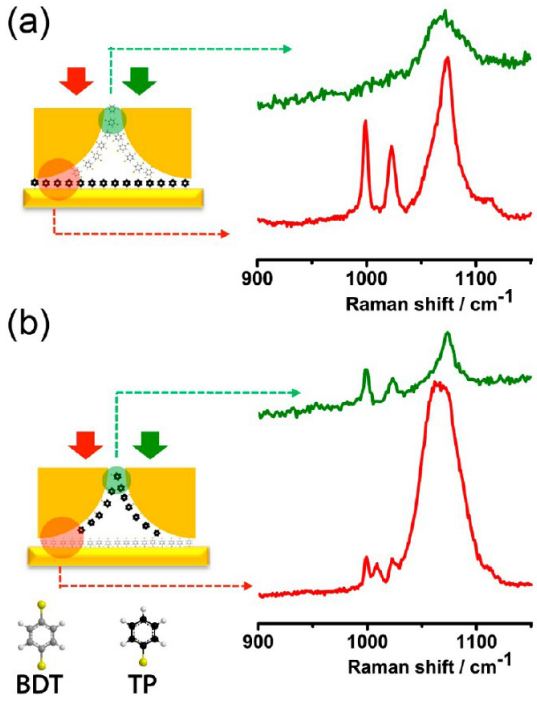

Figure 3.1.12 – (a) Two probe molecules adsorbed to different regions of the nanoparticle dimer system with their respective SERS spectra. Thiophenol (TP) is situated within the nanoparticle gap and benzenedithiol (BDT) is between the particle and the film. Green lines indicate 532 *nm* excitation, whereas the red lines correspond to the 633 *nm* excitation wavelengths. (b) Same system with molecule sites exchanged [27].

intense, the distribution of field is not localised specifically to either the dimer gap or the gold surface. However, with a slightly weaker signal, the 532 and 633 *nm* excitations produce near-field intensities localised to these regions specifically.

The study used two probe molecules, thiophenol (TP) and 1,4-benzenedithiol (BDT) to investigate SERS at different regions of the dimer system. These materials were chosen due to their similarities in Raman cross sections and adsorption characteristics on the gold surface. Due to the fidelity of Raman spectroscopy, it is possible to distinguish their similar molecular structure from the 1000 cm^{-1} band which is present in TP but absent in the BDT.

It should be noted however, that although the nanoparticle dimer is simulated in the FDTD measurements, the experimental work is a result of a monolayer of gold nanoparticles over the surface of the gold film, the contributions of other plasmon coupling modes could well have an effect on this. Not only this, but also a contributing factor for any discrepancies stems from the gold layer in the simulation being only 50 *nm* thick. At

these thicknesses, fields are able to penetrate and leak through to the opposite side, this is not taken into consideration during the report. The benefits of using a system with a partial nano-gap arrangement can be further shown in Figure 3.1.13

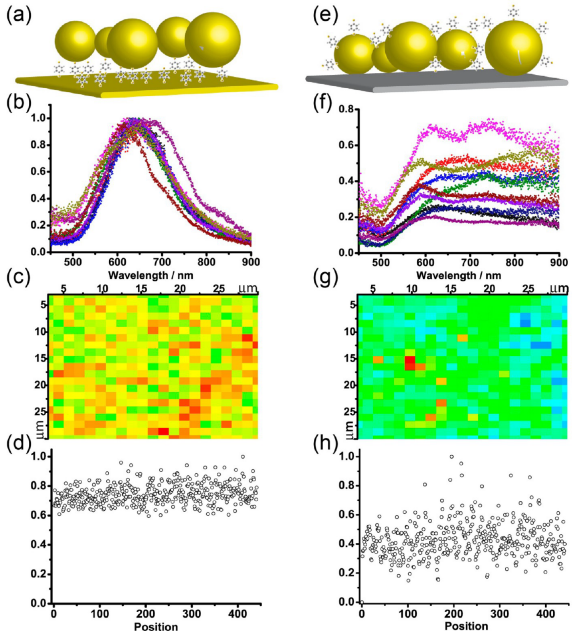

Figure 3.1.13 – A comparison of two substrate designs (a-d) vs (e-h). (a and e) Schematic with and without the nano-gap. (b and f) Scattering spectra for the gap structure using dark field measurements. (c and g) Raman mapping images via normalised intensity of the 1064 cm^{-1} peak with step size 1.5 μm over a region of 30×30 μm^2. (d and h) Intensity distribution of the SERS peak for both respective substrates [27].

The scattering spectra shown for the nano-gap substrate is much narrower than that without the gap. Also, by using Raman mapping through a 633 *nm* laser over an area of 30×30 μm^2 for a single mode of the target molecule, we can see the uniformity is much better for the gap based structure. Finally, through the Relative Standard Deviations (RSD) from the SERS intensity, it can be shown that a RSD of about 9.3% and 10.9% is present for the gap-mode SERS substrates. Whereas, the RSD for the two traditional SERS substrates are 28.4% and 28.7%. Therefore, it can be concluded that the gap mode substrate outperforms traditional SERS substrates.

Huang *et al.* investigates the plasmonic effect exhibited between dimers of nano-particles [136]. The study uses a dipole model in Finite Element Method (FEM) calculations to analyse the power dependence of the near-field enhancement as a function of gap size. It should be mentioned that there are distinct differences between near and far-field

characteristics of plasmon resonances, therefore a quantitative description of the system requires both near and far-field descriptions of the system. Using COMSOL and 0.33 *nm* meshing parameters, the study used the Drude-Lorentz model for the silver and gold nanoparticle dimers in the near-field. Far-field calculations were performed by integrating the power flow through the system via time averaged Poynting vectors, S_{ext}, over the surface, Ω, encompassing nanoparticle dimers.

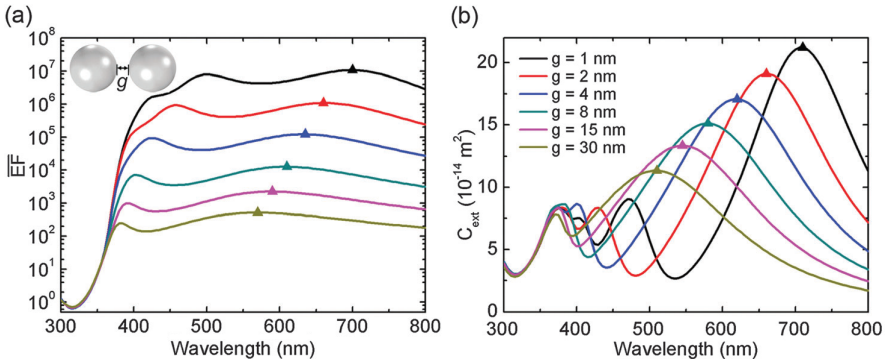

Figure 3.1.14 – (a) Near-field electric field. (b) Extinction spectra of $d = 120$ *nm* silver dimers with gap size g ranging from $1 - 30$ *nm* with triangles to represent the bonding mode between the nanoparticles [136].

It can be seen from Figure 3.1.14 that the enhancement can range from 10^3 for a 30 *nm* gap up to a massive 10^7 for gaps as small as 1 *nm*. Also, as gap size decreases the resonant mode red-shifts, and due to increased coupling strength, the extinction spectrum broadens leading to broader resonances.

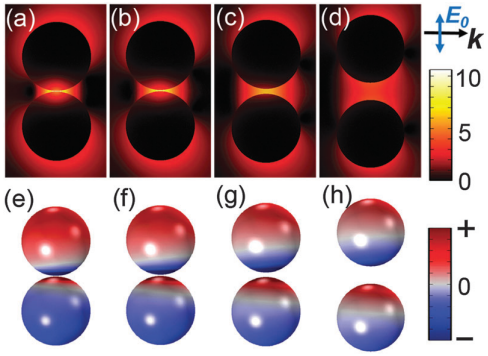

Figure 3.1.15 – (a-d) Local normalised electric field E^4/E_0^4 for nanoparticle dimers at resonance wavelength. (e-h) Surface charge distributions with red and blue representing positive and negative charges respectively. Gaps sizes and resonance wavelengths are; $g = 1$ *nm* ($\lambda = 700$ *nm*), $g = 2$ *nm* ($\lambda = 660$ *nm*), $g = 8$ *nm* ($\lambda = 610$ *nm*) and $g = 30$ *nm* ($\lambda = 570$ *nm*) [136].

Figure 3.1.15 shows E^4/E_0^4 for nanoparticle dimers as well as the corresponding sur-

face charge distributions, with red and blue representing positive and negative charges respectively. From the surface charge distributions, a generalised power-law dependence was established for the near-field electric field and the gap size. For perfect electric conductors, a $E^4 \approx 1/g^4$ dependence is drawn, however, for practical systems the behaviour more closely resembles $E^4 \approx 1/g^2$. This paper shows the significance of investigating both the near-field, and the far-field, for nano-gap systems using nanoparticle dimers, emphasizing the differences between them as a function of gap width.

Zhang *et al.* investigates a novel cavity design for excellent tunable SERS detection via a rolled, tubular nano-resonator with silver nanoparticles deposited onto its inner surface [141]. This design approach yields a further 10^5 enhancement in comparison to the non-resonant flat SERS structures by supporting Whispering Gallery Modes (WGMs) within the cavity.

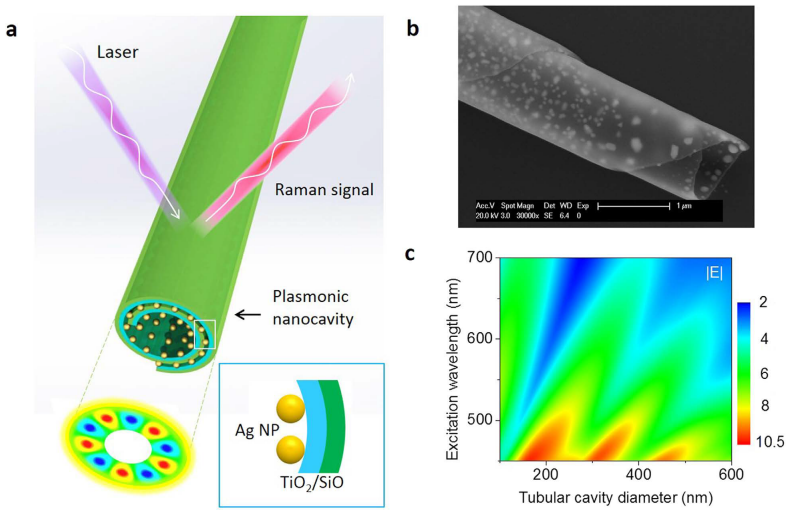

Figure 3.1.16 – (a) Plasmonic structure diagram schematic. (b) SEM image of WGM nano-cavity. (c) Simulated electric field over tube wall with WGM plasmon nano-cavity as a function of the cavity diameter and excitation wavelength demonstrating tunability [141].

Figure 3.1.16 shows the schematic diagram of the WGM device. The tubular nano-cavity consists of a 3 *nm* layer SiO_2 and a 3 *nm* layer of TiO_2 patterned with 25 *nm* silver nanoparticles. The SPR between the silver NPs is transferred to enhance the Raman signals of chemicals on the cavity walls.

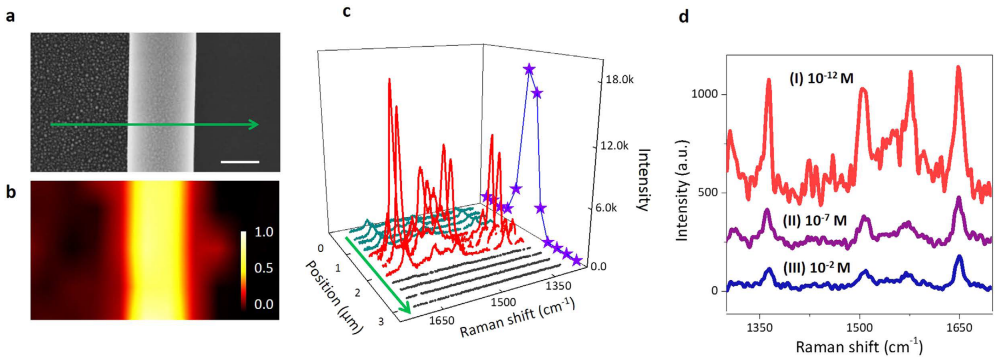

Figure 3.1.17 – (a) SEM image of WGM. (b) Raman intensity mapping of R6G signal from the 1364 cm^{-1} mode using 514.5 *nm* excitation. (c) Raman spectra via scans of the WGM where the purple line refers to the intensity of the 1650 cm^{-1} mode. (d) Comparison of Raman spectra between; (I) Silver NP nano-cavities on flat substrate, (II) nanotubes in absence of nanoparticles and (III) full WGM NP nanotube. It is also noteworthy to mention the concentration of the target analyte from the acquired spectra is significantly lower for the nanotube design [141].

The study investigated three configurations of the device; silver nanoparticle nano-cavities on flat substrate, nanotubes in absence of nanoparticles and full a WGM NP nanotube, all with R6G concentrations ranging from 10^{-1} to 10^{-13} M deposited via drop casting onto the respective devices. The substrates were excited with a 514.5 *nm* laser line, and it can be seen from Figure 3.1.17 that the lowest detectable concentration came from the nanotube patterned with the silver nanoparticles.

The tunability of the device is owed to the diameter of the tube coupled with the excitation wavelength. When using different tube diameters different resonant modes are accessed. The calculated electric field and measured Raman intensity is plotted in Figure 3.1.18. For (a), where WGMs for 500 *nm* (mode 3) and 820 *nm* (mode 5) tube diameters are shown for 514.5 *nm* excitation, whereas (e), demonstrates the modes achieved via a 632.8 *nm* laser line.

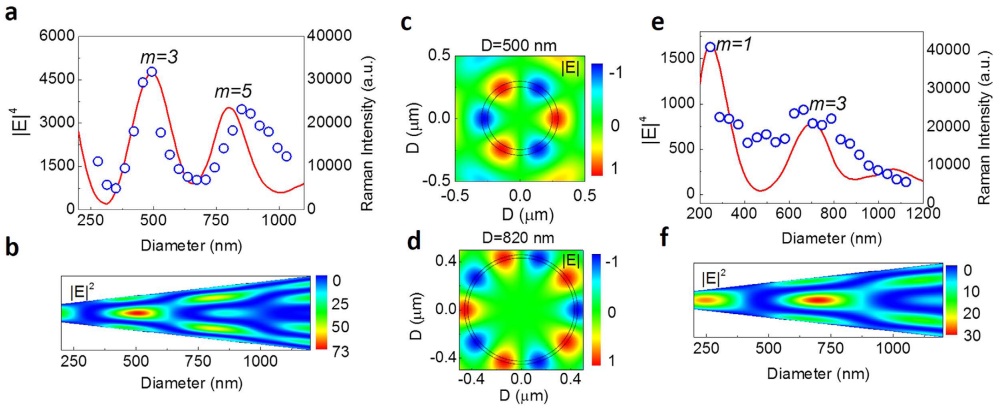

Figure 3.1.18 – (a) Calculated field enhancement (red line) with measured Raman intensity (blue dots). (b) FDTD calculated electric field distribution with 514.5 *nm* excitation with varying tube diameter (conical cavity). (c) Calculated field profiles for the resonant cases in plasmon nano-cavities with a 514.5 *nm* excitation. This shows the WGM for the 500 *nm* and (d) 820 *nm* respectively. (e) Modes achieved via a 632.8 *nm* laser line simulated (red) and experimental (blue dots). (f) FDTD calculated electric field distribution with 632.8 *nm* excitation with varying tube diameter (conical cavity) [141].

To further demonstrate the potential of the device, it can be shown that by using *cm* lengths of the nanotube, the device can be used as a optofluidic sensor with the material flowing through its centre. This allows for trace sensing of analytes and a potential cost effective nano-fluidic sensor for trace materials.

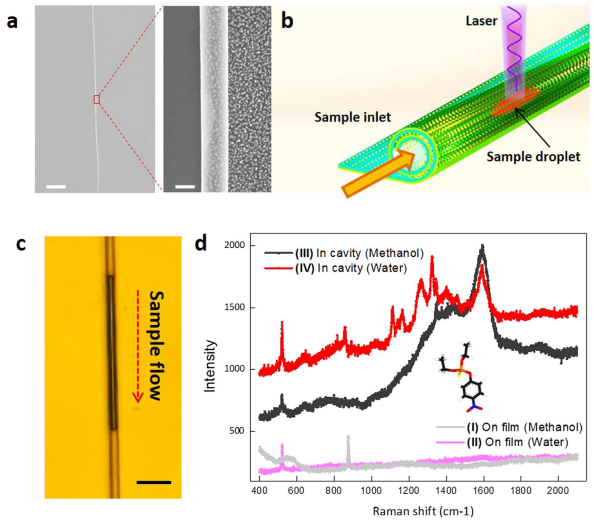

Figure 3.1.19 – (a) SEM image of a long and uniform WGM tube plasmonic nano-cavity. Scaler bars: left 10 μm; right 500 *nm*. (b) Illustrated representation of the plasmon nano-cavity functioning as a nanoscale optofluidic detector. (c) Microscopy image of small-volume pesticide solution pumped in the plasmon nano-cavity. Scale bar is 3 μm. (d) Measured Raman spectra of parathion in four configurations of the device and solvents. (I) On a flat silver NP array using methanol and (II) water as the solvent. (III) In the tubular plasmon nano-cavity using methanol and (IV) water as solvent. Concentration of pesticide parathion is 10^{-5} *M* [141].

Figure 3.1.19 demonstrates successful proof of this concept and overall successful use of a unique plasmonic geometry designed for optical sensing based on a whispering-gallery-nanoparticle coupled nano-cavity. Here we can see that at low concentration of the pesticide parathion, in low solution volumes (0.02 pL) much higher enhancements of the target materials vibrational fingerprint are observed.

3.1.2 Single Molecule Detection

Different methods have been used throughout recent years to push SERS to the ultimate limits of detection. This section details the techniques researchers have used to manipulate plasmonic nanostructures to be able to achieve single molecule spectroscopy and overcome the low signals generated from Raman.

The pioneering work in this field stems from two papers back in early 1997 [52, 53]. The first work from Kneipp *et al*. describes the exploitation of the large cross sections ($10^{-17} - 10^{-16}\ cm^2/molecule$) obtainable from SERS probes. In this study, spectra from individual molecules of Crystal Violet (CV) were measured from solution using colloidal silver. The sample solution consisted of $3.3 \times 10^{-14}\ M$ CV in methanol with colloidal silver. The study provides a statistical analysis of Raman spectra to conclude single molecule detection capabilities of the system.

Research performed by Nie and Emory also used low concentrations of the target analyte (in this case R6G) to achieve single molecule detection. This work studies single particles and aggregates non-uniform in size and shape. The concentration at which single molecule detection is observed here is within the range of $10^{-10}\ M$. This work is the fundamental basis for establishing that single molecule detection is possible via SERS and opened the door for this research environment.

The bi-analyte technique for single molecule measurements was first shown in 2006 by Eric Le Ru and Pablo Etchgoin, the paper provides evidence of single molecule activity by performing SERS measurements from two different analytes [120]. It begins by explaining the shortcomings of the current techniques proposed in other papers for single molecule detection, focussing on low concentration analysis and the low probability of

single molecule events. In their approach, they use higher concentration samples to ensure that each nanostructure will pertain to a scattering event from one or more molecules. These samples are made by the combination of two dyes and use probability to determine the number of active molecules in a given SERS event.

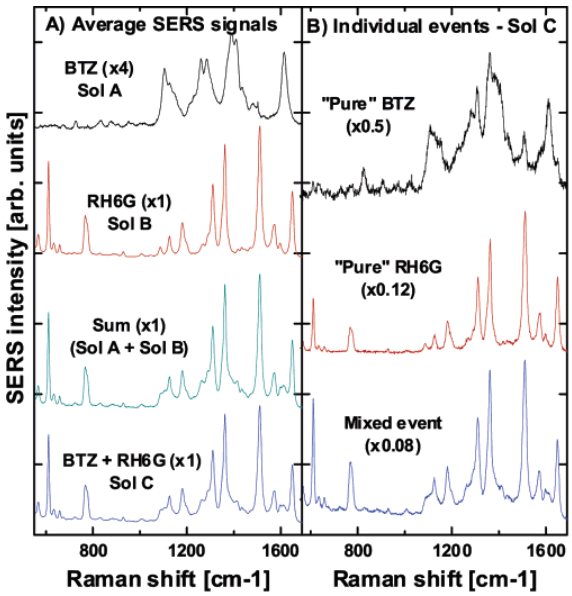

Figure 3.1.20 – (a) Average SERS spectra taken from solutions A (BTZ), B (R6G) and C (mixture), all at 100 *nM* concentrations. (b) Individual spectra of the dye mixture where SERS from pure BTZ, R6G and a mixed signal is shown [120].

Given the large number of scans and the fact that the two analyte's spectra can be differentiated from one another, when two representative scans comprising of a single dye is discovered, the researchers determine that it must undeniably be derived from a single (or few) molecule scattering event. By using statistical analysis and assigning the proportion of total signal to be ρ_B with signal on average attributed to each analyte and ρ_B being typically equal to 0.5, events where ρ_B is very low for either molecule would indicate a low number of molecules influencing the SERS spectra. The data is then summarised in histograms and shows that for the collection time used in this experiment, most nanoparticle clusters are capable of generating SM detection. The experiment goes on to confirm that the measurements are statistically less probable from larger concentrations by observing the effects of a 200 *nM* concentration solution. Here the extreme events of $\rho_B < 0.2$ or $\rho_B > 0.8$ are not seen.

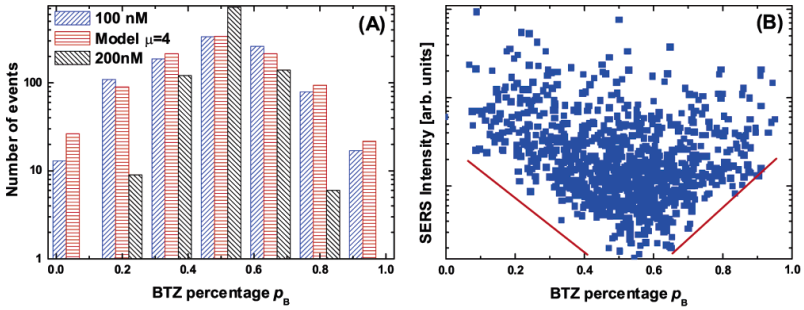

Figure 3.1.21 – (a) Histograms representing the distribution of ρ_B for SERS measurements from solution C, which contained a mixture of both dyes with 100 *nM* concentration (blue), a Poissonian model with $\mu = 4$ as well as measurements from the doubled concentration solution 200 *nM* for comparison. (b) A scatter plot showing total SERS intensity vs the ρ_B value for the respective spectra [120].

It is promising that this research demonstrates that single molecule events can be obtained from relatively high concentrations of target analytes. The techniques used in this study, however, have no control over the nanostructures used to generate the enhancement. They state that the origin of the single molecule scattering events is a result, not only of the generation of hot spots in the particle-particle gaps, but also due to the molecule actually being within this region. Something that is looked into more detail within our theoretical study.

In 2006, Katrin and Harold Kneipp published a SM-SERS study utilising non-resonant excitation of two variant nanostructure configurations [56]. Firstly, clusters of gold and silver nanoparticles in solution and secondly, fractal silver surfaces. Due to their inhomogeneous nature, structures like this are less applicable to our work than the nano-gap formations we have previously discussed. However, they are worth mentioning due to the large enhancement characteristics associated to them. Also, in these cases the target analyte will likely bind to the nanostructure in question leading to chemical enhancement and potentially blinking at low concentrations (in this case 10^{-11} *M*). Low concentration measurements took a statistical approach, where on average 0.6 CV molecules were predicted to be within the target accumulation area and Poisson distributions of the spectra showed they were associated with 1, 2 or 3 molecules.

Moving through this era of research, an extensive summary compiling the details of the approaches used in SM-SERS were then given shortly after in 2008. Where a review

encompassing techniques such as Tip Enhanced Raman Spectroscopy (TERS), as well as the Langmuir Blodgett (LB) technique [58].

A follow on from Le Ru's work in single molecule detection came in 2011, where a more in depth understanding of the properties of single molecule bi-analyte SERS detection was studied. A clearer picture is drawn from the interpretation of the inhomogeneous peak broadening of SERS spectra [61]. They do so by implementing the bi-analyte technique, which observes contrasting SERS spectra from different materials and uses the statistical fluctuations in the signal relative to its partner. Therefore, detecting signal from both molecules simultaneously with one serving as a reference as well as an analyte. Doing so leads to analysis of the spacial information from the hot spot scattering process. The study uses Nile Blue (NB) and R6G for the two analytes, and an excitation wavelength of 633 *nm*, specifically investigating the 590 and 612 *nm* peaks from both materials respective Raman fingerprint to spectrally resolve from one another.

Following this, in early 2013 Wang *et al.* measured highly directional Raman scattering from nano-antennae comprised of optical gaps between nano-rods, surrounded by a ring of plasmonic metallic material [64]. The study investigates more than a thousand single molecule events implementing the isotopologue method of single molecule detection.

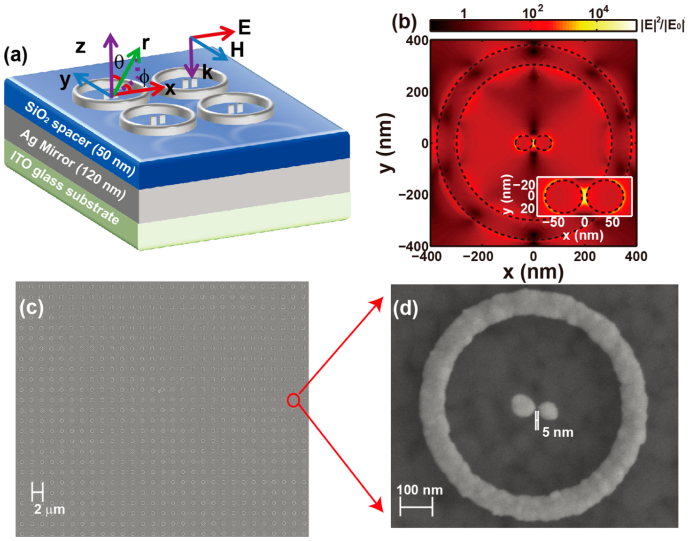

Figure 3.1.22 – (a) Structure used throughout experiment with each antenna consisting of two silver particles separated by 5 *nm*, surrounded by a silver ring, deposited onto a SiO_2 spacer layer on a silver mirror on ITO-coated glass. Silver rings have inner and outer radii of 300 and 380 *nm*, respectively. The rings are 40 *nm* thick (in z-direction), whereas the silver particles are rods (70 *nm* long and 60 *nm* wide in x and y-directions) with rounded ends (30 *nm* radius). Periodicities of the antennas in x and y-directions are both 2 μm. (b) Profile of the simulated intensities of electric field at the wavelength of $\lambda = 532$ *nm* on $x-y$ plane in the centre of the silver ring structure, including a zoomed view of the central nano-rods. (c,d) SEM images of optical antenna chip. Optical antenna array is 100 $\mu m \times 100$ μm. Left-hand rod of optical antenna is 80 *nm* long and 70 *nm* wide. Right-hand rod of optical antenna is 68 *nm* long and 62 *nm* wide [64].

The structure configuration seen in Figure 3.1.22 shows the experimental schematic used throughout the study. The silver ring excites surface plasmons on the mirror which then converge to the ring's centre, further enhancing the signal between the particle pairs. Simulations in the supporting information in this report show that the device allows for 2.5$\times$ larger signals with the silver ring when compared to the nanoparticle dimer alone.

The study uses the isotopologue method for characterisation of single molecule detection as opposed the the bi-analye method seen in other studies [61, 120]. This method was implemented over the bi-analyte approach as with the bi-analyte method, a complete understanding of the differences between the Raman cross sections, absorption spectra and surface binding properties to the metals is required. Here, this is not necessary, as the molecules in the isotopologue approach are just isotopes of one another. This study uses two types of R6G (d0 and d4), where SM-SERRS from a 532 *nm* laser reveals Raman spectra from each isotope from thousands of nano-antenna investigated, specifically

investigating the 620 and 610 cm^{-1} line which appears for the R6G-d0 and R6G-d4 respectively. The spectra is divided into 3 categories; spectra from R6G-d0, R6G-d4 and spectra which contain both analytes.

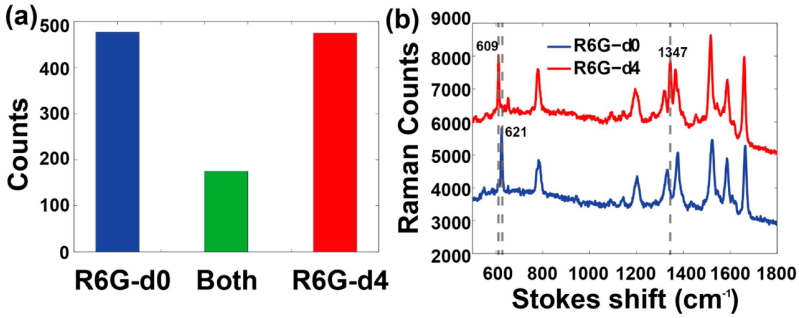

Figure 3.1.23 – (a) Histogram of three cases of target analyte spectra recorded from antenna. (b) Raman spectra from R6G-d0 and R6G-d4 [64].

From the 1120 events recorded, the supporting information in the report predicts that the SERS signal originates from 1.097 molecules on average per hot spot. The histogram of results regarding the relevant target analyte spectra can be seen in Figure 3.1.23. We can also see the high directionality of the device from Figure 3.1.24, calculated from the far-field simulations for both the nanoparticle dimer with and without the surrounding ring (red and blue lines respectively).

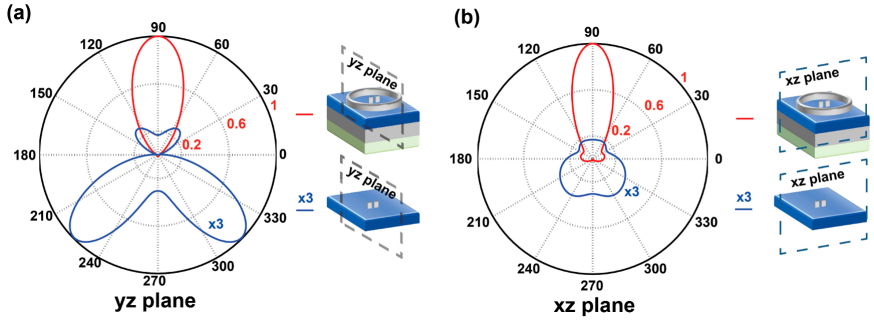

Figure 3.1.24 – (a) $y-z$ plane far-field and (b) $x-z$ plane for the far-field radiation power intensity where the red lines show the structure with the ring encompassing the device and the blue lines show the structure without the ring [64].

The SEM images show the cavity being 15 *nm*, whereas simulations were taken at a 5 *nm* gap so enhancement factors may be disproportionate. We have shown in this thesis the exponential increase of enhancement characteristics relative to nano-gap size, so it may suggest that all the nano-antennae in this study wouldn't posses the capability of enhancement levels required for SM-SERS. The ring surrounding the structure provides

additional enhancement, and in-depth analysis of the near and far-field dynamics of this system could be investigated further. Overall though, the paper shows successful single molecule behaviour of R6G isotopes with a highly directional nano-antenna device.

Just shortly after, during the middle of 2013 Zhang *et al.* published work pertaining to single molecule detection via TERS [63]. By using the Scanning Tunnelling Microscope (STM) setup to form a cavity between the tip, and the silver surface, selectively locating single molecules of H_2TBPP imaged via STM topography of the substrate, SERS measurements were possible with immense precision.

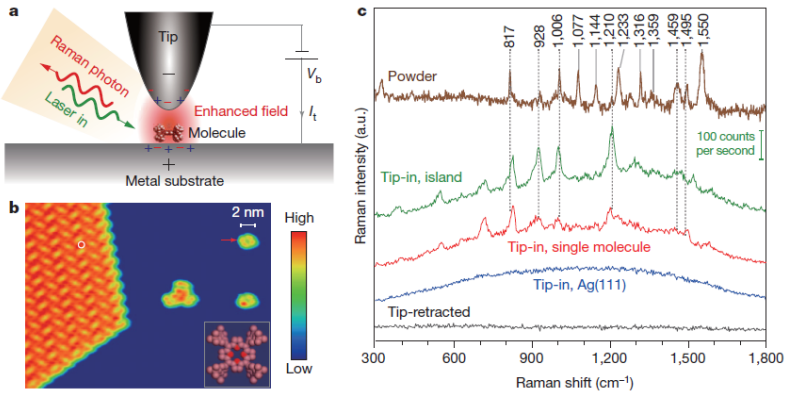

Figure 3.1.25 – (a) TERS schematic diagram where the cavity is formed between the tip and silver film below. (b) STM topography of the H_2TBPP molecules deposited onto the silver film. (c) TERS spectra under different film geometry and tip conditions. In these cases the measurements were taken at 120 mV with an $NA = 0.5$ lens for 3 s accumulation time. Spectra were taken from the tip in a powder sample of the material (brown), above the molecular island (green), above the single molecule (red), on bare silver surface (blue) and on the molecular island with the tip retracted 5 nm (black) [63].

The study also shows orientational effects of the molecule and its relationship to the associated Raman spectra, where different molecules produce different intensities of certain peaks. This is important as it will form the basis of our understanding of the single molecule regime in our experiments.

More work came in 2013, in this case using gold nanoparticle dimers with small separations to achieve the fields necessary for SM-SERS [113]. The paper discusses a number of approaches to SM-SERS nanostructure fabrication, with notable efforts at biosensing from Gold-Silver Core-Shell Nano-Dumbbells (GSNDs), which exhibit the blinking effect from sequential Raman measurements. Intensity blinking is a characteristic of single molecule events. By using these GSNDs functionalised with DNA to the gold surface,

and allowing the silver layer to grow around the nanoparticle, SM events were measured from a Raman probe located in the gap between the nanoparticle dimer. This example of intensity blinking is shown to be achievable from our gap structure later in Chapter 7, where we exhibit the same characteristic intensity blinking from the fluorescent conjugated polymer F8-PFB.

It can be said that the potential of SM-SERS is becoming more and more evident. With techniques being constantly refined and developed and more accurate control of nano-geometry becoming possible, SM-SERS has a promising future. Functionalising SM detection into microfluidics, investigating orientational properties of molecules, and measuring Raman events from specific molecules are all interesting territory which need to be explored [38, 62].

3.2 Biosensing

Biosensing is of key interest when it comes to plasmonic research, the fields generated and enhanced by the confinement of light associated with metallic nanostructures are massively beneficial towards detection of complex molecules in biological systems. Also, when combined with spectroscopic methodology such as Raman, it becomes a refined tool for detecting not only binding events, but also the chemical processes that take place during them.

Both SPP and LSP based biosensing exist, and each have their own inherent advantages and disadvantages. The two types for SPR based biosensing are reflection and transmission, conventionally the Kretschmann configuration is generally used for reflection based measurements [4, 42, 142]. Since this report mainly focusses on LSP based nanosensors, SPP types are neglected here. However, useful studies using their methods can be found from the following resources [42, 142], which describe their sensing techniques and configurations to light to couple to flat metal surfaces.

Proteins are an important study focus for biosensing, performing many vital functions within the human body. Through their detection and characterisation, early diagnosis becomes more viable. Two well characterised proteins include BSA [41, 44, 118, 143–

145] and lysozyme [40, 43, 118, 146, 147]. By modifying the surface properties of silver nanoparticles with an iodide layer, Xu *et al.* provides a novel method for SERS detection of proteins. The surface characteristics are changed to prevent any direct interaction between the nanoparticle and the protein, thus allowing the protein to remain unaltered by any surface contaminants. This would allow for reproducible, reliable results. The study uses BSA and lysozyme from AMRESCO, mixed in high purity water with colloidal silver nanoparticles with an average diameter of 50 *nm*. Figure 3.2.1b shows the spectra taken from BSA with Raman and SERS methods. The schematic diagram for the iodide modified nanoparticle analysis technique from this paper can be seen in Figure 3.2.1a.

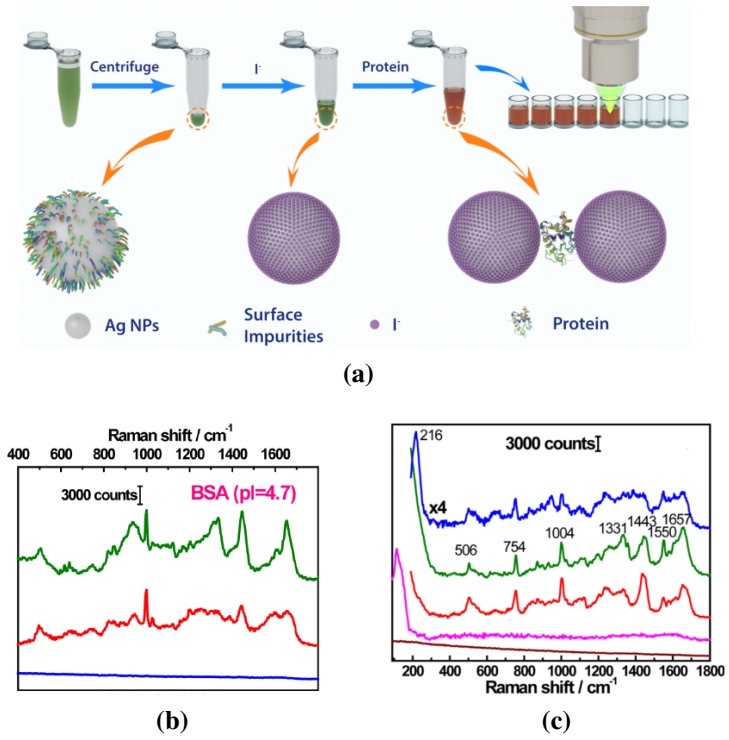

Figure 3.2.1 – (a) Iodide modified silver nanoparticle detection schematic diagram. (b) Raman spectrum for BSA (green) SERS spectrum from BSA (red) at 300 $\mu g/ml$. (c) Lysozyme spectra at 300 $\mu g/ml$ using regular silver NPs (blue), silver IMNPs (red), their respective references with no material (brown and pink) and regular Raman from lysozyme solution at 100 $\mu g/ml$ (green) [118].

Observation shows that the SERS signal and conventional Raman measurements are not identical, this can be accounted for by the following reasons; firstly, strong chemical interactions between the target analyte and the metal surface may lead to electromagnetic changes in the materials characteristics. Secondly, is the surface selection rule, which will selectively enhance the vibrational mode with the closest proximity to the nanoparticle.

It is still uncertain why the modified nanostructures with iodide layers allow for more reproducible Raman measurements. However, the paper hypothesises that it may be a result of the iodide layer reducing the interference from the surface impurities [118].

Another BSA paper from David *et al.* also investigates the reproducibility of biomolecule detection with SERS methods. Using gold nano-cylinders with dimensions from $100-180$ *nm* in diameter at a constant height of 50 *nm* and with spacings of 200 *nm* between them, SERS is performed on BSA samples at 1 *mM* concentration in water solution, purchased from Sigma Aldrich and drop cast onto substrates. The study performs measurements at the characteristic LSPR for the nanostructure using a 632.8 *nm* laser. SERS spectra were collected through a $100\times$ objective, the spectra are shown in Figure 3.2.2.

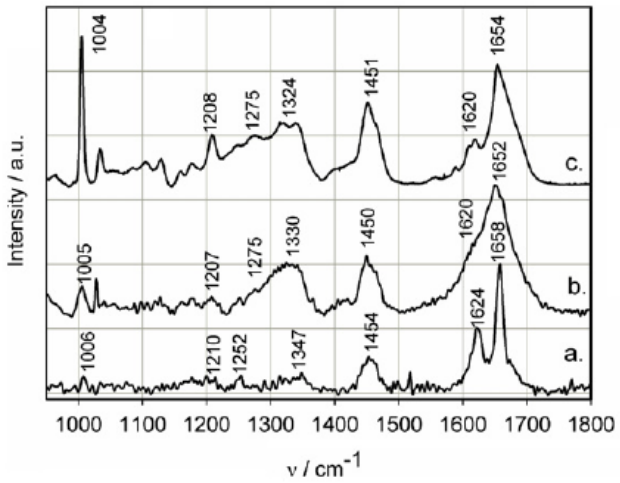

Figure 3.2.2 – Raman spectra for BSA (a) 1 *mM* concentration, 100 *s* exposure time, (b) in aqueous solution, (c) powder form [41].

These spectral peaks will be further analysed along with the experimental data taken in this report for comparison of peaks. This study provides reproducible results using gold nanoparticles at this particular wavelength, and is important to consider the Raman signal characteristics for different nanostructure geometry. The paper gives strong indications that SERS is a reliable method for protein analysis [41].

These methods and reference spectra are important for fabricating and analysing samples, they will be essential for efficient lab practice and taking accurate measurements. Raman spectra has been shown to provide deep insight into the structural properties of proteins.

Chapter 4

Experimental Setup and Methodology

In this chapter, we outline the methods used for fabrication of the plasmonic nano-gap devices. These nano-gaps are formed between metallic nanoparticles and an extended metal film below. Here, we describe the techniques used to make these structures as well as the equipment involved. Following this, we show the experimental setup used for Raman measurements and outline the experimental methods that were used to study these nano-gaps.

4.1 Nano-gap Fabrication Methods

4.1.1 Cleaning Substrates

The structures used throughout the experiment consist of a nano-gap formed between a metallic nanoparticle and an extended metal film. These structures had to be prepared in a consistent manner to allow results to be reproducible at a later date. Glass slides were cut to size and marked to distinguish the top from bottom. Cleaning the glass substrates took place in a three stage process: First, they were cleaned in deionized water, and then acetone and finally with isopropanol for 10 minutes periods in an ultrasonic bath with each solvent. This allowed any debris to be removed from the glass surface and would allow for a more homogeneous layer to be added. Afterwards the slides were left to dry.

4.1.2 Thermal Evaporation of Metallic Layers

Throughout the work in this thesis, we used an Edwards $E306A$ bell jar evaporation system to deposit the metallic films. This setup suspends the blank substrates in a mask above

the tungsten boat which is heated to evaporate the material of choice onto the slides. The heater functions via current passing through the boat supplied by two electrodes at either end, this then forms a high current, low voltage circuit. By increasing the current passing through the boat, the metal will vaporise and deposit onto the substrates. While the source is heated and a stable evaporation rate is achieved, a shielding plate blocks the samples. This allows for a consistent rate of evaporation to take place once evaporation rates stabilise.

The deposition rate and thickness of the film is monitored via a quartz crystal oscillator. The thickness is measured by the change in resonant frequency of the quartz crystal suspended between two electrodes as a function of the mass deposited on its surface. The change in frequency is linear as a function of the change in mass on its surface, and hence can be used to accurately monitor the thickness of the samples within the dome. With this type of quartz crystal micro-balance, it is possible to measure films to within an angstrom [148].

The evaporation process allowed samples to be coated with metallic layers, the thickness of the layers evaporated onto the samples could be controlled using different masses of the material. By passing a current around $55-60$ amps through a tungsten boat the material was heated to boiling temperature inside a vacuum container pumped down to a pressure of 5×10^{-6} *mbar*, this prevented oxidisation within the chamber. The evaporation took place using gold or silver wire supplied from the university with $\leq 0.01\%$ trace metal impurity.

It was discovered however, that the Edwards $E306A$ coating system shown in Figure 4.1.1 had a large spread of thicknesses when applied to multiple target samples in a template mask held at a distance 15 *cm* above the evaporated material. The evaporator is shown in Figure 4.1.1 along with the position of the samples relative to the tungsten boat via the overhead view.

(a) **(b)**

Figure 4.1.1 – Edwards *E*306*A* coating system. (a) Evaporator setup with vacuum dome removed. (b) Overhead view of evaporator used to ensure accurate repeatable placement of sample template mask.

Figure 4.1.2 shows the variation in the average thickness across the evaporated silver layers relative to their position on the mask.

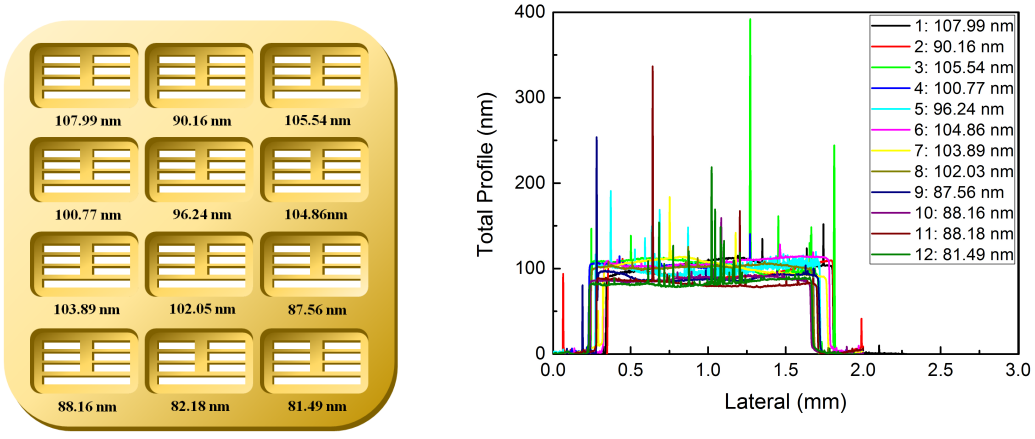

(a) **(b)**

Figure 4.1.2 – (a) Thicknesses measured using Dektak of samples taken from centre of each sample. (b) Dektak measurements for material profiles with relative mask position.

As shown in Figure 4.1.2, the sample variation in thickness could range with a difference of $\sim 26\ nm$, this could easily affect the outcome of results where the thickness of the metal layer is important to the design of the structure. This happens due to the distance

between the sample and source as well as the dispersion of the evaporation process. In order to reduce this occurring, the samples are selected from certain regions of the mask for the desired thickness and measured with Bruker's DektakXT® Stylus Profiler to ensure the correct thickness. Figure 4.1.3 shows the surface profile and thickness of a 100 *nm* silver film.

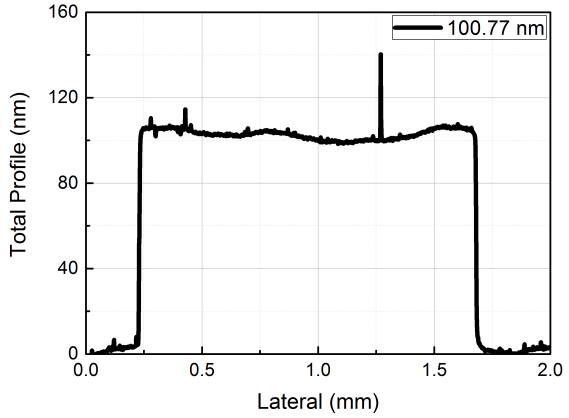

Figure 4.1.3 – Dektak measurements for a layer of silver (100 *nm*)

The Dektak we used allows for surface profilimitry measurements to take place. It does so by using a fine stylus tip with a 12.5 μm radius to scan across the substrate surface, quantifying the roughness over a given region by measuring the vertical displacement of the stylus from the surface as a function of its position. For accuracy, the thickness measurements are repeated from different regions of the sample near the edge and close to the centre of the substrate and averaged.

4.1.3 Spin-Coating Thin Films

Preparation of solutions required accurate measurements for the masses of the analytes involved, we used the Sartorius Micro-balance $ME5$ when weighing out sample materials as it is capable of weighing up to 5 g with 1 μg readability. In order to create a good thin film, the materials and matrixes had to completely dissolve in the solution. First attempts proved unsuccessful mixing R6G with solvents such as toluene, ethanol and chlorobenzene due to sediment remaining in the mixture (this would lead to inhomogeneous layers and inconsistent solution concentrations). By changing the solvent to chloroform, the

mixture completely dissolved the R6G and polynorbornene (C_7H_{10}) matrix. Polynorbornene (more commonly referred to as zeonex) has molar mass 94.16 $g \cdot mol^{-1}$ and in order to achieve a 5 nm nano-gap we used a concentration of 1×10^{-2} M. Further details of concentrations used are given in the results section in conjunction with the resultant spectra discussion. Once the solutions were prepared, they could be applied to the structures using a Gilson pipette pipetman classic $P100$ which has a working range of $20 - 100\,\mu l$. The material was dispersed onto the substrate surface using the spin coater at 2000 rpm or by drop casting the mixture and allowing for it to dry overnight. Throughout our work, we used the Suss Microtec Delta $10TT$ spin coating system.

Analysing surface thicknesses of layers added to the structures could not be carried out directly due to potential damage to the structure. Therefore, a replica slide was made under the same conditions to check for surface characteristics. The Dektak allowed for surface profilimetry to be carried out, by scoring the surface of the duplicate structure, the surface profiler enabled high resolution, detailed analysis of thin film thickness and surface roughness. These repeatable measurements were essential to demonstrate that the thin film had been applied to the correct thickness without inhomogeneity to a resolution of < 1 nm. We can see the thicknesses for the thin films of zeonex at different concentrations in Figure 4.1.4.

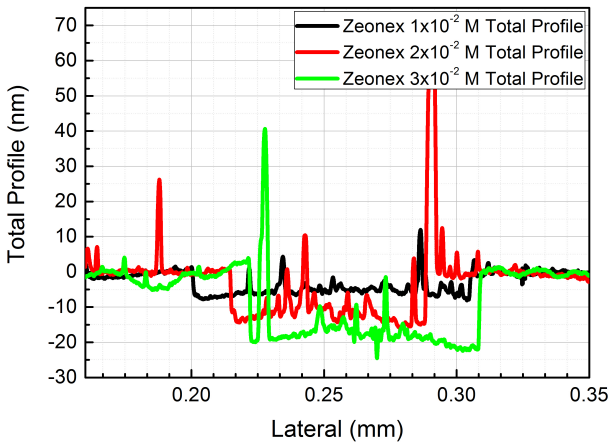

Figure 4.1.4 – Dektak measurements for a thin film zeonex matrix at; 3×10^{-2} M (18.94 nm), 2×10^{-2} M (12.52 nm) and 1×10^{-2} M (5.00 nm) respectively.

The final step was to deposit the nanoparticles onto the surface of the thin film. This

was carried out in the same way as the thin film itself, however the nanoparticles were suspended in solution of ethanol at a concentration of 2.7×10^6 $particle \cdot L^{-1}$. This is to ensure there would be sufficient spacing between them when spin coated onto the substrate surface. Therefore, Raman measurements could be taken from discrete nano-gap areas.

The zeonex matrix was used as it would not dissolve in ethanol, allowing it to protect the layer of R6G to remain intact when depositing the nanoparticles. These results enable the thin film to establish a nano-gap under the nanoparticles of the desired thickness based on the concentration of the zeonex as seen in Figure 4.1.5.

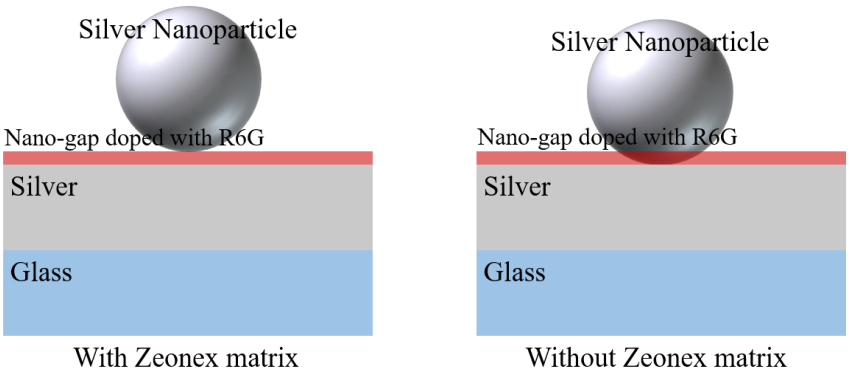

Figure 4.1.5 – Nano-gap thin film, the effect of thin film structure with and without a zeonex matrix.

4.2 Raman Setup

This section details the instrumentation and methods used throughout the thesis for collecting data during Raman scattering experiments. Our optical bench is set up with three laser lines, we use a 532 *nm* *LSR*532*NL* diode laser with a < 2 *mm* beam diameter for Raman spectroscopy. In conjunction with this, we also use a 405 *nm* *LSR*405*NL* diode laser in a dark field configuration with a beam size of 5 *mm*, this allows us to image the particles from their scattering. We also have a 635 *nm* *LSR*635*NL* diode laser with a beam size of < 4 *mm* set up for Raman spectroscopy. All of our diode lasers are supplied by LASEVER. In order to analyse data in the experimental sections, each laser's central peak position was taken for calibration. This data can be seen in Figures 4.2.1a and 4.2.1b.

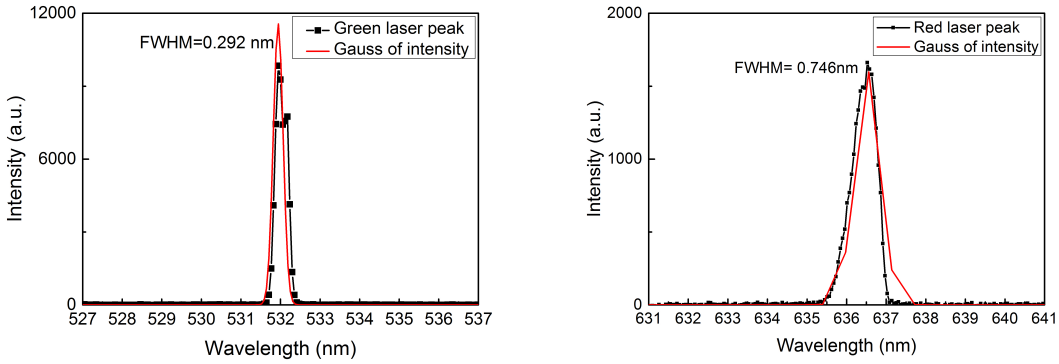

(a) **(b)**

Figure 4.2.1 – Laser peak spectra taken with notch filters removed using a 0.01 *mm* slit width with 0.05 *s* integration time. (a) Green laser central peak. (b) Red laser central peak. Both graphs include peak width information and position via Gaussian fit.

4.2.1 Experimental Setup

The optical configuration for the experiment was carried out via direct illumination, whereby the light is incident perpendicular to the sample surface and the scattered light is collected back through the same objective lens. The experimental setup is shown in Figure 4.2.2.

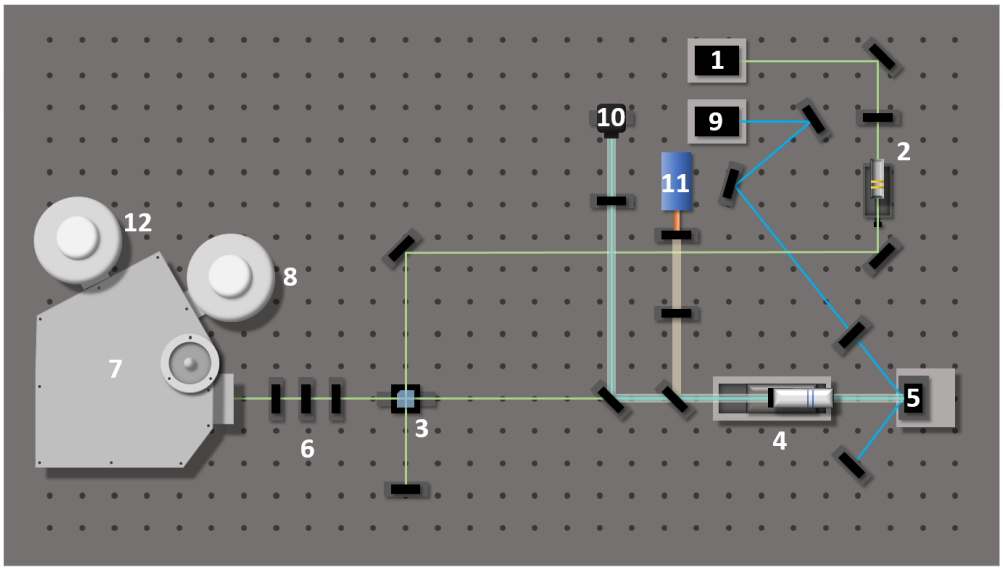

Figure 4.2.2 – Optical bench diagram used for Raman experiments. (1) 532 *nm* diode laser (2) Beam expander. (3) Beam-cube. (4) Objective lens $NA = 0.55$. (5) Sample stage. (6) Focussing lens and notch filters used to remove Rayleigh scattering. (7) Horiba *iHR*320 Imaging spectrometer. (8) Liquid N_2 cooled CCD (visible). (9) 405 *nm* diode laser. (10) Thorlabs CMOS camera. (11) Fibre optic white light source. (12) Liquid N_2 cooled CCD (IR).

We perform Raman measurements in reflection using a 532 *nm* laser. In this configur-

ation, two Kaiser holographic notch and super-notch filters centred at 532 *nm* were used to reject the Rayleigh scattering. We can see that the laser line begins by passing through the beam expander (BMX) (2). This is used to expand the beam to the desired spot size for the objective pupil, accomplished by using two lenses in the Keplarian configuration shown in Figure 4.2.3. This allowed for a consistent spot size through the line at the same diameter of the objective pupil.

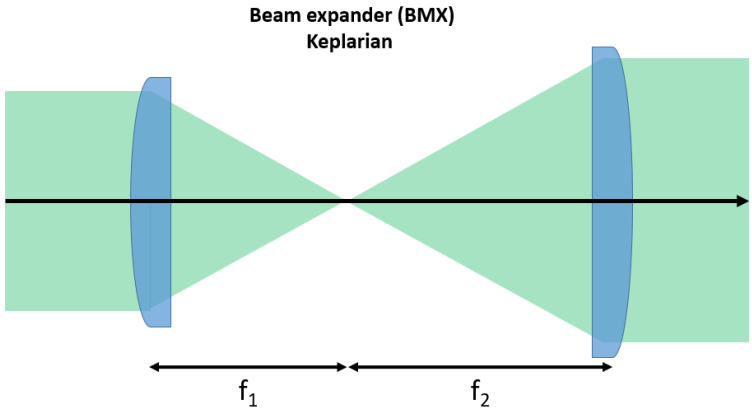

Figure 4.2.3 – Keplarian beam expander

The two lenses were used at a distance between them equal to the sum of their focal lengths f_1 and f_2. The optical setup works most efficiently when the beam size is collimated to the same diameter as the optics used, therefore with the initial beam diameter from the laser D_1 being ~2 *mm* the required beam diameter D_0 can be calculated from equation 4.2.1 [149].

$$D_0 = (M_p \times D_1) + L\tan\frac{\theta_1}{M_p} \tag{4.2.1}$$

Where L is the sum of the two lens focal lengths and M_p is the magnifying power given by $M_p = \frac{\theta_1}{\theta_0} = \frac{D_0}{D_1}$. θ_0 and θ_1 correspond to the input and output beam divergences.

The collimated beam was then diverted using the two mirrors onto the beam-cube (3), which diverts the beam back through to the 50× infinity corrected Mitutoyo objective lens with numerical aperture $NA = 0.55$ and a working distance of 13 *mm* (4). The beam-cube is then rotated to optimise the intensity of the spot onto the objective lens. The sample stage (5) is brought within the focal length of the objective lens in order to focus the spot

size down to the smallest size possible. Once the spot is focussed the light is reflected back from the sample through the objective lens and beam-cube onto the notch filters (6). These are used to remove the Rayleigh scattering from the Raman measurements. Afterwards, a lens (focal length 80 *mm*) is used to focus the remaining light onto the spectrometer (7). Inside the spectrometer, a 1200 g/mm ($groove/mm$) diffraction grating is used to generate spectral images by diverting the light onto the Symphony II Horiba charge coupled device (CCD) (8).

The CCD is cooled with liquid nitrogen to allow for low light level detection keeping the noise to a minimum. By cooling to very low temperatures ($-130\ ^{\circ}C$), the system retains a high signal to noise ratio. The resolution of the CCD is 1024×256 pixels, with 1024 pixels in the horizontal direction or spectral range and 256 pixels covering the vertical image height. The light is passed through the entrance slit and the system can also be used for imaging at zero order, where the diffraction grating behaves essentially as a mirror.

Working in conjunction with the Raman line is a 405 *nm* laser in a dark field configuration (9). The scattered spots indicate a nanoparticle is present, therefore allowing the green laser spot to be focused in that area. This allows for spectra to be taken in a specific area of the device in order to ensure plasmonic enhancement is being observed from the nanoparticles. Figures 4.2.4a and 4.2.4b show the surface nanoparticles imaged with the 405 *nm* laser and the focused spot from the 532 *nm* laser.

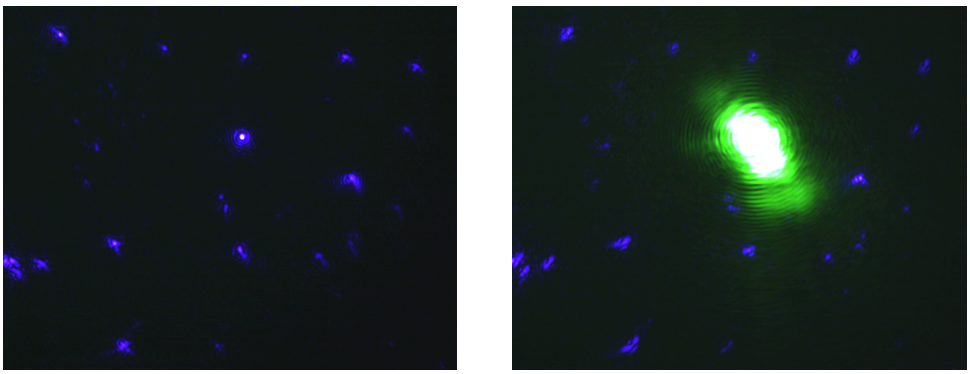

(a) **(b)**

Figure 4.2.4 – 118 *nm* silver nanoparticles of surface of structure. (a) 118 *nm* silver nanoparticle scattered light from 405 *nm* laser. (b) Focused 532 *nm* laser on the silver surface.

The blue spots are a result of the scattered light from the metallic nanoparticles. The image is fundamentally limited in resolution by the diffraction limit of the optical system. The diffraction limit can be described by:

$$d_{spot} = \frac{\lambda}{2n\sin\theta} \tag{4.2.2}$$

where d_{spot} is the diameter of spot size, λ is the wavelength of light, n is the refractive index of the medium the light is travelling in, and θ is the angle of convergence. Also, $n\sin\theta$ is equivalent to the numerical aperture NA. This laser is incident on the sample stage from an angle, from here the scattered light is collected from the objective lens and diverted through beam splitters to the Thorlabs CMOS camera (10). This allows us to image the nanoparticles and focus the Raman line on discreet individual particles. We also have a white light source (11) set up in a similar configuration which is used to find and image the surface of the substrate.

There are a number of challenges when working on a fine tuned optical setup such as this. Physically locating, and imaging the nano-gaps takes precision, however the fine tuning of this process was made easier by working with a motorised two dimensional Newport piezo motor driven linear stage, which has a precision of 50 *nm* in each direction. The focusing of the objective was also motorised using a ThorLabs compact motorised translation stage, which can focus in and out with a precision of 50 *nm*. This allowed for accurate control over the focusing of the individual particles. Due to the small sizes of the particles and high magnification involved, we must also consider the chances of physical movement of the sample from vibration in the setup. This effect is reduced by using an air stabilised optical table.

4.2.2 Detectors and Grating

The Horiba *iHR*320 Imaging spectrometer uses a 1200 g/mm with a typical spectral resolution of 0.18 *nm* to disperse light into its constituent wavelengths [150]. This is achieved by the high density of grooves running from edge to edge across the grating. The relationship between the groove spacing and the angles of the incident and diffracted light

functions under the principle of the grating equation.

$$m\lambda = d\left(\sin\theta_i + \theta_m\right) \tag{4.2.3}$$

Where m is the diffraction order, λ is the wavelength of incident light, d is the groove spacing, θ_i is the incident angle of light and θ_m is the maxima for diffracted angles of light with respect to the grating's normal [151]. We can see the grating configuration in Figure 4.2.5.

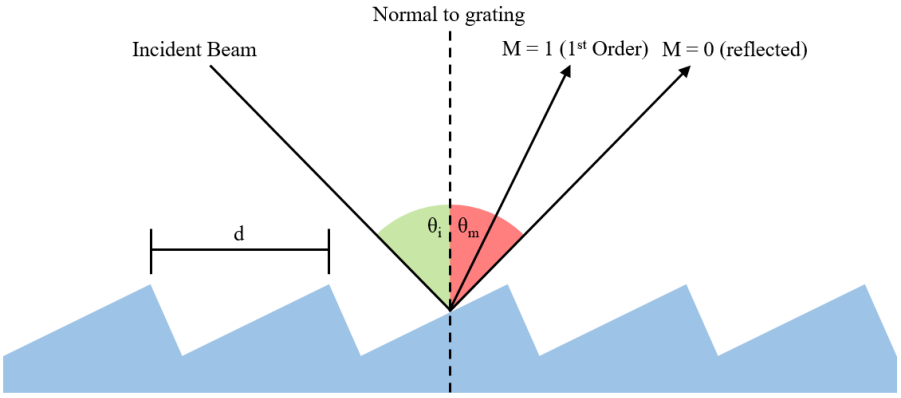

Figure 4.2.5 – Diffraction grating showing the incident and diffracted light for a monochromatic light source.

When $m = 0$, no diffraction occurs and the constructive interference simply yields the reflected light. At the first order when $m = 1$, this corresponds to the first order of diffracted light used for spectroscopy. The Huygens-Fresnel principle states that upon interaction with a diffraction grating at normal incidence, a monochromatic plane wave will act as an individual point source diffracted from each groove [151]. The individual point sources of light from each groove represent light propagating outwards in all directions and will interfere either constructively or destructively with one another. If the path difference $\triangle x$ of a point source is equal to a full or half wavelength to that of the groove adjacent to it, this will create maxima and minima respectively due to constructive and destructive interference of light. We can see this phenomenon occurring when a diffraction grating creates points of intensity at instances where the waves are in phase, and dark regions where the waves are out of phase in Figure 4.2.6.

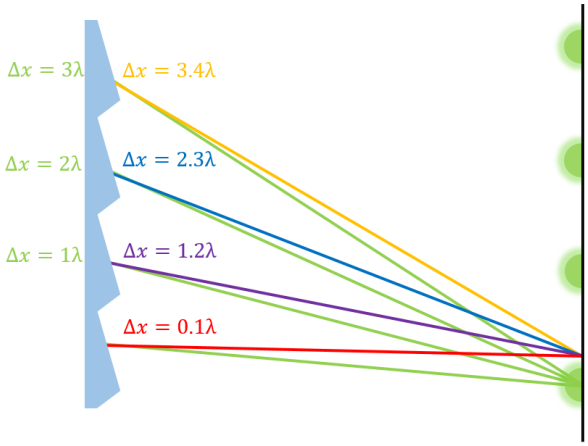

Figure 4.2.6 – Diffraction grating showing the interference of light for a monochromatic light source. The green lines represent light propagating in phase with a path length difference of 1λ, the other coloured lines represent light rays propagating out of phase, these rays destructively interfere with one another leading to dark regions of intensity minima.

The corresponding coloured light paths in Figure 4.2.6 are in phase with one another in the case of the green rays, and out of phase with one another in the cases of the other coloured path lines. Therefore, for these cases when $\triangle x = \frac{\lambda}{2}$, we see dark regions of intensity minima. The constructively interfering green lines produce intense regions of light associated to diffraction gratings. These intensity maxima correspond to the propagation mode of interest.

During Raman spectroscopy, the emitted light will be polychromatic and therefore is required to be split into the individual wavelengths before being recorded by the detector. The grating disperses light onto the CCD in our setup which contains a large array of pixels. By converting the electric charge accumulated in each pixel as a result of the incident light, the detector converts the resultant voltage and produces an image. Alternatively, each pixel can be used to represent a discreet wavelength to produce a spectral image.

4.2.3 Calibration

Calibration of the Raman system was carried out via spectra taken from a silicon chip, using the smooth side as this produced a better scattering signal. Once the 532 *nm* laser light has been focused onto the sample, the white light fibre optic source can be focused onto

the same area allowing the surface of the sample to be imaged. This process guaranteed that the laser spot was focused onto the surface of the sample. Imaging was accomplished using a beam splitter, diverting some of the light back from the sample onto the CCD. Fine tuning of the stage can be done manually or with the Thorlabs stage control system. Now that the sample is imaged the scattered light is made central to the notch filters, these allow the Rayleigh scattering to be filtered out during direct incidence Raman scattering measurements. Once these steps have been carried out, spectra can be taken.

Complete optimisation is required from the system due to the weak intensities of Raman scattering. Therefore, spectra are taken in real time control while slight adjustments are made to the sample's focus and the scattered light position in order to reduce the size of the slit width of the front entrance of the detector and reduce the exposure time.

Figure 4.2.7 shows the optimised signal from silicon gathered during the calibration process at normal incidence using both the 532 *nm* and 635 *nm* lasers. Larger signals are obtained from the 635 *nm* laser for the same detection parameters due to its high output power, 200 *mW* compared to the 100 *mW* of the 532 *nm* laser.

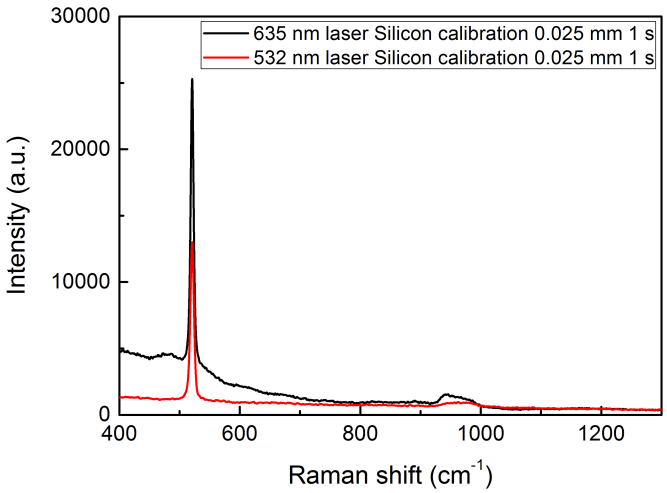

Figure 4.2.7 – Raman spectrum of silicon via direct illumination. Measurements taken with 1 *s* exposure time with a 0.025 *mm* entrance slit at a central wavelength of 570 *nm*. The first order peak for silicon is shown at 520.86 cm^{-1}.

A comparison of silicon spectra taken from an optimised system can be seen in the literature [152–154].

Chapter 5

FDTD Investigations of Metallic Nano-gaps for SERS

By illuminating metallic nanostructures with light, it is possible to enhance the Raman signal from materials in close proximity by several orders of magnitude [4, 8, 74]. The enhancement attributed to these plasmonic nanostructures are a result of highly confined regions of electromagnetic field. Coupling plasmons is known as plasmon hybridization, and leads to extreme field intensities known as ***hot spots*** [155, 156]. One such method of the generation of hot spots is to use a nano-gap formed between a nanoparticle and a metallic film [27, 29, 119, 133, 134, 138, 156–165]. Such systems have been shown to produce the fields necessary to successfully produce Raman spectra from single molecules [119, 156, 161, 162]. In most of these studies, the SERS signal is predominantly attributed to the near-field enhancement in the nano-gap region. Very little attention is paid to the efficiency of collecting the emitted Raman photons in the far-field. Understanding the complex interplay between the near-field enhancements and the efficiency to emit the Raman photons to the far-field are prerequisites for the development of fully optimised plasmonic devices for SERS application.

In this chapter, we proceed with a theoretical, systematic study of the topographical nature of the nano-gap formed between a nanoparticle and an extended metallic film. In these structures, the dielectric spacer would house the analyte under investigation. The study provides an in depth look at the absorption and scattering behaviour of nano-gaps. It then focusses on electric field enhancement attributed to these nano-gaps by investigating the effects of changing certain parameters such as the cavity thickness, the particle size and shape, as well as the metallic film material and thickness. We continue the invest-

igation, by projecting the near-field from our nano-gap to the far-field, to understand the efficiency of emitting the generated Raman photons within the gap to the far-field. The study investigates in detail, nano-gaps in this configuration by linking the near and far-field characteristics all using three-dimensional FDTD calculations via Lumerical solutions. We aim to classify the ideal excitation wavelength of these systems to maximise light output for SERS scattering and hence determine which will be used throughout the experimental sections of the report.

It is integral to optimise these parameters and establish the resonant excitation wavelength which will convert near-field enhancement to far-field scattering most efficiently for Raman. Therefore, we can later apply this knowledge and perform SERS detection of materials approaching the single molecule regime in subsequent chapters. Scattering is typically measured from the entire structure, the novelty of our method lies in the projection of the far-field emission originating directly from the centre of the nano-gap. This is because the molecule under SERS investigation will reside here and will emit light from this position. We explore near-field excitation enhancement and the resultant far-field emission enhancement to discuss the overall contribution of the signal and define this information into a Figure of Merit (FoM) for this geometry.

5.1 FDTD Approach for Modelling Plasmonic Nano-Gaps for SERS

The structure studied throughout this thesis involved a nano-gap formed between a nanoparticle and metallic film, in which, a target analyte would situate within the gap formed between the plasmonic nano structures as illustrated in Figure 5.1.1. The cavity was simulated as a dielectric material with refractive index 1.5 to represent a polymer matrix. The analyte would be mixed with the dielectric layer (in our case we used polynorbornene, more commonly referred to as zeonex), and the refractive index is in accordance with the material properties found in [166]. Material properties of noble metals used throughout the study came from Lumerical's material database which is based on

the work from "Optical constants of the Noble Metals" by Johnson and Christy [75].

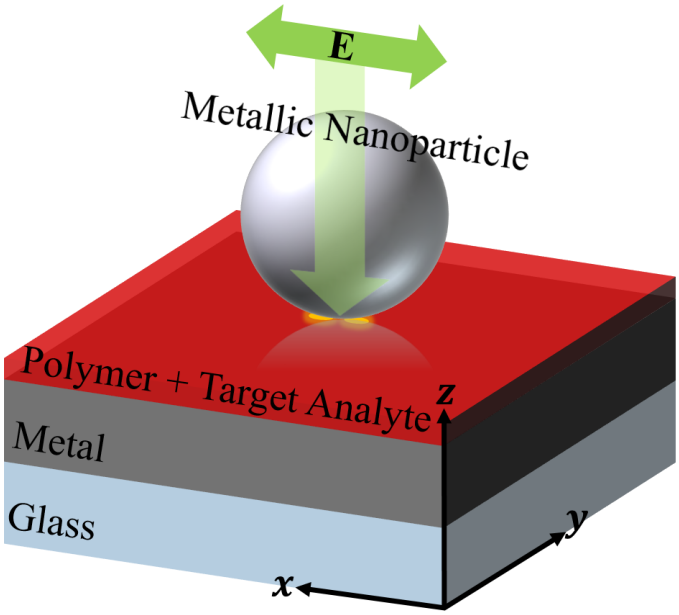

Figure 5.1.1 – Overall schematic of the nano-gap formed between a metal nanoparticle and an extended metallic film. The shape of the particle is defined in the respective section of the text and data. Structures use silver or gold where specified.

5.1.1 Total Field Scattered Field Excitation

Figure 5.1.2 shows the $x-z$ cross section for the schematic diagram of our structure within the FDTD environment. Simulations used a 0.75 *nm* sub-mesh surrounding the nanoparticle and nano-gap region. This ensures the curved surfaces of the structure are adequately meshed. We also use Lumerical's conformal variant 1 mesh, which evaluates the fields in each cell but accounts for sub-cell properties where more than one material can occupy the same Yee-cell. It utilises the Yu-Mittra method and accounts for all materials including metals [131].

The boundaries of the structure utilise stretched co-ordinate PML to eliminate the fields at these interfaces based on formulation proposed by Gedney and Zhao [127]. The glass, metal and dielectric layers extended through this PML region to simulate an extended film. The sensors are located at the centre of the gap in the $x-y$ plane and through the centre of the structure taking a cross section in the $x-z$ plane. The sensors allow us to quantify the properties of absorption and scattering, while also retrieving information regarding the electric fields passing through these regions as a function of frequency.

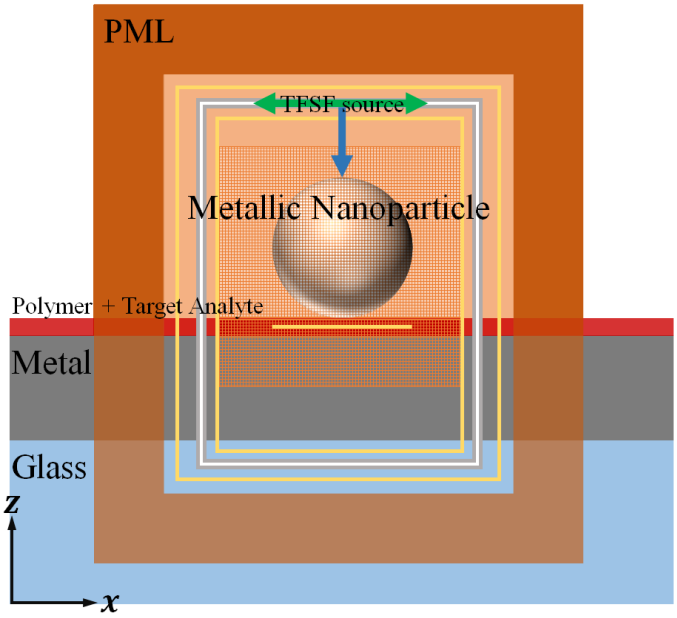

Figure 5.1.2 – $x-z$ view of the simulation environment with a nanoparticle-cavity system. Here, we see the electric field monitors for the $x-z$ profile and the $x-y$ within the cavity for hot spot analysis.

Additionally, we are able to project these electric fields to the far-field to determine the scattering properties from specific regions of the device, namely, the nano-gap. We allow for long pulse lengths from our sources with simulation times being set in excess of 1000 fs, such that fields deteriorate to 1×10^{-5} of their original value and the auto shut off is triggered.

The simulations took place using a total field scattered field (TFSF) source to begin with. The TFSF source works on the basis of two regions, the internal region of the source contains the total field which is a contribution of the incident and scattered fields. Whilst the external region contains only the scattered fields. We can obtain the absorption, scattering and therefore extinction characteristics of a system with this source type with the plane wave injection axis of the source in the z direction above the particle and the electric field oscillating in the x axis.

5.1.2 Charge Distribution

The charge distribution over the nano-cavity system allows the modes of the electric field to be visualised more clearly. We calculate this charge distribution ρ using the current charge density analysis group from the advanced analysis section of Lumerical's object

library. It works by treating the system as a cloud of free electrons. We obtain ρ from the differential form of Gauss's law [4, 11]:

$$\nabla \cdot \mathbf{D} = \rho_{ext} \tag{5.1.1}$$

Where $\nabla \cdot \mathbf{D}$ is the divergence of the electric displacement field $\mathbf{D}$ and ρ_{ext} is the external charge density.

5.1.3 Gaussian Beam Excitation

The Gaussian source functions differently to the TFSF source which is limited to a wave injected from a single planar direction. Because it is formed from a contribution of many plane waves at varying angle, it will give more realistic scattering dynamics, allowing coupling from light we would not have previously observed from a single injection axis. The custom Gaussian field profile uses the superposition of plane waves (in this case 200 plane waves were used to give a realistic beam profile). The beam can also be focused to a specific region of the device and an *NA* can be defined. These simulations use $NA = 0.55$ which is more realistic than a single injection plane wave and identical to the objective we use in our practical setup. The source positioned above the structure has its focal point at the centre of the 5 *nm* cavity. This was the most beneficial approach as the target material would be ideally contained within the cavity and excited directly by the laser setup.

The Gaussian calculations differ slightly relative to the TFSF counterparts, where previously, TFSF performs the calculations for the structure and reference simultaneously Gaussian excitation require that the two calculations to be performed in succession. First, a reference structure is simulated (here we used an empty simulation region), then, a second calculation is performed with the structure and the difference in the fields from the two calculations constitutes the scattering field.

We performed calculations from three particle sizes, the 118 *nm* silver particle, as well as 60 and 200 *nm* particle cavity systems (owing to the fact that these sizes are physically available to us). We demonstrate the size dependency with regards to the near-field confinement and far-field scattering characteristics.

5.2 The Figure of Merit Linking Near to Far-Field SERS Emission

The papers we have discussed in section 5.1 generally discuss the near-field contribution to SERS and the high field confinement generated from plasmonic nano-gaps. However, there is very little work regarding the transmitted light to the far-field directly from the nano-gap and how efficiently this enhances the Raman signal. Therefore, in our study we use the FoM discussed in section 2.7 of Chapter 2, which takes into consideration both the enhancement in the near-field excitation (G_{ex}), as well as the far-field emission (G_{em}) [74]:

$$FoM(\lambda) = \langle G_{ex} \rangle \times G_{em}(\omega) \tag{5.2.1}$$

To account for the random distribution of target molecules within the gap, the near-field is averaged across the particle cross section. We express the excitation enhancement as the spatial average of G_{ex} over the cross sectional area of the nano-gap:

$$\langle G_{ex} \rangle = \frac{1}{a} \int \frac{|\mathbf{E}(\omega_0)|^2}{|\mathbf{E}_0(\omega_0)|^2} da \tag{5.2.2}$$

Where $\mathbf{E}_0$ is the incident electric field, $\mathbf{E}$ is the electric field at the location of the molecule, ω_0 is the frequency of the incident photon and $a = \pi R^2$ is the area of under the particle with radius R. For the emission enhancement, G_{em}, the ratio of the radiated power in the presence and the absence of the metallic nanostructure is equal to the ratio of the electromagnetic density of states [74].

$$G_{em}(\omega) = \frac{\rho(\omega_1)}{\rho_0(\omega_1)} = \frac{W_{rad}}{W_0} \approx \frac{\sum_{\theta} \mathbf{E}^2(\omega_1, \theta)}{\sum_{\theta} \mathbf{E}_0^2(\omega_1, \theta)} \tag{5.2.3}$$

Here, we approximate the ratio of the radiated power in the presence and absence of the metallic structure W_{rad}/W_0, which is equal to the ratio of the electromagnetic density of states $\rho(\omega_1)/\rho_0(\omega_1)$, to the far field emission enhancement from the position of the

analyte. Where, $\mathbf{E}^2(\omega_1,\theta)$ and $\mathbf{E}_0^2(\omega_1,\theta)$ are the far-field intensities as a function of the frequency after Raman scattering ω_1, and emission angle θ, in the presence and in the absence of the plasmonic nano-gap.

Together, $\langle G_{ex}\rangle$ and G_{em} give the overall Raman enhancement which we characterise as our FoM for our FDTD calculations:

$$FoM(\lambda) = \langle G_{ex}\rangle \times G_{em}(\omega) \approx \left[\frac{1}{a}\int \frac{|\mathbf{E}(\omega_0)|^2}{|\mathbf{E}_0(\omega_0)|^2} da\right] \times \frac{\sum_\theta |\mathbf{E}(\omega_1)|^2}{\sum_\theta |\mathbf{E}_0(\omega_1)|^2} \tag{5.2.4}$$

By investigating the influence of the excitation enhancement from the centre of the nano-gap, which is where the material under investigation would be localised, as well as the emission enhancement and how effectively the light is emitted from the device, we have compiled the data necessary to completely define our system. The FoM encapsulates both near-field excitation as well as far-field emission from particle on a film nano-gap systems, cataloguing in detail their behaviour under the influence of electric field excitation. We have done this by the amalgamation of the excitation enhancement $\langle G_{ex}\rangle$, and the emission enhancement G_{ex}. The system is far more complex than what can be described by simple scattering from the entire structure or near-field enhancement alone, and the ideal excitation wavelength must be specified systematically from its near-field, as well as the far-field emission properties from this specific region. The emission enhancement from our calculations is extrapolated via Lumerical's built in near to far-field transformation functions based on the work in Computational Electrodynamics: The Finite-Difference Time-Domain Method [130].

5.3 Nano-Gap Results

In this section, we explore the physics of the nano-gap formed between a metallic particle and an extended metallic film. We investigate the near-field enhancement and far-field scattering characteristics of nanoparticles ranging in size from $60-200$ *nm* as we have

particles of these sizes available to us. The purpose of this section is to explore the physics of these nano-gaps, comparing them to isolated particles on their own, and to discuss their potential use for SERS. These particles are deposited onto a thin film of the polymer matrix which houses the target analyte at a specified concentration. This is then defined as the nano-gap between the particle and the extended metal film below. By investigating the effects of changing certain parameters such as the cavity thickness, the particle size and shape, as well as the metallic film material and thickness, we demonstrate the versatility of this plasmonic nanostructure. We fully investigate the optimal conditions for excitation which will produce the most efficient Raman scattering from our optical setup.

5.3.1 Nano-Gap vs Single Nanoparticle

We begin by comparing the fundamental physics for a single 118 *nm* diameter silver particle and a gap formed between it and a 100 *nm* silver film as this is shown to be a realistic particle size. By comparing the extinction calculated from the FDTD simulations of the nano-cavity system with the particle on its own, we can see that the cavity demonstrates two distinct modes. Both of these modes are much narrower than that seen from the particle in absence of the metallic film below. The cavity based structure has a much stronger extinction spectrum than that of the isolated particle, this can be broken down into two regions, one with a peak at 415 *nm* and the other peaking at 523 *nm* as seen in Figure 5.3.1.

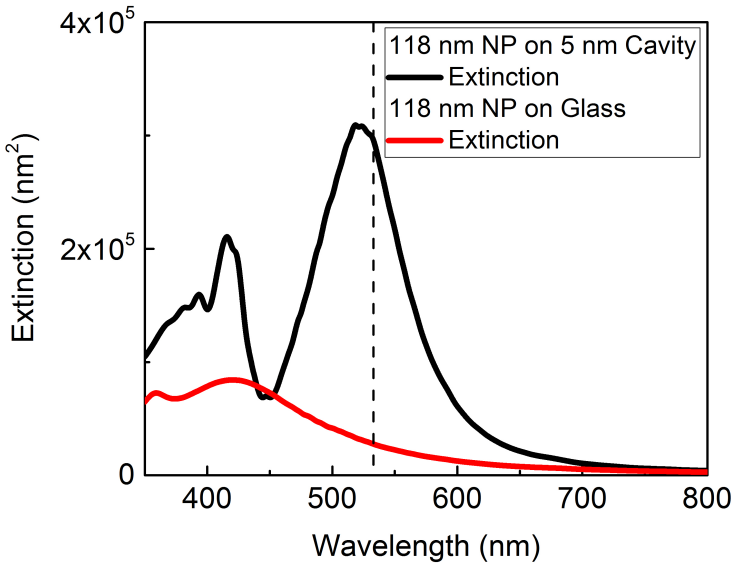

Figure 5.3.1 – A comparison of the extinction spectrum from the cavity system (black) and the nanoparticle on its own (red). The dashed line represents 532 *nm*.

5.3.2 Near-Field Distribution

The aim of this section is to describe the near-field characteristics at the peak wavelengths for the modes of the hybridized system shown in Figure 5.3.1. By doing so, we will be able to show which wavelength generates the highest field confinement in the near-field. By analysing the spacial distribution of the electric field, we can see the difference between the system with a cavity below and without.

Figure 5.3.2 gives the field enhancement for the system in the $x-z$ plane for the nanoparticle in the absence of the nano-gap for 415 *nm* in Figure 5.3.2a and Figure 5.3.2c. As well as the same scenario for the peak at 523 *nm* in region 2 of the extinction spectrum given by Figure 5.3.2b and Figure 5.3.2d respectively. These wavelengths are selected as they are the peak intensities for the extinction of the system.

The graphs show high confinement and enhancement of the electric fields from the devices when used in conjunction with the cavity system. The field enhancement, defined by the 4^{th} power of the electric field is boosted by a factor of 10^7 for region 1 and 10^5 for region 2. It is therefore evident that the cavity system provides huge amplification to the electric fields within the nano-gap. This means that coupling from nano-gaps in

this geometry has the potential to enhance the generated Raman signal of the material confined to these regions.

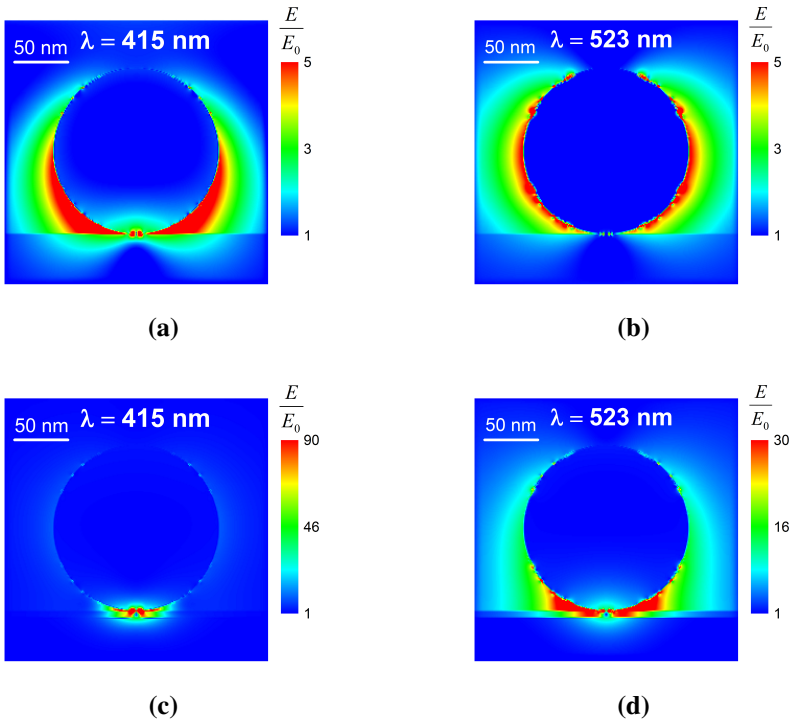

Figure 5.3.2 – The field enhancement plotted as a function of area for the nanoparticles without the cavity system (a and b) and the nanoparticles with the nano-gap below (c and d). (a and c) and (b and d) relate to the 415 *nm* and 523 *nm* resonant modes respectively, where all data is recorded as $|E|/|E_0|$.

Figure 5.3.3 provides insight to the behaviour of the electric field located at the centre of the cavity itself.

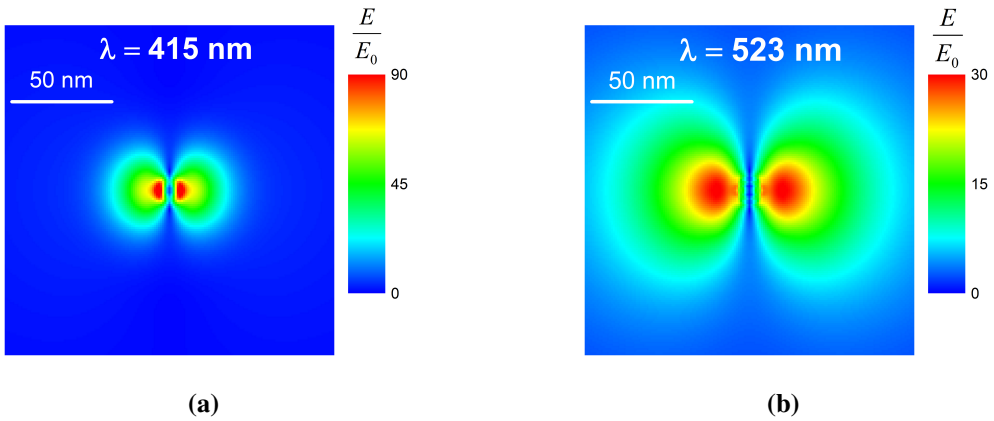

Figure 5.3.3 – Field enhancement for the $x-y$ plane sensor taken from the centre of the cavity showing the hot spots for the (a) 415 *nm* and (b) 523 *nm* resonant modes, where all data is recorded as $|E|/|E_0|$.

The FWHM of the hot spot regions differ dramatically. Although the 415 *nm* excitation has the benefits of the larger G_{ex}, its hot spot diameter is only 13.3 *nm*. This is less than 3 times the size of the hot spot generated by the 523 *nm* excitation, which is shown to be 40.6 *nm* over the most intense regions. SERS requires maximum field intensity, we can see there is far more confinement of the fields in the near-field from the 415 *nm* region. Through further investigation of the far-fields, we will find how much of this is scattered into a collectable region.

5.3.3 The Origins of the Two Extinction Peaks

We can see from Figure 5.3.4, that for a nanoparticle 118 *nm* in diameter, the scattering dominates the absorption. Therefore, the main contribution to extinction will be from the scattering component.

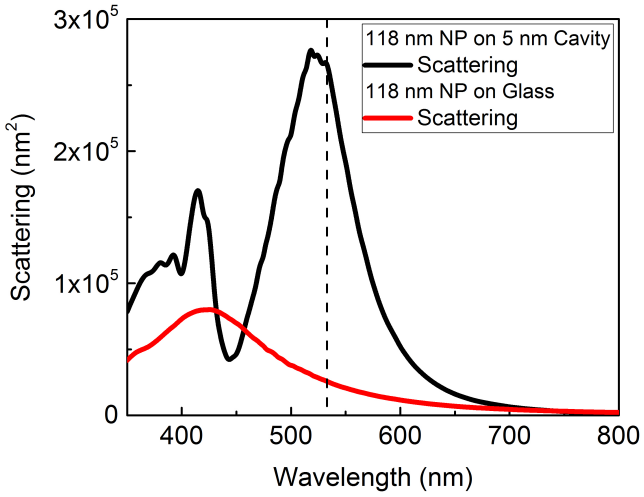

Figure 5.3.4 – Absorption and scattering spectra from the 118 *nm* silver nano-cavity system. The dashed line represents 532 *nm*.

This is important for this system as a strong scatterer will be required for SERS measurements. Two regions arise as a result of this coupling plasmon hybridisation phenomenon. The first peak in the scattering spectra can be attributed to the hybridized quadrupole mode of the coupled system, and the second peak to the dipolar mode We utilise the method for calculating the charge distribution highlighted in section 5.1.2 using equation 5.1.1.

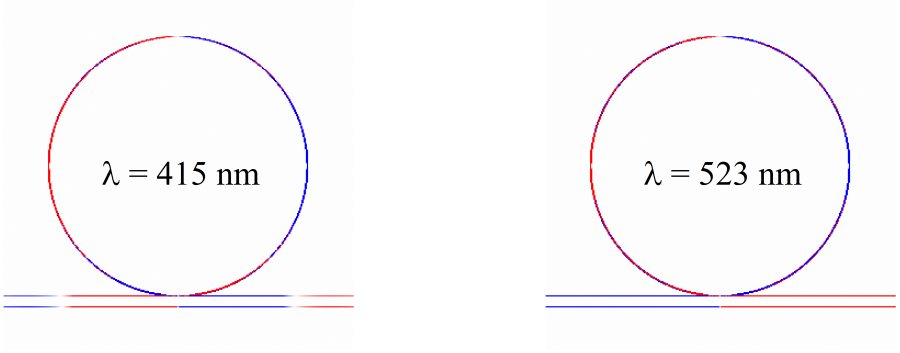

Figure 5.3.5 – Charge distribution for the 118 *nm* particle cavity system under the influence of a TFSF source using 0.5 *nm* meshing for (a) 415 *nm* and (b) 532 *nm* excitation. The red regions indicate positive charge and the blue regions depict the negative.

We can see here that the 523 *nm* mode behaves more like a dipolar mode, whereas the 415 *nm* excitation would generate a quadrupolar mode. Where the red regions indicate positive charge and the blue regions depict the negative. When compared to the same sized particle on glass taken at its respective peak extinction maximum, we see there is a dipolar mode for this system shown in Figure 5.3.6.

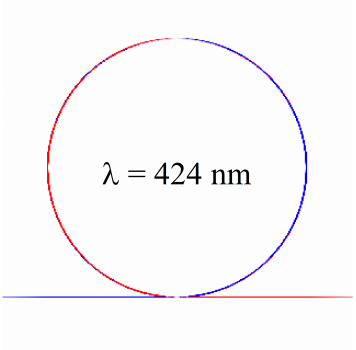

Figure 5.3.6 – Charge distribution for the 118 *nm* particle on glass under the influence of a TFSF source using 0.5 *nm* meshing for 424 *nm* excitation. The red regions indicate positive charge and the blue regions depict the negative.

Now, we have introduced the nano-gap geometry, the following sections of the report will detail the effects of changing certain parameters of the system such as film thickness, particle size and shape. We can then see the effect that changing these criteria has on the electric fields both in the near-field and the far-field projection.

5.3.4 Gap Thickness Dependence

Figure 5.3.7 studies the effect of varying a gap width from a nano-gap formed between a 118 *nm* silver nanoparticle and a 100 *nm* thick extended silver film. By looking into the maximum field enhancement achieved (E^4_{max}) within the nano-gap, we can see the relationship between the gap thickness and enhancement in the near field [76].

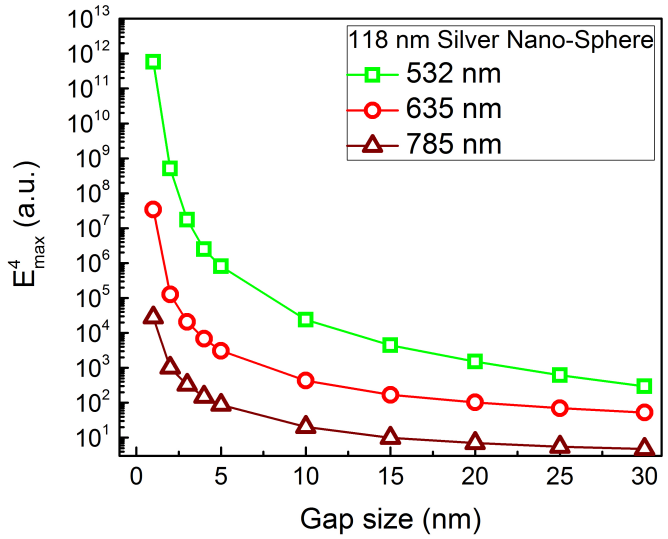

Figure 5.3.7 – Field enhancement as a function of gap size for a 118 *nm* silver particle on a nano-gap of varying thickness formed between the particle and the extended metal film below. The data shows the maximum field enhancement as a function of gap thickness collected at 3 common Raman laser wavelengths, 532 *nm*, 635 *nm*, and 785 *nm* and the meshing of the system was set to 0.75 *nm* until gap thickness reached 5 *nm* and gridding was reduced to 0.2 *nm*.

Also, by looking at the extinction for the system during the gap thickness sweep, in Figure 5.3.8a the extinction peak gets narrower when reducing the gap width from $30-5$ *nm* but does not shift significantly. Therefore, the system retains a stable plasmon resonance for gap thickness with peak intensity becoming larger with a narrower cavity.

However, when the cavity thickness decreases below 5 *nm* the peaks shift and new modes arise, see Figure 5.3.8b. These effects are seen similarly in literature [79], where at separations approaching 1 *nm* higher order modes arise. This is to be expected as classical representations depicted by Maxwell solvers such as Lumerical do not account for non-linear effects at these spatial separations of plasmonic structures even with the

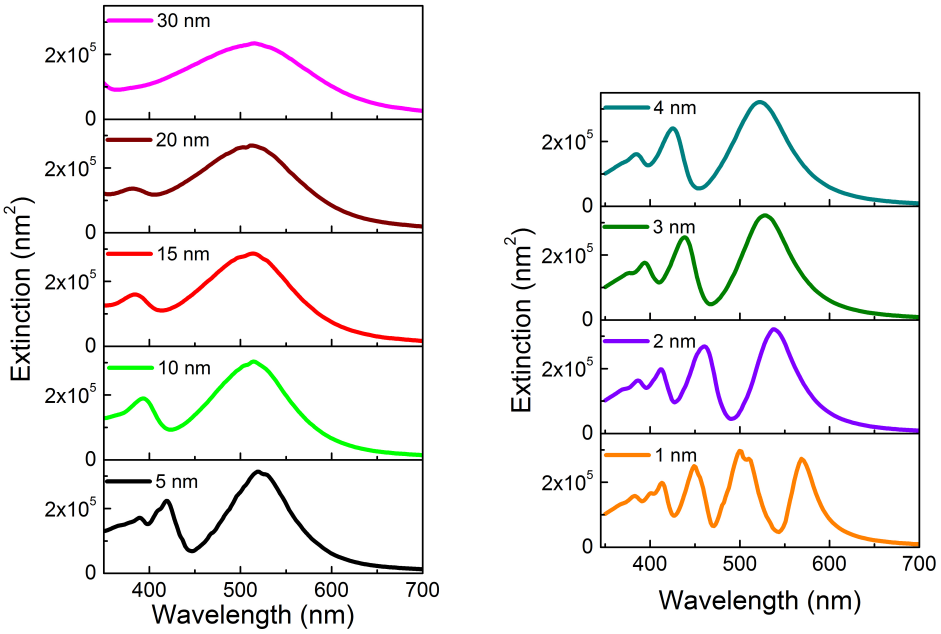

(a) **(b)**

Figure 5.3.8 – Extinction spectrum for a 118 *nm* spherical silver nanoparticle on a nano-gap ranging from $30-1$ *nm* in thickness (a) from $30-5$ *nm* in 5 *nm* intervals with meshing set to 0.75 *nm* and (b) from $4-1$ *nm* in 1 *nm* intervals using a 0.2 *nm* mesh for more accuracy.

fine meshing of 0.2 *nm* used through these calculations. Therefore, as a 5 *nm* cavity predicts strong coupling and significant field enhancement while being experimentally reproducible via spin coating of materials, we proceed with this value.

5.3.5 Altering the Metallic Film Thickness

By altering the thickness of the silver film below the cavity, it is possible to show how the changes to field enhancement and scattering. Figure 5.3.9 shows the differences between a 20 *nm*, 100 *nm* and infinite silver film. We can see from Figure 5.3.9 that when using a thinner film both modes become far broader.

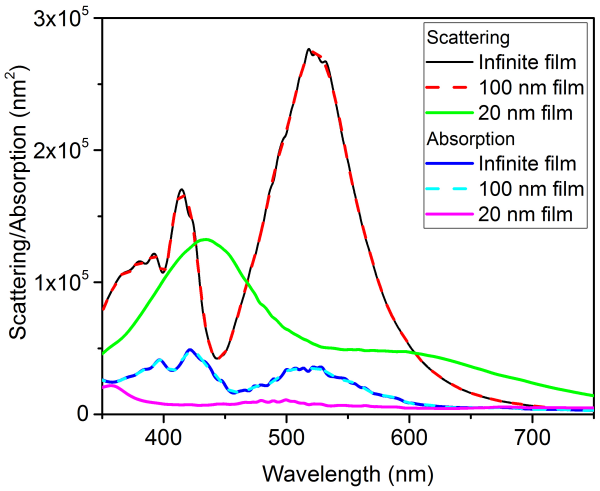

Figure 5.3.9 – Scattering and absorption spectra of the silver nanoparticle system using 20 *nm*, 100 *nm* and infinite film thicknesses.

We can also see a shift in the peak position, the quadrupolar mode shifts from 415 *nm* to 433 *nm*, while the dipolar mode shifts from 523 *nm* to 605 *nm*. This tunability is credited to the coupling to the plasmon continuum [89], which we discussed in more detail in section 2.3.3. Although this mode is weaker than the strongly coupled system with the 100 *nm* metallic film, it does have potential for added optimisation of the ideal excitation wavelength.

The 20 *nm* film is detrimental to the scattering properties of the system, whereas the 100 *nm* system behaves exactly the same as if the film were infinite. When comparing the 415 *nm* quadrupole mode of the 100 *nm* thickness metallic film to the 433 *nm* mode of the 20 *nm* thickness system, the scattering is $\sim 1.3\times$ stronger. Whereas comparing the 523 *nm* dipole mode of the 100 *nm* metallic film with the 605 *nm* mode of the 20 *nm* thick film, we find a difference of $\sim 5.8\times$ for the scattering intensity. Therefore, the 100 *nm* film gives the ideal characteristics we are looking to achieve in terms of scattering. Although scattering characteristics of the system are relevant, they do not show the entire picture for how the system behaves. Further investigation is required regarding the different properties in terms of directionality and electric field confinement characteristics.

By observing the electric field at the resonant modes from the scattering data, we can see their confinement as a result of the localised surface plasmons. Figure 5.3.10 gives us

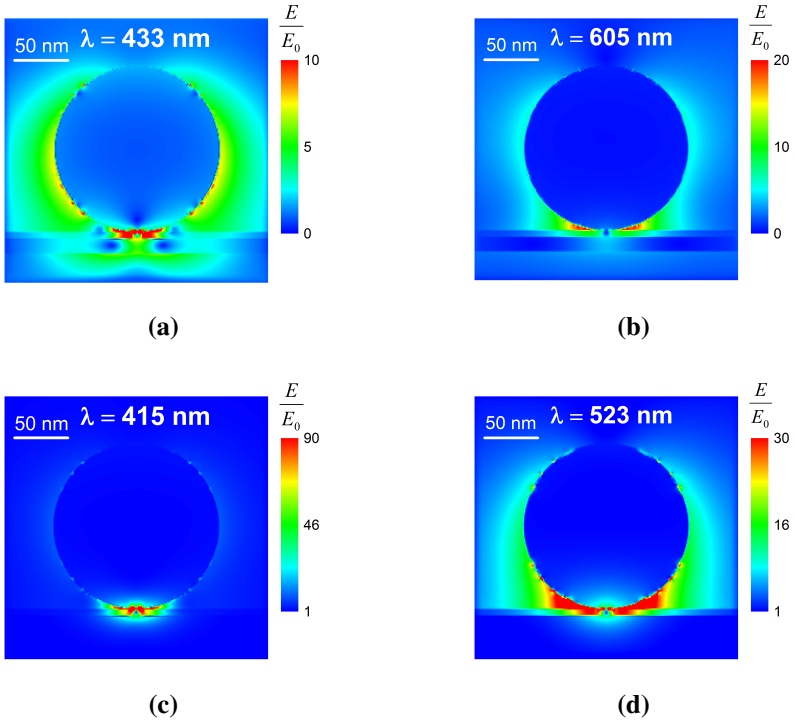

Figure 5.3.10 – The electric field enhancement plotted as a function of area in the $x-z$ plane for nano-gaps formed between a 118 *nm* silver nanoparticle and an extended metallic film. Where (a and b) give the electric field at 433 *nm* and 605 *nm* which are the resonant modes for the 20 *nm* thick metallic film and (c and d) show the 415 *nm* and 523 *nm* resonant modes for the 100 *nm* thick silver film, where all data is recorded as $|E|/|E_0|$.

the magnitude of the electric field enhancement for the 118 *nm* silver nanoparticle and a 20 *nm* thick continuous silver film in the $x-z$ plane.

We can see from Figure 5.3.10 that at this thickness, the electric field penetrates below the metallic film. This is an undesirable effect from our perspective as our experimental setup works in reflection of the target surface. We can also see the confinement of the field hot spots for the system in Figure 5.3.11.

The 433 *nm* and 605 *nm* wavelengths for the 20 *nm* metallic film system are shown to have relatively strong coupling with the hot spots localised to two small regions below the particle. This is characteristic of the nano-gap formation and gives field strength to be double what we observe from the isolated particle in absence of a nano-gap in Figures 5.3.2a and 5.3.2b. However, when examined in contrast to the 100 *nm* film electric field profiles, the 20 *nm* thickness system at 433 *nm* and 605 *nm* shows fields are $\sim$ 7.5$\times$ weaker within the cavity for the quadrupole mode and $\sim 3\times$ weaker for the dipolar

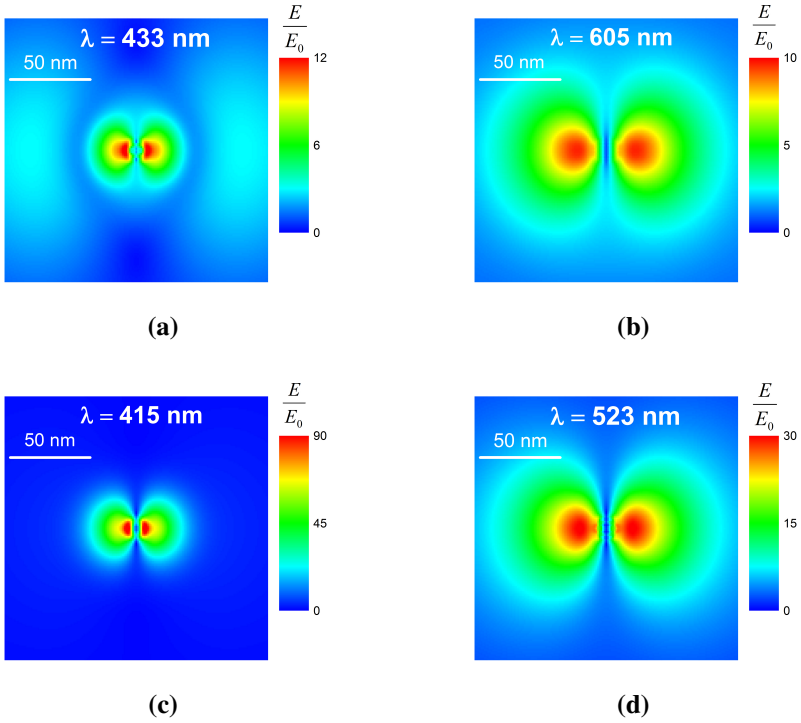

Figure 5.3.11 – The electric field enhancement plotted as a function of area in the $x-y$ plane sensor taken from the centre of the cavity for nano-gaps formed between a 118 *nm* silver nanoparticle and an extended metallic film. Where (a and b) give the electric field at 433 *nm* and 605 *nm* which are the resonant modes for the 20 *nm* thick metallic film and (c and d) show the 415 *nm* and 523 *nm* resonant modes for the 100 *nm* thick silver film, where all data is recorded as $|E|/|E_0|$.

mode respectively. This means electric fields in this configuration are less confined and near-field enhancement of materials within the gap are likely to suffer during Raman scattering.

5.4 Silver Nanoparticle Shape and Size Analysis

An advantageous characteristic of plasmonic nanostructures is that by changing the size, shape and material of the metallic particle used in the simulations, it is possible to tune the resonant frequency of the structure. Therefore, by studying the extinction characteristics of the structures, it is possible to customise the peak wavelength and hence determine the ideal working incident laser wavelength to use. Our experimental setup has two functional Raman lines, one at 532 *nm* and the other at 635 *nm* so we will be focussing on these wavelengths. The 532 *nm* laser is more ideal as there is less background intensity

from the beam, hence when working at low concentrations of materials, their signal will not be lost. In conjunction with this, a study of the electric field as a function of space in the $x-z$ and $x-y$ configuration of the simulation the total field enhancement for the structure at that wavelength can be given for each structure.

5.4.1 Silver Nano-Spheres

By investigating the extinction spectrum of the spheres under the influence of a TFSF plane wave source as a function of their diameter, it is possible to determine the resonant wavelength of excitation hence the structure can be tuned to the desirable wavelength for the setup used in the experiment. Here, we present calculations conducted on nano-gaps formed between silver particles with silver surfaces using particles of varying size. The metallic film below was kept at a constant 100 *nm* thickness and the 5 *nm* nano-gap consisted of a dielectric material with refractive index $n = 1.5$.

We can see in Figure 5.4.1, that the extinction spectrum consists of two peaks for each cavity system, each peak shifts as a function of particle size at different rates. By dividing the two peaks into regions (region 1 and region 2), we can see how they shift individually with increased particle diameter as shown in Figure 5.4.2. Region 1 (blue) and region 2 (green) denote the peaks for the quadrupolar and dipolar mode respectively, as discussed in section 5.3.3. It is notable to mention that the peaks also broaden as particle size increases due to retardation effects.

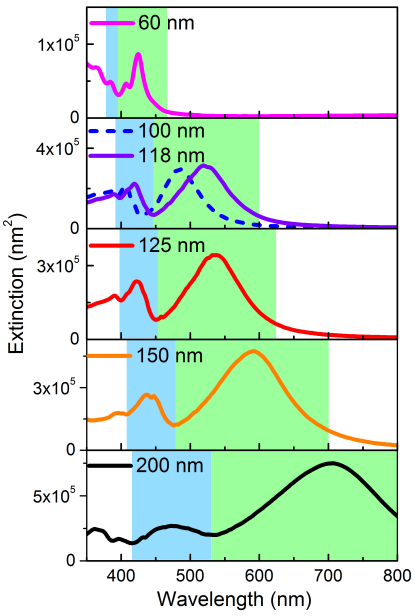

Figure 5.4.1 – Extinction spectra for spherical silver nanoparticles moving from 60 – 200 *nm*.

Figure 5.4.2 shows the peak wavelength from the extinction spectrum vs the particle size. We include 60 *nm* and 118 *nm* diameter as we have these particle sizes physically available to us. The peaks associated to the dipolar mode are far more tunable than the quadrupole. They also shift throughout the majority of the visible spectrum.

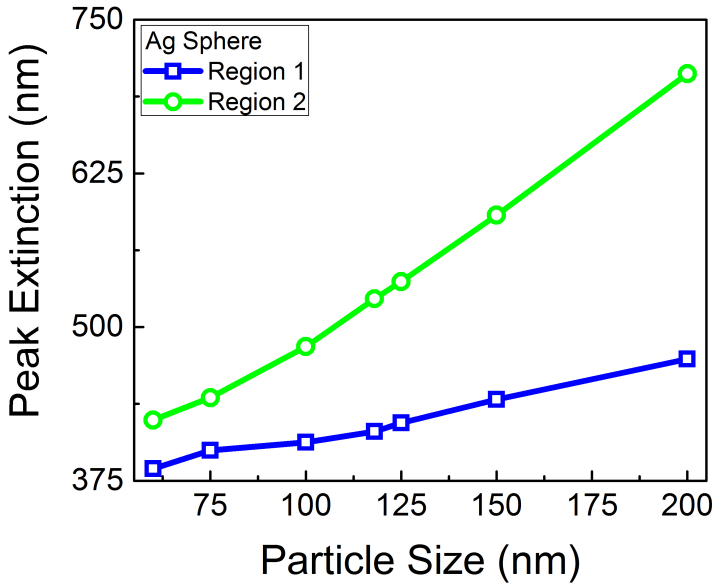

Figure 5.4.2 – Peak extinction wavelength as a function of particle size for spherical silver nanoparticles moving from 75 – 200 *nm* in 25 *nm* intervals.

In Figure 5.4.2, the peak from region 2 has a much larger tunability than region 1, moving a total of 263 *nm* from 75 *nm* to 200 *nm* in diameter compared to 74 *nm* from region 1 over the same size distribution. This means region 2 has more range from resonant excitation when compared to region 1.

5.4.1.1 Excitation Enhancement

Excitation enhancement of the electric field was theoretically analysed via the sensor located in the middle of the nano-gap in the $x-y$ plane with the same dimensions as the diameter of the particle in question. By performing a $2D$ integral over the cavity area, we can extract the field within the cavity as a function of wavelength spatially averaged to the cross section of the particle. Our near-field contribution represented by $\langle G_{ex} \rangle$, is given from equation 5.2.2.

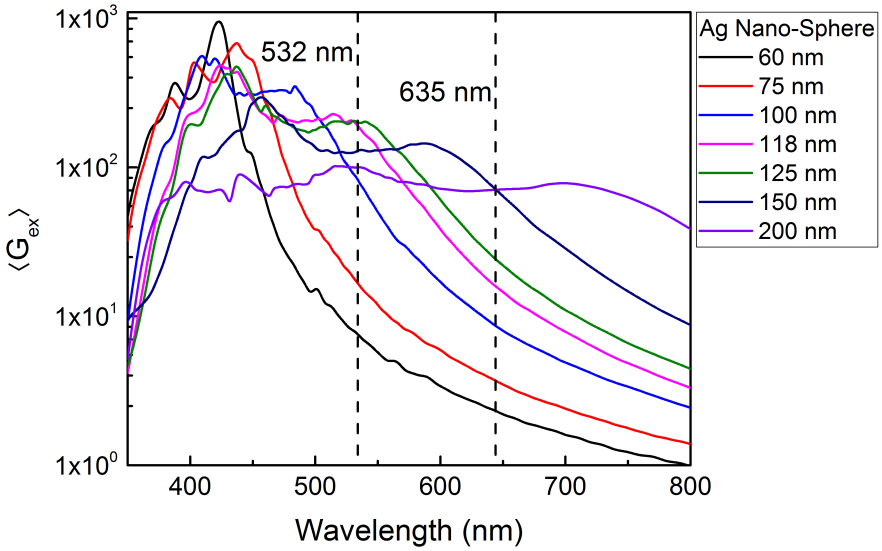

Figure 5.4.3 – $\langle G_{ex} \rangle$ as a function of wavelength for a distribution of spherical silver nanoparticles moving from $60-200$ *nm* in diameter.

As we can see in Figure 5.4.3, the excitation enhancement for the higher energy modes is much stronger than at longer wavelengths. However, when considering the laser lines available to us in our experimental setup, the 125 *nm* diameter particle has the strongest $\langle G_{ex} \rangle$ value at 532 *nm*. Also, we observe that the quadrupole mode for near-field excitation is stronger than the dipolar mode.

The excitation enhancement however only shows half of the picture. We must consider the fields scattered to the far-field in order to justify which structure to use for a given excitation wavelength.

5.4.1.2 Emission Enhancement

We can show the far-field emission enhancement as a function of angle and wavelength for three of the particles, which represent realistic sizes for experimental purposes, shown in Figure 5.4.4.

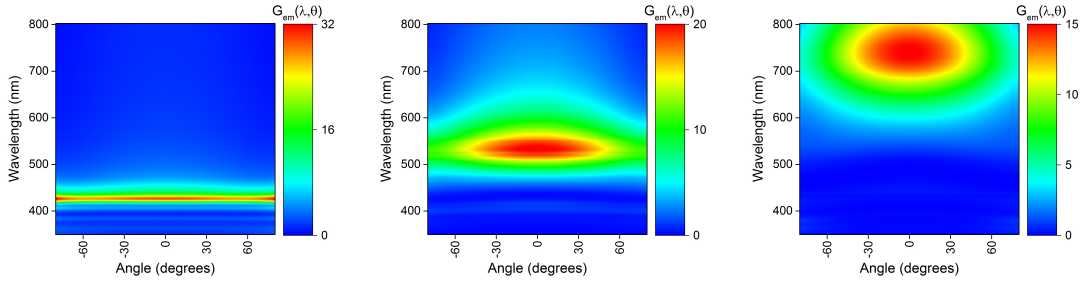

Figure 5.4.4 – G_{em} heat maps for showing the angular dependency as a function of wavelength for the far-field scattering. For 5 *nm* nano-gaps formed between an (a) 60 *nm*, (b) 118 *nm* and (c) 200 *nm* silver nanoparticle and an extended silver film.

As we can see, the far-field emission distribution shifts to longer wavelength as a function of particle size covering the majority of the visible spectrum over our size range. For the 60 *nm* particle, the emission enhancement is relatively uniform across all angles. However, for the 118 *nm* particle, G_{em} becomes more directional, where emission is mainly confined within a 30° cone of collection. Our emission enhancement integrated over all angles ($\theta = -90°$ to 90°) for these particles is shown in Figure 5.4.5. We can see that as particle size increases the main emission mode of the system red-shifts. There is also a decrease in intensity, with G_{em} becoming broader and weaker.

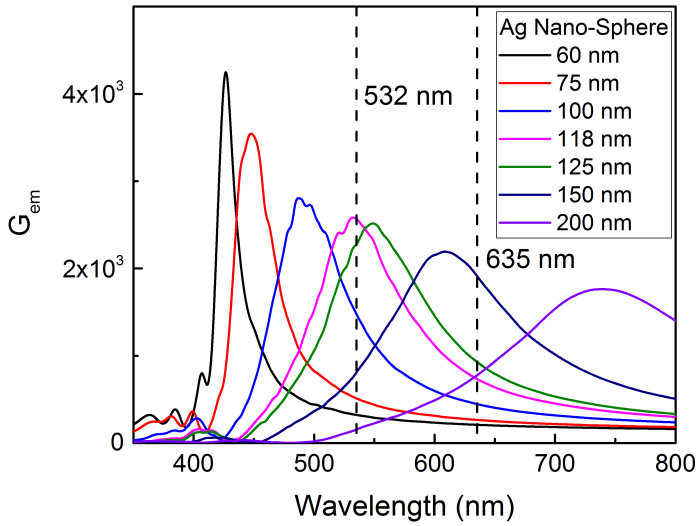

Figure 5.4.5 – G_{em} as a function of wavelength for a distribution of spherical silver nanoparticles moving from $60 - 200$ *nm*.

By taking into consideration the far-field component, our understanding of these nano-gaps changes. In this case, the emission peaks red shift relative to the near-field excitation seen previously, and the 118 *nm* nano-sphere peaks directly at 532 *nm*. The near-field contribution seen previously would suggest that the larger silver nanoparticles are unsuitable for SERS, however, their G_{em} is almost on a par with the smaller nanoparticles but just shifted to longer wavelengths. Another contrast we observe from the near-field, is that the dipolar mode becomes dominant over the quadrupolar mode. The quadrupolar mode is weaker due to internal processes [167]. By combining this information, we arrive at the FoM for the system.

5.4.1.3 FoM: Silver Nano-Sphere Size Distribution

The FoM for the nano-gaps formed between a continuous silver surface and a distribution of silver nanoparticle sizes is shown in Figure 5.4.6.

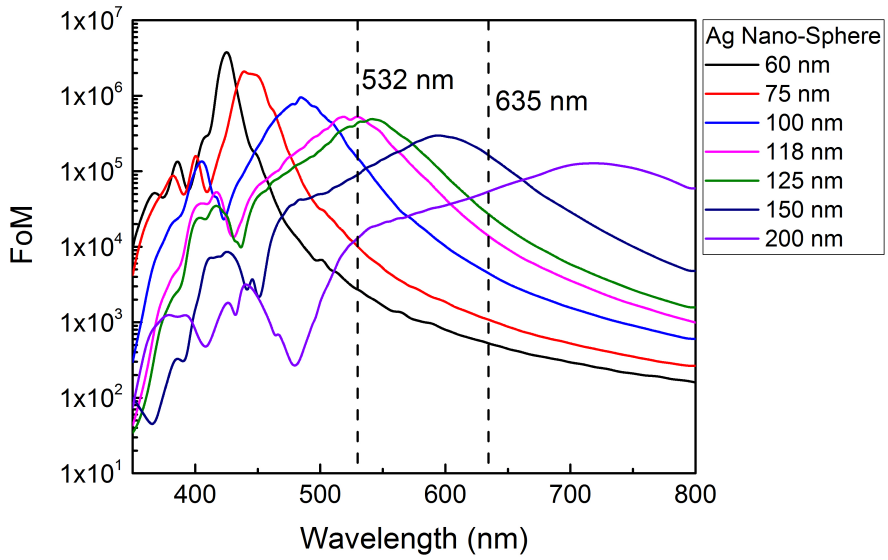

Figure 5.4.6 – FoM for a distribution of spherical silver nanoparticles moving from 60 – 200 *nm* in diameter.

We can see that the most prominent maximum in the FoMs is attributed to the system using the 60 *nm* silver sphere. The 424 *nm* mode for this particle size is 7.09× stronger than the most intense maximum in the FoM for the 118 *nm* silver nanoparticle, which is located closest to the 532 *nm* excitation we are interested in at 519 *nm*. However, when comparing the two systems specifically at 532 *nm*, the FoM for the 118 *nm* systems is 2 orders of magnitude stronger. Although the quadrupolar mode in the near-field is more intense for the 118 *nm* nano-sphere gap, when considering the combination of the excitation and the emission enhancement, the FoM shows that the dipolar mode is more suitable for SERS. Therefore the 118 *nm* nano-sphere gap is most suited for 532 *nm* excitation when considering the near and far-field components contributing to SERS scattering in Figure 5.4.7.

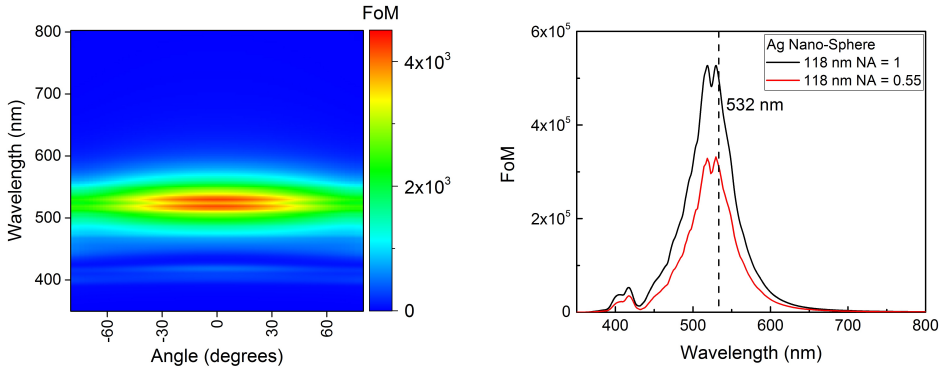

(a) **(b)**

Figure 5.4.7 – FoM for the nano-gap formed between the 118 *nm* silver particle and an extended silver film under TFSF excitation. (a) Shows the heat-map representation of the emission enhancement as a function of wavelength and angle, and (b) the wavelength dependence of the FoM summed over all angles for both $NA = 1$ (black line) and $NA = 0.55$ (red line).

We can see that the FoM for this device covers the excitation wavelength of our Raman system, it also scatters within a cone of collection suitable for collection using an objective lens with $NA = 0.55$.

5.4.2 Silver Nano-Cubes

This study investigates the extinction curves produced by silver nano-cubes as a function of their size. Here, we use 25 *nm* intervals for the x, y and z lengths of the cubes allowing the peak shifting and broadening effect to be observed relative to their size. The extinction spectrum for the silver nano-cube cavity system seen in Figure 5.4.8 is more complex than the spherical system. In this scenario, there are 3 regions (which we have highlighted with blue, green and red boxes) to track relative to particle size as shown in Figure 5.4.8.

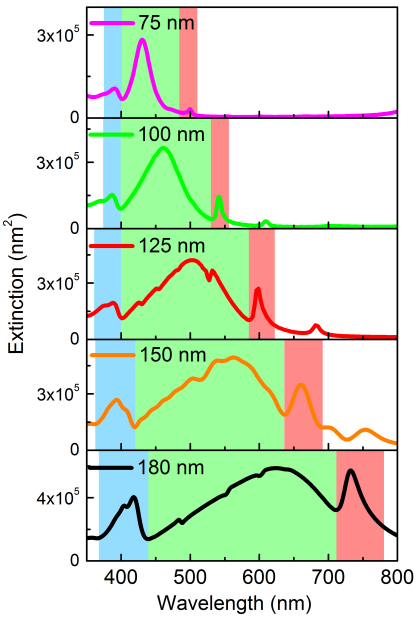

Figure 5.4.8 – Extinction spectrum for silver nano-cubes moving from 75 – 180 *nm* in size via 25 *nm* intervals. In this case, the 200 *nm* particle is omitted for the 180 *nm* as we possess this size.

Figure 5.4.8 shows the extinction spectrum for nano-gaps formed between silver cubes of varying size and an extended silver film below, moving in size intervals of 25 *nm* from 75 – 180 *nm*. We substitute the 200 *nm* for the 180 *nm* cube in this case as we have this size for Raman measurements.

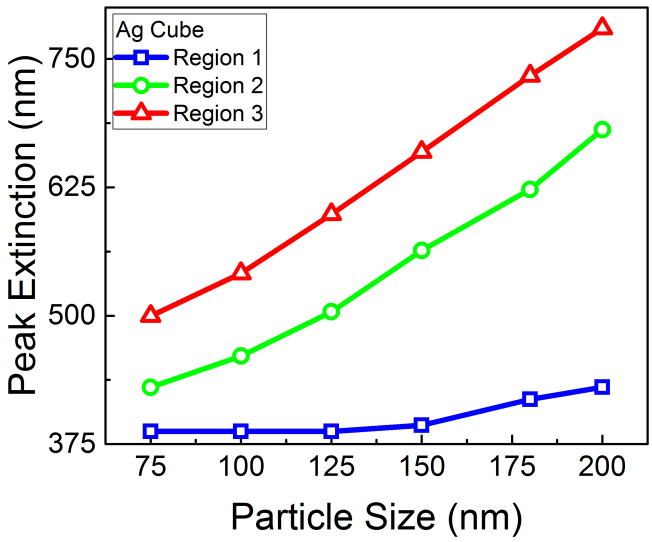

Figure 5.4.9 – Peak extinction wavelength as a function of particle size for silver nano-cubes moving from 75 – 200 *nm* in size via 25 *nm* intervals.

Figure 5.4.9 shows that for the silver nano-cubes the extinction is more complex than in the case of the spherical particles. Region 2 is very broad and is typically the most intense from the simulation batch sweep. The two sub modes either side are labelled as region 1 and region 3. Region 2 has an average FWHM of 90 *nm* ranging from $25-127$ *nm* for particle sizes $75-200$ *nm*. Region 2 covers 251 *nm* of the visible spectrum from the $75-200$ *nm* size distribution, whereas region 3 covers 280 *nm* of the visible spectrum. Both are extremely tunable, however on average the peak in region 2 is $1.45\times$ more intense.

5.4.2.1 Excitation Enhancement

Excitation enhancement was calculated from a sensor located in the middle of the nano-gap in the $x-y$ plane. Our near-field contribution represented by $\langle G_{ex} \rangle$ is given from equation 5.2.2. Figure 5.4.10 shows $\langle G_{ex} \rangle$ for the silver nano-cube size distribution study.

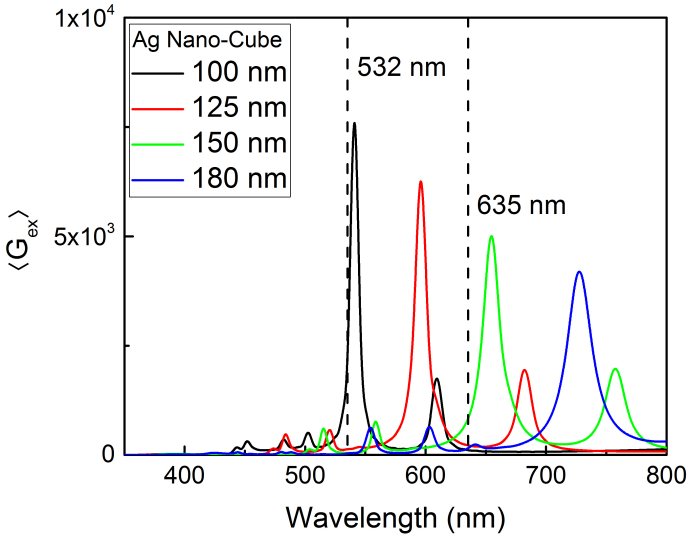

Figure 5.4.10 – $\langle G_{ex} \rangle$ as a function of wavelength for a distribution of silver nano-cubes moving from $100-180$ *nm* in diameter in 25 *nm* intervals.

As we can see, there are very narrow, intense near-field enhancement associated with these nano-gaps. The 100 *nm* cube has huge potential for strong localisation of fields at the 532 *nm* excitation we intend to use (although this peaks at 541 *nm*, there is a shift potential due to size variation of particles under practical circumstances). Larger

cubes shift the value of $\langle G_{ex} \rangle$ further to the red side of the spectrum, while systematically lowering the peak intensity. In order to see how much of these intense fields are useful in a practical sense for SERS purposes, we look at the emission enhancement in the far-field.

5.4.2.2 Emission Enhancement

We can see in Figure 5.4.11 that the directionality of the 100 *nm* and 180 *nm* silver cubes using these nano-gaps is more narrow than what we saw previously from the silver spheres.

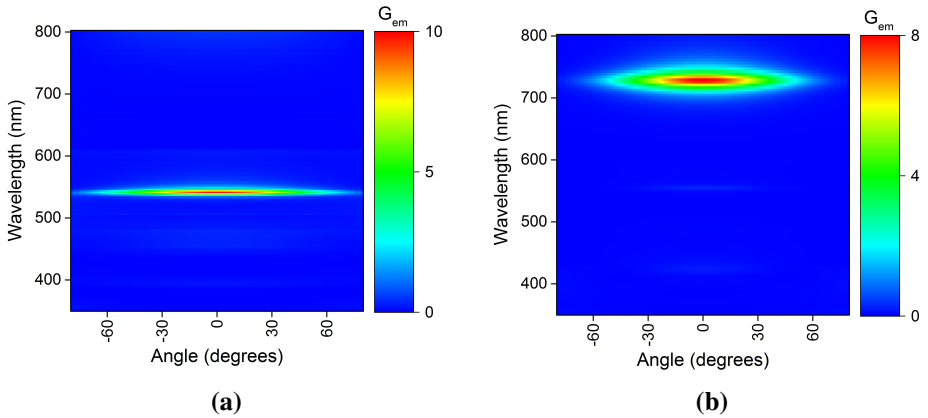

Figure 5.4.11 – G_{em} heat maps for showing the angular dependency as a function of wavelength for the far-field scattering. For 5 *nm* nano-gaps formed between an (a) 100 *nm* and (b) 180 *nm* silver nano-cubes and an extended silver film.

The collection from the most intense region for these gaps are confined between $\pm 27^{\circ}$ for the 100 *nm* cube, and $\pm 20^{\circ}$ for the 180 *nm* cube. Although the excitation enhancement of these nano-cubes is far superior to the nano-spheres, the emission enhancement for this system is weaker in comparison as seen in Figure 5.4.12.

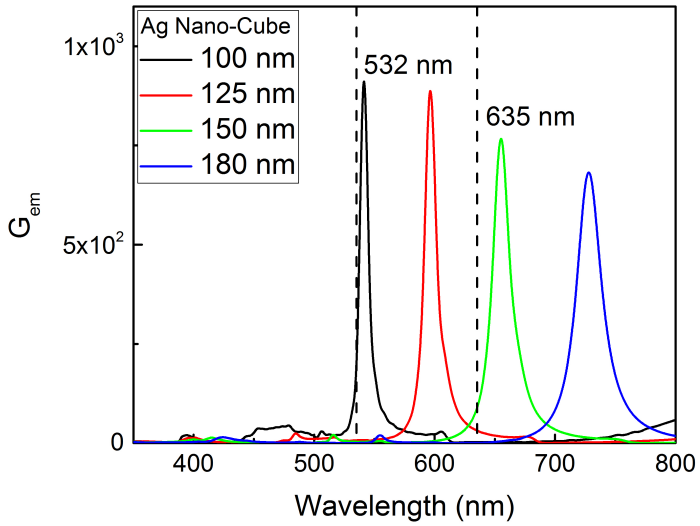

Figure 5.4.12 – G_{em} as a function of wavelength for a distribution of silver nano-cubes moving from $100-180$ *nm* in diameter in 25 *nm* intervals.

This means that although these nano-gaps are excellent at confining electric fields in the near-field, they do not efficiently scatter light to the far-field.

5.4.2.3 FoM: Silver Nano-Cube Size Distribution

To culminate the data acquired from the nano-cubes, the near and far-field contributions are combined into the FoM as shown previously for the nano-spheres.

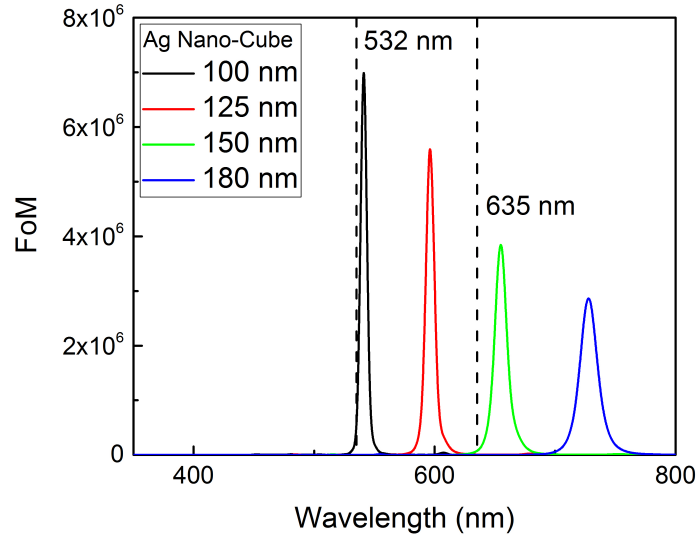

Figure 5.4.13 – FoM for a distribution of silver nano-cubes moving from $100-180$ *nm* in diameter where $NA = 1$.

There is a sharp, highly intense mode associated to the nano-cube nano-gap systems. The 100 *nm* particle has the most intense mode peaking at 541 *nm* which is very close to our 532 *nm* excitation line. This could possess massive potential for enhancement of Raman signal under practical circumstances. These calculations should be considered tentatively however, because the sharp corners of the nano-cubes would not be present in reality [139], and may be major contributors to the intense fields generated in the near-field [164]. Considering the data shown, the system has the potential to be 2.15× more effective than the spheres for Raman enhancement.

Another thing to consider with these systems, is that due to the narrowness of the peaks, they may not cover both the excitation, and emission wavelength of light which is enhanced in SERS. This will lead to detrimental effects for enhancement of the Raman signal.

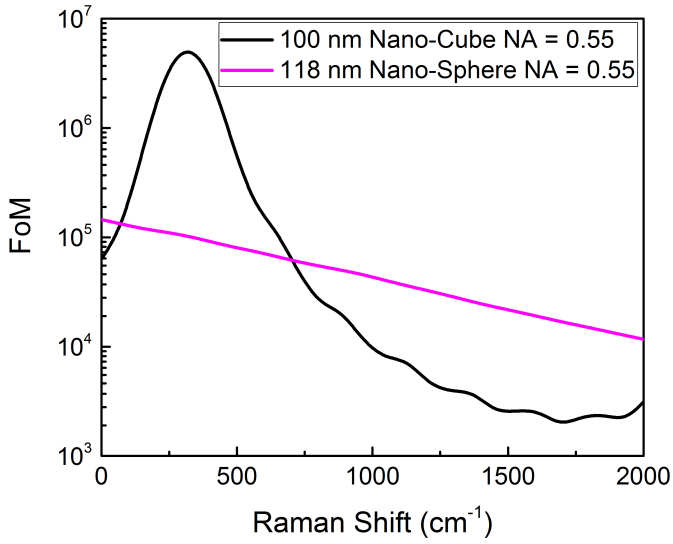

Figure 5.4.14 – FoM plotted as a function of wavenumber for the 100 *nm* silver nano-cube and 118 *nm* silver nano-sphere under 532 *nm* TFSF excitation. The FoMs here are summed from angles within the collection cone from $NA = 0.55$.

From Figure 5.4.14, we can see a comparison of the silver nano-cube and nano-sphere cavity systems which show FoMs most suited for the 532 *nm* laser line. By plotting the FoMs as a function of Raman shift over a region where Raman modes occur for our material of interest, we can see that the sharp mode from the silver nano-cube only covers the beginning portion of the spectrum. This would relate to the excitation, the signal then

lessens significantly. On the other hand, the nano-gap formed using the spherical particles has a relatively consistent FoM across the whole region covering both the excitation and emission portions of the spectra.

5.5 Gold Nanoparticle Shape and Size Analysis

5.5.1 Gold Nano-Spheres

By changing the materials of the nanoparticles to gold, we can see how the behaviour of the extinction spectrum changes. In Figure 5.5.1, the extinction of the gold particles are generally broader than previously seen from the silver. They also begin in the middle of the spectrum at 575 *nm* for the 100 *nm* particle.

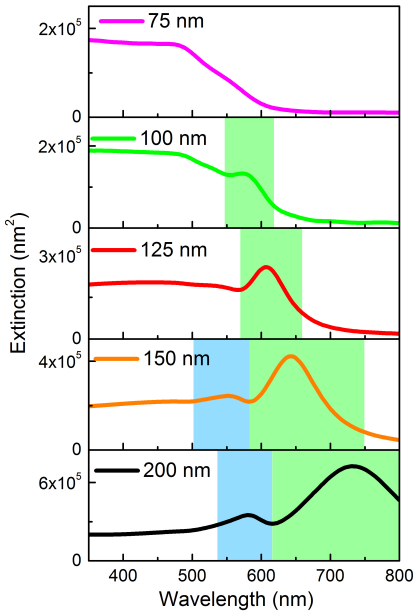

Figure 5.5.1 – Extinction spectrum for spherical gold nanoparticles moving from 75 – 200 *nm* in 25 *nm* intervals.

When compared to the silver nanoparticle extinction seen in Figure 5.4.1, we can see there is less tunability and the resonance for these particles are more localised to the red region of the visible spectrum. This is due to interband transitions and absorption at shorter wavelengths. We can also see that the two extinction modes for this system are far less tunable than what we saw previously with the silver spheres. The dipolar mode shifts

159.8 *nm* in wavelength from 573.84 *nm* to 733.6 *nm*. Whereas, the quadrupolar mode only shifts 28.6 *nm* from 555.8 *nm* to 579.2 *nm*. This is mainly due to the quadrupolar mode not being as distinct as seen from the silver system and only being visible from larger nanoparticle sizes.

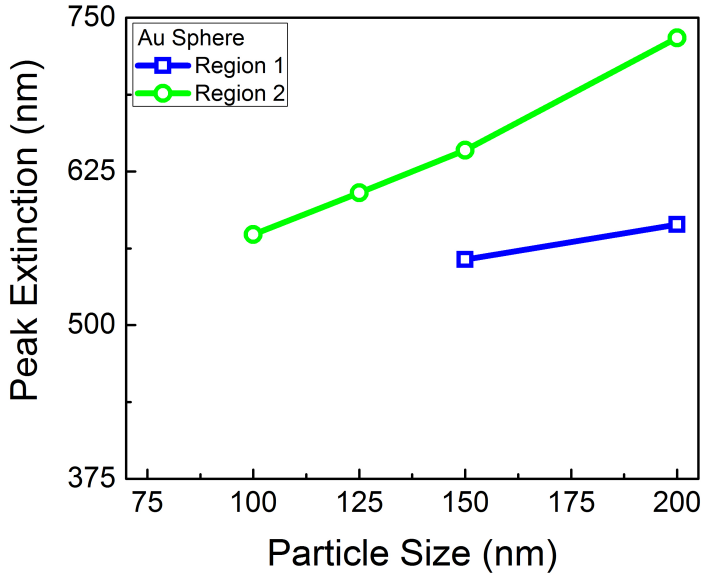

Figure 5.5.2 – Peak extinction wavelength as a function of particle size for spherical gold nanoparticles moving from 75 – 200 *nm* in 25 *nm* intervals.

5.5.1.1 Excitation Enhancement

Once again, the near-field enhancement of the electric field was analysed via a sensor located in the middle of the nano-gap in the $x-y$ plane. $\langle G_{ex} \rangle$ for the nano-gap formed between the continuous gold film and a spherical gold nanoparticle of varying size is shown in Figure 5.5.3.

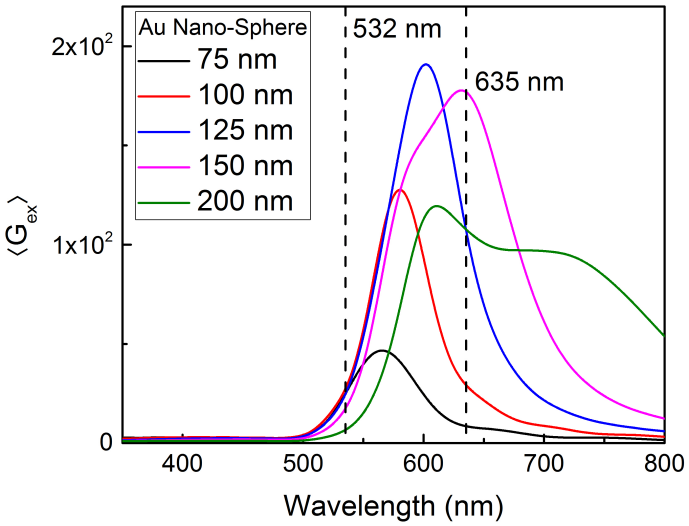

Figure 5.5.3 – $\langle G_{ex} \rangle$ as a function of wavelength for a distribution of spherical gold nanoparticles moving from $75 - 200$ *nm* in diameter in 25 *nm* intervals.

These particles show very little excitation enhancement for the 532 *nm* excitation. In this case, for the gold sphere nano-gap formation, the 150 *nm* diameter spheres produce the maximum excitation enhancement at 635 *nm*. Therefore from a near-field confinement perspective, the 150 *nm* gold particle nano-gap system would appear to be the most suitable for 635 *nm* excitation. To fully classify the system and determine how effectively it scatters light, we investigate the far-field emission enhancement characteristics.

5.5.1.2 Emission Enhancement

Our far-field emission contribution (G_{em}) for these particles is shown in Figure 5.5.4. It shows that as particle size increases the main emission mode of the system red-shifts. There is a peak in emission intensity for the system occurring for the 150 *nm* diameter particle which has a peak intensity at 656 *nm*.

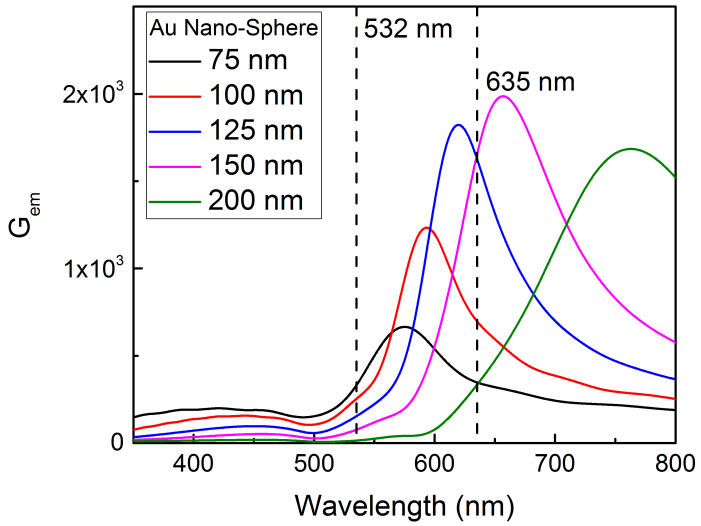

Figure 5.5.4 – G_{em} as a function of wavelength for a distribution of spherical gold nanoparticles moving from $75 - 200$ *nm* in diameter in 25 *nm* intervals.

The information from the far-field correlates closely with the near-field for this system. We see that the optimal G_{em} for SERS is generated from the 150 *nm* diameter particle. This was also seen previously where the highest field intensity in the near-field was associated to the same sized particle. By combining this information and completing the study, we arrive at the FoM for the system.

5.5.1.3 FoM: Gold Nano-Sphere Size Distribution

Taking into consideration the far-field component and combining with the near-field contribution, we can generate a FoM given from equation 5.2.1. The FoM for the nano-gaps formed between a continuous gold surface and a distribution of gold nanoparticle sizes is shown in Figure 5.5.5.

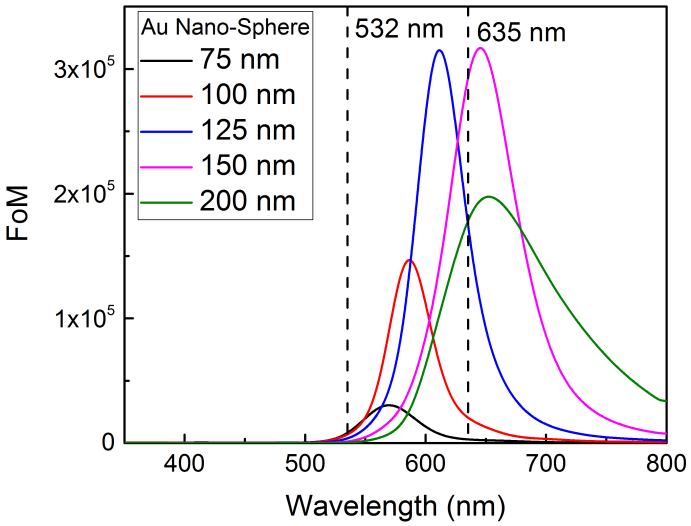

Figure 5.5.5 – FoM for a distribution of spherical gold nanoparticles moving from 75 – 200 *nm* in diameter in 25 *nm* intervals.

We can see that the most prominent mode is attributed to the system using the 150 *nm* gold sphere. This mode is $\sim 2.6\times$ stronger than the peaks generated from the 150 *nm* silver spheres at this wavelength, but it is half as intense as the 150 *nm* silver cubes. It is also very close to the excitation wavelength of our 635 *nm* red laser line peaking at 646 *nm*. However, when comparing to the 518 *nm* mode of the 118 *nm* silver particle, it is considerably weaker with the silver system being $1.74\times$ the intensity. The bandwidths of the 118 *nm* silver spherical particle system FoM and the 150 *nm* gold spherical particle system FoM are relatively comparable at 67.4 *nm* (for the dipolar mode) and 72.3 *nm* respectively.

5.5.2 Gold Nano-Rod

As well as investigations into size distributions of silver and gold nanoparticles, we also investigate gold nano-rods which we have available for experimental SERS measurements. Therefore, we also simulated nano-gaps formed between nano-rods and the metallic film below. The gold nano-rods we have available practically have diameter $d = 50$ *nm* and length $l = 100$ *nm*. As nano-rods are not symmetrical in the x and y axis as seen from previous systems, we investigate calculations from electric field polarised along the trans-

verse and longitudinal axis of the rod. Figure 5.5.6 displays the schematic diagram for how the calculations were performed with the direction of the incoming electric field.

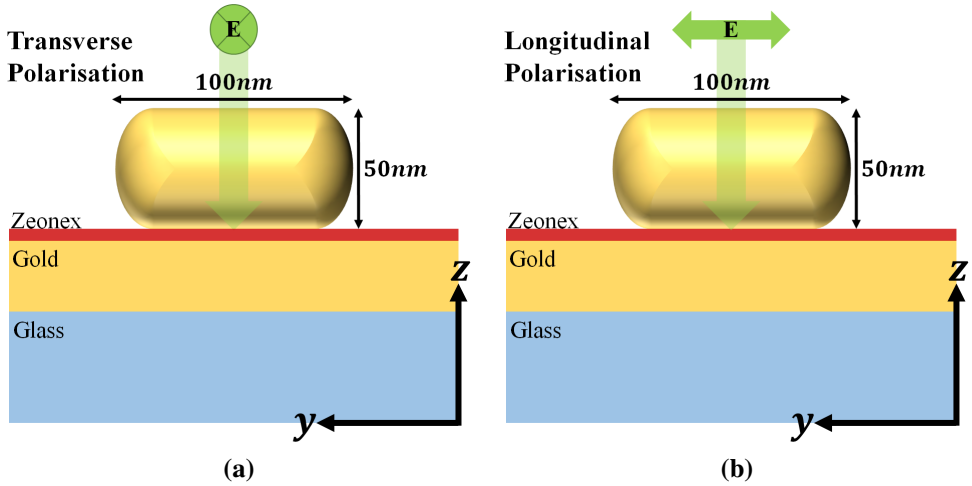

Figure 5.5.6 – Schematic of the nano-gap formed between the gold nano-rod and an extended gold film where the electric field is polarised in (a) the x and (b) the y direction

We can see that the extinction from the system in the two configurations produces different intensity resonances. Figure 5.5.7a and 5.5.7b show the respective extinction spectra for the system when under the influence of transverse and longitudinal excitation respectively. Excitation along the width of the rod yields extinction spectra dominated by absorption whereas excitation polarised along the length of the rod produces an intense mode at 716 *nm*.

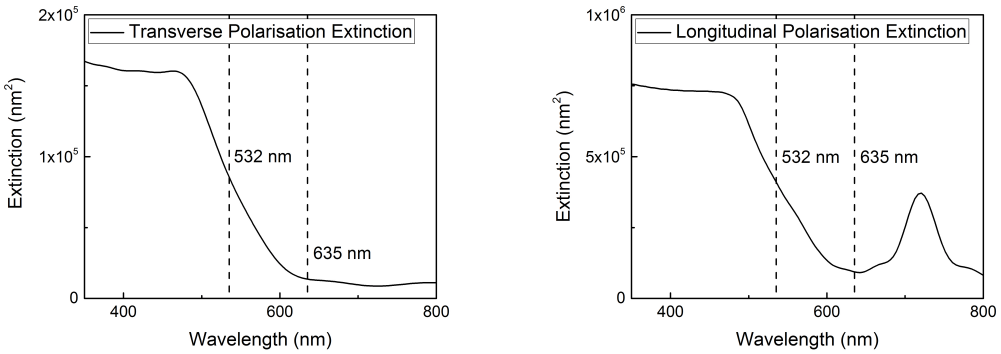

Figure 5.5.7 – Extinction spectrum for gold nano-rod with diameter $d = 50$ *nm* and length $l = 100$ *nm*. Where the electric field is polarised along (a) the transverse and (b) the longitudinal axis.

To fully classify this system, near-field data must be analysed at these extinction max-

ima. Following this, the far-fields need to be calculated for the transverse and longitudinal polarisations.

5.5.2.1 Near-Field Distribution

The near-field is shown for the $x-z$, $y-z$ and from the centre of the nano-gap in the $x-y$ plane for the system. This gives us a full picture of the localisation of fields for the nano-rod. Figure 5.5.9 displays the longitudinal polarised excitation electric field for the system at the 716 *nm* mode (Figures 5.5.8a and 5.5.8b) in both the $x-z$ and $y-z$ plane respectively. We can see from Figure 5.5.8b that when excited at 716 *nm* the field is most intense for the system polarised along the length of the nano-rod.

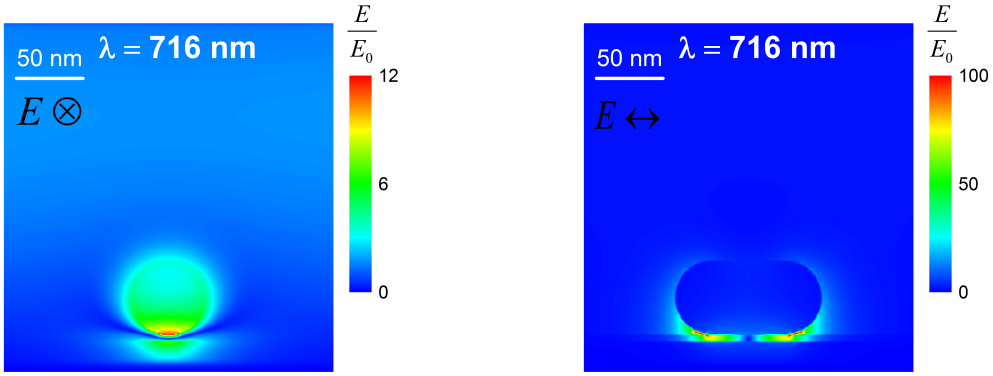

(a) **(b)**

Figure 5.5.8 – Electric field enhancement for longitudinal excitation of the gold nano-rod with diameter $d = 50$ *nm* and length $l = 100$ *nm* taken from (a) the $x-z$ and (b) $y-z$ sensor at the 716 *nm* extinction mode.

This is also confirmed when looking at the hot spots generated in the $x-y$ plane.

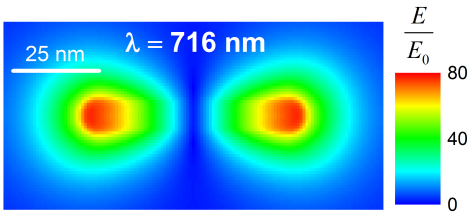

Figure 5.5.9 – Electric field enhancement from the $x-y$ sensor for longitudinal excitation of the gold nano-rod with diameter $d = 50$ *nm* and length $l = 100$ *nm* at the 716 *nm* extinction mode.

5.5.2.2 Excitation Enhancement

When averaging the fields as a function of area under the rod, we show the excitation enhancement $\langle G_{ex} \rangle$ as a function of wavelength. Figures 5.5.10a and 5.5.10b show the excitation enhancement for the transverse and longitudinally polarised light respectively.

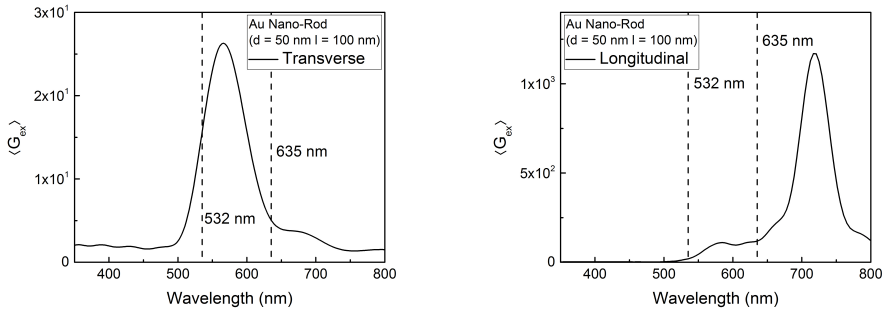

Figure 5.5.10 – $\langle G_{ex} \rangle$ as a function of wavelength for a gold nano-rod with diameter $d = 50$ *nm* and length $l = 100$ *nm*. Where the electric field is polarised along (a) the transverse and (b) the longitudinal axis.

We can see that there are now distinct modes for both the transverse and longitudinal polarisations. Transverse polarisation yields a maximum in the near-field at 566 *nm*, whereas longitudinal polarisation produces a mode at 585 *nm* with an additional maximum field at 718 *nm*. The transverse polarisation overlaps with the 532 *nm* excitation so there is potential for this system to be useful for excitation at this wavelength. This shows the information that is lost when focussing completely on the extinction modes and their associated field enhancements. In order to determine fully if this is the case, we must investigate the far-field distribution.

5.5.2.3 Emission Enhancement

The emission enhancement reveals that there is a shift in the resonant mode for the transverse polarisation. The near-field is centred at 566 *nm* whereas the far-field shifts to 572 *nm*, this is important as it becomes less beneficial for the 532 *nm* line. Also, in comparison to the 118 *nm* silver nano-sphere which also peaks close to the 532 *nm* line, we observe that these rods are 5$\times$ less effective at scattering to the far-field.

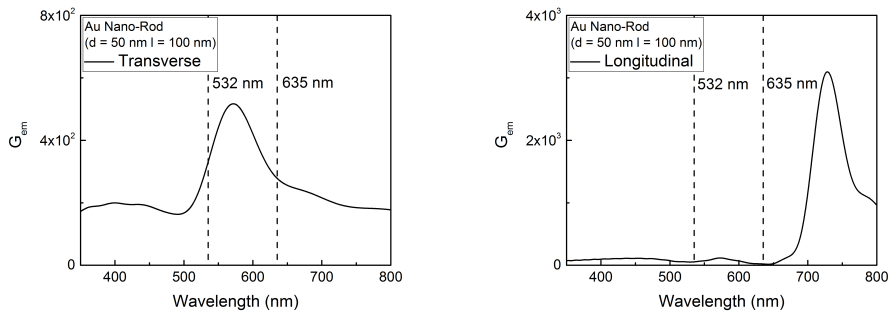

(a) **(b)**

Figure 5.5.11 – G_{em} as a function of wavelength for a gold nano-rod with diameter $d = 50$ *nm* and length $l = 100$ *nm*. Where the electric field is polarised along (a) the transverse and (b) the longitudinal axis.

The longitudinal polarisation is also red-shifted to 729 *nm* approaching the near-infrared making it less favourable for our 635 *nm* excitation. We can see the emission enhancement as a function of wavelength and angle for the transverse and longitudinal polarisation excitation in Figure 5.5.12.

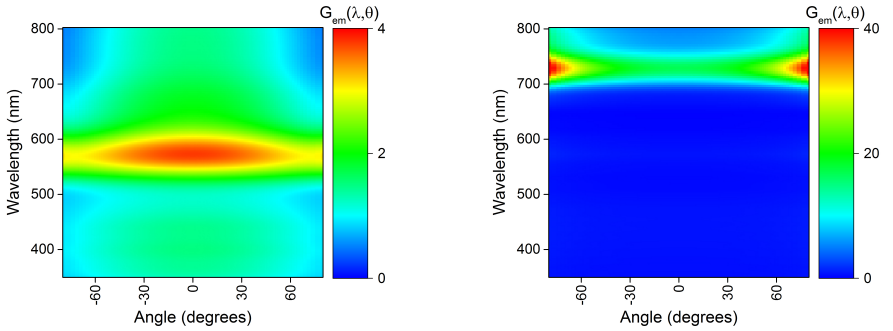

(a) **(b)**

Figure 5.5.12 – G_{em} as a function of wavelength and scattering angle for a gold nano-rod with diameter $d = 50$ *nm* and length $l = 100$ *nm*. Where the electric field is polarised along (a) the transverse and (b) the longitudinal axis.

In terms of directionality, we can see that although the transverse polarisation is weaker, it does scatter to the far-field within a $\pm 50^{\circ}$ cone of collection. Whereas, for the longitudinal polarisation, the highest regions of emission enhancement intensity are mainly found at the larger scattering angles.

5.5.2.4 FoM: Gold Nano-Rod

To quantify this data fully, we use equation 5.2.1 to combine the near-field enhancement with the far-field distribution of the system for both polarisations discussed previously. Figure 5.5.13 shows the field maps for the two polarisations as a function of wavelength and angle. In this configuration, we can see that the FoM for the transverse polarisation displayed in Figure 5.5.13b scatters most intensely normal to the surface of the substrate, dissipating towards larger scattering angles. Whereas, when dealing with the light polarised along the length of the nanoparticle in the y plane shown in Figure 5.5.13a, we observe higher intensity at the larger scattering angles, where 0 is normal to the substrate surface and $\pm 90^{\circ}$ is parallel.

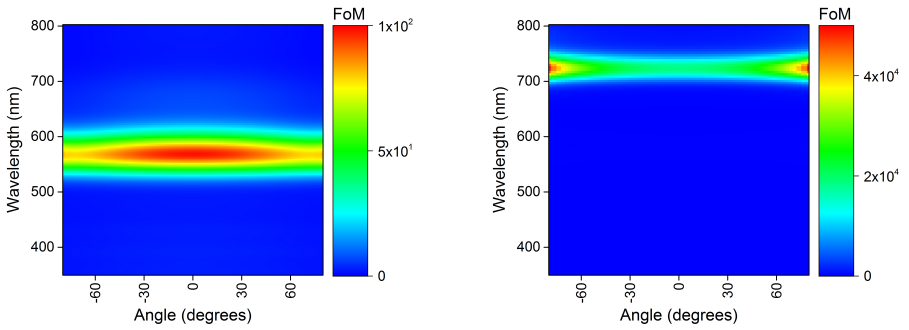

Figure 5.5.13 – FoM for a distribution of a gold nano-rod with diameter $d = 50$ *nm* and length $l = 100$ *nm*. Where the electric field is polarised along (a) the transverse and (b) the longitudinal axis.

This is a result of the far-field emission enhancement distribution for this system. To take this into consideration, the final FoM for the nano-rods has both the sum of the field maps across all angles representing Numerical Aperture $NA = 1$. As well as the sum of the angles collected from a lens with $NA = 0.55$, which will be available to us in our experimental setup for SERS. This data shown in Figure 5.5.14 will be represented by the black and red lines plotted for the FoM respectively.

We can see in Figure 5.5.14a for transverse polarisation, the FoM peaks at 569 *nm*. Whereas, in Figure 5.5.14b for longitudinally polarised light, the peak modes occur at 576 *nm* and 724 *nm* respectively. The FoM acquired via transverse polarised excitation

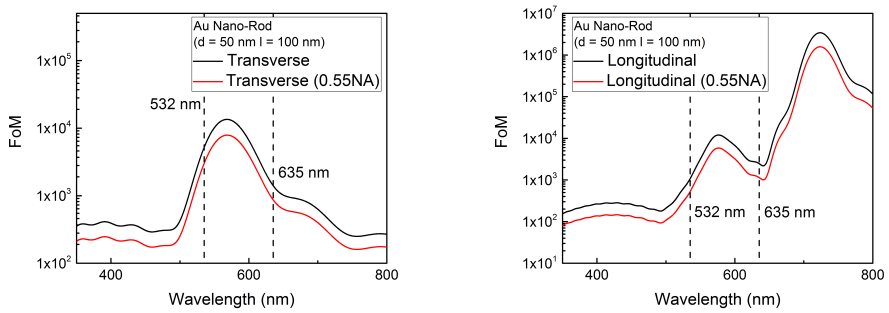

(a) **(b)**

Figure 5.5.14 – FoM for a distribution of a gold nano-rod with diameter $d = 50$ *nm* and length $l = 100$ *nm*. Where the electric field is polarised along (a) the transverse and (b) the longitudinal axis. The difference between $NA = 1$ (black line) and $NA = 0.55$ (red line) is also shown in each case.

is $5.76\times$ more intense at 532 *nm* than the longitudinal polarisation so therefore possess more potential for resonant excitation under the influence of 532 *nm* light. We can see that due to the directionality of the system when comparing the $NA = 1$ to the $NA = 0.55$ for each polarisation, the transverse polarisation loses 42% of its intensity whereas the longitudinal polarisation loses 49% due to the highest FoM intensities occurring at the larger scattering angles.

Although this system has a peak mode overlapping with the 532 *nm* laser line, when in comparison to the silver nano-spheres, the FoM is $\sim 121\times$ weaker. Therefore, for our investigations from an experimental perspective, it would be more beneficial to use silver structures as our main Raman line is centred at 532 *nm*.

This study thoroughly investigates nano-gaps formed between nano-spheres, cubes and rods and a metallic film below, analysing the behaviour in the near as well as the far-field. Doing so has allowed us to establish the ideal working conditions for excitation and generation of surface plasmons in each case. We have performed an in depth analysis to the size dependencies of each system demonstrating the tunable wavelength properties the nano-gap is capable of, as well as determining which system would be suitable for our work. We have found that the silver nano-spheres possess the ideal properties for SERS measurements under the influence of 532 *nm* excitation. In order to corroborate our findings, we switch from the TFSF plane wave excitation to a Gaussian source to

provide a more realistic excitation profile which will allow an *NA* to be defined for the source.

5.6 Gaussian Source: More Realistic Excitation

Contrary to the TFSF source which is limited to a wave injected from a single planar direction, the Gaussian source is composed of many plane waves to produce a Gaussian beam profile. The beam is focused to a specific region of the device and an *NA* can be defined. These simulations use $NA = 0.55$ which is identical to the objective we use in our practical setup, therefore giving more realistic scattering properties. The source positioned above the structure has its focal point at the centre of the 5 *nm* cavity. This was the most beneficial approach as the target material would be ideally contained within the cavity and excited directly by the laser setup.

We performed calculations from three particle sizes, the 118 *nm* silver particle, as well as 60 and 200 *nm* particle cavity systems (owing to the fact that these sizes are commercially available), to demonstrate the size dependency with regards to the near-field excitation and far-field emission enhancement.

5.6.1 Absorption, Scattering and Extinction

Using Gaussian source excitation; absorption, scattering and extinction cross sections were measured for each particle size. The characteristic two region curve can be seen again from the 118 *nm* particle nano-gap system in Figure 5.6.1. This was demonstrated previously with the TFSF source.

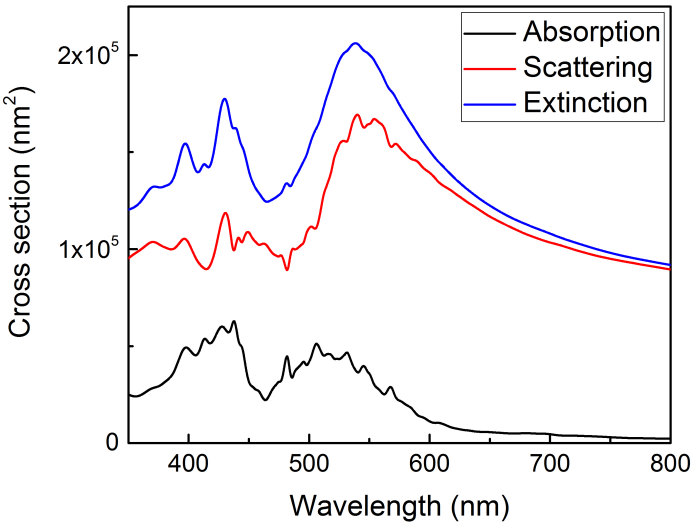

Figure 5.6.1 – Absorption, scattering and extinction cross section from the 5 *nm* cavity using 118 *nm* particle diameter under Gaussian illumination.

In this case however, the 415 *nm* and 523 *nm* peaks from the 118 *nm* particle system have shifted to 430 *nm* and 543 *nm* respectively. This is most likely due to the system coupling to more modes due to the nature of the Gaussian source [93].

5.6.2 Near-Field Distribution

Here, the near-field calculations were performed for the 60, 118 and 200 *nm* particle sizes to show where the areas of high intensity field would be localised. We can see that for the $x-z$ components higher localisation is again found to be given at shorter wavelength excitation. The field for the 430 *nm* excitation would be $\sim 3\times$ larger than that of the 543 *nm* excitation and more confined. We can also see that the higher confinement of shorter wavelength excitation generates the smaller hot spots with larger electric field.

For the 60 *nm* particle, the extinction peaks are very broad and essentially the same as the system in absence of the nanoparticle. The near-field intensity was extracted at 393 *nm* and 430 *nm* for its extinction maxima and is shown in Figure 5.6.2.

There is extremely high field enhancement localisation associated with the extinction maxima for the 60 *nm* particle. We also see confined regions of higher intensity field for the 118 *nm* particle cavity system from the 430 *nm* excitation relative to the 543 *nm*

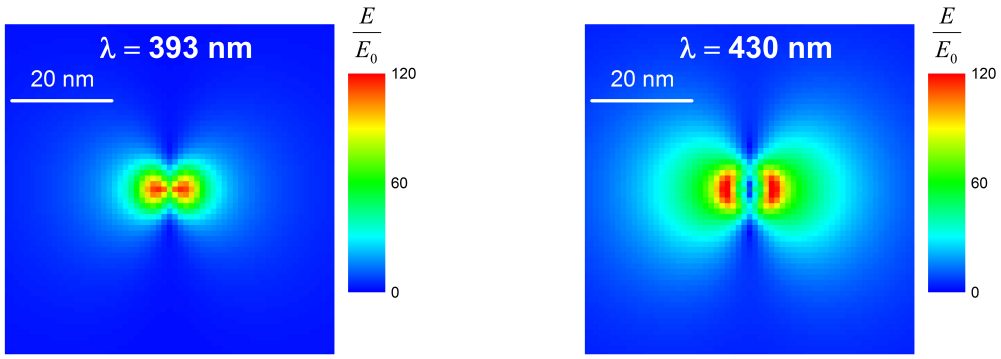

(a) **(b)**

Figure 5.6.2 – Electric field distribution for the system in the $x-y$ plane taken from the centre of the nano-gap at (a) 393 *nm* and (b) 430 *nm* for the 60 *nm* particle cavity system.

excitation in Figure 5.6.3.

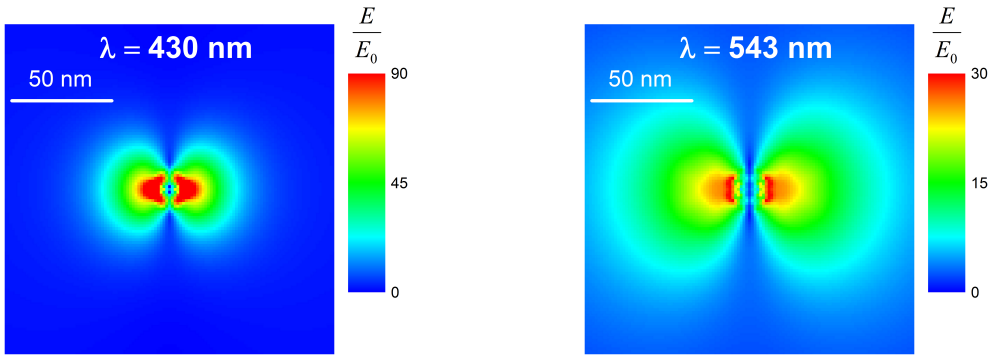

(a) **(b)**

Figure 5.6.3 – Electric field distribution for the system in the $x-y$ plane taken from the centre of the nano-gap at (a) 430 *nm* and (b) 543 *nm* for the 118 *nm* particle cavity system.

We now observe strong coupling between the particle and the film below. This system demonstrates the two regions associated with the strong coupling due to the nano-gap. The field from the quadrupolar mode is around 3 times more intense than that generated from the dipolar mode. Finally, the 200 *nm* system generates the fields shown in Figure 5.6.4 at its respective extinction peaks.

We can see that in this case the field intensities in region 1 and region 2 are weaker than what we see from the 118 *nm* particle system. Therefore, when considering the near-field at the extinction peaks for these gaps, the smaller particle sizes generate the larger field enhancements.

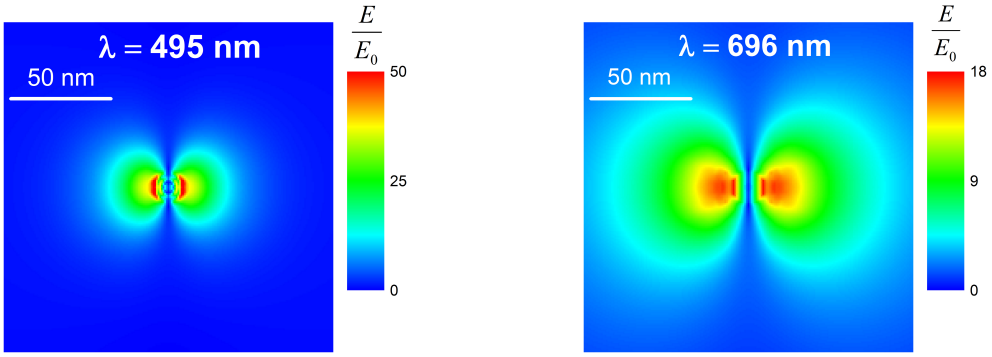

(a) **(b)**

Figure 5.6.4 – Electric field distribution for the system in the $x-y$ plane taken from the centre of the nano-gap at (a) 495 *nm* and (b) 696 *nm* for the 200 *nm* particle cavity system.

We can then extract the excitation enhancement for these nano-gap systems using the same method as we did for the TFSF calculations.

5.6.3 Excitation Enhancement

By averaging the fields across all the sensors located at the centre of the nano-gap in the $x-y$ plane, we obtain Figure 5.6.5.

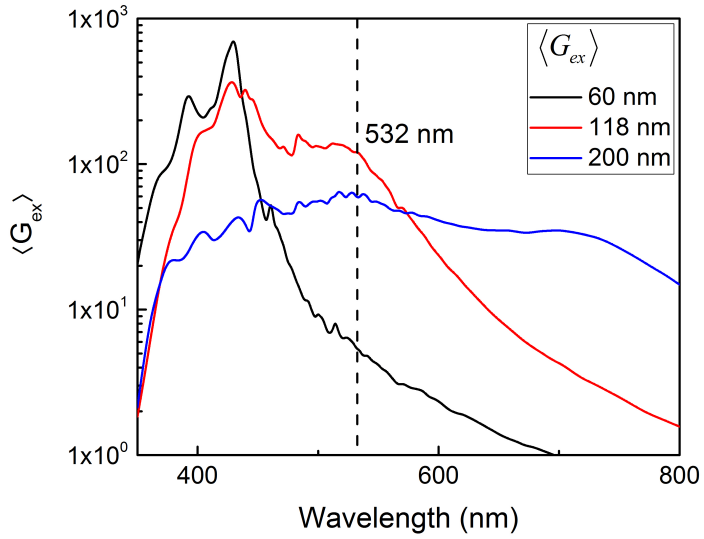

Figure 5.6.5 – $\langle G_{ex} \rangle$ as a function of wavelength for nano-gaps formed between 60 *nm*, 118 *nm* and 200 *nm* spherical silver nanoparticles and an extended silver film under Gaussian excitation.

This shows that the 60 *nm* particle generates a larger excitation enhancement at the

shorter wavelengths in the near-field. At 532 *nm*, the 118 *nm* particle nano-gap system generates 2.02× the excitation enhancement as the 200 *nm* particle and 24.02× that of the 60 *nm* particle gap geometry. We can see the two regions which represent the dipolar and quadrupolar modes of the system more clearly with much higher field intensities shown for the higher frequencies. This would give the impression that the field is more favourably excited from shorter wavelengths in the region of 430 *nm* but this investigation has so far only considered the field in the local sense i.e. the near-field. Further examination is required to determine how the generated Raman signal is scattered to the far-field.

5.6.4 Far-Field Emission Enhancement Contribution to SERS signal

After investigating the near-field behaviour of the system, we now look to the emission enhancement of the generated Raman signal in the gap to the far-field. We calculated the far-field profile from the centre of the cavity in the $x-y$ plane projected from the same monitor used to calculate $\langle G_{ex} \rangle$. This is because the Raman signal would radiate from the target material located at this position in experimental circumstances. The angular dependency of the far-field shows how the generated Raman signal is scattered to the far-field.

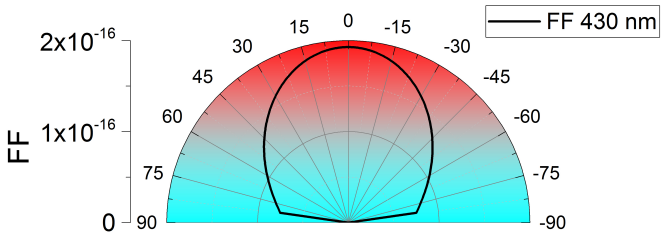

(a)

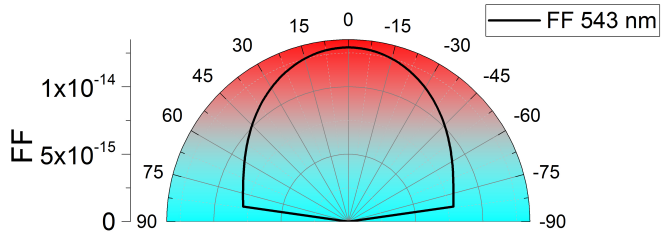

(b)

Figure 5.6.6 – Far-field angular dependence for (a) 430 *nm* and (b) 543 *nm* emission wavelengths.

Figure 5.6.6 shows the difference in the far-field distribution for peak emission wavelengths of the 118 *nm* particle nano-gap structure. We can see in Figures 5.6.6a and 5.6.6b that there is a stark difference for far-field emission of the 430 *nm* and 543 *nm* mode for the 118 *nm* system with a difference of two orders of magnitude.

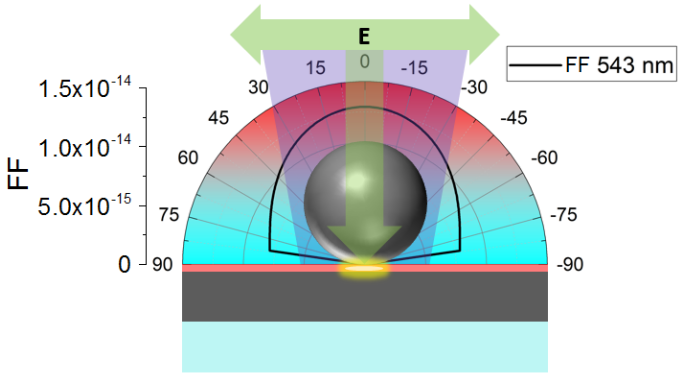

Figure 5.6.7 – Far-field angular distribution with cone of collection overlaid considering an $NA = 0.55$ objective lens.

Clearly, from a practical standpoint the Raman photons scattered from the longer wavelength emission will be done so more efficiently to the far-field, whereas with the higher energy emission more will be lost due to internal processes. Therefore, despite having a larger enhancement in the near-field, the quadrupolar mode is far less effective than the dipolar mode when considering the far-field emission. We also observe in Figure 5.6.7, that the far-field from this system is moderately directional, with the majority of the far-field profile residing within our cone of collection represented by the purple region. This region highlights a 33.37° light cone which is equivalent to an objective lens collecting at $NA = 0.55$. Therefore, our system could collect the majority of the emitted light from this geometry.

To make sense of the practicality of the nano-gap geometry, it is important to plot the emission diagram of the system. First, we can extract the far-field reference for a simulation region containing no structure i.e a perfect vacuum as a reference. Then by performing the same calculation for the nano-gap structure and dividing them by this reference, we obtain the far-field emission as a function of angle across all wavelengths. The emission enhancement (G_{em}) of the system is therefore given from equation 2.7.3. This is shown in Figures 5.6.8, 5.6.9 and 5.6.10. for a 60 *nm*, 118 *nm* and 200 *nm* particle

system respectively.

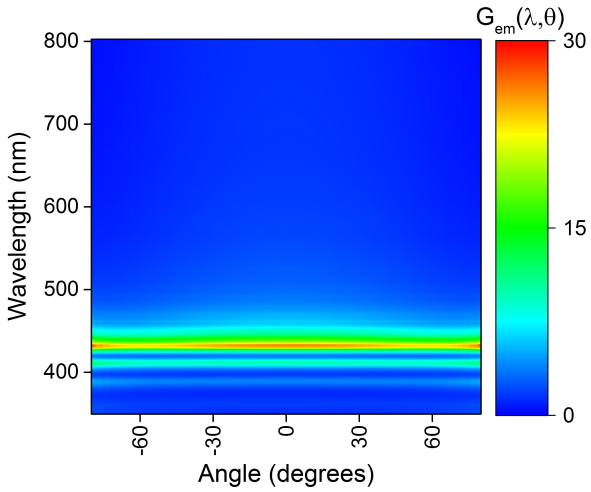

Figure 5.6.8 – Emission enhancement for the system with angular dependence as a function of wavelength normalised to the reference simulation for the 60 *nm* particle system.

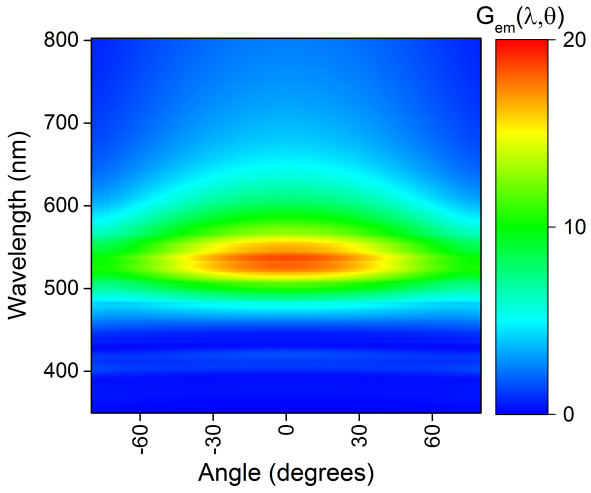

Figure 5.6.9 – Emission enhancement for the system with angular dependence as a function of wavelength normalised to the reference simulation for the 118 *nm* particle system.

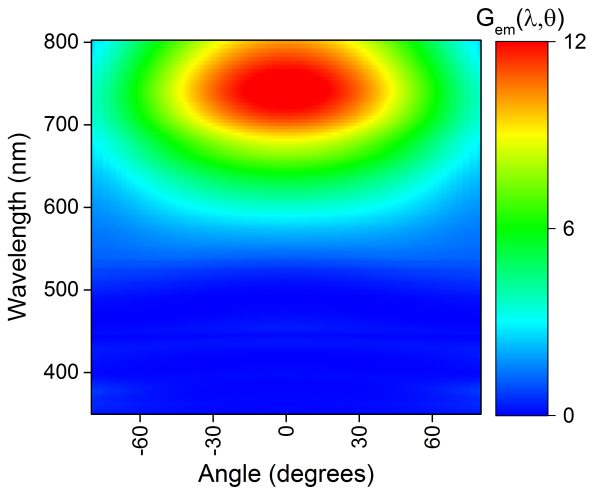

Figure 5.6.10 – Emission enhancement for the system with angular dependence as a function of wavelength normalised to the reference simulation for the 200 *nm* particle system.

In terms of intensity, the 60 *nm* shows to have the largest emission enhancement, however the distribution is spread over all angles and therefore making it less directional than the larger particles.

For the 118 *nm* particle system, G_{em} shows that the high intensity mode at 430 *nm* is weak due to Ohmic losses by the metal [167]. However, the 543 *nm* mode in region 2 yields excellent antenna-like properties scattering within the cone of collection of the $0-30^{\circ}$ half angle region, with 0° representing normal incidence to the structure. This is well within the parameters of our practical setup which utilises a $50\times$ magnification objective lens with $NA = 0.55$, which corresponds to a collection half angle of 33.37°.

Finally, the 200 *nm* particle is the most directional in the far-field emission enhancement but in this case the emission enhancement intensity is sacrificed.

Taking the sum of this data now across all angles gives the emission enhancement as a function of wavelength, and shows how each particle system behaves when scattering light, shown in Figure 5.6.11.

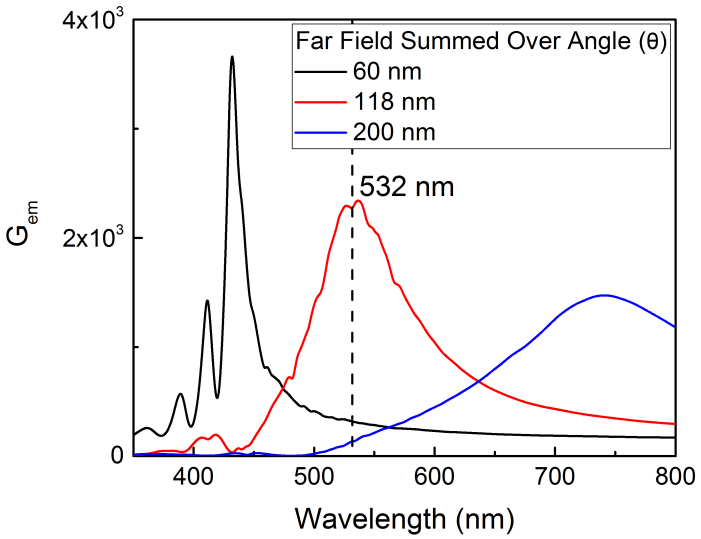

Figure 5.6.11 – Sum of normalised emission enhancement for the cavity systems across all angles (a) 60 *nm* (b) 118 *nm* and (c) 200 *nm* particle nano-gap systems.

The data shows that the emission enhancement is most intense for the 60 *nm* silver nano-sphere. As the particle size increases, the modes broaden and decrease in intensity. The signal transmitted to the far-field is most intense at 532 *nm* for the mid sized nano-particles. Whereas, the 200 *nm* spheres are most suitable for the larger wavelength regions approaching the near-IR. To evaluate the near-field excitation and far-field emission, we combine the two into our FoM and analyse the effectiveness of these systems for SERS.

5.6.5 Figure of Merit

By combining the data from the near-field excitation and far-field emission, we can use equation 5.2.1 to define the SERS enhancement for each system and characterise the ideal excitation wavelength in each case.

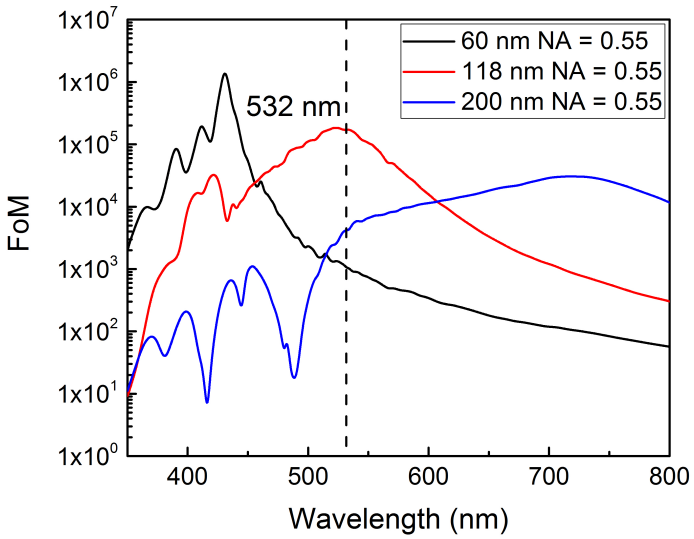

Figure 5.6.12 – Figure of merits for each sized particle nano-gap system considering the angles collected from an $NA = 0.55$ objective lens.

Figure 5.6.12 gives us the FoM for all three particle sizes. This data tells us that when taking into consideration all factors, nano-gaps formed between a particle on a film system can effectively be tuned to an excitation wavelength of choice. However, due to the properties of the excitation and emission enhancement of such structures we see that choosing the correct excitation wavelength becomes more complicated than looking at the hybridised extinction modes or the highest region of field intensity in the near-field. We can see in Figure 5.6.13 that for the 118 *nm* particle the most intense region of the FoM peaks closest to our 532 *nm* laser line.

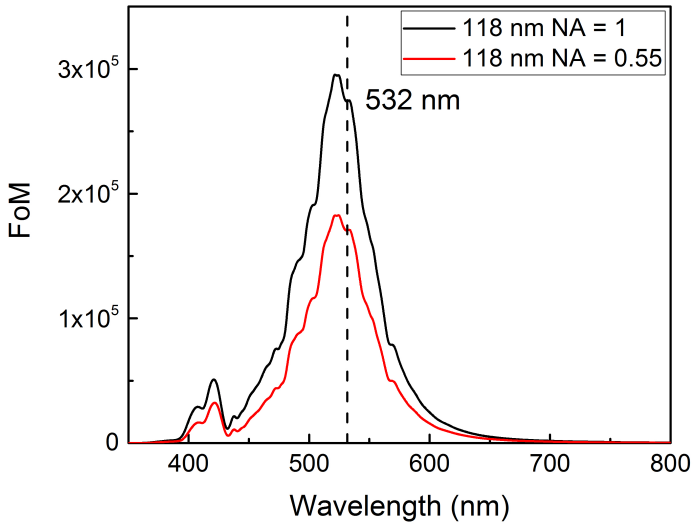

Figure 5.6.13 – Figure of merit for the 118 *nm* particle nano-gap system showing the difference between $NA = 1$ (black line) and $NA = 0.55$ (red line).

The graph in Figure 5.6.13 uses equation 5.2.1 to give the FoM for the 118 *nm* particle system. We can see the difference from collecting with an objective of $NA = 0.55$ and $NA = 1$ from the red and black lines respectively by integrating G_{em} over these angles. The FoM tells us that when using the 118 *nm* particle, the ideal excitation is from a 532 *nm* laser line. The 200 *nm* particle produces less signal, however functions relatively well when approaching the near-infrared region. Smaller particles such as the 60 *nm* shown here produce intense peaks in the blue region of the spectrum but perform the worst for our 532 *nm* laser line. The nano-gap formed between the 118 *nm* silver nano-sphere and the extended silver film produces 40.99$\times$ the enhancement relative to the 200 *nm* sphere system, and 162.48$\times$ that what we observe from the 60 *nm* particle system.

Although the 60 *nm* particle seems to produce the largest FoM when excited at its peak wavelength, when considering the data in terms of the output with respect to Raman shift, we produce the graph shown in Figure 5.6.14.

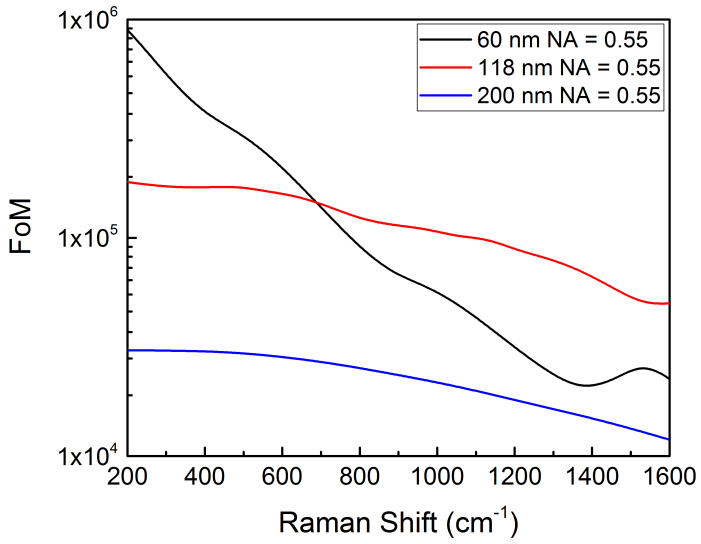

Figure 5.6.14 – FoM plotted as a function of wavenumber for the 60, 118 and 200 *nm* silver nano-particle nano-gap systems, considering the angles collected from an $NA = 0.55$ objective lens.

We can see that although the 60 *nm* particle has a more intense FoM, in terms of Raman shift it will only enhance the lower wavenumbers of the Raman spectra. When compared to the 118 *nm* particle nano-gap system we can see that there is a more stable enhancement produced from this across the entirety of the spectrum. Therefore, smaller particles are less likely to benefit Raman enhancement.

5.7 Summary

Overall, this work gives a complete picture of the system behaviour and demonstrates the characteristics of the nano-gap with a clear systematic approach to its field enhancement and emission properties. We can see the tunability of the system in this configuration as well as the extreme confinement of light the structure is capable of. By fully investigating the excitation and emission enhancement, we are able to determine the optimal wavelength of Raman excitation which will yield us the best photon output within the visible regime. We can say from this study, that simply investigating the extinction spectrum or the near-field confinement is not conclusive for determining the ideal SERS enhancement of the system. Our study has investigated a range of nanoparticle sizes and shapes

from both gold and silver to determine the ideal characteristics of near-field excitation enhancement and far-field emission enhancement to be used in SERS experiments. By investigating these structures through FDTD calculations, we have formulated the ideal working conditions for SERS.

Our FDTD modelling showed that the SERS signal from the investigated nano-gaps is strongly dependent on the particle size and choice of excitation wavelength. This behaviour is attributed to the complex interplay between the near-field excitation enhancement, and the far-field emission enhancement for various particle size nano-gaps. We have performed an in depth analysis to the size dependencies of each system, demonstrating the tunable wavelength properties the nano-gap is capable of, as well as determining which system would be suitable for our work. Using our FoM, we have simulated the resonant properties of each nano-gap. Our findings show that the 118 *nm* silver nano-sphere nano-gap possesses the ideal properties for SERS measurements under the influence of 532 *nm* excitation.

Not only did we investigate nano-gaps from plane wave excitation but we also provided further evidence of our claims by studying the effects of using a Gaussian source excitation. The Gaussian beam functions differently to the TFSF source used in the preliminary calculations, where TFSF uses a single plane wave from one plane injection axis the Gaussian beam gives a more realistic excitation profile. The Gaussian source can also be focused to a specific region of the device and an *NA* can be defined. These simulations use $NA = 0.55$ which is more representative of practical SERS measurements. The Gaussian source excitation revealed that the 118 *nm* silver nanoparticle system produces the highest intensity FoM at the 532 *nm* laser line. Therefore, we can conclude that of the systems we have studied, this optimised structure is theoretically most capable to produce the maximum signal for SERS measurements. The information obtained from this chapter will be applied practically to our subsequent experimental chapters, where nano-gaps are used to probe materials at low concentrations via Raman spectroscopy.

Chapter 6

Plasmonic Nano-gaps for Single-Molecule SERS

This chapter deals with experimental methodology for detection of trace substances using SERS. We utilise the plasmonic nano-gap formed between a metallic nanoparticle and an extended metal film below. In Chapter 5, comprehensive 3*D* FDTD calculations were performed to explore the near-field and far-field behaviour of the nano-gaps. We investigated the effect of changing the particle size and shape, as well as the materials used for both the particle and the film below. We also altered the thickness of the nano-gap as well as the film below and discussed the effects of changing these parameters. Using the information obtained from these calculations, we refined the characteristics of the plasmonic cavity for use with 532 *nm* excitation as this laser line is available to us practically. This chapter aims to investigate through SERS experiments the effect of changing the nanoparticle shape, size and materials in order to design a cavity structure capable of single molecule detection. From this investigation, we will discuss the relative enhancement from each plasmonic structure and its effectiveness at SERS detection comparing where possible to the theoretical study. We show through practical experimentation that our structure is capable of detection of common Raman probes, Rhodamine 6G (R6G) and Crystal Violet (CV), when approaching the single molecule level. We define the single molecule SERS (SM-SERS) characteristics in this study by the observation of orientational effects attributed to the enhancement of specific Raman modes due to the

alignment of molecular dipoles with the cavity dipole moment.

6.1 SERS from Nano-Gaps Using Different Shaped Silver Nanoparticles

Practical investigations of the nanostructure geometry support the simulation data and theoretical investigations from Chapter 5. We can provide spectroscopic information for a fluorescent SERS probe, in this case R6G, for different cavity systems formed between the nanoparticle and the metallic film below it with varying particle sizes and shape. To analyse these spectra, we average SERS data from many nano-gaps formed between each particle size. By doing so, we eliminate any variation in the SERS signal intensity. Any fluctuations in enhancement can be attributed to variance in particle size, molecular position in the cavity relative to the hot spot as well as the number of molecules in each particular cavity. This is due to the low concentration of the Raman probe within the gap and the manufacturing process. Because of this, the distribution of the analytes is not guaranteed to be uniform. Throughout the course of these investigations, the metal film below the cavity is fixed at 100 *nm* and the nano-gap is a constant 5 *nm*.

By using these dyes with our 532 *nm* excitation source, we take advantage of Surface Enhanced Resonance Raman or SERRS. The excitation wavelength coincides with the electronic transition of the Raman probe. This means that SERRS could be exploited to further enhance the radiated light by exciting electrons near the electronic transition of the molecule of interest [112, 168]. This allows maximum enhancement to take place and increases the possibility of SM-SERS to occur.

There was slight variations in the nanoparticle sizes when observed via SEM. The size distribution of a sample of the 100 *nm* silver nano-spheres is shown in Figure 6.1.1.

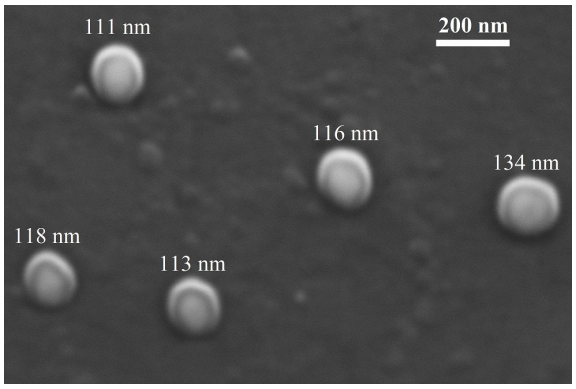

Figure 6.1.1 – SEM image of silver nanoparticles on the substrate with an average diameter of 118 *nm*.

The average size from this sample is shown to be 118 *nm*. We have used the average size throughout our simulations to allow for enhancement comparisons with our experimental work.

6.1.1 SERS from Silver Nano-Sphere Size Study

To start with, simple particle radius changes for silver nanoparticles are used to produce spectra from R6G at $2 \times 10^{-6}\ M$. At this concentration, the cavity effect was evident and the enhancement of the Raman probe from the nano-gap was measurable relative to the system in absence of the particle. Figure 6.1.2 shows Raman spectra of varied intensities for the nano-gaps formed between silver spheres and the 100 *nm* silver layer below.

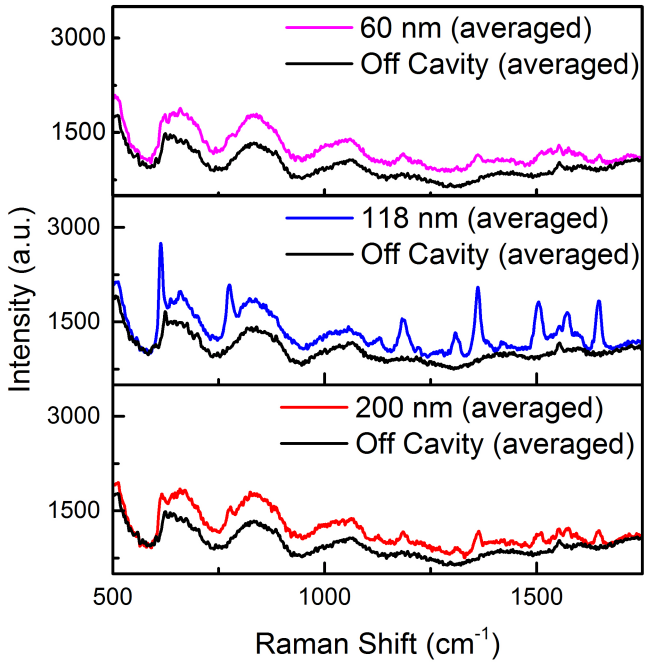

Figure 6.1.2 – SERS spectra measured from a 5 *nm* nano-gap doped with the molecular dye R6G at a concentration of 2×10^{-6} *M*. In a nano-gap formed between a 60 *nm* silver particle and a 100 *nm* thick silver film, a nano-gap formed between a 118 *nm* silver particle and a 100 *nm* thick silver film, and a nano-gap formed between a 200 *nm* silver particle and a 100 *nm* thick silver film. For comparison, we also plot the measured SERS from off nano-gap regions. SERS measurements used 3 *s* collection time from 532 *nm* excitation with a slit width of 0.1 *mm*.

We performed our Raman measurements on systems with particle sizes used in the theoretical Gaussian study in section 5.6. Where, a comprehensive study of the extinction profiles as well as the near and far-field electric field coupling effects of 60, 118 and 200 *nm* particle cavity-systems were compared to one another. We can see the 118 *nm* particle nano-gap system produces large enhancements relative to the other particle sizes. This follows a close agreement with our simulation results which demonstrated that the 118 *nm* silver system to be well optimised for a 532 *nm* excitation. In order to demonstrate the power of the cavity system, the enhancement of the nano-gap formed between the 118 *nm* silver sphere and the 100 *nm* silver film below it was measured and compared to the the system with no nanoparticle as well as the with no fluorescent material all shown in Figure 6.1.3.

From this, we notice a huge signal intensity dependence on this system. The fluores-

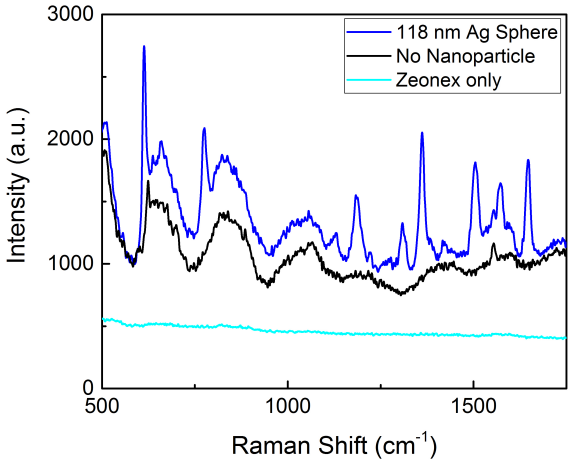

Figure 6.1.3 – Raman spectra from the 118 *nm* silver nanoparticle cavity system at $2 \times 10^{-6} M$ concentration as well as a comparison without the nanoparticle and a cavity without the fluorescent material.

cent dye on its own is practically undetectable, but by confining the electric field with our plasmonic nano-gap, we enhance the signal and produce a Raman spectra with defined peaks.

This data shows a distinct comparison to our theoretical work, there is a likeness to our FoM (see Figure 5.6.12 section 5.6.5), where our simulations suggested an enhancement of $40.99\times$ between the 118 *nm* and 200 *nm* FoM and a much larger difference of $162.48\times$ between the 118 *nm* and 60 *nm* particles at 532 *nm* excitation. Experimentally, by using the data in Figure 6.1.2, we are able to quantify the relative enhancement of the most prominent peaks in the spectra.

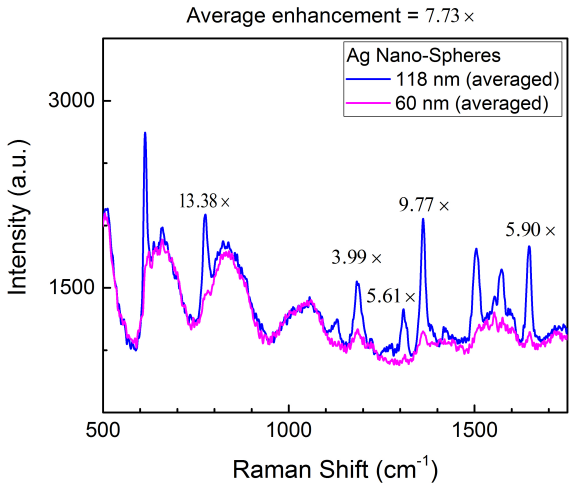

(a)

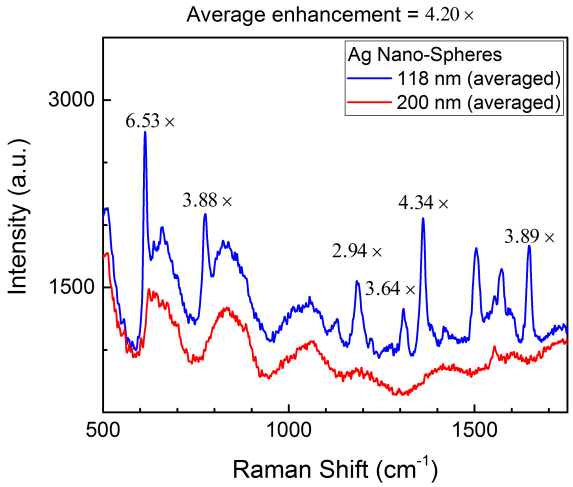

(b)

Figure 6.1.4 – A comparison of SERS spectra measured from a 5 *nm* nano-gap doped with the molecular dye R6G at a concentration of 2×10^{-6} *M*. We show spectra from a nano-gap formed between (a) 60 *nm*, and (b) 200 *nm* silver nano-spheres and a 100 *nm* thick silver film. As a comparison, we quantify the relative enhancement at the Raman modes considered in relation to the nano-gap formed between the 118 *nm* spherical system and an extended silver film. SERS measurements used 3 *s* collection time from 532 *nm* excitation with a slit width of 0.1 *mm*.

Figure 6.1.4a shows that the 118 *nm* system on average produces enhancement of $\sim 7.73\times$ the signal compared to the 60 *nm* particle on a metallic film geometry. Whereas, for the larger particle nano-gap system, Figure 6.1.4b shows that the 118 *nm* system on average produces enhancement of $4.2\times$ the signal in comparison to the 200 *nm* particle nano-gap plasmonic structure.

6.1.2 Relative Enhancement of the Spherical Silver Particle Nano-Gaps

To quantify the enhancement from each nano-gap, we take the relative enhancement from each system when used to detect R6G at low concentration. Figure 6.1.5 shows the relative enhancement the 118 *nm* particle nano-gap system is capable of, relative to the nano-gaps using the 60 *nm* and 200 *nm* particles.

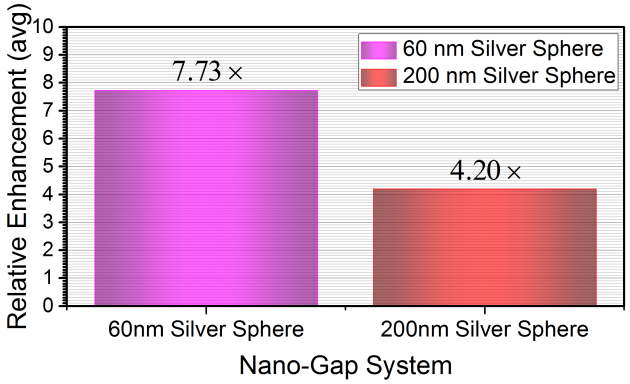

Figure 6.1.5 – The relative enhancement of the nano-gap systems from averaged SERS spectra measured from a 5 *nm* nano-gap doped with the molecular dye R6G at a concentration of 2×10^{-6} *M*. The enhancement is quantified from Raman modes in the spectra and averaged relative to the same modes from the strongest scattering system. In this case, the nano-gap formed between the 118 *nm* silver particle and the silver film below.

By taking the average of the relative enhancement from the most prominent peaks in the SERS spectra, we average this data and determine the relative enhancement for these systems in comparison to the 118 *nm* cavity structure. The 200 *nm* system is closest in intensity to the 118 *nm* particle, having a quarter of the relative enhancement of our optimised plasmonic device. The 60 *nm* silver sphere system is notably weaker than the 118 *nm* particle cavity as predicted in our calculations, the relative enhancement is shown to be 7.73× for the 118 *nm* compared to the smaller sphere.

As a comparison, we can see in Figure 6.1.6 the relative enhancement of the FoM for the FDTD calculations performed using a Gaussian beam excitation on nano-gaps formed between the silver nanoparticles and an extended silver film.

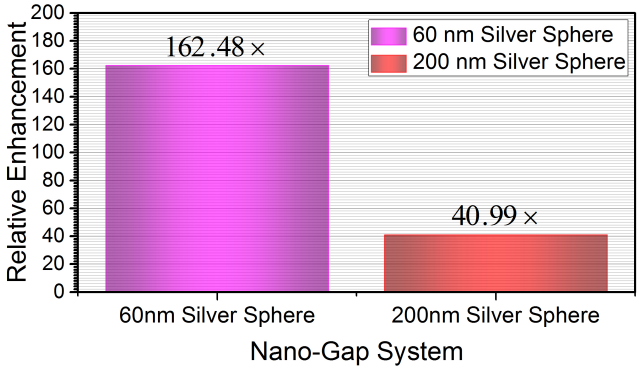

Figure 6.1.6 – The relative enhancement of the nano-gap system's FDTD calculations using Gaussian source excitation at 532 *nm*. The structures consisted of a 5 *nm* nano-gap formed between spherical silver nanoparticles of specified size and an extended 100 *nm* thick silver film. The enhancement is shown relative to the strongest scattering system, in this case, the nano-gap formed between the 118 *nm* silver particle and the silver film below.

Although the simulation data predicts much larger relative enhancement between each system, the trend of the data is very similar. We can see the correlation in the relative enhancements and that the 200 *nm* nanoparticles in both the simulated and experimental results produce more enhancement than the 60 *nm* particle system. The difference in intensities is attributed to the difficulties when working with practical substrates. The simulations use a perfectly flat silver substrate with spherical particles, under practical circumstances there are effects such as surface roughness and oxidisation, which reduce the intensity of the signal. Surface roughness can cause unexpected enhancement due to surface plasmons coupling to the film directly. Also, due to the distribution of nanoparticle sizes, it is likely that 532 *nm* excitation will not always coincide with the resonant mode of the system. As well as these factors, the background signal associated with the Raman spectra makes quantifying relative enhancement levels problematic.

6.2 SERS from Nano-Gaps Using Different Shaped Gold Nanoparticles

To complete our study of different particle geometry for nano-gaps, we also invest-

igated systems with nano-gaps formed between gold nanoparticles and a 100 *nm* gold film below. We used the same fabrications methods as with the silver structures and illuminated individual particles with 532 *nm* excitation to obtain SERS spectra from these nano-gaps. We acquired spectra from a number of nano-gaps and averaged the SERS spectra for each system, from this, we are able to compare the intensity of the Raman modes to determine the relative enhancement. By averaging the SERS spectra, we are able to eliminate the variation caused by deviation in particle size, molecular position in the cavity relative to the hot spot as well as the number of molecules in each particular cavity. This is important because at low concentration of the Raman probe within the gap and due to the manufacturing process, the distribution of the analytes is not guaranteed to be uniform.

6.2.1 SERS from Gold Nano-Sphere Size Study

The gold nano-spheres produced very little SERS scattering, this is predicted in our theoretical chapter. Figure 6.2.1 shows the Raman spectra from averaged measurements from a nano-gap formed between a 100 *nm* diameter gold sphere and a metallic film as well as a 250 *nm* diameter spherical particle and the gold film.

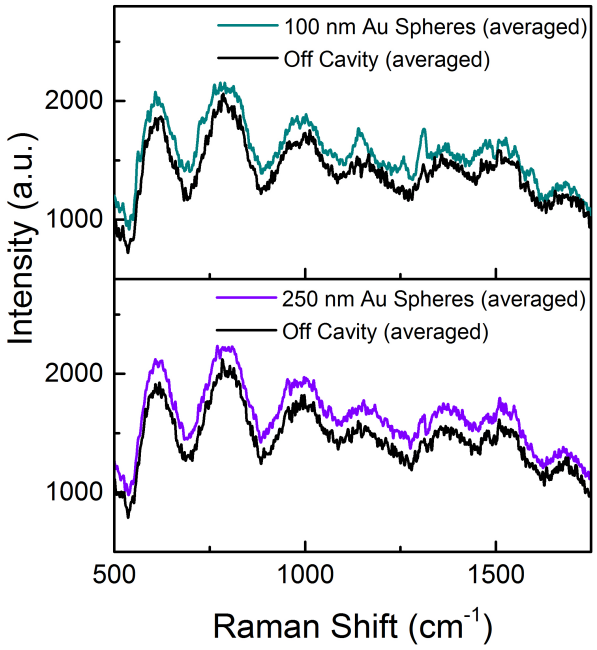

Figure 6.2.1 – SERS spectra measured from a 5 *nm* nano-gap doped with the molecular dye R6G at a concentration of 2×10^{-6} *M*. In a nano-gap formed between a 100 *nm* gold particle and a 100 *nm* thick gold film as well as a nano-gap formed between a 250 *nm* gold particle and a 100 *nm* thick gold film. For comparison, we also plot the measured SERS from off nano-gap regions.

The spectra from these systems revealed very little if any enhancement relative to the film in absence of the particles. This information correlates well with our simulation data which showed the FoM for gold systems to peak in the red region of the spectrum. Therefore, we can conclude that these systems are unsuitable for 532 *nm* excitation.

6.2.2 SERS from Gold Nano-Rods

As well as this particle size sweep for gold systems, we explored more exotic geometry in the form of nano-rods with $d = 50$ *nm* and $l = 100$ *nm*, where d and l represent the rod's diameter and length. Figure 6.2.2 shows the averaged Raman spectra from nano-gaps formed between these gold rods and a metallic film below. Also included is the TEM image of the gold nano-rods.

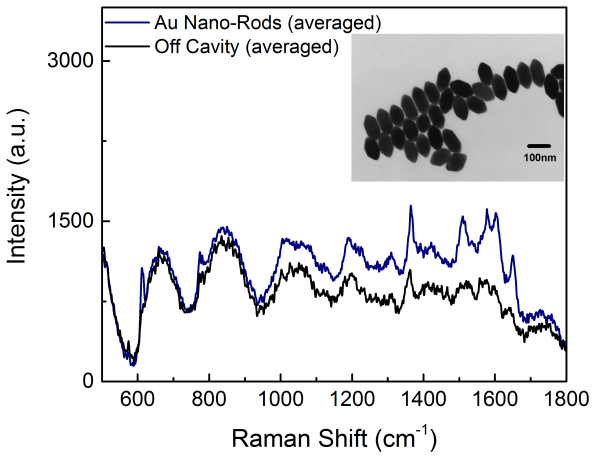

Figure 6.2.2 – SERS spectra measured from a 5*nm* nano-gap doped with the molecular dye R6G at a concentration of $2 \times 10^{-6}\,M$. In a nano-gap formed between gold nano-rods with $d = 50\ nm$ and $l = 100\ nm$, where d and l represent the rod's diameter and length and a 100 *nm* thick silver film. For comparison, we also plot the measured SERS from off nano-gap regions [169].

We can see that these nano-rods produce decent enhancement characteristics for the nano-gaps. It is shown that for the 1364 cm^{-1} mode, the relative enhancement on a nano-gap as opposed to simply on the film is 1.55×. Although this is not expected when solely considering the extinction in our theoretical study which shows no maxima at 532 *nm*, we do show that the far-field emission enhancement, and hence the FoM for the nano-rod in the case of transverse polarised light across the width of the nano-rod produces enhancement in this region. This enhancement is most likely due to the mode from light having electric field polarised along the widths of the particles. For our work, we do not align the polarisation with the rod in any specific direction, therefore we partially benefit from this effect.

Overall, the data shows the nano-gap is capable of good enhancement of the electric field. This study emphasises that choosing the correct size and shape nanoparticle is integral to maximising the SERS signal from these plasmonic structures. We have shown that the 118 *nm* particle nano-gap system is the optimal device for SERS detection for 532 *nm* excitation of the structures that we studied both theoretically and experimentally. Therefore, we can use this structure to investigate the limits of its detection and demonstrate single molecule SERS from fluorescent materials.

6.3 Single Molecule SERS

Now that the design of the structure has been refined and shown to consistently produce enhancement of SERS signal, further investigations take place via material analysis of fluorescent dyes approaching the single molecule level. Single Molecule SERS or SM-SERS is defined in this scenario by the rotational properties of the material within the gap.

In this section, we aim to measure Raman signal from our most optimal nano-gap, the 5 *nm* gap between a 118 *nm* silver sphere and an extended 100 *nm* thick silver film, at concentrations sufficiently low such that SM-SERS is observed. We measure SERS from two Raman probes, R6G and CV. To define the full spectrum, measurements were first taken at 5×10^{-5} M. These high concentration samples would allow the entire spectrum to be observed due to the random orientation properties of the molecules within the film. Then, for comparison, we show three typical single molecule SERS spectra for each material recorded from three different nano-gaps at 2×10^{-7} M. The results in this investigation analyse R6G and CV both separately as well as in a mixture at significantly low concentrations.

6.3.1 Defining the Single Molecule Regime

At high concentrations, the alignment of the transition dipole moment with respect to the local enhanced field averages to 1 as a contribution from many molecules within the cavity. This leads to the full fingerprint spectrum of the material being observed. However, upon entering the single molecule regime, certain orientations of the molecule will correspond to alignment of the molecular bonds with the cavity field. We can see the difference between two cavities with different concentrations of a Raman probe in Figure 6.3.1.

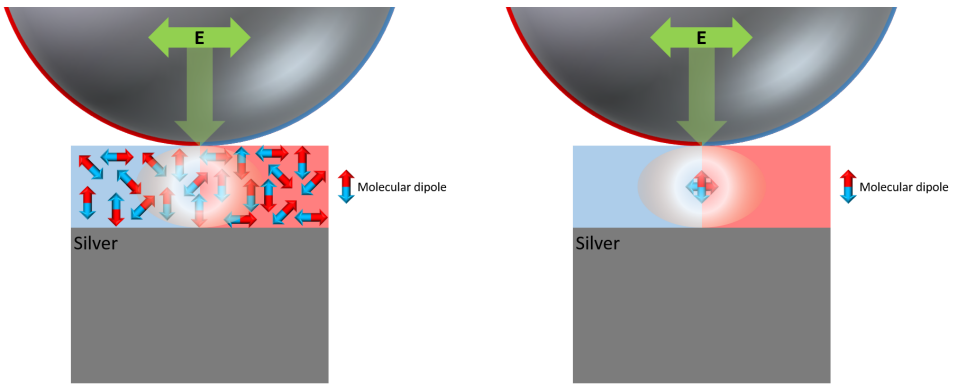

Figure 6.3.1 – Diagram of the orientation dependency of the molecule within the nano-gap. The red and blue regions highlight the positive and negative regions of the charge distribution of the system based on the dipolar mode. A simplified example of a molecular dipole is represented by double ended arrow.

Figure 6.3.1a represents the cavity at higher concentration, whereas 6.3.1b is more representative of the single molecule regime. In Figure 6.3.1a, the contribution of the Raman signal will stem from many molecules randomly oriented within the cavity. Therefore, in this case the entire Raman spectrum will be observable for the probe. However, in the case of Figure 6.3.1b only one molecule occupies the hot spot generated between the particle and the film below, so the Raman spectrum originates from this molecule alone. Hence, at this concentration the molecular orientation will become a factor of what modes in the Raman spectrum are enhanced. Bonds aligned with the field of the nano-gap will be enhanced more effectively than bonds that are perpendicular. As Raman signal is produced from the shift in frequency from scattered photons from molecular vibrations between the bonds of the molecule, this alignment is an effective way to determine when concentrations reach the single molecule regime.

Verification of SM-SERS can also be categorised by the bi-analyte [120], or isotopologue method [64]. Where, for each approach, observations of two target analytes are seen at low concentrations and preferential observation of either analyte in any given measurement is indicative of the statistical probability of a SM-SERS event. Isotopologues are preferably used in this type of study as they have identical Raman cross sections and surface binding affinities to the plasmonic structures [170]. We discuss these methods in

more detail in Chapter 3.

6.3.2 SM-SERS: Rhodamine 6G

The Raman active modes for R6G were identified at 5×10^{-5} M, this concentration was gradually reduced and single molecule activity was observed at 2×10^{-7} M. When working on the practical devices to produce single molecule behaviour, concentrations of the targets were gradually reduced until the spectra showed distinctive qualities from each cavity. Figure 6.3.2 shows that at higher concentrations all of the material's peaks which correspond to its subsequent vibrational mode in the molecule's geometry are visible.

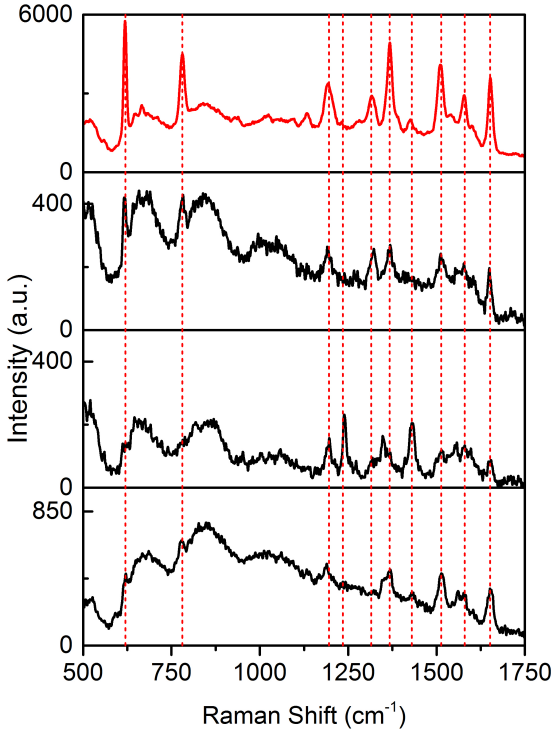

Figure 6.3.2 – Raman spectra from 5×10^{-5} M (red line) and 2×10^{-7} M from 3 nanoparticle cavity system examples (black lines) where all modes are highlighted from the higher concentration spectrum.

When concentrations are higher, there are many molecules varying in orientation within the gap, leading to the full fingerprint spectrum of the material. However, when concentrations reach 2×10^{-7} M, the molecules are at sufficiently low concentrations such that Raman spectra from these nanoparticle systems yield specific modes from the material under investigation. Therefore, reason suggests that the molecules in the gap in these instances are solitary, showing specific rotation of the molecules dipoles in align-

ment with the dipole moment of the plasmonic structures geometry.

We can see more clearly over a specific Raman shift region that certain vibrational modes are present in one low concentration nano-cavity system, which are subsequently absent in the next. Figure 6.3.3 shows specific regions of the spectra where peaks are enhanced or missing due to the orientational effect of the system.

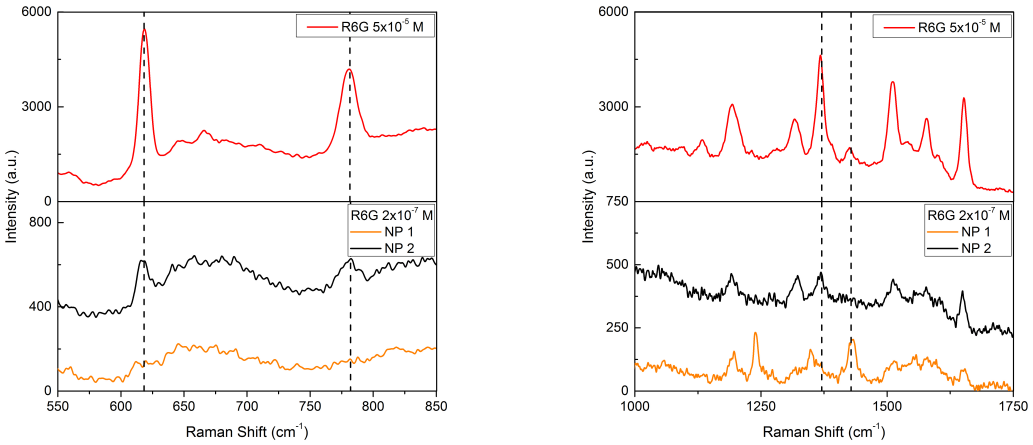

Figure 6.3.3 – Specific region for the R6G Raman spectra for the high (5×10^{-5} M) and low concentration (2×10^{-7} M) mixture with the relevant peaks highlighted with dashed lines.

At concentration of 2×10^{-7} M, we can see differences in the relative intensities of the SERS peaks between the spectra in the bottom 3 panels with the higher concentration sample suggesting that we are in the single molecule regime with changes in the molecular orientation from one gap to another. For example, the two peak intensities between $600 - 800$ cm^{-1} which correspond to the C-C-C ring in-plane bending mode and C-H out-of-plane bending mode respectively have completely diminished in panel 3, whereas its modes in the longer Raman shift region are still present [171].

It should also be mentioned that Density Functional Theory (DFT) calculations allow recovery of the orientation of individual molecules within the gap. This work has been carried out for these structures and can be read in further detail elsewhere [2].

6.3.3 Successive Measurements on the Same Nano-Gap

To show the system did not photo-bleach the analyte, and that the measurements were repeatable with no blinking of modes, measurements were taken from a sample with a 3 second time interval of collection and a cool down period between each measurement of the same time frame. In Figure 6.3.4, we show that the Raman peaks are stable throughout, therefore the structure is purely enhancing the electromagnetic effect from SERS and chemical enhancement is negligible.

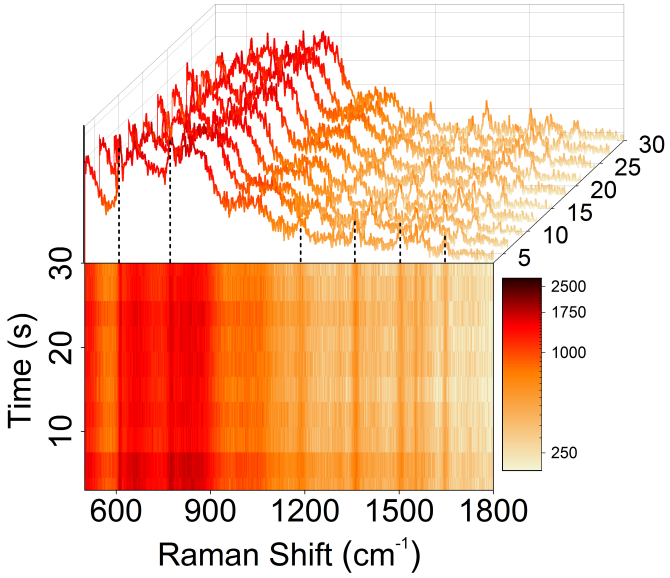

Figure 6.3.4 – 10 time dependent single molecule SERS spectra (accumulation time 3 *s*, total time 30 *s*).

Ten measurements were taken from a single particle cavity system and a heat map was plotted to compare the relative intensity of each Raman mode throughout the data collection. The Raman spectra for the R6G is overlaid above the heat map to indicate where the peaks are shown. The observed differences in the relative intensities of the SERS peaks from one molecule to another cannot be attributed to Raman photo-bleaching or due to blinking as a result of photo-induced chemical process in the close proximity of the metal surface [36, 72]. Therefore, orientation dependence is evident from nanoparticle to nanoparticle.

6.3.4 SM-SERS: Crystal Violet

To provide further evidence that this structure is capable of producing SM-SERS, we re-iterate the same conditions for the previous single molecule work with a different Raman probe. Figure 6.3.5 shows the full spectrum of CV at 6×10^{-5} M, as well as three spectra from different nano-gaps at 2.5×10^{-7} M).

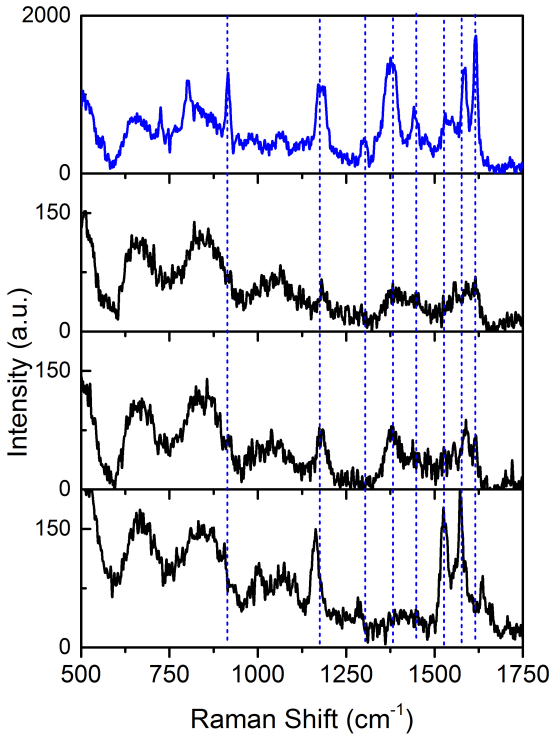

Figure 6.3.5 – Raman spectra from 6×10^{-5} M (blue line) and 2.5×10^{-7} M from 3 nanoparticle cavity system examples (black lines) where all modes are highlighted from the higher concentration.

In this case, a comparison of SERS spectra from CV at 2 different concentrations (6×10^{-5} M and 2.5×10^{-7} M) were measured from different nano-gaps using a particle size of 118 nm. At a high concentration of 6×10^{-5} M, the SERS signal shows the expected Raman signal of CV, corresponding to the averaging of the analyte orientation in the nano-gap. At the low concentration of 2.5×10^{-7} M however, differences in the relative intensities of the SERS peaks can be observed between spectra, suggesting the single molecule regime with changes in the molecular orientation from one gap to another.

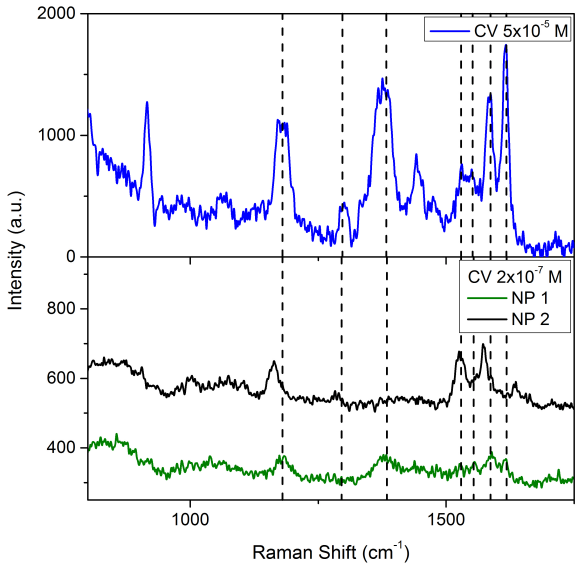

Figure 6.3.6 – Specific region for the Raman spectra of CV for the high (5×10^{-5} M) and low concentration (2×10^{-7} M) mixture with the relevant peaks highlighted with dashed lines.

The 1370 cm^{-1} mode, assigned to the ϕ-C-ϕ (where ϕ is a phenyl group) or C-N asymmetric stretch present in one low concentration spectra is absent in the other [69]. We also see that the 1290 cm^{-1} and 1530 cm^{-1} peaks, which are Raman modes associated with CV, are visible in the first spectra but not visible in the second [69].

Thus, orientational effects for SM-SERS are shown individually for both R6G and CV in Figure 6.3.2 and Figure 6.3.5 respectively.

6.3.5 SM-SERS: Rhodamine 6G and Crystal Violet Mixture

To conclude the study, and to show the fidelity of detection via Raman spectroscopy, we show the two materials in a mixture in our nano-gap at the concentration single molecule characteristics took place previously. Due to the defined modes of the Raman spectra we can see in Figure 6.3.7, the peaks from Raman spectra are shown to have such high resolution that the materials are distinguishable from one another.

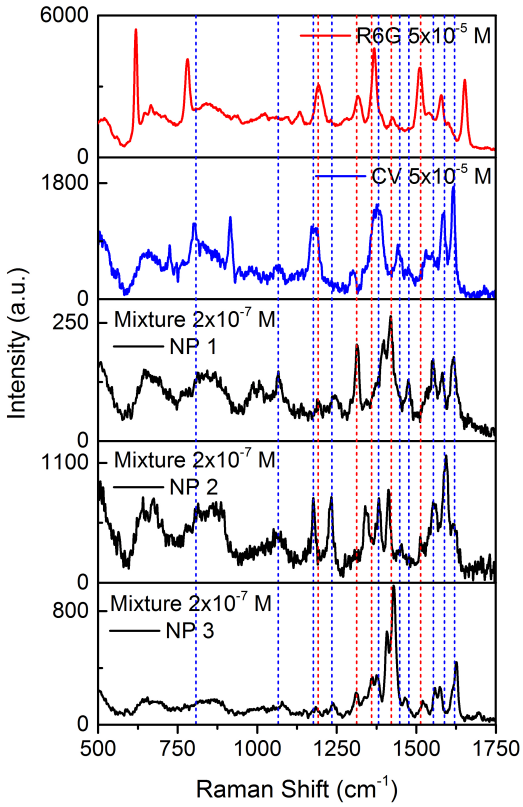

Figure 6.3.7 – Raman spectra from R6G at 5×10^{-5} M and CV at 6×10^{-5} M (red and blue lines). As well as mixtures of the two dyes at low concentration, 2×10^{-7} M for R6G and 2.5×10^{-7} M for CV, from 3 nanoparticle cavity systems (black lines). Where all modes are highlighted from the higher concentration and colour coded to the specific dye molecule, i.e. red dashed lines for R6G and blue dashed lines corresponding to CV.

By using red and blue dashed lines, the modes associated with either R6G or CV are identified. The Raman spectra in Figure 6.3.7 is then shown more accurately in Figure 6.3.8 for R6G, CV and the mixture of the two respectively.

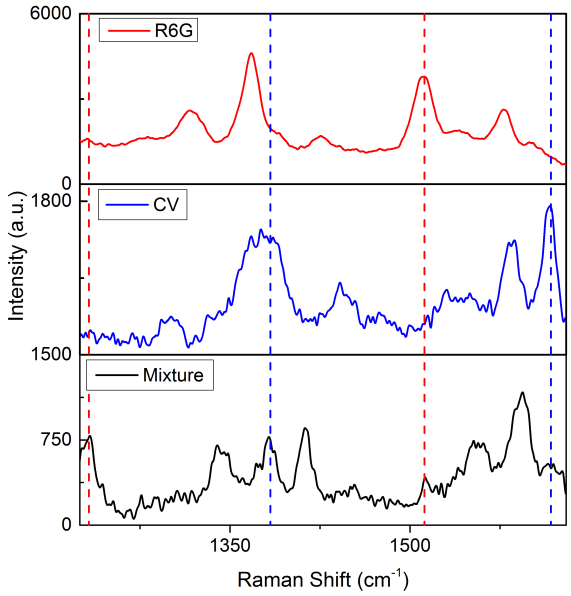

Figure 6.3.8 – Specific region for the Raman spectra for the high concentration samples (5×10^{-5} M for R6G and 6×10^{-5} M for CV), and the low concentration (2×10^{-7} M for R6G and 2.5×10^{-7} M for CV) mixture. The relevant peaks corresponding to each molecule are highlighted with red dashed lines for R6G and blue dashed lines corresponding to CV.

We can see the modes attributed to R6G at 1230 cm^{-1} for the C-O-C stretching, and 1512 cm^{-1} for the aromatic C-C stretching. Furthermore, a doublet mode appears around 1370 cm^{-1} which can be seen in both the CV and R6G for aromatic C-C stretching. Also, for CV we observe a Raman band at 1616 cm^{-1}. Each peak in Figure 6.3.7 is labelled with a colour coded line corresponding to the material it is from, red for R6G and blue for CV.

6.4 Summary

In summary, this chapter has shown the importance of using the correct nano-structure with the resonant incident wavelength excitation. Our particle size study showed that the optimal nano-gap for 532 *nm* excitation is the nano-gap formed between the spherical silver 118 *nm* particle and an extended silver film with thickness 100 *nm*. This system was shown to enhance the Raman signal by at least 4.2×, and up to 7.73× relative to the other structures. When compared to our simulation results for the same structures excited

with a Gaussian source with $NA = 0.55$, we showed the information collected from the Raman study correlated well with the theoretical data.

The research has shown evidence to support single molecule behaviour of target analytes within a nano-gap plasmonic structure, where SERS measurements taken from individual nanoparticle sites exhibited peaks from different Raman modes. The fidelity and precision of the Raman spectral information enabled the distinction of more than one analyte within the target area at low enough concentrations, such that single molecule effects would be shown. The project holds a wealth of applications to material analysis as well as biosensing. Along with this, the study shows the importance of using FDTD simulation environments for optimisation of plasmonic devices and how they can be used to engineer the ideal circumstances for enhancement of light and optical phenomena.

Chapter 7

SM-SERS from Conjugated Polymers

Conjugated polymers are of significant interest in the fields of optics with functionality extending to light emitting diodes [103], photovoltaics [104] and even bio-sensing [105]. Work in this field has shown that it is possible to detect signal from single chains of the polymers using fluorescence and Raman spectroscopy [172, 173]. However, little work has been carried out for investigations into these materials at the single molecule level using SERS with plasmonic nano-gaps. Their interest stems from their processability characteristics and their ability to form solution based optical devices [102].

In this chapter, we define single molecule behavioural characteristics differently to that seen in previous chapters. Previously, we showed orientational effects from the molecule suspended within the nano-gap and its influence on the Raman peaks aligned with the dipole of the system. In this study, we examine a conjugated polymer at low concentrations defining the single molecule regime by the intensity ***blinking*** effect. When concentrations of analytes become sufficiently low such that scattered signal is attributed to single molecules intensity blinking occurs, this is a characteristic effect for SM-SERS when chemical enhancement takes place. Intensity blinking is seen from Raman modes at ultra-low concentrations where the peak intensity becomes unstable [36]. By taking Raman spectra from our samples at decreasing concentration, we are able to detect poly(9,9´-dioctylfluorene-co-bis-N,N´-(4-butylphenyl)-bis-N,N´- phenyl-1,4-phenylenediamine) otherwise known as F8-PFB ($\sim 355,000\ g/mol$), down to the single molecule level.

The source of these fluctuations is not fully understood but explanations suggest it to be a result of a number of physical and chemical processes such as molecular movement or thermal diffusion in and out of the hot spot, photo-ionisation from charge transfer states, or changes to the substrate morphology [72]. During our concentration study of F8-PFB, we were able to observe intensity blinking from the 1605 cm^{-1} Raman mode. Between

concentrations of 2.8×10^{-9} M and 2.8×10^{-10} M intensity blinking clarified the system was within the single molecule regime.

The nano-gaps used throughout the single molecule detection of fluorescent dyes are designed to eliminate the chemical enhancement effects by being suspended in a polymer matrix. We showed with consecutive measurements that there would be continuous signal intensity thus showing that chemical effects were eliminated. However, in this case, the polymer forms its own nano-gap between the silver surface and the metallic particle, so there is no matrix material forming a barrier between the target analyte and the metallic nanostructure. Therefore, chemical enhancement effects can take place [36, 72, 73].

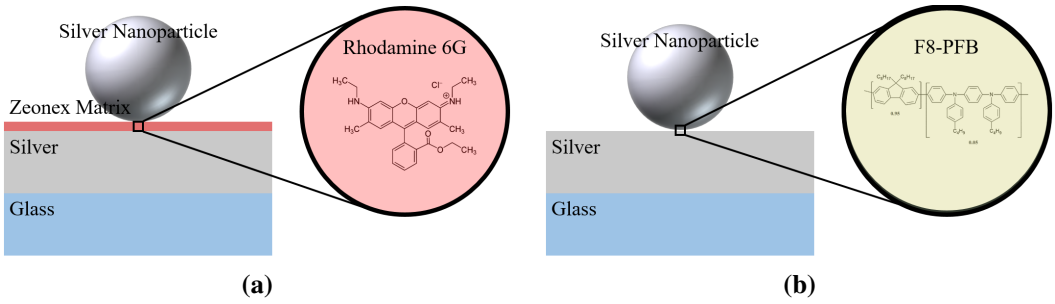

Figure 7.0.1 – Nano-gap alterations between (a) the fluorescent dyes and (b) the conjugated polymer. In the case of the polymer, no secondary polymer matrix is used to suspend the material, therefore the analyte is in direct contact with the nanostructure.

Chemical enhancement can contribute an additional $10^1 - 10^2\times$ enhancement in electron rich molecules where analytes adsorbed to the surface of the SERS active site develop a charge transfer complex, the excitation radiation in this case generates an electron-hole pair and charge is transferred between the metal and analyte through the bond generated between them [71]. Additionally, the new nano-gap design in this study results in the molecule residing in much higher field enhancement region because the gap-width is smaller. This increase in near-field enhancement is shown in section 7.2.

Another important difference to the previous experimental chapter on SM-SERS where we took advantage of the additional enhancement properties of resonance Raman, while in this case there is no overlap of the excitation with the absorption of the target material so these effects are not exploited. Initially, we began work investigating the Raman spectra of the concentration study of F8-BT ($(C_{35}H_{42}N_2S)_n$) on silver using the 532 *nm*

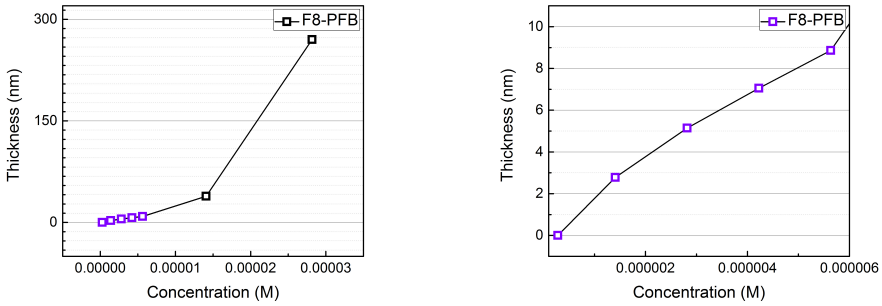

(a) **(b)**

Figure 7.1.1 – Concentration vs thickness for thin films of F8-PFB spun at 2000 *rpm* on glass slides. Figure (a) shows the full concentration study, whereas (b) shows just the lowest detectable concentrations. Thickness values at each concentration are an average taken from measurements at different points on the sample.

laser line, and the nano-gap formed between the 118 *nm* silver spherical particle and the 100 *nm* silver film we optimised in previous chapters. However, due to the F8-BT having strong fluorescence characteristics with this excitation, this leads to it overshadowing the Raman spectra making it ineffective for this material. F8-BT was much more fluorescent than R6G, so the fluorescence background was not entirely quenched as was the case previously. When dealing with the conjugated polymer, the dipole moment is in-plane and therefore not coupled to the cavity as was the case with the fluorescent dyes. Therefore, even though the fluorophore is in contact with the metallic structure, its fluorescence is not entirely quenched. This led to the decision to use non-resonance Raman excitation of F8-PFB.

7.1 Thickness Measurements

F8-PFB was supplied by CDT (Cambridge Display Technology). We performed the calibration of film thickness for F8-PFB in toluene spun at 2000 *rpm* onto glass. Due to the high molecular weight of F8-PFB, the concentrations for this thickness range are between 2.8×10^{-5} *M* and 1.4×10^{-6} *M*. Figure 7.1.1 shows the film thicknesses generated from these solutions at the relevant concentrations.

Figure 7.1.1b shows the average thicknesses of F8-PFB at its lowest detectable concentrations. At 1.4×10^{-6} *M*, we expect to achieve a nano-gap thickness of ~ 3 *nm* for

F8-PFB, past this point the film was no longer detectable via the stylus profilometer. In order to fabricate nano-gaps, samples were prepared with the target material deposited at low concentrations down to 2.8×10^{-10} *M* in a solution of toluene at 2000 *rpm* onto a 100 *nm* thick silver layer. After this, the 118 *nm* spherical silver nanoparticles were spun on top forming the nano-gap.

7.2 FDTD Analysis of the 3 nm Nano-Gap

We performed FDTD calculations with a TFSF source incident upon the 3 *nm* nano-gap formed between the 118 *nm* silver particle and a 100 *nm* silver film, this structure is representative of the F8-PFB spun at 1.4×10^{-6} *M*. The calculations utilised a meshed region of 0.2 *nm* over the nano-gap and 0.75 *nm* over the particle region. First, Figure 7.2.1 shows the absorption and scattering for the 3 *nm* nano-gap.

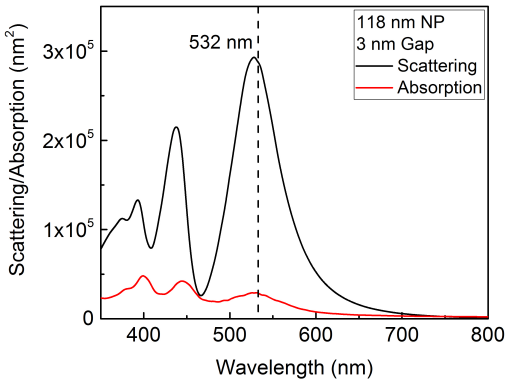

Figure 7.2.1 – Scattering and absorption spectra for the 3 *nm* nano-gap where the gap is formed between a 118 *nm* silver particle and a 100 *nm* silver film.

Figure 7.2.1 shows that the main contribution of the extinction for this system will stem from the scattering component. Figure 7.2.2 shows the extinction for the 3 *nm* gap in comparison to the 5 *nm* gap used previously in the fluorescent dye study.

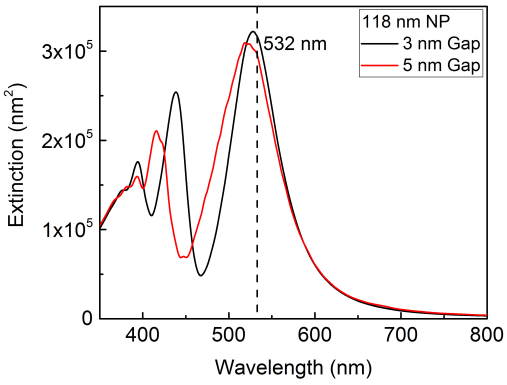

Figure 7.2.2 – Extinction spectra for the 3 *nm* vs the 5 *nm* nano-gap where the gap is formed between a 118 *nm* silver particle and a 100 *nm* silver film.

The extinction between the two systems does not change drastically from one to the other. The dipolar mode at 523 *nm* for the 5 *nm* gap shifts to 527 *nm* for the 3 *nm* gap. We can see the electric field at the centre of the nano-gap in Figure 7.2.3 at their respective extinction maxima.

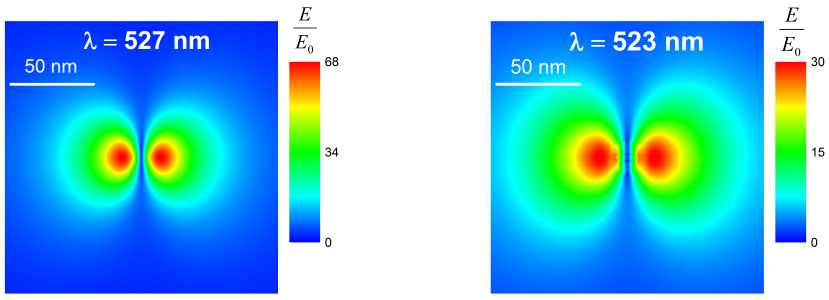

(a) **(b)**

Figure 7.2.3 – Hot spot for the nano-gap formed between a 118 *nm* silver particle and a 100 *nm* silver film. Where the thickness of the gap is (a) 3 *nm*, and (b) 5 *nm*. In each case, the field is shown at the extinction maxima for the structure closest to the 532 *nm* excitation, 527 *nm* for (a) and 523 *nm* for (b).

When compared to the 3 *nm* gap shown in Figure 7.2.3a, the electric field in the near-field for the 5 *nm* gap (shown in Figure 7.2.3b) is just under half the intensity. This gives 26× enhancement in E^4_{max}. This is due to the gap thickness relationship to field enhancement which we saw in Figure 5.3.7 in section 5.3.4.

7.3 F8-PFB

In this work, we investigated non-resonant SERS from F8-PFB. Although this experiment can be done using either resonant, or non-resonant Raman, we were unsuccessful with low concentration studies of F8-BT due to the strong fluorescence from the material not being quenched from our metallic nanostructure. Our theoretical study showed that the nano-gap formed between the 118 *nm* spherical silver particle and a 100 *nm* thick silver film produced the optimal field enhancement and far-field scattering characteristics under the influence of 532 *nm* excitation. Therefore, using the silver nanostructure along with the 532 *nm* laser line it seemed more appropriate to choose a material that would work in conjunction with this. F8-PFB has an absorption peak further into the blue region than F8-BT at 383 *nm*, this made Raman more viable for the F8-PFB. Looking at Figure 7.3.1, we can see that the absorption in this case for the F8-PFB is much further away our excitation wavelength. Therefore, we can perform non-resonant SM-SERS from this material without the possibility of the signal being overshadowed by the fluorescence.

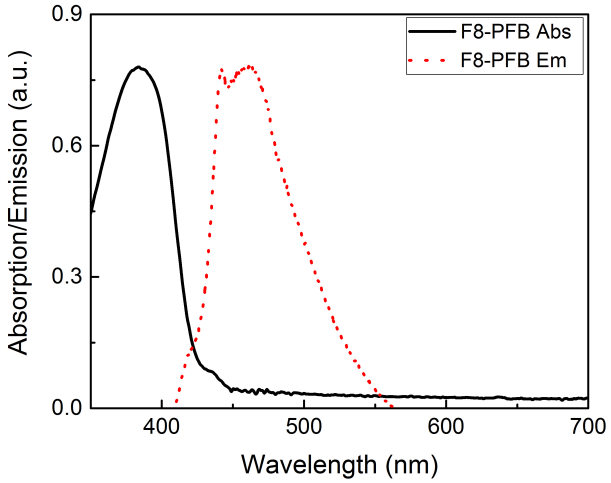

Figure 7.3.1 – F8-PFB Absorption (black line) and Emission (red dotted line) spectra peaking at 383 *nm* and 463 *nm* respectively taken on glass at 2.5×10^{-5} *M*.

We began measurements of the Raman spectra of the material at relatively high concentration. This would allow us to produce clear spectra of the material and categorise its respective peaks and help identify them when concentration was lowered. Figure 7.3.2

shows the Raman spectrum for F8-PFB at 2.8×10^{-5} M which produced a film with thickness 270.2 nm.

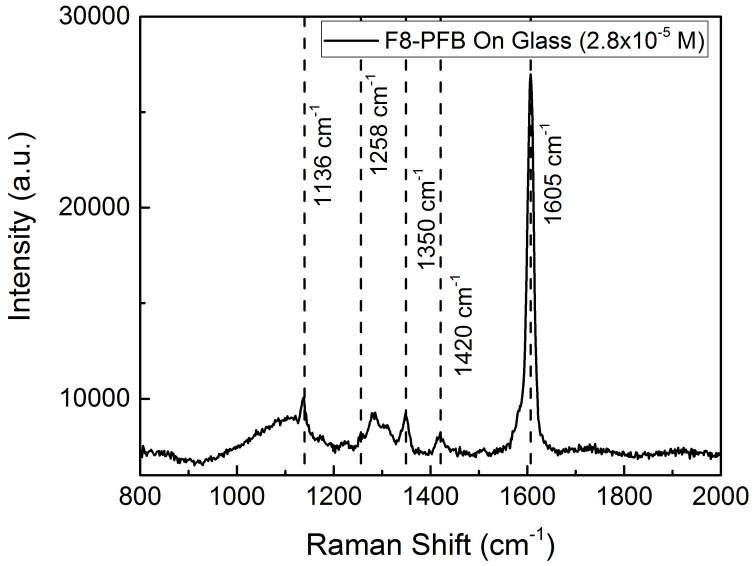

Figure 7.3.2 – F8-PFB Raman spectra taken on glass at 2.8×10^{-5} M. The most prominent peak visible is the 1605 cm^{-1} $C-C$ stretching mode.

We can see from Figure 7.3.2 that the most prominent mode in the Raman spectra is at 1605 cm^{-1}, which is attributed to the C-C stretching vibration of the material. Other, less intense peaks are also observed appearing between 1136 cm^{-1} and 1421 cm^{-1}. Where the 1136 cm^{-1} mode is also due to C-C stretching. The 1258 cm^{-1} mode is weak but most likely due to C-H bending and C-C stretching. The modes located at 1281 cm^{-1} and 1350 cm^{-1} are attributed to the PFB and are most likely due to the backbone C-C stretch within the monomer unit. We can also see a mode at 1420 cm^{-1} which is a result of C-C stretch motion between adjacent monomers [172, 174].

Now that we have categorised the Raman fingerprint of the material, we show a concentration study of F8-PFB at decreasing concentrations. Figure 7.3.3 shows the SERS spectra for samples at concentrations between 2.8×10^{-6} M and 2.8×10^{-10} M inside the gap.

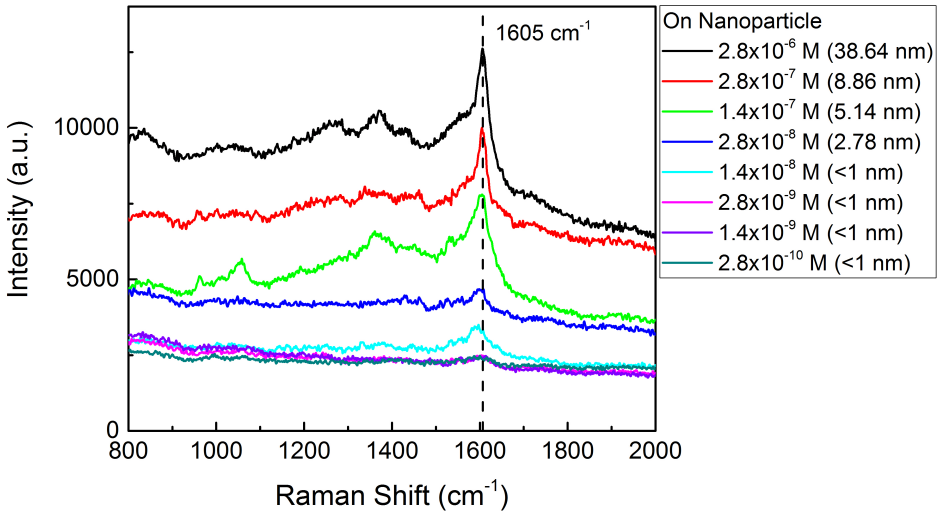

Figure 7.3.3 – Concentration study of F8-PFB for 118 *nm* silver nanoparticles on a silver film using 532 *nm* excitation with 3 *s* collection time.The most prominent peak visible is the 1605 cm^{-1} C-C stretching mode marked with a dashed line.

It should be noted that as concentration is decreased the nano-gap thickness also decreases as there is no supporting polymer matrix in this case. We showed these thicknesses down to 1.4×10^{-6} M in Figure 7.1.1b, but past this concentration the thickness could not be measured. By looking more closely at the lowest concentration samples, we can see that there is no concentration dependence with the signal. Figure 7.3.4 shows the Raman signal at the lowest concentrations we investigated.

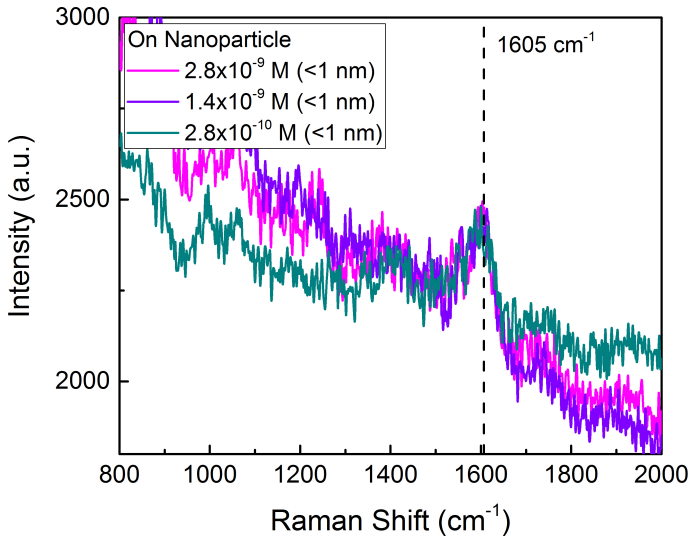

Figure 7.3.4 – SERS signal from F8-PFB for 118 *nm* silver nanoparticles on a silver film using 532 *nm* excitation with 3 *s* collection time. Here we look at the lowest concentration samples from the study and show the signal is no longer dependant on the concentration. The most prominent peak visible is the 1605 cm^{-1} C-C stretching mode marked with a dashed line.

We can see that once a concentration no longer affects the Raman signal intensity, the SERS signal is being attributed to by single conjugated polymer chains. Once the concentration reached 2.8×10^{-9} M, we can see the intensity of the 1605 cm^{-1} becomes minimum, no longer decreasing in intensity with concentration. Therefore, at this concentration we have reached the point where there is potential to observe single molecule characteristics. The system below this concentration provides similar intensity for this mode but less frequently from each particle nano-gap system that Raman spectra is collected from. This is because of the random distribution of molecules within the nano-gap and their position relative to the hot spot regions located beneath the particle.

We also provide a peak intensity ratio between spectra taken from a nano-gap system formed between the 118 *nm* silver sphere and the 100 *nm* silver film, showing the relative enhancement in comparison to measurements taken from the material on a flat metal surface. Figure 7.3.5 shows the Raman spectra for F8-PFB at 1.4×10^{-6} M (which has shown to produce a film thickness of ~ 3 *nm*), taken from the nano-gap and off of the particle where the thin film of material is on the silver layer.

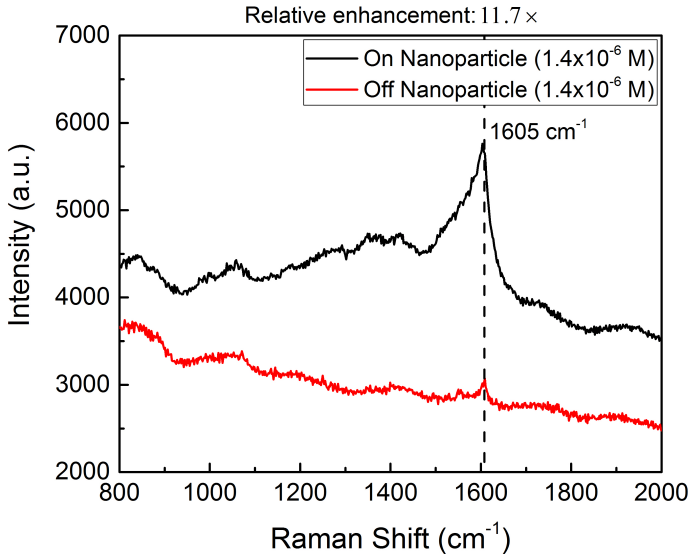

Figure 7.3.5 – F8-PFB Raman spectra taken on and off of a nanoparticle at 1.4×10^{-6} M. The most prominent peak visible is the 1605 cm^{-1} C-C stretching mode. Enhancement between the two spectra at this wavenumber is 11.7×

We can see from Figure 7.3.5 that the peak intensity from the measurement taken from the nano-gap at 1605 cm^{-1}, which represents the C-C stretching bond, is 11.7× more intense than that taken off of the particle. This means that the field is enhanced this much by the nano-gap when coupling occurs in this system. This extra enhancement relative to the R6G samples is most likely due to the nano-gap being narrower at this concentration which we gathered from our Dektak calibration in Figure 7.1.1, where the insert suggests a gap of 3 *nm* for in this case. The broadness of the peaks is representative of conformation of the material: broader spectra is associated to looser packed geometry whereas the narrower spectra is conducive with closer packed molecules [172].

7.3.1 SM-SERS of F8-PFB

We define the single molecule regime for our study of conjugated polymers at low concentrations by observations of the SERS intensity with changing concentration reaching a minimum, as well as intensity blinking effect. The intensity blinking effect is observed at ultra-low concentrations where Raman modes fluctuate in intensity during real time measurements [36, 72].

When preparing samples with lower concentrations relative to that used in Figure

7.3.5, Raman peak intensity from these gaps began to diminish. The spectra taken at concentrations approaching $2.8 \times 10^{-9} M$ can be shown to be contributed from few to single molecules at a time.

We demonstrate the intensity blinking effect occurring by examining nano-gaps, taking a series of measurements from individual particle gap systems. By producing a heat map of a series of 10 Raman spectra acquired from a nano-gap from a sample at $2.8 \times 10^{-9}\ M$, we can see the 1605 cm^{-1} mode fluctuating throughout the measurements relative to the background signal.

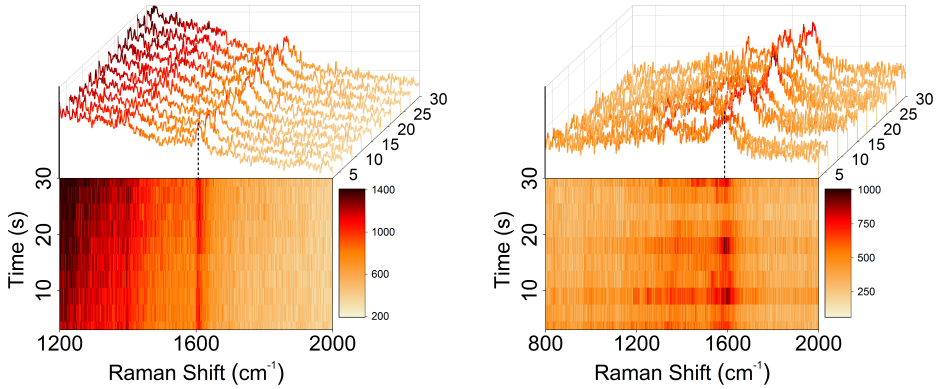

(a) **(b)**

Figure 7.3.6 – 10 consecutive measurements for F8-PFB Raman spectra at (a) $2.8 \times 10^{-8}\ M$, and (b) $2.8 \times 10^{-9}\ M$. The 1605 cm^{-1} C-C stretching mode varies in intensity each time a measurement is taken.

The signal shown in Figure 7.3.6b is more intense at the darker regions. We can see a continuous rising and falling instability in the intensity which shows this effect is not a result of photo-bleaching which would be observed as a continuous decline in the intensity of the signal. As a comparison, 10 consecutive measurements from a sample at $2.8 \times 10^{-8}\ M$ shows much more stability in the 1605 cm^{-1} mode, as seen in Figure 7.3.6a.

10 measurements were recorded consecutively from 3 nano-gaps with measurements being performed for 3 s with a 0.1 mm slit using the 532 nm laser line. Figure 7.3.7 shows consecutive spectra acquired from 3 different nano-gaps at $2.8 \times 10^{-9}\ M$ in comparison to a series from a $2.8 \times 10^{-8}\ M$ sample nano-gap.

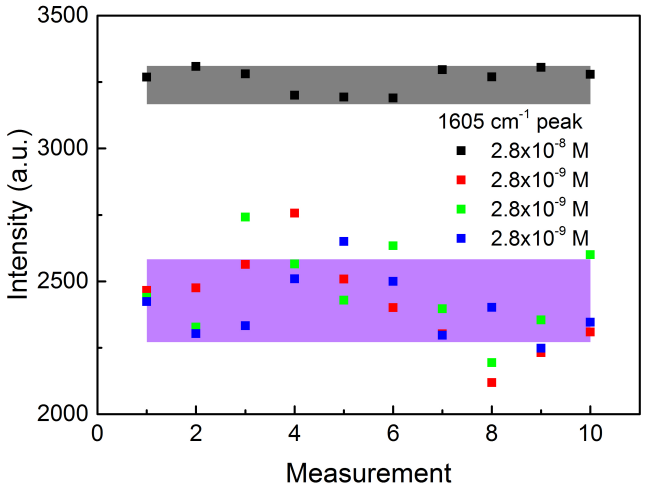

Figure 7.3.7 – 3 series of 10 consecutive measurements for F8-PFB Raman spectra at 2.8×10^{-9} M compared to 2.8×10^{-8} M. The low concentration series (red, green and blue) all show intensity blinking with points straying outside of the standard deviation. Whereas, the black series does not due to its concentration being $10\times$ higher. The coloured bars (black for 2.8×10^{-8} M and purple for 2.8×10^{-9} M) in each series represent the average of the measurements with the thickness being $2\times$ the standard deviation.

We can see in Figure 7.3.7 that there is a difference when passing this concentration threshold from 2.8×10^{-8} M to 2.8×10^{-9} M. The fluctuation in peak intensity of the 1605 cm^{-1} mode becomes much more turbulent with points deviating from the standard deviation of the mean average of each series frequently, an effect not previously observed in the 2.8×10^{-8} M sample.

Dropping the concentration even further down to 2.8×10^{-10} M, we can show in Figure 7.3.8 that the same effect still occurs. To further emphasise the blinking effect, consecutive scans over longer time-frames were taken. Figure 7.3.8 shows the heat map of 20 Raman measurements acquired from a nano-gap with F8-PFB at 2.8×10^{-10} M.

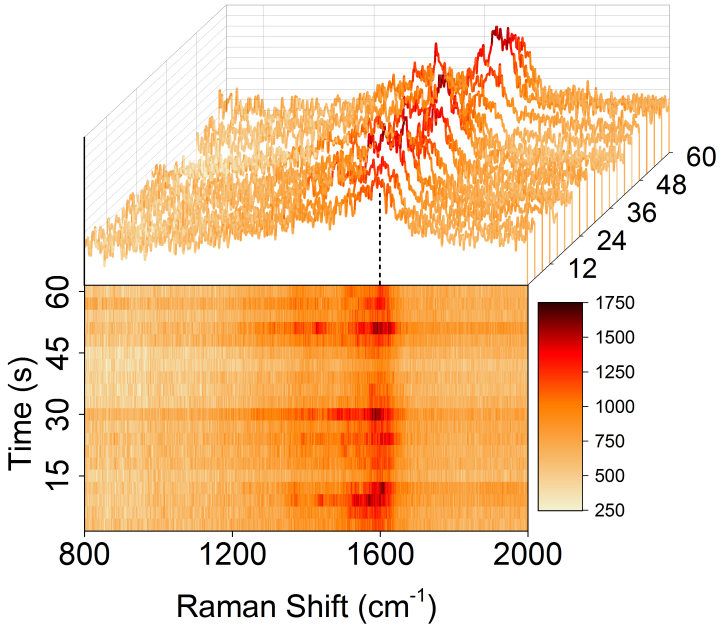

Figure 7.3.8 – 20 consecutive measurements for F8-PFB Raman spectra at 2.8×10^{-10} M. The 1605 cm^{-1} C-C stretching mode varies in intensity each time a measurement is taken.

We observe once again intensity fluctuations from the 1605 cm^{-1} mode. However, due to the concentration being extremely low the likelihood of molecules being situated within the nano-gap hot spot regions is far less probable. So it can be said that $2.8 \times 10^{-9} - 2.8 \times 10^{-10}$ M is sufficient for single molecule detection to be observed.

7.4 Summary

Overall from this study, we have established the capabilities of this nano-gap configuration for enhancement of Raman signal. We have shown that using these nano-gaps we have the ability to detect materials down to the ultimate limits of detection, giving detailed information of molecular targets in trace quantities. From our study, we have shown that the single molecule regime has been achieved due to the SERS intensity reaching a minimum at 2.8×10^{-9} M and no longer changing below this concentration. This indicates that the SERS signal is attributed to the same number of molecules or single polymer chains at this concentration. We have confirmed this through continuous Raman spectra

that intensity blinking occurs from this formation of plasmonic nanostructure which is characteristic of entering the single molecule regime.

We began the work with thickness measurements of the conjugated polymer F8-PFB. Because the nano-gap thickness is dependant on the concentration of the material for this study, it is important to categorise these gaps with a concentration study. At a concentration of 1.4×10^{-6} M, the surface profilimitry measurements from the thickness study showed that the nano-gap of our practical substrates would be ~ 3 *nm* thick. Therefore, we demonstrated FDTD calculation data from the 3 *nm* nano-gap in terms of the scattering and absorption from the structure as well as near field enhancement. We provided the data in comparison to the 5 *nm* nano-gap we investigated in previous sections and showed that additional enhancement to the near field in this case. The findings show that the narrower gap gives $26\times$ enhancement in E^4_{max} (near field contribution).

From performing a concentration study of F8-PFB, we have shown that choosing the correct wavelength of excitation in conjunction with its ideal plasmonic nanostructure and material is integral to reaching single molecule concentrations with observable signal still present. There were challenges with working on resonance with F8-BT using 532 *nm* excitation because of the strong background fluorescence, therefore moving to non-resonant Raman with F8-PFB was necessary.

We were able to quantify the enhancement of the system from a 3 *nm* nano-gap formed between the 118 *nm* silver nano-sphere and the 100 *nm* silver film, with the material at 1.4×10^{-6} M, in comparison to the 3 *nm* film on silver in absence of the particle. We found that the system provides $11.7\times$ enhancement when using the nano-gap at this thickness.

Designing nano-gaps from the material itself rather than using a secondary polymer does have its drawbacks. By fabricating structures in this way, we are less likely to have a continuous film. This therefore leads to non-uniformity of the sample surface and irregular enhancement levels at times. Overall, the devices performed well and data was relatively consistent to collect especially when working in the 2.8×10^{-9} M range as we show from Figure 7.3.7 where measurements taken from different nanoparticles all produced the intensity fluctuations representative of the single molecule domain.

Chapter 8

SERS Biosensing

Spectroscopy on the nanoscale is a rapidly expanding field and due to recent developments in plasmonics, improvements in sensitivity have facilitated detection towards single molecule binding events [175]. These steps forward can be attributed to the high field enhancements generated around nanoparticle systems. Biosensing through plasmonics is proving to have high potential for detection of materials in real time at low concentrations, due to the large enhancement of fields and the information they encompass [84, 119, 176]. Protein analysis is a major branch of biosensing: proteins perform vital functions in the body, so understanding their processes in real time is key to understanding their roles in living systems. This can be achieved with SERS, which provides details of changes in molecular architecture in close proximity to metallic nanostructures. SERS provides intrinsic features which relate to vibrations in the molecular bonds of a material via shifts in the frequency of inelastically scattered light. Because of this, any change in a material's structure will be shown by a change in the spectrum's peak relative to that molecular bond.

In this chapter, we implement protein analysis through the use of the particle on a film geometry we have discussed throughout previous chapters. We show Raman spectra from two bio-molecules, Bovine Serum Albumin (BSA) and lysozyme. The aim is to use SERS to selectively exhibit the change in lysozyme, a protein which functions as a part of the immune system and is ubiquitous within most living organisms. Changes in concentration levels of lysozyme within the body are affiliated with diseases such as leukaemia and meningitis [43]. Therefore, device sensitivity towards detection of proteins such as lysozyme are effective for early identification of diseases in patients leading to earlier treatment. We investigate the material after it has undergone illumination via UV light exposure for given periods of time. Observations of lysozyme are carried out via

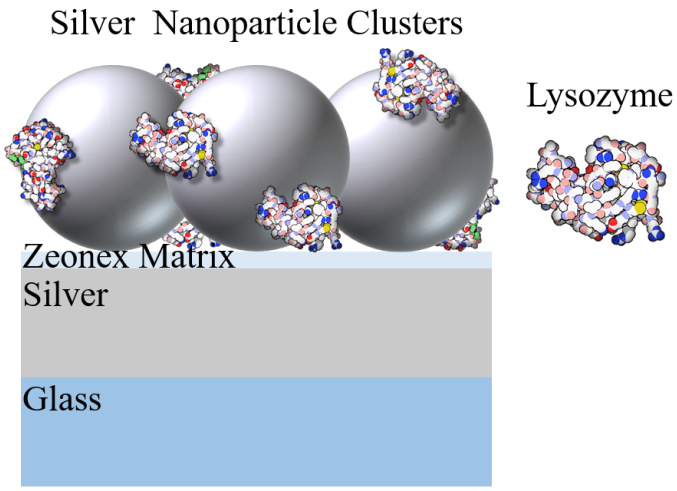

Figure 8.0.1 – Schematic diagram for silver nano-clusters mixed with the bio-molecule target (in this case lysozyme) on a 5 *nm* zeonex cavity.

Raman spectroscopy to fully realise the change in molecular configuration via the unique fingerprint generated in its spectrum. Raman spectra are collected from nano-gaps formed between silver nanoparticle clusters mixed with the target bio-molecules and an extended silver film. Their structure would typically look as Figure 8.0.1 depicts.

Samples were produced in a relatively straight forward manner. First, glass slides were thermally coated with a 100 *nm* layer of silver at a rate of $\sim 0.2\ nm/s$. This slow rate was selected to ensure a flat smooth metal. 1 mg/ml concentration zeonex in chloroform was produced and spun onto the silver substrate, this allowed for a 5 *nm* thick cavity to be fabricated between the metal surface and the nanoparticles deposited on top. Stock solutions of lysozyme exposed to, as well as non-exposed to UV light, provided by Professor Steffen Petersen from the Medical Photonics Group at Aalborg University in Denmark were prepared at a concentration of 1 μM and 10 μM in PBS at pH 7.4, and kept at $4-8\ ^{\circ}C$. 100 *nm* diameter silver nanoparticles in an aqueous solution at 0.2 mg/ml mass concentration were then mixed with the lysozyme solutions in a 1 : 1 ratio and spun onto the substrate surface.

8.1 Protein analysis: Lysozyme

Figure 8.1.1 shows the SERS spectrum for the non UV exposed lysozyme which forms the reference for our study. We can see the sharp modes in the 1300 and 1600 cm^{-1} re-

gions most distinctly. These are attributed to vibrations in the Tryptophan (Trp) amino acid group, and Amide I functional group respectively. With sufficient energy, it is possible for light to induce structural changes in proteins. The integrated power of the UV light incident on the samples was 0.4 *mW* at 280 *nm*. Under the influence of UV light, photo-oxidisation can occur which can lead to conformational changes in the protein. Alterations in the conformation of proteins are often indicative of them performing functions in real world environments.

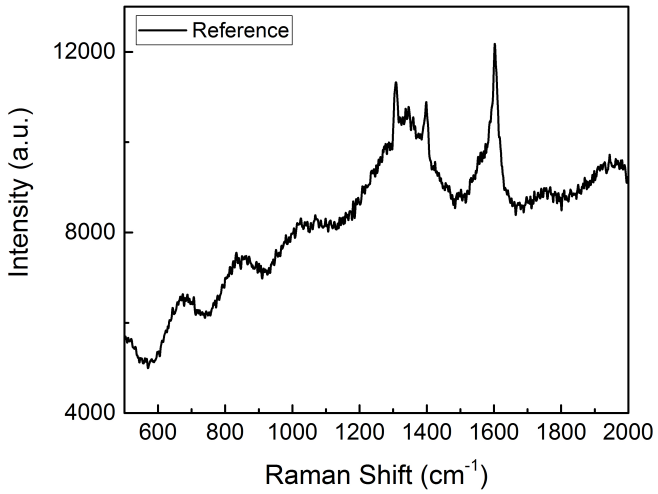

Figure 8.1.1 – Raman spectra from silver nano-clusters mixed with lysozyme on a 5 *nm* zeonex cavity.

When exposed to 280 *nm* UV light for given periods of time, hen egg white lysozyme undergoes photo-physical and photo-chemical structural modifications. In particular, we observe weakening of the Trp vibrational lines in the SERS spectra with new modes arising elsewhere indicating that conformation changes have occurred within the material during the illumination period. In Figure 8.1.2, we show the obtained SERS spectra for the UV exposed lysozyme with successive panels demonstrating the progression under subsequent exposure times.

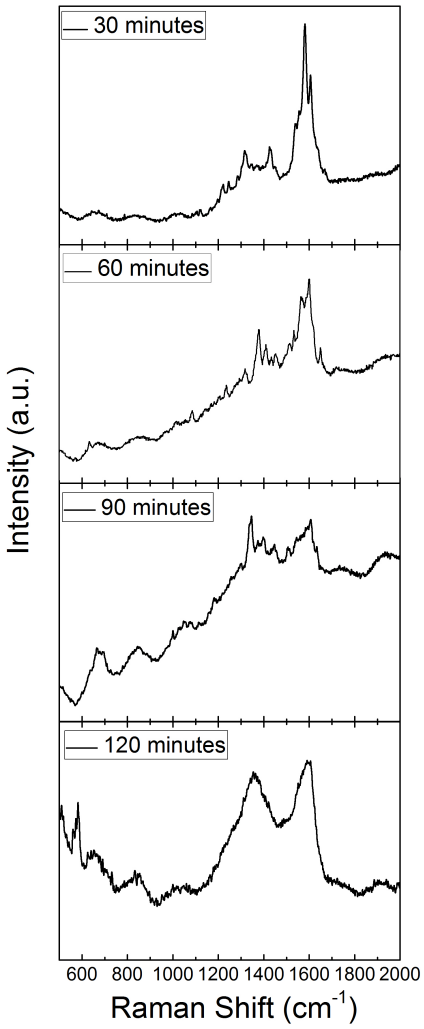

Figure 8.1.2 – Raman spectra from silver nano-clusters mixed with lysozyme on a 5 *nm* zeonex cavity after progressively longer exposure to UV light.

The Raman spectra have very strong signals in the region corresponding to the protein backbone vibrations. It can be seen that the Raman modes associated to Trp between $1330-1360\ cm^{-1}$ become less distinct and broaden as a function of UV light exposure. It is evident that vibrational modes associated to Amide III located between $1200-1300\ cm^{-1}$ are more prominent as time progresses; however, at the longest time exposure, Raman modes have become far less defined. Also, it is notable to mention the appearance of the $580\ cm^{-1}$ mode at 120 minutes of UV exposure which could be analogous with S-S vibrations [118, 143]. This leads us to believe there has been deterioration in the Trp and consequently disulphide bonds have formed elsewhere on the molecule. Changes also

occur at 60 minutes of exposure where the mode at 1080 cm^{-1} could be a C-N bond or representative of Phenylalanine (Phe). There is also a mode occurring at 630 cm^{-1} which could be either Phe or Tyrosine (Tyr). The Amide I modes given in the 1600 cm^{-1} region are prominent throughout the spectra and are also characteristic of lysozyme measurements [177].

There were a number of challenges when working with proteins as opposed to more basic materials such as fluorescent dyes. For example, the proteins have to be kept in an aqueous suspension so no nano-gap could be formed by mixing the materials with a polymer in a solvent. This means most of the enhancement which is localised to the gap is inaccessible. We do however, see fields from the simulation data in previous sections around the base of the particle as fields couple between the particle and film below shown from the $x-z$ cross sections. This means the cavity formation we have tested here can still take advantage of this coupling when proteins are situated close to the base of the particles.

It should be taken into consideration that collection times for Raman spectra from these systems were adjusted to be comparable with one another. Beyond 30 minutes of UV light exposure, signals became quite weak, therefore the 532 *nm* laser line power was increased from $0.15\ mW - 0.3\ mW$. However, slit widths of 0.05 *mm* and collection times of 10 *s* remained the same throughout the measurements. The unpredictable enhancement levels of Raman scattering were most likely due to the random geometry of nanoparticle clustering.

As stated, the geometry in these devices is ambiguous. Particles were drop cast with the proteins together, therefore, the clusters of particles under investigation are non uniform so we cannot use the model from previous chapters of the single particle on a film geometry. It means that the system will behave differently and unanticipated coupling effects can occur. The likelihood is that hot spots will be generated between particles as well as the nano-gap. Overall though, we see precursor evidence for the potential for this system to be used with proteins and how they can determine conformation changes in biological materials. If Raman spectra could be taken from lysozyme while it is under

the influence of UV light in real time, it would have the potential to show the materials changes as the process occurs.

The information obtained from this study indicates that the particle on a film geometry has substantial potential for early detection of conformation changes in proteins which could lead to disease analysis if fully developed. Thorough testing would be required to optimise the devices such that the ideal circumstances can be used to enhance light radiated from them, and more experience working with proteins is necessary to understand their behaviour under these conditions.

8.2 Protein analysis: Bovine Serum Albumin

Additionally, along with the lysozyme analysis we also examined Bovine Serum Albumin or BSA using the particle on a film geometry. BSA is one of the main carriers of fatty acids in the body, as well as this, it also functions to isolate oxygen free radicals and inactivating numerous toxic lipophilic metabolites (substances which are necessary for metabolic function and are soluble in lipids/fats) [40]. BSA is a well documented protein with regards to its respective Raman spectra making it ideal for this study [41, 145]. BSA is a useful protein to detect as, similarly to the lysozyme, it possesses Trp locations. A purified sample purchased from Sigma Aldrich was used at a concentration of $3 \times 10^{-5}\ M$ drop cast overnight in a mixture with 100 *nm* silver nanoparticles in aqueous buffer at a concentration of 0.02 mg/ml. This produced a layer of the protein over the sample in the same configuration as the lysozyme samples.

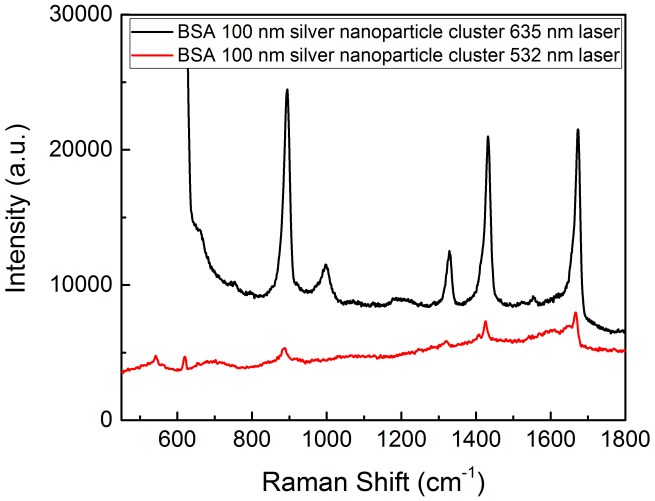

Figure 8.2.1 – Raman spectra from silver nano-clusters mixed with BSA drop cast onto a 100 *nm* silver film. SERS measurements were acquired using a 635 *nm* source excitation (black) and a 532 *nm* source excitation (red) with 3 *s* collection time and 0.02 *mm* slit width.

The 532 *nm* line exposes the 543 cm^{-1} mode which can be seen from disulphide bonds, 621 cm^{-1} synonymous with Phe, 886 cm^{-1}, known to be the Tyr mode, as well as 1322 cm^{-1} which, similarly to the lysozyme represents the Trp mode. The peak located at 1425 cm^{-1} with a shoulder at 1407 cm^{-1} is associated with C-H_2 and C-H_3 side chain scissoring modes and finally, the 1665 cm^{-1} peak corresponds to the Amide I mode and is mainly contributed to via vibrations in C=O [40, 118, 143]. Alternately, in the 635 *nm* excitation we see an additional mode arise at 1000 cm^{-1}. This mode is relatively strong and is a contribution in vibrations from the aromatic ring breathing mode of Phe [177]. There is also evidence for a weak mode observable at 1552 cm^{-1} which relates to the Amide II region of the protein.

As we can see, both laser sources are suitable for measurements from this material from these devices, however, with the added complexity brought into the system by the clustering of the silver nanoparticles an additional 14$\times$ enhancement is observed when using the 635 *nm* laser, most likely due to the shift in plasmon resonance of the system. The drawback we observed from our setup is that some of the shorter wavenumber modes were lost in the tail of the red laser, however this could potentially be improved using the correct filters. To build upon this, we can also demonstrate the 635 *nm* laser line on and

off the clustered particles to observe the relative enhancement of BSA in this system as seen in Figure 8.2.2.

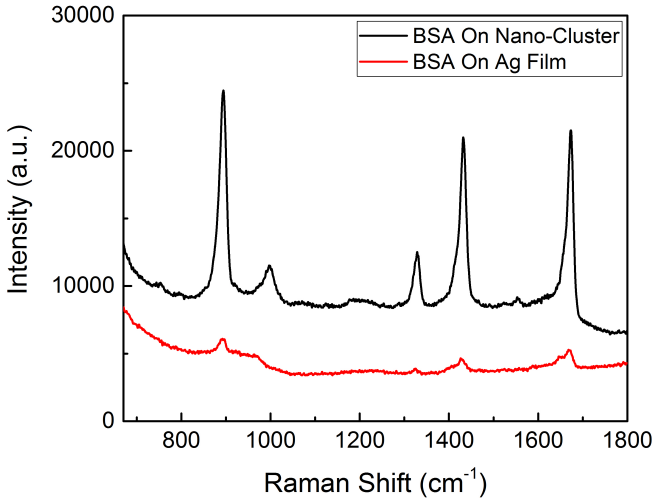

Figure 8.2.2 – Raman spectra from silver nano-clusters mixed with BSA drop cast onto a 100 *nm* silver film using 635 *nm* excitation with 3 *s* collection time and 0.02 *mm* slit width.

In this case, we note an enhancement of $\sim 15.5\times$ from the nano-clusters relative to the film. This figure would be less consistent than the particle film geometry we saw before in previous chapters due to the unpredictable nature of the clusters particles especially when concentrations are significantly lower.

8.3 Summary

Overall, this work has demonstrated the potential for this configuration of plasmonic nanostructures to be used in conjunction with biological materials. It is possible to observe intense, defined peaks of the proteins, at relatively low concentrations, and deduce changes in their conformation when under the influence of UV light exposure. In particular, the deterioration in the Trp modes and appearance of disulphide bonds as time under UV light exposure progresses.

We have also shown through SERS measurements of BSA that the nano-gap formed between a particle and an extended metallic film model which we investigated in previous chapters, is no longer reliable for clustering of the particles and the LSPR of the system

red-shifts. We demonstrate this by showing the difference in spectra between the 532 and 635 *nm* laser lines where 14× enhancement is observed for the longer wavelength excitation. The drawback for our 635 *nm* laser line is that some modes are lost due to the background signal attributed to it.

There are many obstacles to overcome for this work owing to the difficulties with working materials which are sensitive to environmental changes and are therefore less robust than polymers or fluorescent dyes. We conclude therefore that with sufficient work into this area the potential to formulate a SERS based particle on a film sensor is achievable and this work sets the necessary starting point to develop from.

Chapter 9

Improving the Quality Factor of Plasmonic Devices

As we have shown previously, metallic nanoparticles apply excellently in SERS. However, in terms of optical sensing, they do have limitations, for example their sensing range is limited to several tens of nanometres [178, 179]. Also, LSP based sensors typically have broad plasmonic resonance line-width caused by intrinsic absorption of the metal. By coupling the metal nanoparticle to a dielectric slab or Distributed Bragg Reflectors (DBRs), strong dipolar resonances can be achieved in the system where scattering outperforms nanoparticles on their own. For refractive index sensing, optical sensors can be categorised by a FoM [180]:

$$FoM = S \times \frac{Q}{\lambda_{res}} \tag{9.0.1}$$

The sensitivity, S, can be described by:

$$S = \frac{\Delta\lambda}{\Delta n} \tag{9.0.2}$$

Where $\Delta\lambda$ is the change in wavelength as a response to the change in refractive index Δn, λ_{res} is the resonance wavelength of the system and Q is the Quality-factor (Q-factor). The Q-factor is a measure of the resolution of shift in the resonant mode for the device [181–190]. The Q-factor can be described by the following relationship [191]:

$$Q = \frac{\lambda_{res}}{\Delta\lambda_{FWHM}} \tag{9.0.3}$$

Where $\Delta\lambda_{FWHM}$ is the full width half maximum of λ_{res}. The aim of this chapter is to

improve upon the Q-factor for particle on a film geometry. We present FDTD simulations of plasmonic structures coupled to alternative substrates such as dielectric slabs or DBRs. We aim to show that by replacing these extended metallic films in previous chapters with a dielectric slabs or DBRs, we are able to improve upon the narrowness of the hybrid modes of the system and hence increase the Q-factor. Our DBR simulations investigate both size dependencies of gold nanoparticles coupled to these substrates, as well as the optimal particle size coupled to DBRs with a distribution of stop-band sizes to tune the LSPR with the central wavelength of the Bragg reflector.

9.1 Refractive Index Sensing

Surface plasmon sensors have often been used for refractive index sensing, and have been shown to produce high FoMs (up to 108 for gold mushroom arrays [30, 31]) and sensitivity [28, 31, 192]. However, when compared to photonic devices, FoMs of 2060 have been achieved with Q-factors of 7010 [180]. Refractive index sensing in plasmonics relies on measuring the spectral shift of resonant modes of the structures relative to changes in the refractive index of the surrounding media [185, 187, 192–197]. It has also been applied to biological systems [175, 198].

Changes to the dielectric environment in proximity to plasmonic nanostructures produce shifts in the LSPR peak location. This attribute is particularly useful for detection of materials and measuring the binding affinities for molecules. With the introduction of functionalisation of the surface of the plasmonic structure with ligands, specificity of the analyte under investigation is possible [114, 194].

Coupling nanoparticles with micro-cavities such as dielectric slabs leads to narrowing of the spectral line-width of the system. These hybrid systems have shown to improve sensing FoMs by up to 36 times in Fabry-Perot (FP) micro-resonators [28].

9.1.1 Distributed Bragg Reflectors

DBRs are a type of reflector used in photonics consisting of a multilayer structure using materials of alternating refractive indexes. By using periodic layers of two materials at specific thicknesses the central frequency for the system can be tuned. Each layer of the dielectric produces a partial reflection from the incoming electromagnetic wave. These reflections can interfere with one another constructively resulting in the DBR behaving as a high quality reflector [197, 199, 200]. By using the material properties for TiO_2 and SiO_2 as the bilayers within the DBR, the thicknesses of each material can be calculated from the central peak wavelength (known as the photonic stop-band) by using:

$$d = \frac{\lambda_{stopband}}{4n} \tag{9.1.1}$$

An alluring property of DBRs and dielectric slabs alike for sensing purposes, is the ability to couple these optical modes in the DBR to metallic nanoparticles. A schematic diagram of the DBR nano-gap structure we used throughout this study is shown in Figure 9.1.1.

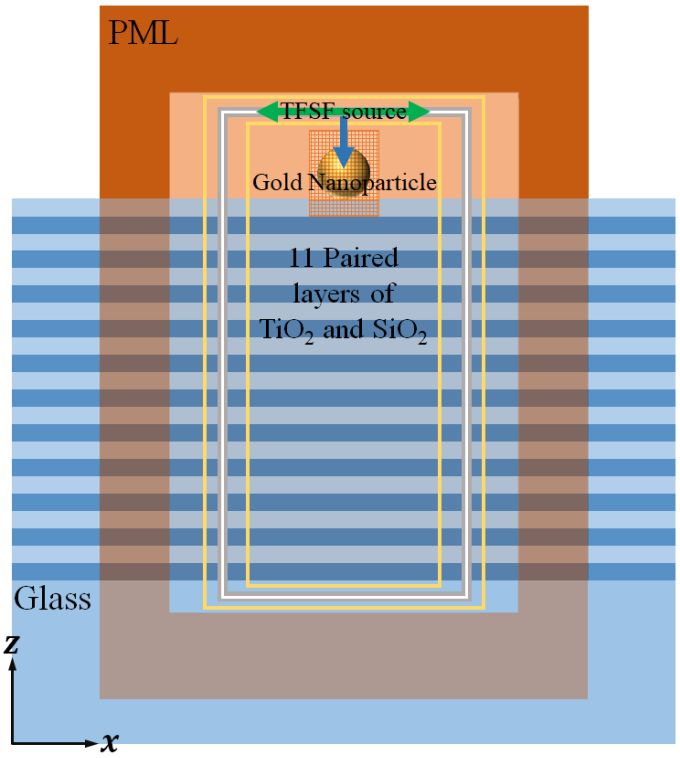

Figure 9.1.1 – Schematic of a gold nanoparticle coupled to a 11 bilayer DBR composed of TiO_2 and SiO_2 with refractive indexes set as 2 and 1.45 respectively.

The nano-gap in this case is formed between the gold nanoparticle and DBR which is comprised of 11 paired layers of titanium dioxide TiO_2 and silicon dioxide SiO_2 with refractive indexes 2 and 1.45 respectively.

9.1.2 Dielectric Slabs

By coupling nanoparticles to dielectric slabs, it is possible to produce hybridised modes. These hybridised modes are discretized around the LSPR of the nanoparticle, and improve the sensing properties of the system due to the narrowness of the hybridised peaks, as well as the sensing range physically from the particle [28, 201]. The dielectric slabs employed throughout this study consist of a slab of Si_3N_4 with refractive index 2.1 and thickness ranging from 400 *nm* to 2 μm suspended in air. We can see a schematic representation of this in Figure 9.1.2.

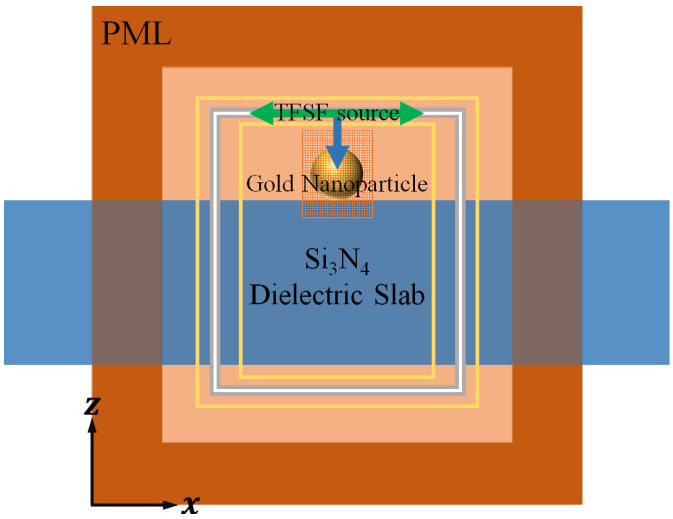

Figure 9.1.2 – Schematic of a gold nanoparticle coupled to a dielectric slab composed of Si_3N_4 with refractive index set as 2.1.

9.2 FDTD Calculations of Nanoparticles Coupled to Dielectric Slabs and DBRs

The simulations took place using a total field scattered field (TFSF) geometry described in 5.1.1 from Chapter 5. We can obtain the absorption, scattering and therefore extinction characteristics of a system with this source type. Where the plane wave injection axis of the source is in the z direction above the particle and the electric field oscillating is in the x axis.

Simulations used a 1 *nm* sub-mesh surrounding the nanoparticle. This ensures the curved surfaces of the structure are adequately meshed. We also used Lumerical's conformal variant 1 mesh, which evaluates the fields in each cell but accounts for sub-cell properties where more than one material can occupy the same Yee-cell. It utilises the Yu-Mittra method and accounts for all materials including metals [131].

The boundaries of the structure utilise stretched co-ordinate PML to eliminate the fields at these interfaces based on formulation proposed by Gedney and Zhao [127]. The substrate layers are extended through this PML region to simulate an extended film. The sensors are located through the centre of the structure taking a cross section in the $x-z$ plane. The sensors allow us to quantify the properties of absorption and scattering, while

also retrieving information regarding the electric fields passing through these regions as a function of frequency.

We allow for long pulse lengths from our sources with simulation times being set in excess of 1000 fs, such that fields deteriorate to 1×10^{-5} of their original value and the auto shut off is triggered.

9.2.1 Gold Nanoparticle in Vacuum and on an Extended Gold Film

First, we can show the scattering from a 200 *nm* gold nanoparticle on its own in a vacuum in Figure 9.2.1.

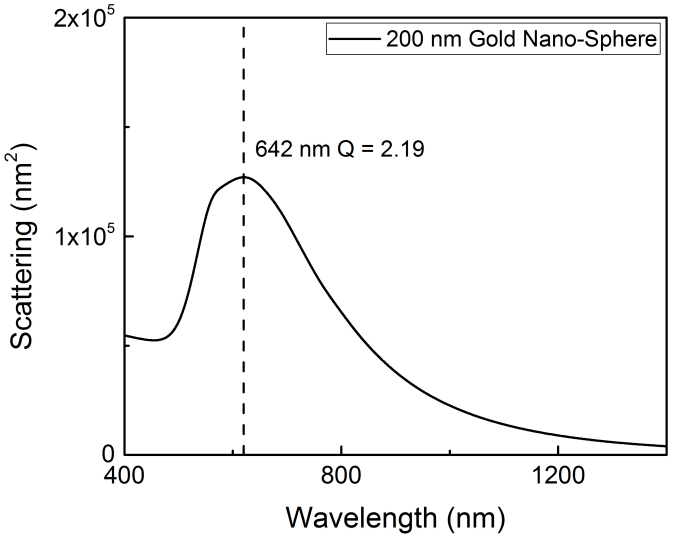

Figure 9.2.1 – Scattering from a 200 *nm* gold nanoparticle under the influence of a TFSF plane wave source.

The scattering spectrum for the 200 *nm* gold particle peaks at 620 *nm*. As we can see, the Q-factor is quite low at 2.19. By coupling the particle to different films, we can see the effect this has on the Q-factor.

We can then show the modification of this mode by combining the nanoparticle with a 100 *nm* metallic gold film. The particle on an extended gold film produces two modes similar to what we saw in Chapter 5, representing the quadrupolar and the more tunable dipolar mode.

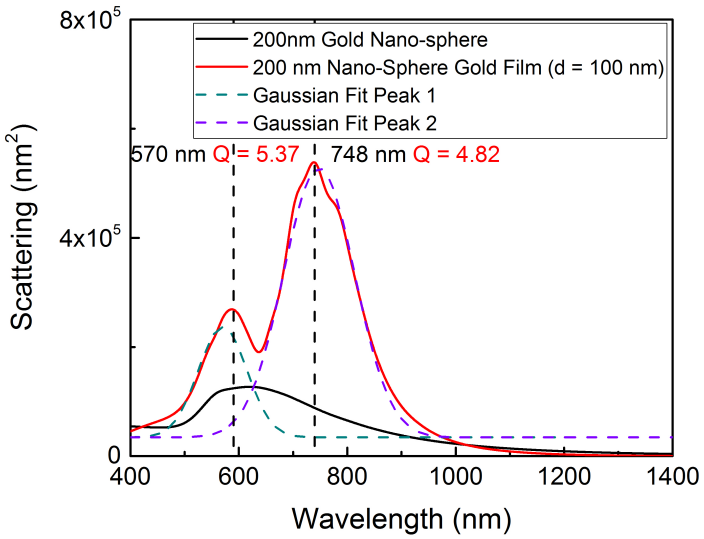

Figure 9.2.2 – 200 *nm* gold nanoparticle scattering (black) compared to the nanoparticle on a 100 *nm* gold film (red).

The Q-factors were estimated throughout by fitting Gaussian peaks to the curves as seen in Figure 9.2.2. The Q-factor here is much better with a value of 5.37 for the quadrupolar mode and 4.82 for the dipolar. These modes can be further refined through coupling to other hybrid gaps as we will show in the upcoming sections.

9.2.2 Gold Nanoparticle on a Dielectric Slab: Thickness Study

We can then show the modification of this mode by combining the nanoparticle with a dielectric slab with refractive index 2.1. Figure 9.2.3 shows the scattering spectrum for the 200 *nm* gold particle coupled to dielectric slabs of different thicknesses ranging from $400 - 1600$ *nm*.

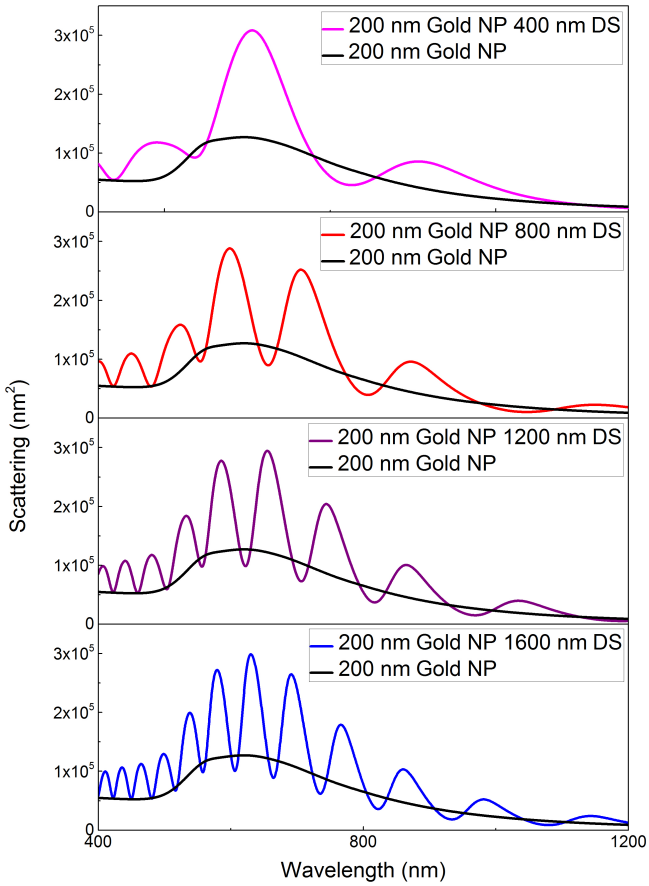

Figure 9.2.3 – Scattering spectrum from a 200 *nm* gold nanoparticle coupled system to a dielectric slab of varying thickness between 400 – 1600 *nm* with refractive index 2.1.

We can see the gradual change in the scattering spectrum from this system as a function of dielectric slab thickness. More modes are produced within the dielectric slab which couple to the LSPR of the nanoparticle. This leads narrower modes and an increase in the Q-factor of the system. When increasing the thickness even further, we see the trend continues and from Figure 9.2.4, we can see the scattering spectrum from a 200 *nm* gold nanoparticle coupled to a 2 μm dielectric slab with refractive index 2.1.

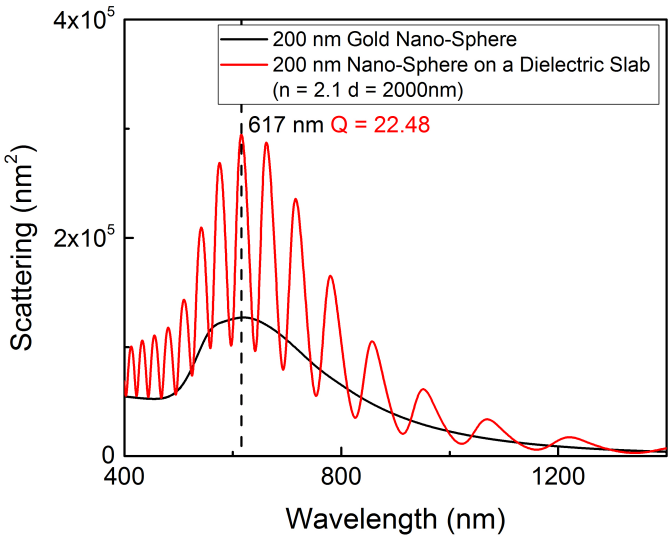

Figure 9.2.4 – Scattering spectrum from a 200 *nm* gold nanoparticle coupled system to a 2 micron dielectric slab with refractive index 2.1 (red). As a comparison, the scattering spectrum for the 200 *nm* gold particle in a vacuum is also shown (black).

As we can see, the Q-factor for this structure is $\sim 10.27\times$ that what we observe from the particle on its own and $\sim 4.66\times$ what we see from the nanoparticle on a gold film in the dipolar mode region. The dielectric slab produces an oscillatory scattering spectrum with the mode at the nanoparticle scattering peak having a FWHM of 27.46 *nm* resulting in a Q-factor of 22.48.

To summarise the data from this section, we can plot the Q-factor to see the trend as the thickness of the dielectric slab changes. This data is shown in Figure 9.2.5.

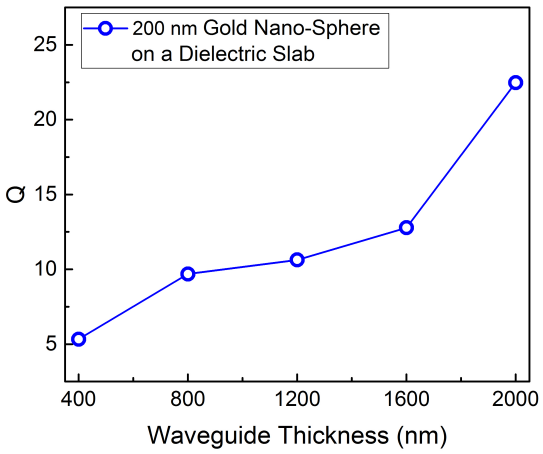

Figure 9.2.5 – Using the scattering data from Figures 9.2.3 and 9.2.4 to show the change in Q-factor of the central scattering peak as a function of dielectric slab thickness.

The Q-factor shows an increase with the thickness of the dielectric slab, this increase in Q-factor is a direct result of dielectric slab modes coupling to the LSPR of the nano-particle. With increased dielectric slab thickness, we see more modes are able to couple to the particle's LSPR. This device has potential to improve upon the nano-gap in terms of LSPR refractive index sensing.

9.2.2.1 Near-Field

By looking as the electric field from the $x-z$ cross section, we can see how the hybrid modes are distributed through the dielectric slab and how their intensity changes through the substrate. This tells us where the majority of the electric field is being confined to in the near-field. Figure 9.2.6 shows the electric field from the 2 μm dielectric slab coupled to the 200 nm gold particle. Due to the large size of the device, for practical purposes we display just over 1 μm into the dielectric slab.

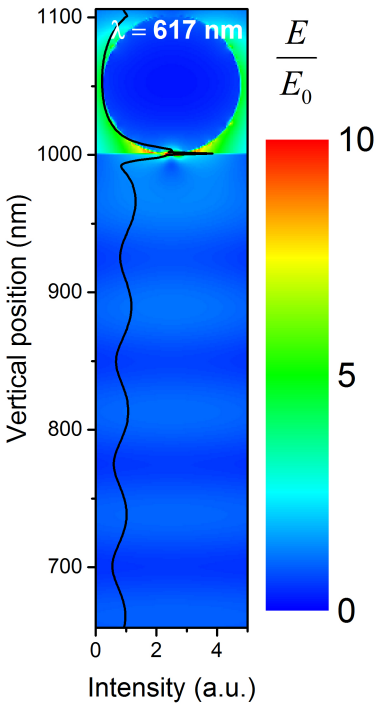

Figure 9.2.6 – Electric field distribution of the 200 *nm* gold nanoparticle deposited on a 2 μm dielectric slab with refractive index 2.1 in the $x-z$ plane under the influence of a TFSF plane wave source at 617 *nm*. Overlaid, is the near-field intensity taken from the centre of the structure.

The intensity of the FP modes are shown to be relatively consistent in intensity through the device, however, most of the field is confined to the regions at the base of the nanoparticle. Next, we display the full device taking the electric field generated vertically in the z axis of the device at its centre from the $x-z$ sensor shown in Figure 9.2.7.

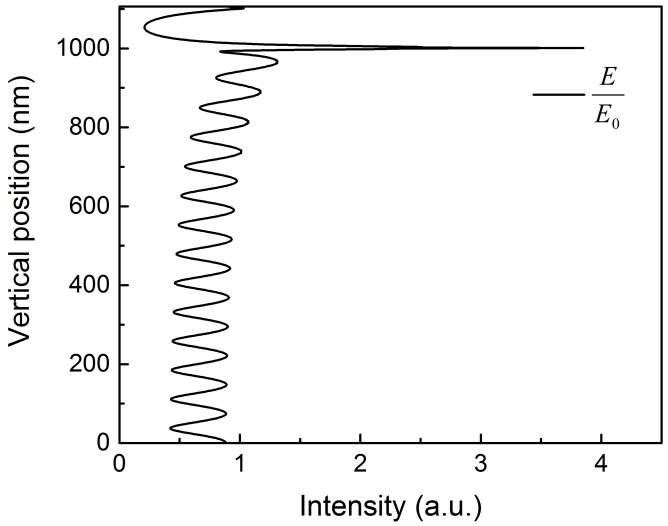

Figure 9.2.7 – Electric field intensity of the 200 *nm* gold nanoparticle deposited on a 2 μm dielectric slab with refractive index 2.1 taken from the centre of the $x-z$ plane sensor under the influence of a TFSF plane wave source at 617 *nm*.

Even though the dielectric slab is very thick, the FP modes are shown to remain fairly consistent in intensity.

9.2.3 Gold Nanoparticle on a DBR

Here, we present a comprehensive study of DBR behaviour when combined with individual nanoparticles regarding their scattering characteristics and electric field coupling. The DBR simulations used a TFSF source incident on a nanoparticle deposited on top of 11 bilayers of TiO_2 and SiO_2 with refractive indexes 2 and 1.45 respectively, where the thickness of each layer was calculated using equation 9.1.1. A schematic diagram for this configuration is shown previously in Figure 9.1.1.

Due to the difference in refractive index for the materials used in the DBR and the reflected light below, these intersections produce standing waves in the form of a FP cavity. Depositing individual nanoparticles onto these substrates allows the cavity and LSPR modes to couple to one another and produces these hybrid plasmonic modes, where the oscillatory nature of the FP modes are enhanced around the LSP resonant frequency. The nanoparticle in a sense behaves essentially as an antenna driving the EM waves into the cavity and upon reflection scatters from the cavity modes of the system.

9.2.3.1 600 nm Stop-Band DBR Nanoparticle Size Distribution Study

Analysing this nanoparticle-DBR hybrid system with a distribution of nanoparticle sizes from $50-300$ *nm*, we see that as the nanoparticle increases in size the system becomes more scattering dominant and a central scattering mode appears. The DBR stop-band in this section is kept at a constant 600 *nm*. The resultant scattering spectra for the nanoparticle size distribution on a DBR can be seen in Figure 9.2.8.

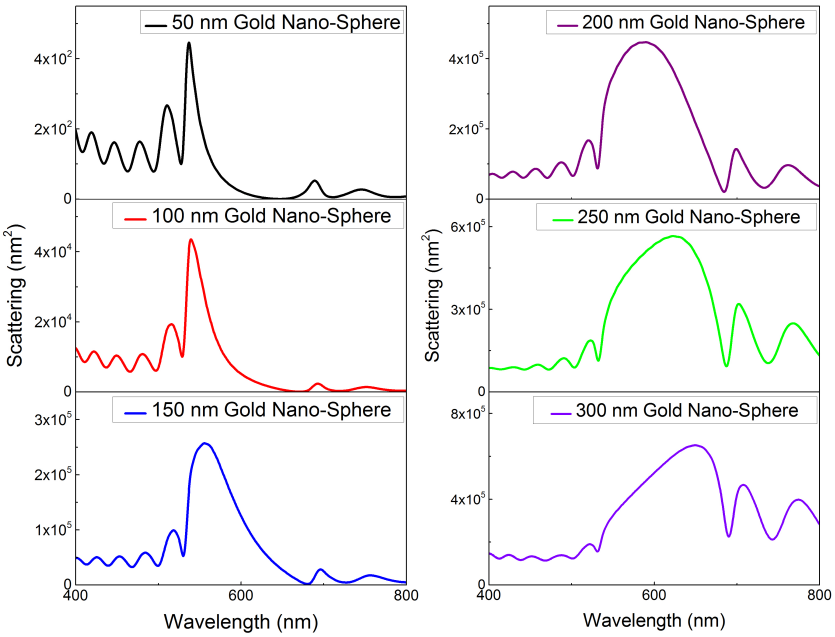

Figure 9.2.8 – Scattering from a 600 *nm* stop-band DBR under the influence of a TFSF plane wave source using a gold nanoparticle size sweep from $50-300$ *nm* at 50 *nm* size intervals.

Once the particle is >150 *nm* in diameter, the extinction is found to be more a result of the scattering than the absorption. Therefore, we use particles larger than this size as the FoM is measured from the scattering under practical circumstances. The 200 *nm* gold particle in this case is the most useful for scattering experiments from a practical standpoint as these sized particles are available commercially.

To understand the scattering spectra in Figure 9.2.8, we summarise the key components of the central mode of the coupled system. Plotting the scattering cross section and peak position as well as the Q-factor derived from equation 9.0.3, we extrapolated the key characteristics of the system in Figure 9.2.9.

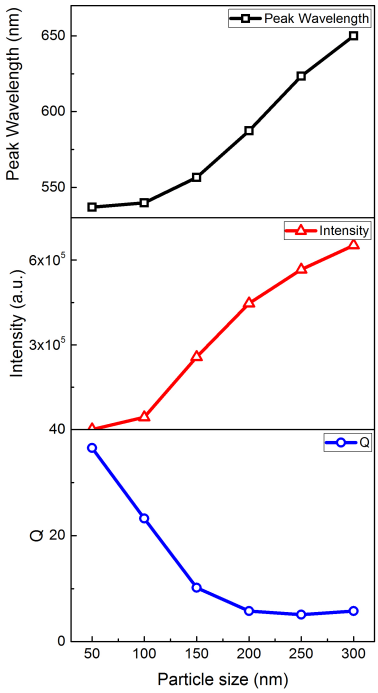

Figure 9.2.9 – Using the scattering data from Figure 9.2.8 to construct graphs depicting the shift in peak wavelength (black) central peak intensity (red) and the Q-factor of shifted peak (blue).

We observe that with increasing particle diameter, there is tunability across the visible spectrum into the near-infrared. As the central mode shifts however, there is broadening in its respective FWHM which results in a lower Q-factor. The overall goal is to narrow the hybrid modes generated in this configuration, therefore the next step is to match the particle with scattering dominated extinction with the narrowest FWHM, in this case, the 200 *nm* gold particle, to its most ideal DBR stop-band.

9.2.3.2 Nanoparticle Coupled to DBR Varying Photonic Stop-Band

Now, by fixing the size of the nanoparticle we can see the effect this has on the scattering when tuning the DBR stop-band wavelength. Each DBR has a different photonic stop-band increasing from $600 - 800$ *nm* in 50 *nm* intervals. Each system produces modes generated from the layers of the DBR, this couples to the plasmon resonance of the nanoparticle and these sub-modes are enhanced at the nanoparticles resonant wavelength. We can see from Figure 9.2.10 that the system is optimised around the 700 *nm* DBR, where

the sub-mode peaks are at their most intense as scattering intensity begins to decline for the 750 *nm* DBR stop-band and onward.

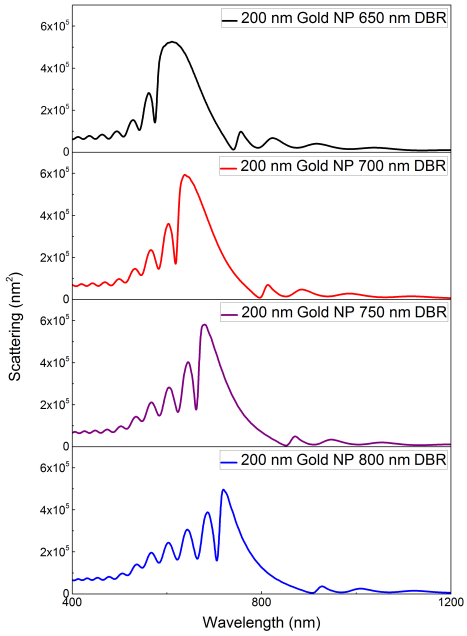

Figure 9.2.10 – Scattering from a 200 *nm* gold nanoparticle under the influence of a TFSF plane wave source on progressively higher photonic stop-band DBRs incrementing at 50 *nm* intervals between 650 – 800 *nm*.

This is shown in Figure 9.2.11 which shows the peak wavelength position of the mode with the largest scattering cross section along with its intensity and Q-factor. The middle panel clearly shows the scattering cross section of the central mode peaks around the 700 *nm* DBR stop-band.

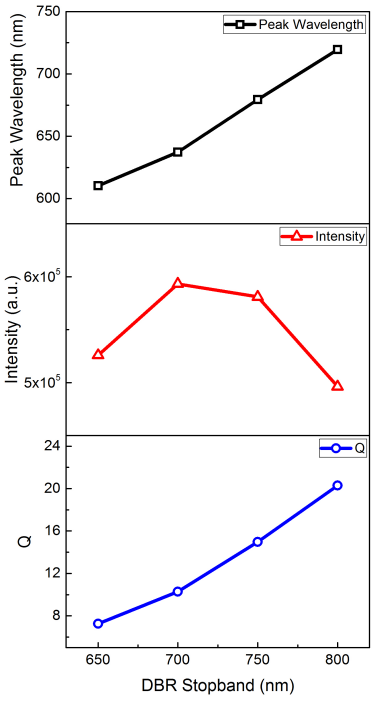

Figure 9.2.11 – Using the scattering data from Figure 9.2.10 to construct graphs depicting the shift in peak wavelength (black) central peak intensity (red) and Q-factor of shifted peak (blue).

We can see the resultant scattering changes associated with the 200 *nm* gold nanoparticle coupled to the DBR in Figure 9.2.11. Once again, the central scattering mode is shifted from the visible into the near-infrared as a function of DBR stop-band. The interesting quality of these structures however, is that although the scattering cross section peaks at the 700 *nm* stop-band, the Q-factor continuously increases past this point. Therefore there is a compromise when choosing the structure.

As a comparison, we show the nanoparticle-DBR hybrid system in this study to have the highest scattering cross section with enhancement of the Q-factor in comparison to the nanoparticle in a vacuum in Figure 9.2.12.

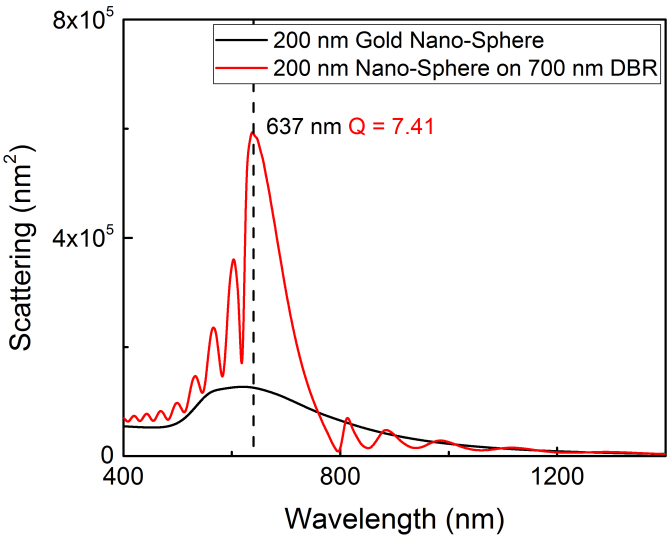

Figure 9.2.12 – 200 *nm* gold nanoparticle coupled system to a 700 *nm* stop-band DBR. As a comparison the scattering spectrum for the 200 *nm* gold particle in a vacuum is also shown (black).

We have therefore shown that, when using 200 *nm* gold particles in conjunction with the DBR, resonant coupling occurs at the 700 *nm* stop-band where extinction is dominated by the scattering component for particles of this size. Although we have a narrower FWHM and subsequently higher Q-factor at 800 *nm* with the central mode being 80% of the width of the 700 *nm* mode, there is a trade-off between the intensities, where the 700 *nm* stop-band peak intensity is $\sim 1.2\times$ larger.

9.2.3.3 Near-Field

To understand the behaviour of light interactions with this structure more intimately, we analyse the $x-z$ cross sectional electric field distribution of the system. This tells us where the majority of the electric field is being confined to in the near-field.

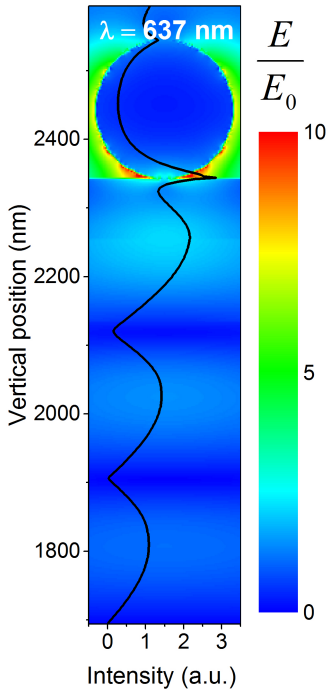

Figure 9.2.13 – Electric field distribution of the 200 *nm* gold nanoparticle deposited on a 700 *nm* stop-band DBR in the $x-z$ plane under the influence of a TFSF plane wave source at 637 *nm*. Overlaid, is the near-field intensity taken from the centre of the structure.

We display just the first few layers of the device here in Figure 9.2.13 as the device is very large, however, the FP modes which are seen, gradually diminish through the device. The majority of the field is confined to the regions at the base of the nanoparticle. For the full device, we can show the electric field generated vertically in the z axis of the device at its centre from the $x-z$ sensor shown in Figure 9.2.14.

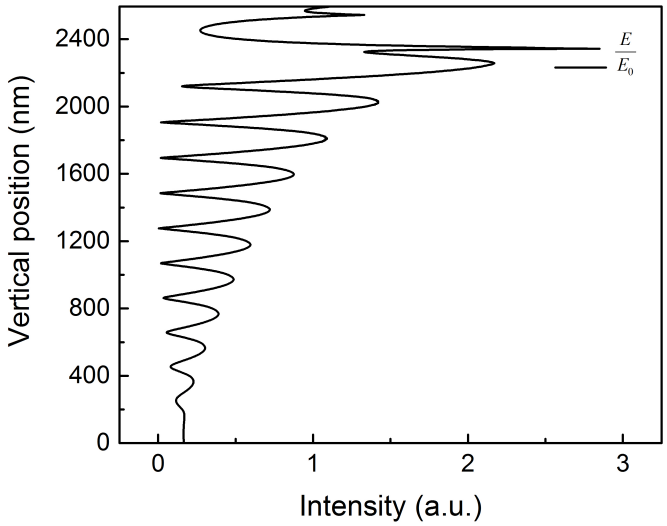

Figure 9.2.14 – Electric field intensity of the 200 *nm* gold nanoparticle deposited on a 700 *nm* stop-band DBR taken from the centre of the $x-z$ plane sensor under the influence of a TFSF plane wave source at 637 *nm*.

Again, the FP modes are shown to gradually diminish and the majority of the near-field is confined to the nanoparticle, more specifically the lower region of the nanoparticle in contact with the DBR. By also analysing the electric field from a monitor placed close to this region of high field intensity 5 *nm* below the particle in the $x-y$ cross section, we see that the hot spot generated here is a result of the nanoparticle and DBR coupling to one another.

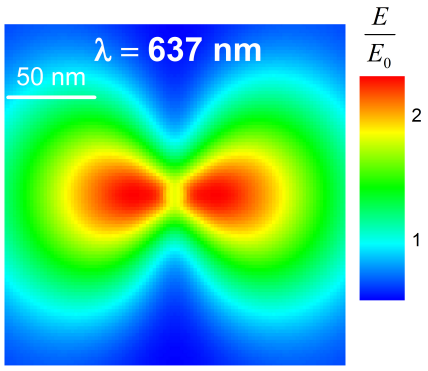

Figure 9.2.15 – Electric field distribution of the 200 *nm* gold nanoparticle deposited on a 700 *nm* stop-band DBR in the $x-y$ plane 5 *nm* below the particle under the influence of a TFSF plane wave source at 637 *nm*.

This electric field is very low in comparison to the nano-gaps we studied throughout

the course of the other chapters. So, this structure would be more suitable for LSPR refractive index sensing as opposed to SERS as we have previously investigated.

9.3 Summary

Overall, the data in this chapter has provided a useful insight into the coupling characteristics of plasmonic systems with photonic devices. We have shown, by coupling nanoparticles to dielectric slabs and DBRs, it is possible to create narrow sub-modes by coupling the cavity modes to the LSPR of the particle. With a higher Q-factor, these hybrid modes have the potential to increase the sensitivity of LSPR based refractive index sensing for events such as molecular binding.

First of all, we studied the effect of different thicknesses of dielectric slabs coupled to the 200 *nm* gold particle. By increasing the thickness of the dielectric slab, we were able to produce more modes for the particle to couple to, this led to narrower hybrid modes and an increased Q-factor. The Q-factor demonstrated an increase in response to dielectric slab thickness. At 2 μm our dielectric slab nanoparticle hybrid system had the highest Q-factor of the systems we investigated at 22.48. In comparison, the particle in a vacuum the Q-factor for this structure is 10.27$\times$ larger and 4.66$\times$ higher than what we see from the nanoparticle on a gold film in the dipolar mode region.

The DBR optimisation study has yielded important results with regard to the scattering mechanisms of these systems, enhancing the Q-factor of the nanoparticle on its own by $\sim 3.4\times$, and showing the device has potential to be a strong contender for its refractive index sensing capabilities. We optimised the size of the nanoparticle to the ideal DBR stop-band to improve the line-width of the device as much as possible. Our final DBR-nanoparticle hybrid system used a 700 *nm* DBR with a 200 *nm* gold particle. It is shown that although in these cases the dielectric slab produces narrow spectral line-width, the DBR has a much larger scattering at its peak photonic stop-band.

It would be interesting to continue this work and investigate the effect of changing the refractive index of the environment surrounding the nanoparticle to see the effect this has on the FoM of the system.

Chapter 10

Conclusion and Future Work

10.1 Conclusions

This thesis describes investigations into plasmonic behaviours of nano-gap geometry and their application towards molecular sensing via Raman spectroscopy. Overall, the work has successfully shown the practical applications of these systems and the enhancement characteristics they provide. We use this final section to discuss the conclusions drawn from each results chapter, considering their implications to the fields of plasmonics and biosensing as well as looking forward to what the work could mean to the future of these research disciplines and how they could be further developed.

Previously, LSPR characteristics have only probed the surface or had been entirely overlooked this area of the research in terms of the optimisation when considering near and far-field scattering characteristics. We show there is now fundamentally deeper comprehension as a result of our work.

Chapter 5 involves an in depth study on the extinction characteristics from a systematic sweep of particle geometry on a nano-gap formed between the particle and the film below (which is usually substantial enough for LSP optimisation for most work). Following this, further study was produced regarding the electric field profiles of the system at cross sections through the particle film geometry plus at the centre of the cavity where fields were mainly confined to. Then, to fully understand the systems behaviour, we looked at the charge density and far-field scattering characteristics. This enabled us to formulate a figure of merit regarding the performance output of the structure that fully encompasses how the particle cavity system scatters its fields and whether they would reach the far-field to be collected by an $NA = 0.55$ objective lens.

The optimisation process we employed via FDTD methods has also been experimentally proven in Chapter 6 given the particle size and shape study we undertook. Due to the evidence for single molecule detection we showed, the results substantiate that the system can achieve this ultimate limit of detection and we can confidently say that the nano-gap based sensor is a powerful tool in the field of plasmonics and nano-sensing capable of SM-SERS.

Not only this, but when taking a comparison of the theoretical (see Figure 5.6.12 section 5.6.5) and experimental enhancement ratios between the 100 *nm* and 200 *nm* particles (or from a practical standpoint the 118 *nm* particles as we observed via SEM imaging), we show there is a striking resemblance in the relative enhancement. In the case of our simulations, the projected enhancement was much higher from the 118 *nm* in comparison to the 60 *nm* than the 200 *nm* particle from Figure 6.1.4b. This was demonstrated experimentally, where we found the relative enhancement between the 118 *nm* and 200 *nm* at 532 *nm* excitation to be $\sim 4.2\times$ on average, and when compared to the 60 *nm* particles it was $\sim 7.73\times$ more intense (from Figure 6.1.5).

Putting this knowledge into practice, we used the system to detect R6G and CV to adequate concentrations such that attributes of orientational single molecule detection were observed. Also, when these materials were used in a mixture within these gaps, it was shown to be possible to distinguish the two molecule's individual unique spectra from one another.

We defined the single molecule behaviour by the rotational properties of the analyte under investigation within the gap. At relatively high concentrations, the molecular orientation would be randomised and many analytes within this region would contribute to the scattered spectra. However, upon entering the single molecule regime certain orientations of the molecule will correspond to alignment of the molecular bonds with the cavity field. Therefore, when a single molecule is present in the nano-gap, the Raman signal response will be dependant on the orientation of the molecule leading to certain modes being enhanced or suppressed relative to the bond alignment with the cavity system and their ability to couple to it. We show evidence for this and thus proof of successful single

molecule Raman from our system in section 6.3.

Following our work investigating single molecule characterisation of fluorescent materials, which analysed the orientation effects from molecules within the nano-gap, and the influence this has on the Raman spectra produced, in Chapter 7, we began looking at trace levels of F8-PFB which is a conjugated polymer. The previous investigation had been from a purely electromagnetic enhancement perspective using a secondary polymer matrix buffer which was optically transparent in the region of interest for the Raman spectra of our target molecule. This polymer provided a barrier between the target material and the metallic nanostructure, thereby minimizing the potential of photo-induced chemical processes in the Raman signal which become more apparent when the material is in contact with the system. In this study however, we utilise the material itself to form the basis of the cavity between the particle and the film below. Therefore, this system classifies the single molecule regime via the presence of intensity blinking events which are characteristic of SM-SERS.

Due to its more favourable absorption region relative to F8-BT which was shown to fluoresce strongly with our 532 *nm* laser line, investigations at low concentrations were performed with F8-PFB using non-resonant Raman. We focussed on the 1605 cm^{-1} mode which equates to the C-C stretching vibration of the material, and is the most prominent vibrational marker in its spectrum. We observed several instances of intensity blinking phenomena, where, over a period of $30-60$ seconds, measurements were collected in 3 second intervals. During this time, the peak intensity of the 1605 cm^{-1} mode fluctuated in and out of the double standard deviation region centred at the data series average. This was not the case when successive measurements were taken at higher concentrations, therefore, we defined a transition region at 2.8×10^{-9} M for when single molecule characteristics occurred. This was further proven when measurements at 2.8×10^{-10} M yielded similar enhancement levels and intensity variation characteristics demonstrating the measurements acquired were a contribution of comparable molecule populations.

Although the resonance condition was not fulfilled in these measurements so the additional contribution of SERRS enhancement could not be taken advantage of, we did see

sufficient field enhancement owing to the exponential increase associated with narrowing of the nano-gap which we proved in Figure 5.3.7 from section 5.3.4 of our theoretical study.

We also showed experimental results obtained when applying the nanoparticle on a film geometry to biological systems in Chapter 8. We investigated the molecular structures of Bovine Serum Albumin (BSA) and lysozyme, two proteins which perform vital roles in living organisms. By analysing the Raman spectra of the materials from clusters of silver nanoparticles, we were able to show conformation changes in lysozyme after it had undergone exposure to UV light for given periods of time. Because lysozyme concentration changes correlate to certain diseases in the body, it is integral to possess the means to detect this material even at low concentrations. Conformation changes of proteins are a good indicator for them undergoing processes within the body, so being able to retrieve data regarding the molecular fingerprint of a material during this is very advantageous. The results indicated a reduction in the peak intensity of the Trp modes as time under UV exposure progressed. We also observed evidence for the formation of disulphide bonds which are synonymous with this kind of reaction.

Evidently, our system is capable to perform as a biological sensor. However, there are some details which need to be further investigate. For example, drop casting particles with the material led to clustering and inconsistent surface geometry, therefore, the optimisation work carried out in Chapter 5 is less applicable. We see further evidence for this when probing BSA, although the spectra obtained from the material from the 532 *nm* laser shows the material very clearly, there is a $14\times$ enhancement when moving to the 635 *nm* line. Therefore, we can state that the resonance position has shifted for many particle systems.

Overall, the work has shown successful investigations of plasmonic nanostructures and has benefited our understanding of the way they behave allowing us to use them for the ultimate limits of detection. We have applied them to various materials and have accomplished many goals set out early in the project. The research presented here opens the potential to be applied to other extensions of the field in terms of sensing and detection

methodology.

Finally, Chapter 9 of this thesis investigated the effect of plasmon hybridisation to alternative substrates than our metallic films. It was shown to be possible to create discrete, hybrid modes at the LSPR of the system. By coupling the metal nanoparticle to a dielectric slab or DBR, a strong dipolar resonance occurred. In this case, scattering from these geometries outperforms nanoparticles on their own.

We demonstrate via a systematic study of particle on dielectric slab and DBR geometry the narrowing of the spectral line-width of the system. Our results provide evidence to support through FDTD methodology the ideal particle size and material to be coupled with its constituent DBR, giving maximum peak intensity and narrowest spectral line-width occurring with 200 *nm* diameter gold nanoparticles coupled to a 700 *nm* stop-band DBR. This nanoparticle-DBR hybrid system produced a Q-factor of 7.41 which is 3.4× what we saw from the nanoparticle on its own.

There is also a large reduction in the spectral line-width of the 200 *nm* gold particle when coupled to a dielectric slab, however, there is a trade-off as these narrower hybrid modes have lower scattering cross sections. The 200 *nm* gold particle coupled to the 2 μm dielectric slab produced a Q-factor of 22.48, this is over 10× what we saw from the particle on its own. Judging from these conclusions, it seems that the nanoparticle coupled to a dielectric slab or DBR in this configuration could have good potential for LSPR sensing in the near infrared region due to their theoretically high Q-factors.

10.2 Future Work

This research has been an excellent opportunity to explore plasmonics and sensing leading to a deeper understanding of light matter interactions. There is however, always more to investigate and the content for this subject is becoming more interesting with every publication being made.

Plasmonics is a rapidly developing research area and focusing efforts to improve the nano-gap geometry used with other more exotic materials would be worthwhile. Ideally, it would be beneficial to create these cavities with arrays to remove the randomness of

depositing nanoparticles at low concentrations, which allows for spectra to be taken from single particles. Also, single molecule studies require many measurements to be taken from the substrate, this is because the potential for a particle cavity system to have a molecule within its hot spot region is reduced significantly. Therefore, by having an automated scanning system to methodically take measurements across this array would allow for a broader distribution of data to analyse. This would allow probability distribution studies to be performed and more evidence of SM-SERS to be generated to back our claims [61, 69]. Along with this, it would be interesting to examine SERS measurements from a 405 *nm* laser line using the smaller silver nano-spheres which produced larger enhancements in our FoM. We would then see whether their narrow modes would have an effect on the enhancement of the Raman scattering.

As nanoparticles are not the only way to couple light to the metal surface, it would be interesting to observe the enhancement qualities of nano-gaps formed between particles and other geometries. For example, periodic gratings could be tuned to the particle to enhance the signal even further, pushing the boundaries beyond what these devices have shown to be capable of from this thesis.

Along with this, a deeper investigation into conformation changes in proteins would be an interesting direction to take this research. We have seen encouraging results from our investigation, however, more thorough exploration into the effects of particle clustering and alternative approaches to localising the target biological material to the hot spot of the nanostructure are necessary. Atomic Force Microscopy (AFM) could have potential for better understanding of the geometry we have currently used and allow us to perform more refined simulations. By using TERS, it may be possible to move the location of the hot spot to the analyte as opposed to attempting to localise the molecule below the particle.

References

[1] C. J. Eling, T. W. Price, A. R. L. Marshall, F. Narda Viscomi, P. Robinson, G. Firth, A. M. Adawi, J.-S. G. Bouillard, and G. J. Stasiuk. A Dual-Modal SERS/Fluorescence Gold Nanoparticle Probe for Mitochondrial Imaging. *ChemPlusChem*, 82(5):674–680, may 2017.

[2] A. R. L. Marshall, J. Stokes, F. N. Viscomi, J. E. Proctor, J. Gierschner, J.-S. G. Bouillard, and A. M. Adawi. Determining molecular orientation via single molecule SERS in a plasmonic nano-gap. *Nanoscale*, 9(44):17415–17421, 2017.

[3] D. Smith, M. A. Hakeem, P. Parisiades, H. E. Maynard-Casely, D. Foster, D. Eden, D. J. Bull, A. R. L. Marshall, A. M. Adawi, R. Howie, A. Sapelkin, V. V. Brazhkin, and J. E. Proctor. Crossover between liquidlike and gaslike behavior in CH4 at 400 K. *Physical Review E*, 96(5):052113, 2017.

[4] S. A. Maier. *PLASMONICS: FUNDAMENTALS AND APPLICATIONS*. Springer, Bath, 1st edition, 2007.

[5] R. P. H. Kooyman. Chapter 2: Physics of Surface Plasmon Resonance. In R. B. M. Schasfoort and A. J. Tudos, editors, *Handbook of Surface Plasmon Resonance*, pages 15–34. Royal Society of Chemistry, London, 1st edition, 2008.

[6] Y. Wang, E. W. Plummer, and K. Kempa. Foundations of Plasmonics. *Advances in Physics*, 60(5):799–898, 2011.

[7] S. Zouhdi, S. Ari, and A. P. Vinogradov. *Metamaterials and Plasmonics Fundementals, Modelling, Applications*. Springer, New York City, 1st edition, 2013.

[8] Heinz Raether. *Surface Plasmons on Smooth and Rough Surfaces and on Gratings*, volume 111 of *Springer Tracts in Modern Physics*. Springer Berlin Heidelberg, Berlin, 1st edition, 1988.

[9] I. Freestone, N. Meeks, M. Sax, and C. Higgitt. The Lycurgus Cup-A Roman Nanotechnology. *Gold Bulletin*, 40(4):270–277, 2007.

[10] M. Faraday. The Bakerian Lecture: Experimental Relations of Gold (and Other Metals) to Light. *Philosophical Transactions of the Royal Society of London*, 147:145–181, jan 1857.

[11] J. C. Maxwell. The Theory of Molecular Vortices applied to Magnetic Phenomena. *Philosophical Magazine and Journal of Sciences*, 3:168–172, 1861.

[12] G. Mie. Contributions to the optics of turbid media, particularly of colliodal metal solutions. *Ann. Phys.*, 25(3):377–445, 1908.

[13] R. H. Ritchie. Surface plasmons in solids. *Surface Science*, 34(1):1–19, 1973.

[14] M. E. Stewart, C. R. Anderton, L. B. Thompson, J. Maria, S. K. Gray, J. A. Rogers, and R. G. Nuzzo. Nanostructured Plasmonic Sensors. *Chemical Reviews*, 108(2):494–521, feb 2008.

[15] K. L. Kelly, E. Coronado, L. L. Zhao, and G. C. Schatz. The Optical Properties of Metal Nanoparticles: The Influence of Size, Shape, and Dielectric Environment. *The Journal of Physical Chemistry B*, 107(3):668–677, jan 2003.

[16] E. Ringe, J. M. McMahon, K. Sohn, C. Cobley, Y. Xia, J. Huang, G. C. Schatz, L. D. Marks, and R. P. Van Duyne. Unraveling the Effects of Size, Composition, and Substrate on the Localized Surface Plasmon Resonance Frequencies of Gold and Silver Nanocubes: A Systematic Single-Particle Approach. *The Journal of Physical Chemistry C*, 114(29):12511–12516, jul 2010.

[17] W. Hermoso, T. V. Alves, C. C. de Oliveira, E. G. Moriya, F. R. Ornellas, and P. H. Camargo. Triangular metal nanoprisms of Ag, Au, and Cu: Modeling the influence of size, composition, and excitation wavelength on the optical properties. *Chemical Physics*, 423:142–150, sep 2013.

[18] H. Shen, G. Lu, T. Zhang, J. Liu, Y. Gu, P. Perriat, M. Martini, O. Tillement, and Q. Gong. Shape effect on a single-nanoparticle-based plasmonic nanosensor. *Nanotechnology*, 24(285502):1–8, jul 2013.

[19] M. A. Mahmoud and M. A. El-sayed. Different Plasmon Sensing Behavior of Silver and Gold Nanorods. *The Journal of Physical Chemistry Letters*, 4(9):1541–1545, 2013.

[20] C. Sönnichsen, B. M. Reinhard, J. Liphardt, and A. P. Alivisatos. A molecular ruler based on plasmon coupling of single gold and silver nanoparticles. *Nature biotechnology*, 23(6):741–745, jun 2005.

[21] A. Grimault, A. Vial, and M. Lamy de la Chapelle. Modeling of regular gold nanostructures arrays for SERS applications using a 3D FDTD method. *Applied Physics B*, 84(1-2):111–115, jul 2006.

[22] L. J. Sherry, S.-H. Chang, G. C. Schatz, R. P. Van Duyne, B. J. Wiley, and Y. Xia. Localized Surface Plasmon Resonance Spectroscopy of Single Silver Nanocubes. *Nano Letters*, 5(10):2034–2038, oct 2005.

[23] W. Cao, T. Huang, X.-H. N. Xu, and H. E. Elsayed-Ali. Localized surface plasmon resonance of single silver nanoparticles studied by dark-field optical microscopy and spectroscopy. *Journal of applied physics*, 109(034310):1–6, feb 2011.

[24] A. M. Adawi, M. M. Murshidy, P. W. Fry, and D. G. Lidzey. An Optical Nanocavity Incorporating a Fluorescent Organic Dye Having a High Quality Factor. *ACS Nano*, 4(6):3039–3044, 2010.

[25] J. J. Mock, R. T. Hill, A. Degiron, S. Zauscher, A. Chilkoti, and D. R. Smith. Distance-Dependent Plasmon Resonant Coupling Between a Gold Nanoparticle and Gold Film. *Nano Letters*, 8(8):2245–2252, 2008.

[26] D. Y. Lei, A. I. Fernández-Domínguez, Y. Sonnefraud, K. Appavoo, R. F. Haglund, J. B. Pendry, and S. A. Maier. Revealing Plasmonic Gap Modes in Particle-on-Film Systems Using Dark-Field Spectroscopy. *ACS Nano*, 6(2):1380–1386, 2012.

[27] X. Wang, M. Li, L. Meng, K. Lin, J. Feng, T. Huang, Z. Yang, and B. Ren. Probing the Location of Hot Spots by Surface-Enhanced Raman Spectroscopy: Toward Uniform Substrates. *ACS Nano*, 8(1):528–536, 2014.

[28] M. A. Schmidt, D. Y. Lei, L. Wondraczek, V. Nazabal, and S. A. Maier. Hybrid nanoparticle-microcavity-based plasmonic nanosensors with improved detection resolution and extended remote-sensing ability. *Nature communications*, 3(May):1108, oct 2012.

[29] R. T. Hill, J. J. Mock, Y. Urzhumov, D. S. Sebba, S. J. Oldenburg, S.-Y. Y. Chen, A. A. Lazarides, A. Chilkoti, and D. R. Smith. Leveraging nanoscale plasmonic modes to achieve reproducible enhancement of light. *Nano Letters*, 10(10):4150–4154, oct 2010.

[30] Y. Shen, J. Zhou, T. Liu, Y. Tao, R. Jiang, M. Liu, G. Xiao, J. Zhu, Z.-K. Zhou, X. Wang, C. Jin, and J. Wang. Plasmonic gold mushroom arrays with refractive index sensing figures of merit approaching the theoretical limit. *Nature communications*, 4:2381, 2013.

[31] Y. Shen and C. Jin. Double-layered gold gratings as refractive index sensors with ultrahigh figure of merits. *Advanced Photonics*, pages 10–12, 2015.

[32] Y. H. Jang, Y. J. Jang, S. Kim, L. N. Quan, K. Chung, and D. H. Kim. Plasmonic Solar Cells: From Rational Design to Mechanism Overview. *Chemical Reviews*, 116(24):14982–15034, dec 2016.

[33] S. Kawata, Y. Inouye, and P. Verma. Plasmonics for near-field nano-imaging and superlensing. *Nature Photonics*, 3(7):388–394, 2009.

[34] S. Hayashi and T. Okamoto. Plasmonics: visit the past to know the future. *Journal of Physics D: Applied Physics*, 45(433001):1–24, 2012.

[35] C. Raman and K. Krishnan. A New Type of Secondary Radiation. *Nature*, 121(3048):501–502, 1928.

[36] T. Itoh and Y. S. Yamamoto. Recent topics on Single-Molecule fluctuation analysis using blinking in surface-enhanced resonance Raman scattering: clarification by the electromagnetic mechanism. *Analyst*, 141(17):5000–5009, 2016.

[37] M. Fleischmann, P. J. Hendra, and A. J. McQuillan. Raman spectra of pyridine adsorbed at a silver electrode. *Chemical Physics Letters*, 26(2):163–166, 1974.

[38] P. G. Etchegoin and E. C. Le Ru. A perspective on single molecule SERS: current status and future challenges. *Phys. Chem. Chem. Phys.*, 10(40):6079–6089, 2008.

[39] B. Sharma, R. R. Frontiera, A.-I. Henry, E. Ringe, and R. P. Van Duyne. SERS: Materials, applications, and the future. *Materials Today*, 15(15):16–25, 2012.

[40] G. Das, F. Mecarini, F. Gentile, F. De Angelis, H. Mohan Kumar, P. Candeloro, C. Liberale, G. Cuda, and E. Di Fabrizio. Nano-patterned SERS substrate: Application for protein analysis vs. temperature. *Biosensors and Bioelectronics*, 24(6):1693–1699, feb 2009.

[41] C. David, N. Guillot, H. Shen, T. Toury, and M. L. de la Chapelle. SERS detection of biomolecules using lithographed nanoparticles towards a reproducible SERS biosensor. *Nanotechnology*, 21(475501):1–6, nov 2010.

[42] K.-M. Byun. Development of Nanostructured Plasmonic Substrates for Enhanced Optical Biosensing. *Journal of the Optical Society of Korea*, 14(2):65–76, jun 2010.

[43] P. He, Y. Zhang, L. Liu, W. Qiao, and S. Zhang. Ultrasensitive SERS Detection of Lysozyme by a Target-Triggering Multiple Cycle Amplification Strategy Based on a Gold Substrate. *Chemistry - A European Journal*, 19(23):7452–7460, 2013.

[44] W. Ji, L. Chen, X. Xue, Z. Guo, Z. Yu, B. Zhao, and Y. Ozaki. Design of an anti-aggregated SERS sensing platform for metal ion detection based on bovine serum albumin-mediated metal nanoparticles. *Chemical communications (Cambridge, England)*, 49(66):7334–7336, aug 2013.

[45] C. Fu, Y. Gu, Z. Wu, Y. Wang, S. Xu, and W. Xu. Surface-enhanced Raman scattering (SERS) biosensing based on nanoporous dielectric waveguide resonance. *Sensors and Actuators B: Chemical*, 201:173–176, oct 2014.

[46] D. Radziuk and H. Moehwald. Prospects for plasmonic hot spots in single molecule SERS towards the chemical imaging of live cells. *Phys. Chem. Chem. Phys.*, 17(33):21072–21093, 2015.

[47] Y. Chen, X. Bai, L. Su, Z. Du, A. Shen, A. Materny, and J. Hu. Combined Labelled and Label-free SERS Probes for Triplex Three- dimensional Cellular Imaging. *Scientific Reports*, 6(19173):1–12, 2016.

[48] C. L. Brosseau, F. Casadio, and R. P. Van Duyne. Revealing the invisible: Using surface-enhanced Raman spectroscopy to identify minute remnants of color in Winslow Homer's colorless skies. *Journal of Raman Spectroscopy*, 42(6):1305–1310, 2011.

[49] R. A. Álvarez-Puebla and L. M. Liz-Marzán. Environmental applications of plasmon assisted Raman scattering. *Energy & Environmental Science*, 3(8):1011, 2010.

[50] S. Senapati, S. K. Srivastava, S. B. Singh, and A. R. Kulkarni. SERS active Ag encapsulated Fe@SiO2 nanorods in electromagnetic wave absorption and crystal violet detection. *Environmental Research*, 135:95–104, nov 2014.

[51] E. L. Izake. Forensic and homeland security applications of modern portable Raman spectroscopy. *Forensic Science International*, 202(1-3):1–8, 2010.

[52] S. Nie and S. Emory. Probing Single Molecules and Single Nanoparticles by Surface-Enhanced Raman Scattering. *Science*, 275(5303):1102–1106, 1997.

[53] K. Kneipp, Y. Wang, H. Kneipp, L. T. Perelman, I. Itzkan, R. R. Dasari, and M. S. Feld. Single Molecule Detection Using Surface-Enhanced Raman Scattering (SERS). *Physical Review Letters*, 78(9):1667–1670, 1997.

[54] K. Kneipp, H. Kneipp, I. Itzkan, R. R. Dasari, and M. S. Feld. Surface-enhanced Raman scattering and biophysics. *Journal of Physics: Condensed Matter*, 14(18):597–624, 2002.

[55] B. Tolaieb, J. L. Constantino, and R. F. Aroca. Surface-enhanced resonance Raman scattering as an analytical tool for single molecule detection. *The Analyst*, 129:337–341, 2004.

[56] K. Kneipp and H. Kneipp. Single Molecule Raman Scattering. *Focal point*, 60(12):322–334, 2006.

[57] E. C. Le Ru, E. Blackie, M. Meyer, and P. G. Etchegoin. Surface Enhanced Raman Scattering Enhancement Factors: A Comprehensive Study. *The Journal of Physical Chemistry C*, 111(37):13794–13803, sep 2007.

[58] N. P. W. Pieczonka and R. F. Aroca. Single molecule analysis by surfaced-enhanced Raman scattering. *Chemical Society reviews*, 37(5):946–954, 2008.

[59] S. Buchanan, E. C. Le Ru, and P. G. Etchegoin. Plasmon-dispersion corrections and constraints for surface selection rules of single molecule SERS spectra. *Physical Chemistry Chemical Physics*, 11(34):7406, 2009.

[60] Y. Wu, P. Nordlander, D. Substrates, Y. Wu, and P. Nordlander. Finite-Difference Time-Domain Modeling of the Optical Properties of Nanoparticles near dielectric substrates. *J. Phys. Chem.*, 114(713):7302–7307, 2010.

[61] P. G. Etchegoin, E. C. Le Ru, and A. Fainstein. Bi-analyte single molecule SERS technique with simultaneous spatial resolution. *Phys. Chem. Chem. Phys.*, 13(10):4500–4506, 2011.

[62] H. M. Lee, S. M. Jin, H. M. Kim, and Y. D. Suh. Single-molecule surface-enhanced Raman spectroscopy: a perspective on the current status. *Phys. Chem. Chem. Phys.*, 15(15):5276–5287, 2013.

[63] R. Zhang, Y. Zhang, Z. C. Dong, S. Jiang, C. Zhang, L. G. Chen, L. Zhang, Y. Liao, J. Aizpurua, Y. Luo, J. L. Yang, and J. G. Hou. Chemical mapping of a single molecule by plasmon-enhanced Raman scattering. *Nature*, 498(7452):82–86, jun 2013.

[64] K. Wang, Dongxing. Zhu, Wenqi. Michael, Best. Camden, Jon. Crozier, D. Wang, W. Zhu, B. Michael, J. Camden, K. Crozier, and K. Wang, Dongxing. Zhu, Wenqi. Michael, Best. Camden, Jon. Crozier. Directional Raman Scattering from Single Molecules in the Feed Gaps of Optical Antennas. *Nano letters*, 1(5):2194–2198, 2013.

[65] K. B. Crozier, W. Zhu, D. Wang, S. Lin, M. D. Best, and J. P. Camden. Plasmonics for Surface Enhanced Raman Scattering: Nanoantennas for Single Molecules. *IEEE Journal of Selected Topics in Quantum Electronics*, 20(3):1–11, 2014.

[66] A. M. Michaels, M. Nirmal, and L. E. Brus. Surface enhanced Raman spectroscopy of individual rhodamine 6G molecules on large Ag nanocrystals. *Journal of the American Chemical Society*, 121(43):9932–9939, 1999.

[67] A. M. Michaels and L. Brus. Ag Nanocrystal Junctions as the Site for Surface-Enhanced Raman Scattering of Single Rhodamine 6G Molecules. *The Journal of Physical Chemistry B*, 104(50):11965–11971, dec 2000.

[68] S. A. Meyer, E. C. L. Ru, and P. G. Etchegoin. Quantifying Resonant Raman Cross Sections with SERS. *Journal of Physical Chemistry A*, 114(17):5515–5519, 2010.

[69] S. L. Kleinman, E. Ringe, N. Valley, K. L. Wustholz, E. Phillips, K. A. Scheidt, G. C. Schatz, and R. P. Van Duyne. Single-Molecule Surface-Enhanced Raman Spectroscopy of Crystal Violet Isotopologues: Theory and Experiment. *Journal of the American Chemical Society*, 133(11):4115–4122, 2011.

[70] Z. Luo, W. Hunter Woodward, and A. W. Castleman. Distinguishable behavior of multiple and individual rhodamine-6G molecules on spherical Ag nanoparticles examined via time dependence of the SERS spectra. *Journal of Raman Spectroscopy*, 43(12):1905–1912, 2012.

[71] K. Kim and K. S. Shin. Surface-Enhanced Raman Scattering: a Powerful Tool for chemical Identification. *Analytical sciences : the international journal of the Japan Society for Analytical Chemistry*, 27(8):775–783, 2011.

[72] Z. Wang and L. J. Rothberg. Origins of Blinking in Single-Molecule Raman Spectroscopy. *J. Phys. Chem.*, 8(109):3387–3391, 2005.

[73] J. R. Lombardi and R. L. Birke. Single Molecule SERS Spectral Blinking and Vibronic Coupling. *Journal of Physical Chemistry C*, 115(11):4540–4545, 2011.

[74] M. Pelton and G. Bryant. *Introduction to Metal-Nanoparticle Plasmonics*. Wiley-Blackwell, New Jersey, 1st edition, 2013.

[75] P. Johnson and R. Christy. Optical Constants of the Noble Metals. *Physical Review B - Condensed Matter and Materials Physics*, 6(12):4370–4379, 1972.

[76] E. C. Le Ru and P. G. Etchegoin. *Principles of Surface Enhanced Raman Spectroscopy and related plasmonic effects*. Number 1. Elsevier Ltd, Amsterdam, 1st edition, 2009.

[77] A. Vial, A. S. Grimault, D. Macías, D. Barchiesi, and M. Lamy De La Chapelle. Improved analytical fit of gold dispersion: Application to the modeling of extinction spectra with a finite-difference time-domain method. *Physical Review B - Condensed Matter and Materials Physics*, 71(8):1–7, 2005.

[78] L. Mao, Z. Li, B. Wu, and H. Xu. Effects of quantum tunneling in metal nanogap on surface-enhanced Raman scattering. *Applied Physics Letters*, 94(243102):16–19, 2009.

[79] K. J. Savage, M. M. Hawkeye, R. Esteban, A. G. Borisov, J. Aizpurua, and J. J. Baumberg. Revealing the quantum regime in tunnelling plasmonics. *Nature*, 491(7425):574–577, 2012.

[80] N. F. van Hulst. Plasmon quantum limit exposed. *Nature nanotechnology*, 7(12):775–777, 2012.

[81] M. Scalora, M. A. Vincenti, D. D. Ceglia, and J. W. Haus. Nonlocal and Quantum Tunneling Contributions to Harmonic Generation in Nanostructures: Electron Cloud Screening Effects. *Physical Review A*, 90(1):1–8, 2014.

[82] R. Esteban, A. G. Borisov, P. Nordlander, and J. Aizpurua. Bridging quantum and classical plasmonics with a quantum-corrected model. *Nature Communications*, 3:1–9, may 2012.

[83] O. Benson. Plasmonics. In *Elements of Nanophotonics*, chapter 7, pages 208–239. Wiley, Berlin, 1st edition, 2009.

[84] D. Mortazavi, A. Z. Kouzani, and A. Kaynak. Nano-plasmonic Biosensors : A Review. *IEEE/ICME*, 2011:31–36, 2011.

[85] K. Kneipp. Surface-Enhanced Raman Scattering. *Physics Today*, 60(11):40–46, 2007.

[86] C. Bohren and D. Huffman. *Absorption and Scattering of Light by Small Particles*. Wiley, New York, 1st edition, 1983.

[87] Nanocomposix. http://nanocomposix.com/pages/tools, 2017.

[88] E. Prodan, C. Radloff, N. J. Halas, and P. Nordlander. A hybridization model for the plasmon response of complex nanostructures. *Science (New York, N.Y.)*, 302(5644):419–422, 2003.

[89] F. Le, N. Z. Lwin, J. M. Steele, M. Käll, N. J. Halas, and P. Nordlander. Plasmons in the Metallic Nanoparticle-Film System as a Tunable Impurity Problem. *Nano Letters*, 5(10):2009–2013, 2005.

[90] L. Polavarapu, J. Pérez-Juste, Q.-H. Xu, and L. M. Liz-Marzán. Optical sensing of biological, chemical and ionic species through aggregation of plasmonic nanoparticles. *Journal of Materials Chemistry C*, 2(36):7460–7476, 2014.

[91] V. D. Miljković, T. Shegai, M. Käll, and P. Johansson. Mode-specific directional emission from hybridized particle-on-a-film plasmons. *Optics Express*, 19(14):12856–12864, 2011.

[92] P. Nordlander and E. Prodan. Plasmon Hybridization in Nanoparticles near Metallic Surfaces. *Nano Letters*, 4(11):2209–2213, 2004.

[93] B. Yu, J. Woo, M. Kong, and D. M. O'Carroll. Mode-specific study of nanoparticle-mediated optical interactions in an absorber/metal thin film system. *Nanoscale*, 7(31):13196–13206, 2015.

[94] K. Uetsuki, P. Verma, P. Nordlander, and S. Kawata. Tunable plasmon resonances in a metallic nanotip-film system. *Nanoscale*, 4(19):5931–5935, 2012.

[95] J. R. Lakowicz. *Principles of Fluorescence Spectroscopy*. Number 3. Springer, New York City, 3rd edition, 2013.

[96] A. Jablonski. Efficiency of Anti-Stokes Fluorescence in Dyes. *Nature*, 131:839–840, 1933.

[97] M. Fox. *Optical Properties of Solids*. Oxford University Press, Oxford, 1st edition, 2001.

[98] K. Ray and J. R. Lakowicz. Metal-enhanced fluorescence lifetime imaging and spectroscopy on a modified SERS substrate. *J. Phys. Chem. C*, 117:15790–15797, 2013.

[99] E. Fermi. Quantum Theory of Radiation. *Reviews of Modern Physics*, 4(1):88–132, 1932.

[100] S. V. Gaponenko. *Introduction to Nanophotonics*. Cambridge University Press, Cambridge, 1st edition, 2010.

[101] M. Fox. *Quantum Optics An Introduction*, volume 53. Oxford University Press, Oxford, 1st edition, 2013.

[102] J. Kalinowski, C. Sekine, Y. Tsubata, T. Yamada, and M. Kitano. Recent progress of high performance polymer OLED and OPV materials for organic printed electronics. *Science and Technology of Advanced Materials*, 15(3):1–15, 2014.

[103] R. H. Friend. Conjugated polymers. New materials for optoelectronic devices*. *Pure Appl. Chem.*, 73(3):425–430, 2001.

[104] H. Hoppe and N. S. Sariciftci. Organic solar cells: An overview. *Materials Research Society*, 19(7):1924–1945, 2004.

[105] T. C. Gokoglan, S. Soylemez, M. Kesik, I. B. Dogru, O. Turel, R. Yuksel, H. E. Unalan, and L. Toppare. A novel approach for the fabrication of a flexible glucose biosensor: The combination of vertically aligned CNTs and a conjugated polymer. *Food Chemistry*, 220:299–305, apr 2017.

[106] G. W. Ford and W. H. Weber. Electromagnetic Interactions of Molecules With Metal Surfaces With Metal Surfaces. *Physics Reports*, 113(4):195–287, 1984.

[107] D. A. Long. *The Raman effect: A Unified Treatment of the Theory of Raman Scattering by Molecules*, volume 8. Wiley, New Jersey, 1st edition, 2002.

[108] K. D. Beffield, K. D. Beffield, D. J. Hagan, D. J. Hagan, R. a. Negres, R. a. Negres, M. Fan, and M. Fan. Two-photon photochromism of a photorefractive organic material for holographic recording. *Chemistry of Materials*, 14(5):3663–3667, 2002.

[109] M. G. Papadopoulos, A. J. Sadlej, and J. Leszczynski. *Non-Linear Optical Properties of Matter: From Molecules to Condensed Phases*. Springer, Dordrecht, 1st edition, 2006.

[110] T. Hart, R. Aggarwal, and B. Lax. Temperature Dependence of Raman Scattering in Silicon. *Physical Review B*, 1(2):638–642, 1970.

[111] S. Gaponenko. Effects of photon density of states on Raman scattering in mesoscopic structures. *Physical Review B*, 65(14):1–4, 2002.

[112] G. McNay, D. Eustace, W. E. Smith, K. Faulds, and D. Graham. Surface-Enhanced Raman Scattering (SERS) and Surface-Enhanced Resonance Raman Scattering (SERRS): A Review of Applications. *Applied Spectroscopy*, 65(8):825–837, 2011.

[113] Y. Wang and J. Irudayaraj. Surface-enhanced Raman spectroscopy at single-molecule scale and its implications in biology. *Philosophical transactions of the Royal Society of London. Series B, Biological sciences*, 368(1611):1–10, 2013.

[114] A. J. Haes and R. P. Van Duyne. A Nanoscale Optical Biosensor: Sensitivity and Selectivity of an Approach Based on the Localized Surface Plasmon Resonance Spectroscopy of Triangular Silver Nanoparticles. *Journal of the American Chemical Society*, 124(35):10596–10604, 2002.

[115] J. Zhao, X. Zhang, C. R. Yonzon, A. J. Haes, and R. P. Van Duyne. Localized surface plasmon resonance biosensors. *Nanomedicine*, 1(2):219–228, aug 2006.

[116] B. Sepúlveda, P. C. Angelomé, L. M. Lechuga, and L. M. Liz-Marzán. LSPR-based nanobiosensors. *Nano Today*, 4(3):244–251, jun 2009.

[117] M. Vendrell, K. K. Maiti, K. Dhaliwal, and Y.-T. Chang. Surface-enhanced Raman scattering in cancer detection and imaging. *Trends in biotechnology*, 31(4):249–257, apr 2013.

[118] L.-J. Xu, C. Zong, X.-S. Zheng, P. Hu, J.-M. Feng, and B. Ren. Label-free Detection of Native Proteins by Surface-enhanced Raman Spectroscopy Using Iodide-Modified Nanoparticles. *Analytical chemistry*, 86(4):2238–2245, mar 2014.

[119] J. N. Anker, W. P. Hall, O. Lyandres, N. C. Shah, J. Zhao, and R. P. Van Duyne. Biosensing with plasmonic nanosensors. *Nature Materials*, 7(6):442–453, jun 2008.

[120] E. C. Le Ru, M. Meyer, and P. G. Etchegoin. Proof of single-molecule sensitivity in Surface Enhanced Raman Scattering (SERS) by means of a two-analyte technique. *Journal of Physical Chemistry B*, 110(4):1944–1948, 2006.

[121] P. J. G. Goulet and R. F. Aroca. Distinguishing Individual Vibrational Fingerprints: Raman Scattering from One-to-One Binary Mixtures in Langmuir-Blodgett Monolayers. *Anal. Chem.*, 79(7):2728–2734, 2007.

[122] S. Schlucker. Surface-Enhanced Raman Spectroscopy: Concepts and Chemical Applications. *Angewandte Chemie - International Edition*, 53(19):4756–4795, 2014.

[123] C. Oubre and P. Nordlander. Optical Properties of Metallodielectric Nanostructures Calculated Using the Finite Difference Time Domain Method. *The Journal of Physical Chemistry B*, 108(46):17740–17747, 2004.

[124] K. S. Yee. Numerical Solution of Initial Value Problems of Maxwells Equations in Isotropic Media. *IEEE Trans. Antennas Propag*, 14(3):302–307, 1966.

[125] J. B. Schneider. *Understanding the Finite-Difference Time-Domain Method*. School of Electrical Engineering and Computer Science Washington State University, Washington, 1st edition, 2014.

[126] J.-P. Berenger. A perfectly matched layer for the absorption of electromagnetic waves. *Journal of Computational Physics*, 114(2):185–200, oct 1994.

[127] S. D. Gedney and B. Zhao. An Auxiliary Differential Equation Formulation for the Complex-Frequency Shifted PML. *IEEE*, 58(3):838–847, 2010.

[128] Lumerical. Near to far field projections, https://kb.lumerical.com/en/ref_scripts_near_to_far_field_projections.html, 2017.

[129] R. J. Luebbers, S. Member, K. S. Kunz, S. Member, M. Schneider, and F. Hunsberger. A Finite-Difference Time-Domain Near Zone to Far Zone Transformation. *IEEE Trans. Antennas Propag*, 39(4):429–433, 1991.

[130] A. Taflove and S. C. Hagness. *Computational Electrodynamics: The Finite-Difference Time-Domain Method*. Artech House, London, 3rd edition, 2005.

[131] W. Yu, S. Member, R. Mittra, and L. Fellow. A Conformal Finite Difference Time Domain Technique for Modeling Curved Dielectric Surfaces. *IEEE Microw. Compon. Lett*, 11(1):25–27, 2001.

[132] S. Kubo, A. Diaz, Y. Tang, T. S. Mayer, I. C. Khoo, and T. E. Mallouk. Tunability of the Refractive Index of Gold Nanoparticle Dispersions. *Nano Letters*, 7(11):3418–3423, 2007.

[133] M. Hu, A. Ghoshal, M. Marquez, and P. G. Kik. Single Particle Spectroscopy Study of Metal-Film-Induced Tuning of Silver Nanoparticle Plasmon Resonances. *J. Phys. Chem.*, 114:7509–7514, 2010.

[134] C. Ciracì, R. T. Hill, J. J. Mock, Y. Urzhumov, A. I. Fernández-Domínguez, S. A. Maier, J. B. Pendry, A. Chilkoti, and D. R. Smith. Probing the Ultimate Limits of Plasmonic Enhancement. *Science*, 337(6098):1072–1074, aug 2012.

[135] M. Chirumamilla, A. Gopalakrishnan, A. Toma, R. P. Zaccaria, and R. Krahne. Plasmon resonance tuning in metal nanostars for surface enhanced Raman scattering. *Nanotechnology*, 25(235303):1–7, 2014.

[136] Y. Huang, Q. Zhou, M. Hou, L. Ma, and Z. Zhang. Nanogap effects on near- and far-field plasmonic behaviors of metallic nanoparticle dimers. *Phys. Chem. Chem. Phys.*, 17(43):29293–29298, 2015.

[137] S. L. Kleinman, B. Sharma, M. G. Blaber, A.-I. Henry, N. Valley, R. Gri, M. J. Natan, G. C. Schatz, and R. P. V. Duyne. Structure Enhancement Factor Relationships in Single Gold Nanoantennas by Surface-Enhanced Raman Excitation Spectroscopy. *Journal of the American Chemical Society*, 135(1):301–308, 2013.

[138] A. Lombardi, A. Demetriadou, L. Weller, P. Andrae, F. Benz, R. Chikkaraddy, J. Aizpurua, and J. J. Baumberg. Anomalous Spectral Shift of Near- And Far-Field Plasmonic Resonances in Nanogaps. *ACS Photonics*, 3(3):471–477, 2016.

[139] Q. Fu, D. Zhang, Y. Chen, X. Wang, L. Han, L. Zhu, P. Wang, and H. Ming. Surface enhanced Raman scattering arising from plasmonic interaction between silver nano-cubes and a silver grating. *Applied Physics Letters*, 103(041122):1–5, 2013.

[140] J. P. Litz, J. P. Camden, and D. J. Masiello. Spatial, spectral, and coherence mapping of single-molecule SERS active hot spots via the discrete-dipole approximation. *Journal of Physical Chemistry Letters*, 2(14):1695–1700, 2011.

[141] J. Zhang, J. Li, S. Tang, Y. Fang, J. Wang, G. Huang, R. Liu, L. Zheng, X. Cui, and Y. Mei. Whispering-gallery nanocavity plasmon-enhanced Raman spectroscopy. *Scientific Reports*, 5(15012):1–7, 2015.

[142] I. Choi and Y. Choi. Plasmonic Nanosensors: Review and Prospect. *IEEE Journal of Selected Topics in Quantum Electronics*, 18(3):1110–1121, may 2012.

[143] M. C. Chen and R. C. Lord. Laser-excited Raman Spectroscopy of Biomolecules. VIII. Conformational Study of Bovine Serum Albumin. *Journal of the American Chemical Society*, 98(4):990–992, feb 1976.

[144] B. A. Bolton and J. R. Scherer. Raman spectra and water absorption of bovine serum albumin. *The Journal of Physical Chemistry*, 93(22):7635–7640, nov 1989.

[145] S. Cavalu, S. Cinta-Pinzaru, N. Leopold, and W. Kiefer. Raman and Surface Enhanced Raman Spectroscopy of 2,2,5,5-Tetramethyl-3-pyrrolin-1-yloxy-3-carboxamide Labeled Proteins: Bovine Serum Albumin and Cytochrome c. *Biopolymers*, 62(6):341–348, jan 2001.

[146] R. L. Remmele, P. McMillan, and A. Bieber. Raman Spectroscopic Studies of Hen Egg-White Lysozyme at High Temperatures and Pressures. *Journal of protein chemistry*, 9(4):475–486, 1990.

[147] D. Zhang, Y. Xie, M. F. Mrozek, C. Ortiz, V. J. Davisson, and D. Ben-Amotz. Raman Detection of Proteomic Analytes. *Analytical chemistry*, 75(21):5703–5709, nov 2003.

[148] G. L. Weissler and W. R. Carlson. *Vacuum Physics and Technology (Methods in Experimental Physics Volume 14)*. Academic Press, Massachusetts, 1st edition, 1980.

[149] J. E. Greivenkamp. *Field Guide to Geometrical Optics*. SPIE Press, Bellingham, 1st edition, 2004.

[150] Horiba. www.horiba.com/fileadmin/uploads/Scientific/Documents/Mono/iHR_Brochure-2013.pdf, 2013.

[151] E. Hecht. *Optics*. Addison-Wesley, Boston, 4th edition, 2013.

[152] J. H. Parker, D. Feldman, and M. Ashkin. Raman Scattering by Silicon and Germanium. *Physical Review*, 155(3):712–714, 1966.

[153] V. G. Kravets and V. Y. Kolmykova. Raman Scattering of Light in Silicon Nanostructures: First- and Second-Order Spectra. *Optics and Spectroscopy*, 99(1):68–73, 2005.

[154] M. Khorasaninejad, J. Walia, and S. S. Saini. Enhanced first-order Raman scattering from arrays of vertical silicon nanowires. *Nanotechnology*, 23(27):275706, jul 2012.

[155] J. P. Camden, J. A. Dieringer, Y. Wang, D. J. Masiello, L. D. Marks, G. C. Schatz, and R. P. Van Duyne. Probing the Structure of Single-Molecule Surface-Enhanced Raman Scattering Hot Spots. *J. Am. Chem. Soc.*, 130(38):12616–12617, 2008.

[156] T. Hutter, F. M. Huang, S. R. Elliott, and S. Mahajan. Near-field Plasmonics of an Individual Dielectric Nanoparticle above a Metallic Substrate. *Journal of Physical Chemistry C*, 117(15):7784–7790, 2013.

[157] D.-K. Lim, K.-S. Jeon, H. M. Kim, J.-M. Nam, and Y. D. Suh. Nanogap-engineerable Raman-active nanodumbbells for single-molecule detection. *Nature materials*, 9(1):60–67, 2009.

[158] M. Moskovits. Plasmonic Properties of Gold Nanoparticles Separated from a Gold Mirror by an Ultrathin Oxide. *Nano Letters*, 12:2088–2094, 2012.

[159] Y. Fang and Y. Huang. Electromagnetic field redistribution in hybridized plasmonic particle-film system. *Applied Physics Letters*, 102(153108):1–5, 2013.

[160] P. P. Maharjan, Q. Chen, L. Zhang, O. Adebanjo, N. Adhikari, S. Venkatesan, P. Adhikary, B. Vaagensmith, and Q. Qiao. Photovoltaic devices and characterization of a dodecyloxybenzothiadiazole-based copolymer. *Physical Chemistry Chemical Physics*, 15(18):6856–6863, 2013.

[161] R. W. Taylor, F. Benz, D. O. Sigle, R. W. Bowman, P. Bao, J. S. Roth, G. R. Heath, S. D. Evans, and J. J. Baumberg. Watching individual molecules flex within lipid membranes using SERS. *Scientific reports*, 4(5940):1–6, 2014.

[162] D. O. Sigle, S. Kasera, L. O. Herrmann, A. Palma, B. de Nijs, F. Benz, S. Mahajan, J. J. Baumberg, and O. A. Scherman. Observing Single Molecules Complexing with Cucurbit[7]uril through Nanogap Surface-Enhanced Raman Spectroscopy. *The Journal of Physical Chemistry Letters*, 7(4):704–710, feb 2016.

[163] Y. Huang, L. Ma, M. Hou, J. Li, Z. Xie, and Z. Zhang. Hybridized plasmon modes and near-field enhancement of metallic nanoparticle-dimer on a mirror. *Scientific Reports*, 6(1):1–9, sep 2016.

[164] S.-Y. Ding, J. Yi, J.-F. Li, B. Ren, R. Panneerselvam, and Z.-Q. Tian. Nanostructure-based plasmon-enhanced Raman spectroscopy for surface analysis of materials. *Nature reviews*, 1(16021):1–16, 2016.

[165] J.-M. Nam, J.-W. Oh, H. Lee, and Y. D. Suh. Plasmonic Nanogap-Enhanced Raman Scattering with Nanoparticles. *Accounts of chemical research*, 49:2746–2755, 2016.

[166] N. Sultanova, S. Kasarova, and I. Nikolov. Dispersion Properties of Optical Polymers. *ACTA PHYSICA POLONICA A*, 116(4):585–587, 2009.

[167] A. P. Edwards and A. M. Adawi. Plasmonic nanogaps for broadband and large spontaneous emission rate enhancement. *Journal of Applied Physics*, 115(5), 2014.

[168] D. Cunningham, R. E. Littleford, W. E. Smith, P. J. Lundahl, I. Khan, D. W. McComb, D. Graham, and N. Laforest. Practical control of SERRS enhancement. *Faraday Discuss.*, 132:135–145, 2006.

[169] Nanopartz. http://www.nanopartz.com/Current Stock COAs/ A12-50-600-CTAB.pdf, 2017.

[170] A. B. Zrimsek, N. L. Wong, and R. P. Van Duyne. Single Molecule Surface-Enhanced Raman Spectroscopy: A Critical Analysis of the Bianalyte versus Isotopologue Proof. *Journal of Physical Chemistry C*, 120(9):5133–5142, 2016.

[171] X. N. He, Y. Gao, M. Mahjouri-Samani, P. N. Black, J. Allen, M. Mitchell, W. Xiong, Y. S. Zhou, L. Jiang, and Y. F. Lu. Surface-enhanced Raman spectroscopy using gold-coated horizontally aligned carbon nanotubes. *Nanotechnology*, 23(20):205702, may 2012.

[172] Z. Wang and L. J. Rothberg. Structure and Dynamics of Single Conjugated Polymer Chromophores by Surface-Enhanced Raman Spectroscopy. *ACS Nano*, 1(4):299–306, 2007.

[173] M. J. Walter, J. M. Lupton, K. Becker, J. Feldmann, G. Gaefke, and S. Ho. Simultaneous Raman and Fluorescence Spectroscopy of Single Conjugated Polymer Chains. *Physical Review Letters*, 98(13):137401, 2007.

[174] R. K. Gupta, K. Ghosh, P. K. Kahol, J. Yoon, and S. Guha. Pulsed laser thin film growth of di-octyl substituted polyfluorene and its co-polymers. *Applied Surface Science*, 254(21):7069–7073, aug 2008.

[175] T. Chung, S.-Y. Lee, E. Y. Song, H. Chun, and B. Lee. Plasmonic Nanostructures for Nano-Scale Bio-Sensing. *Sensors*, 11(12):10907–10929, nov 2011.

[176] L. B. Sagle, L. K. Ruvuna, J. A. Ruemmele, and R. P. Van Duyne. Advances in localized surface plasmon resonance spectroscopy biosensing. *Nanomedicine*, 6(8):1447–1462, oct 2011.

[177] E. N. Lewis, W. Qi, L. H. Kidder, S. Amin, S. M. Kenyon, and S. Blake. Combined Dynamic Light Scattering and Raman Spectroscopy Approach for Characterizing the Aggregation of Therapeutic Proteins. *molecules*, 19(12):20888–20905, 2014.

[178] L. He, E. A. Smith, M. J. Natan, and C. D. Keating. The Distance-Dependence of Colloidal Au-Amplified Surface Plasmon Resonance. *Journal of Physical Chemistry B*, 108(30):10973–10980, 2004.

[179] F. Le, N. Z. Lwin, N. J. Halas, and P. Nordlander. Plasmonic interactions between a metallic nanoshell and a thin metallic film. *Physical Review B - Condensed Matter and Materials Physics*, 76(16):2845–2849, oct 2007.

[180] D. Yang, S. Kita, F. Liang, C. Wang, H. Tian, Y. Ji, M. Loncar, and Q. Quan. High sensitivity and high Q -factor nanoslotted parallel quadrabeam photonic crystal cavity for real-time and label-free sensing. *Applied Physics Letters*, 105(6):2013–2016, 2014.

[181] Y. Akahane, T. Asano, B.-S. Song, and S. Noda. High-Q photonic nanocavity in a two-dimensional photonic crystal. *Nature*, 425(6961):944–947, oct 2003.

[182] B.-S. Song, S. Noda, T. Asano, and Y. Akahane. Ultra-high-Q photonic double-heterostructure nanocavity. *Nature Materials*, 4(3):207–210, 2005.

[183] Y. Tanaka, J. Upham, T. Nagashima, T. Sugiya, T. Asano, and S. Noda. Dynamic control of the Q factor in a photonic crystal nanocavity. *Nature materials*, 6(11):862–865, 2007.

[184] J. Y. Lee and S. N. Hwang. A high-gain boost converter using voltage-stacking cell. *Transactions of the Korean Institute of Electrical Engineers*, 57(6):982–984, 2008.

[185] I. M. White and X. Fan. On the performance quantification of resonant refractive index sensors. *Opt. Express*, 16(2):1020–1028, 2008.

[186] B. Min, E. Ostby, V. Sorger, E. Ulin-Avila, L. Yang, X. Zhang, and K. Vahala. High-Q surface-plasmon-polariton whispering-gallery microcavity. *Nature*, 457(7228):455–458, 2009.

[187] Z. Yu and S. Fan. Extraordinarily high spectral sensitivity in refractive index sensors using multiple optical modes. *Opt. Express*, 19(11):10029–10040, 2011.

[188] D. Yang, H. Tian, Y. Ji, and Q. Quan. Design of simultaneous high-Q and high-sensitivity photonic crystal refractive index sensors. *Journal of the Optical Society of America B*, 30(8):2027–2031, 2013.

[189] H. Sekoguchi, Y. Takahashi, T. Asano, and S. Noda. Photonic crystal nanocavity with a Q-factor of ˜9 million. *Optics Express*, 22(1):916–924, 2014.

[190] T. Nakamura, Y. Takahashi, Y. Tanaka, T. Asano, and S. Noda. Improvement in the quality factors for photonic crystal nanocavities via visualization of the leaky components. *Optics Express*, 24(9):9541–9549, 2016.

[191] Y. Panitchob, G. S. Murugan, M. N. Zervas, and J. S. Wilkinson. Q-factor and waveguide-sphere separation effects in waveguide-coupled microsphere resonators. *SPIE*, 6793(1):1–6, 2008.

[192] K. Lodewijks, W. Van Roy, G. Borghs, L. Lagae, and P. Van Dorpe. Boosting the Figure-Of-Merit of LSPR-Based Refractive Index Sensing by Phase-Sensitive Measurements. *Nano Letters*, 12(3):1655–1659, mar 2012.

[193] K. A. Willets and R. P. Van Duyne. Localized surface plasmon resonance spectroscopy and sensing. *Annual review of physical chemistry*, 58:267–97, 2007.

[194] S. Szunerits and R. Boukherroub. Sensing using localised surface plasmon resonance sensors. *Chemical communications (Cambridge, England)*, 48(72):8999–9010, sep 2012.

[195] Y. Liu and C. Z. Huang. Screening sensitive nanosensors via the investigation of shape-dependent localized surface plasmon resonance of single Ag nanoparticles. *Nanoscale*, 5(16):7458–7466, aug 2013.

[196] E. Kazuma and T. Tatsuma. Localized surface plasmon resonance sensors based on wavelength-tunable spectral dips. *Nanoscale*, 6(4):2397–2405, 2014.

[197] B. Auguié, A. Bruchhausen, and A. Fainstein. Critical coupling to Tamm plasmons. *Journal of Optics*, 17(035003):1–8, 2015.

[198] J. Homola. Surface Plasmon Resonance Sensors for Detection of Chemical and Biological Species. *Chemical reviews*, 108(2):462–493, feb 2008.

[199] L. Rodríguez-Cobo, M. Á. Quintela, and J.-M. López-Higuera. DBR Fiber Laser Sensor With Polarization Mode Suppression. *IEEE Journal of Selected Topics in Quantum Electronics*, 20(5):551–554, sep 2014.

[200] P. Lova, G. Manfredi, L. Boarino, A. Comite, M. Laus, M. Patrini, F. Marabelli, C. Soci, and D. Comoretto. Polymer Distributed Bragg Reflectors for Vapor Sensing. *ACS Photonics*, 2(4):537–543, 2015.

[201] X. Fan, I. M. White, S. I. Shopova, H. Zhu, J. D. Suter, and Y. Sun. Sensitive optical biosensors for unlabeled targets: A review. *Analytica Chimica Acta*, 620(1-2):8–26, jul 2008.